Exploring Quantum Magnetism in Various Spin Models: An Experimental Study

by

Aly H. Abdeldaim

A thesis submitted to the University of Birmingham for the degree of

DOCTOR OF PHILOSOPHY

UNIVERSITY OF BIRMINGHAM

School of Chemistry

College of Engineering and Physical Sciences

University of Birmingham

December 2022

Abstract

Correlated many body electron systems provide a rich source of collective quantum phenomena. These depend on the interplay of the spin and orbital degrees of freedom, the hierarchy of the interaction energy scales, alongside the host lattice geometry. This thesis presents an experimental study demonstrating the magnetic properties of various material realizations of spin models that highlight the complex magnetic behavior arising in such strongly correlated systems.

In the first results chapter, a series of $S = 1/2$ Mo^{5+}-based materials, $A\mathrm{MoOP_2O_7}$, where A = Li, Na, K, and Cs, is investigated. Despite a lattice geometry that hosts pairs of Mo^{5+}-containing chains, a combination of magnetometry, specific heat, and inelastic neutron scattering measurements reveals dominant one-dimensional interactions with no frustrating interchain couplings in A = Na, K, Cs. This conclusion is supported by the lack of long-range magnetic order in $\mathrm{KMoOP_2O_7}$, as examined through powder neutron diffraction, and by *ab-initio* calculations which reveal the role of the distortions in the octahedral Mo^{5+} geometry in stabilizing an active magnetic orbital favoring interactions along the chain direction. Meanwhile, $\mathrm{LiMoOP_2O_7}$ was found to adopt an alternative magnetic sublattice comprised of three-legged spin ladders containing octahedrally coordinated Mo^{5+} ions. Evidence for the onset of long-range magnetic order is seen across magnetic susceptibility and specific heat measurements and confirmed through a neutron powder diffraction study. Characterization using inelastic neutron scattering, combined with an *ab-initio*-based simulation of the experimental spectra, confirm this non-frustrated three-legged spin ladder model. However, further optimization of the model parameters remains necessary for an accurate description of the spin Hamiltonian.

Next, the crystal structure and magnetic properties of a novel $j_{\mathrm{eff}} = 1/2$ Ru^{3+}-based system, $\mathrm{RuP_3SiO_{11}}$, are investigated. The trigonal $R\bar{3}c$ crystal structure of this material, which forms a honeycomb magnetic sublattice comprised of Ru^{3+} ions within an octahedral coordination formed by PO_4 groups, is confirmed using synchrotron X-ray diffraction. Magnetometry and specific heat measurements suggest long-range magnetic

order which is revealed to adopt a collinear Néel order through neutron powder diffraction. The relevance of this material to the Kitaev model is then investigated using a combination of inelastic neutron scattering measurements and *ab-initio* models that place RuP_3SiO_{11} within a previously unaccessed region of the extended Kitaev phase diagram. A confirmation of the relevant exchange parameters, however, remains outstanding as a full optimization of the suggested spin model is yet to be completed. The magnetic field and temperature dependence phase diagram is also examined and suggests a critical magnetic field of $H_c = 3.8$ T.

The last results chapter is concerned with the magnetic properties of the α and β psuedo-polymorphs of the $S = 1/2$ Ti^{3+}-based coordination framework, $KTi(C_2O_4)_2{\cdot}xH_2O$. Using a combination of single-crystal X-ray and neutron powder diffraction studies, α-$KTi(C_2O_4)_2{\cdot}xH_2O$ was found to adopt a tetragonal $I4/mcm$ space group with a crystal structure containing a square planar network of Ti^{3+} ions in a square antiprismatic crystal field. Analysis of magnetometry and specific heat data reveal dominant antiferromagnetic interactions along the sides of the squares and minimal frustration across the diagonal. Through a neutron powder diffraction study, a Néel ordered magnetic structure was found to describe the ordered state. These results place α-$KTi(C_2O_4)_2{\cdot}xH_2O$ within the unfrustrated region of the phase diagram of the $S = 1/2$ Heisenberg square antiferromagnet model. In contrast, β-$KTi(C_2O_4)_2{\cdot}2H_2O$, forms a diamond-like magnetic sublattice of Ti^{3+} ions within the the hexagonal $P6_222$ space group. Fitting the $S = 1/2$ Heisenberg diamond lattice antiferromagnet model to the magnetic suscpetibility and specific heat yields exchange parameters that are an order of magnitude larger than in α. *Ab-initio* calculations reveal that it is the interplay of the active magnetic orbital and the superexchange pathway that results in this discrepancy. Finally, an antiferromagnetic structure is characterized by analyzing neutron powder diffraction data. By examining these results, the α and β psuedo-polymorphs are identified as material realizations of the $S = 1/2$ Heisenberg square and diamond lattice antiferromagnet models, respectively.

Acknowledgements

While the experience of a PhD candidacy is quite personal and varied, a commonly expressed sentiment is one of struggle. I am beyond fortunate for having been supervised by Gøran Nilsen and Lucy Clark whose patience, guidance, and kindness has ensured that I will always positively reflect on my time as a PhD student. Your invaluable mentorship and enthusiasm for science has defined the qualities I hold my professional self up to, and I am grateful for having been allowed to follow my curiosity within such a supportive environment. This work would not have been possible without what you have taught me and without your open door policy over the past few years.

I am also thankful for all of the expertise and guidance of the collaborators and instrument scientists whose contributions have enriched this study. The work presented in this thesis is heavily reliant on experiments held at central facilities, and I would like to thank the instrument scientists responsible for these experiments: Dr. Pascal Manuel (WISH), Dr. Alex Gibbs (HRPD), Dr. Dominic Fortes (HRPD), Dr. Jacques Ollivier (IN5), Dr. Clemens Ritter (D20), Dr. Sarah Day (I11), and an additional mention for Dr. Gøran Nilsen (LET). I would also like to acknowledge the fruitful discussions held with Dr. Ross Stewart, Dr. Manh Duc Le, Dr. Aleksandra Krajewska, and Dr. Fabio Orlandi, along with the leads on experiments that have not made it into this thesis including Dr. Hlynur Gretarsson (P01) and Dr. Peter Baker (EMU). All of the *ab-initio* work presented here, which has helped with many of the conclusions of the experimental chapters, has been performed by Prof. Alexander Tsirlin at the University of Leipzig with whom I have been lucky to develop a collaboration with since an early stage of my PhD.

I would also like to acknowledge the University of Liverpool, the University of Birmingham, and the Science and Technology Facilities Council for providing the funding for my PhD and, for the latter, for provision of neutron beam time.

I have worked in multiple laboratories throughout my PhD in which I have been met with nothing but kindness. At the University of Liverpool, I'd like to acknowledge the Rosseinsky group, and in particular Dr. Luke Daniels, Richard Feetham, and Dr. Craig

Robertson for access to furnace and X-ray diffraction facilities. I'd also like to thank Dr. Robin Perry who has been incredibly generous in sharing his laboratory space and equipment during my time at the ISIS Neutron and Muon Source where most of the synthesis for the work presented in Chapter 4 has been conducted. I must also thank Dr. Gavin Stenning who has aided in and performed many of the SQUID and PPMS measurements at the Materials Characterization Laboratory at ISIS.

Having worked across multiple institutes, I have been very fortunate with colleagues and friends that that have been a pleasure to be around. I owe a huge thanks to all past and present members of the Clark group: Katherine Tustain, Jennifer Graham, Tristan Dolling, Sam Ivko, Otto Mustonen, Grady Beckett, and Amie Troath. I would like to extend this especially to Kate and Jen with whom I share many happy memories and who have made beam time much more enjoyable. On the Birmingham side, I'd like to include Tristan who has somehow made the move to the University of Birmingham, in the midst of a global pandemic, a pleasant experience, and to Sam for great company. At ISIS, I have been lucky to find an adoptive group in office G.17 who have been a genuine joy to to be around and who I will very much miss: Anna Herlihy, Edward Stucky, Sarah Mann, Yuan Yue, and Zachary Amato.

Since my move to the UK for this project, I have been immensely fortunate with the support of friends from home and in meeting people who have enriched my life in countless ways. While too many to count, I'd still like to at least try and mention a few: Omar Salah and Shaker Karouni whose friendships have extended across the whole of my adult life; Nour Adilien and Hampus Lindmark whose presence are a joy in itself; Pratik Samant and Anisha Nijhawan with their endless kindness and support; Andreas Laurintzen for the wonderful conversations; and the Castle and Non-books groups who have made the last two years in Oxford just delightful.

Finally, I'd like to thank my wonderful family, especially my father Hazem and mother Azza, for their unwavering support. Your infinite kindness will forever astound me, and nothing of who I am today would have been possible without you.

Contents

List of Figures

List of Tables

Chapter 1

Introduction

The discovery of new materials is essential for the realization of the novel electronic and magnetic properties that are relevant to the needs of modern and future technologies. Ranging from semiconductors[1] to photonics[2] and spintronics[3], amongst many others, at the heart of such technologies is the electron and the competing interactions that it is subject to. Indeed, the physical properties of interacting electron systems are dependent on the extent of electron-electron correlations, the relevant atomic charge, orbital, and spin degrees of freedom, and the geometry of the host lattice. Theoretically describing these interactions and the resulting physical properties, however, is often compromised by the large number of electrons in crystalline solids[4]. This complexity means that model material realizations are essential for both uncovering new physical phenomena and for examining theoretically predicted ground states.

While the analytical tractability of such systems is still quite complicated, great insight on the ground state properties can still be gleaned through approximations. This is notably demonstrated by the Hubbard model in which the energy of an interacting many

electron system on a lattice can be described as

$$H = -t \sum_{<i,j>} \sum_{\sigma} (c^{\dagger}_{i\sigma} c_{j\sigma} + c^{\dagger}_{j\sigma} c_{i\sigma}) + U \sum_{i} n_{i\uparrow} n_{i_{\downarrow}} + \lambda \sum_{i} \boldsymbol{S}_i \cdot \boldsymbol{L}_i \tag{1.1}$$

where the summation only considers the electrons on sites i and j that occupy the same band. The first term is proportional to the kinetic energy whereby an amplitude, t, denotes the energy of electron hopping described by the creation and annihilation operators, $c^{\dagger}_{i\sigma}$ and $c_{j\sigma}$, of an electron moving from site i to the same orbital on site j or vice-versa, for electrons of spin, σ. The second term contains the strength of the on-site electron-electron repulsion that is described by the Coulomb repulsion term, U, whilst considering the number of electrons with spin σ at a particular site i in the orbital such that $n_{i,\sigma} = c^{\dagger}_{i\sigma} c_{i\sigma}$. As depicted in Fig. 1.1, it is through the interplay of these U and t terms that many aspects of the physical properties of even complex systems can be revealed; beyond some critical $U/t \approx 1$ point where U is the dominant energy scale, the Fermi sea of delocalized electrons describing a metallic system is no longer energetically favorable, and a gap develops such that electrons can be assumed to be localized on each site. It is this state, described as a Mott insulator, that characterizes most $3d$ transition metal containing materials and that underlies most of the systems investigated in this study.

For compounds containing heavier transition metal ions with more spatially extended $4d$ and $5d$ orbitals, however, U/t decreases as electron-electron correlations diminish[5]. Meanwhile, the third term in Eq.1.1 which describes the interaction between the electron's spin $\boldsymbol{S}$ and orbital $\boldsymbol{L}$ degrees of freedom—the spin-orbit coupling with strength λ—becomes more significant. As seen in Fig. 1.2, in the presence of λ, which increases proceeding down the periodic table, the interplay of λ and U can result in what is called a spin-orbit assisted Mott insulator[5]. Within this quadrant of the phase diagram, many ground states can arise, and it is the Kitaev materials[6] region that is of interest to a part of this study.

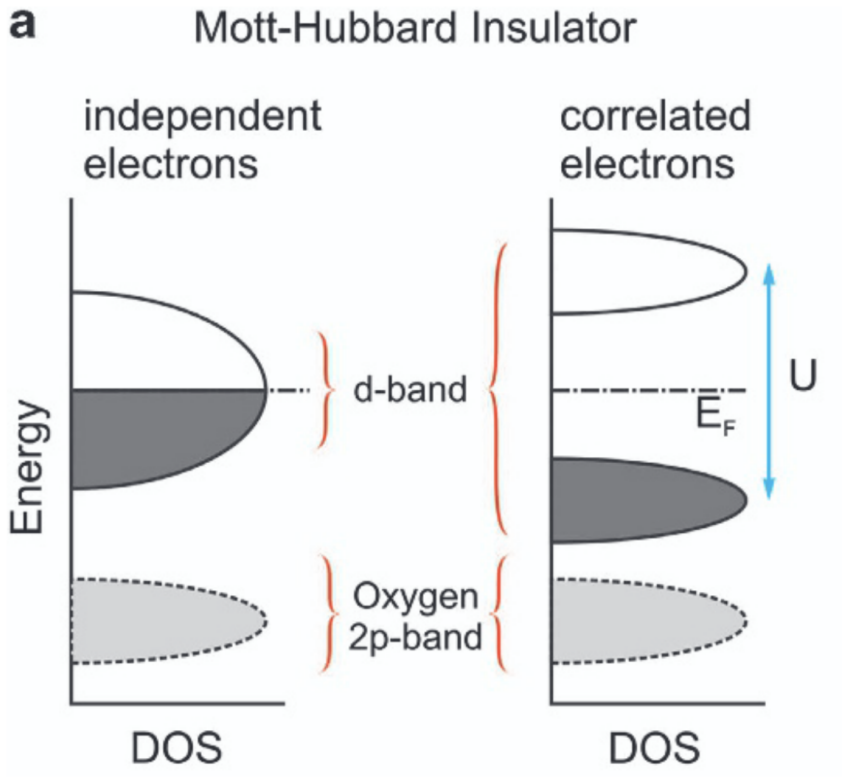

Figure 1.1: Energy diagram of the Hubbard model for (left) independent ($U = 0$, $t > 0$) and (right) correlated d electrons ($U > t$). Figures adapted with permission from reference[7]; copyright CC BY 4.0

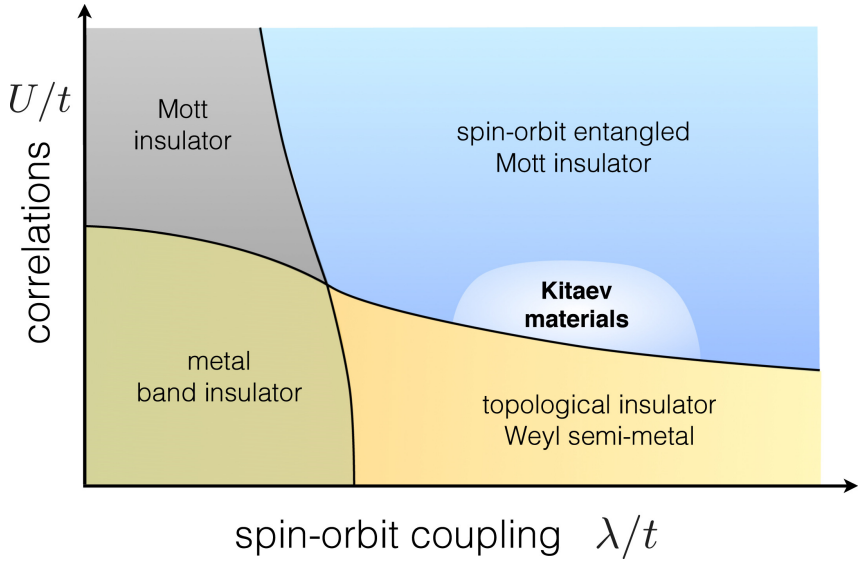

Figure 1.2: Phase diagram of systems where electronic correlations, defined by the Hubbard U, compete with spin-orbit coupling, λ. Figure adapted with permission from reference[8]; copyright CC BY-NC-SA 3.0

This thesis is interested in experimentally examining the unconventional magnetic ground state properties of both spin-orbit assisted and regular Mott insulators for a variety of electronic configurations and on different lattice models. Of particular interest are the dynamic spin ground states, called quantum spin liquids (QSL), that arise when dimensionality and competing energy scales conspire to suppress classical magnetic orders in favor of fluctuating entangled quantum spin states. Interest in such states is motivated by expanding our fundamental understanding of quantum physical phenomena, as well as aspirations of harnessing such states in next-generation technology[9,4]. From an experimentalist's perspective, a crucial aspect for engineering material realizations of these states is uncovering the necessary structural and chemical ingredients that can promote their emergence. This chapter will thus attempt to provide an overview of the underlying physical requirements associated with quantum magnetic ground states. Unless otherwise stated, some of this discussion will be based on Stöhr[10], Khomskii[11,12], and Sakurai[13]. Chapter 2 will focus on highlighting some of the synthetic and the experimental tools necessary for their characterization. The bulk of this thesis will then follow in three experimental chapters covering seven materials that are related to spin models theorized to host unconventional ground states. A summary and concluding remarks will finally follow in Chapter 6 to complete the study.

1.1 Quantum Fluctuations and Anisotropy: Single Ion Physics

The magnetic properties we are concerned with in this thesis arise from unpaired electrons in partially filled d orbitals. To examine the choice of the magnetic ion to study, and to demonstrate the role of isolated magnetic properties in determining the spin Hamiltonian, let us begin by considering the source of magnetism in a single electron. Associated with

electrons are spin ($\boldsymbol{S}$) and orbital ($\boldsymbol{L}$) angular momenta, where the former describes an intrinsic relativistic effect with no classical counterpart, and the latter is the angular momentum due to the orbital motion of an electron around the atomic nucleus. These energies are quantized so that there exist particular eigenvalues that characterize the allowed electronic states with respect to $\boldsymbol{S}$ and $\boldsymbol{L}$. The commuting operators of $\boldsymbol{S}$ and $\boldsymbol{L}$ that characterize a complete description of a spin or orbital angular momentum state are, respectively, $\hat{\boldsymbol{S}}^2$ along with one of its Cartesian $\eta = (x, y, z)$ projection components, conventionally $\hat{S}^z$, and, similarly, $\hat{\boldsymbol{L}}^2$ and $\hat{L}^z$ such that[13]:

$$\hat{\boldsymbol{S}}^2|m_s, s\rangle = \hbar^2 s(s+1)|m_s, s\rangle \tag{1.2}$$

$$\hat{S}^z|m_s, s\rangle = \hbar^2 m_s|m_s, s\rangle \tag{1.3}$$

and

$$\hat{\boldsymbol{L}}^2|m_l, l\rangle = \hbar^2 l(l+1)|m_l, l\rangle \tag{1.4}$$

$$\hat{L}^z|m_l, l\rangle = \hbar^2 m_l|m_l, l\rangle. \tag{1.5}$$

For $\hat{\boldsymbol{S}}^2$ and $\hat{S}^z$, the $|m_s, s\rangle$ eigenstate is described by the spin and spin angular momentum quantum numbers, s and m_s, respectively. For an electron, these take on values of $s = 1/2$ and $m_s^\eta = \pm 1/2$. Meanwhile, the $|m_l, l\rangle$ eigenstate of the orbital angular momentum operators is characterized by the orbital and magnetic quantum numbers, l and m_l, respectively. Here, l can take on integer values up to $n-1$ where $n = 1, 2, 3, \ldots$ is the principle quantum number, and m_l can take on $2l+1$ values ranging between $-l < m_l < l$. In a many electron system with i electrons in the same orbital, the total spin and orbital quantum numbers, $S = \sum_i s_i$ and $L = \sum_i l_i$ are considered instead. A key aspect associated with the quantum-mechanical spin is that only one projection component, here S^z, can be determined at one time, leaving the values of S^x and S^y as undetermined. Associated with this uncertainty are so-called quantum fluctuations which increase with decreasing S and, as we will see, play a large role in stabilizing unconventional magnetic

ground states.

In a similar vein to classical electrodynamics, where the orbital motion of charges give rise to a magnetic moment, both $\boldsymbol{S}$ and $\boldsymbol{L}$ result in atomic magnetic moments, $\boldsymbol{\mu}_{\mathrm{S}}$ and $\boldsymbol{\mu}_{\mathrm{L}}$, whose magnitudes are given by:

$$|\boldsymbol{\mu}_{\mathrm{S}}| = g_{\mathrm{S}}\mu_{\mathrm{B}}\sqrt{S(S+1)}, \tag{1.6}$$

$$\mu_{\mathrm{S}}^{z} = g_{\mathrm{S}}S\mu_{\mathrm{B}} \tag{1.7}$$

and

$$|\boldsymbol{\mu}_{\mathrm{L}}| = g_{\mathrm{L}}\mu_{\mathrm{B}}\sqrt{L(L+1)}, \tag{1.8}$$

$$\mu_{\mathrm{L}}^{z} = g_{\mathrm{L}}L\mu_{\mathrm{B}}. \tag{1.9}$$

Here, $g_{\mathrm{S}} \approxeq 2$ and $g_{\mathrm{L}} = 1$ are g-factors and the Bohr magneton, $\mu_{\mathrm{B}} = q_e\hbar/2m_e$, is a fundamental unit in magnetism dependent on the charge q_e, reduced Planck constant $\hbar$, and the mass of the electron m_e.

The electronic structure of a single ion can then be described following a semi-empirical approach, termed Hund's rules, that minimizes energy[10]:

- Due to Pauli's exclusion principle, where no two electrons can occupy an orbital with the same quantum numbers, the first rule states that spin-spin interactions are minimized by maximizing the total spin angular momentum, S. This can be viewed as minimizing the energy cost, defined by the Hund coupling parameter, J_{H}, of placing spins of identical m_{s} in the same orbital.
- The second rule states that orbital-orbital interactions are minimized by maximizing the total orbital angular momentum, L. In semi-classical terms, this can be seen as minimizing electrostatic interactions by placing electrons in different orbitals of the

closest m_l.

- The third rule states that spin-orbit coupling can be minimized by maximizing the total angular momentum so that $J = L - S$ or $J = L + S$ for less than and more than half filled valence shells, respectively. As explained below, this is also called the Russell-Saunders or LS coupling.

The applicability of Hund's rules is generally restricted to situations in which additional energy scales are small and can be considered as perturbations to the spin Hamiltonian. This distinction defines two spin-orbit coupling schemes, namely LS- and jj-coupling. LS coupling defines the total angular momentum as $\boldsymbol{J} = \boldsymbol{S} + \boldsymbol{L}$ and is generally applicable for $3d$ and some $4d$ transition metal ions where the spin-orbit coupling strength, λ, is $\lambda < J_{\mathrm{H}}$. When $\lambda \gtrsim J_{\mathrm{H}}$, as in $5d$ transition metal ions, Hund's third rule is broken, and jj-coupling is used instead where $J = \sum_i \boldsymbol{j}_i = \sum_i (\boldsymbol{s}_i + \boldsymbol{l}_i)$.

1.1.1 Spin-Orbit Coupling

This picture is further complicated as the spin and orbital angular momenta can interact to produce a total angular momentum, $\boldsymbol{J}$, that can be defined either following the LS-coupling or jj-coupling schemes. Following the same formalism, the commuting operators for $\boldsymbol{J}$, with quantum numbers j and m_j, are:

$$\hat{\boldsymbol{J}}^2 |j, m_j\rangle = J(J+1)\hbar^2 |j, m_j\rangle \tag{1.10}$$

$$\hat{J}^z |j, m_j\rangle = m_j \hbar^2 |j, m_j\rangle. \tag{1.11}$$

The magnitude of the resulting magnetic moment $|\boldsymbol{\mu}_J| = g_{\mathrm{J}}\sqrt{J(J+1)}\mu_{\mathrm{B}}$, is equivalent to the effective magnetic moment used in the experimental chapters, μ_{eff}, where g_{J} is the

Landé g-factor given, for LS coupling, as

$$g_{\mathrm{J}} = g_{\mathrm{L}}\left(\frac{J(J+1)+L(L+1)-S(S+1)}{2J(J+1}\right)+g_{\mathrm{S}}\left(\frac{J(J+1)-L(L+1)+S(S+1)}{2J(J+1)}\right). \tag{1.12}$$

The ordered magnetic moment, μ_{ord}, presented in the experimental chapters is equivalent to the projection of the magnetic moment, $\mu_j^z = g_{\mathrm{j}} J \mu_{\mathrm{B}}$.

The source of this interaction is relativistic in nature but can be motivated semi-classically as arising from a shift in the frame of reference where, along with the electron's orbital motion around a nucleus, a nucleus similarly orbits the electron[14]. Following Maxwell's equations, this orbital motion gives rise to a magnetic field,

$$\mathbf{B} = \frac{1}{2m_e c^2}(\mathbf{p} \times \nabla\Phi), \tag{1.13}$$

that interacts with the electron's intrinsic magnetic moment along a certain projection,

$$\mu_e = 2S\mu_{\mathrm{B}}, \tag{1.14}$$

so that the spin-orbit Hamiltonian, H_{SO}, is given by:

$$H_{\mathrm{SO}} = -\mu_e \cdot \mathbf{B} \tag{1.15}$$

Here, $\mathbf{p}$ is a linear momentum vector where $\boldsymbol{L} = \mathbf{r} \times \mathbf{p}$ when $\mathbf{r}$ is the position vector, c is the speed of light, and $\nabla\Phi = (\mathbf{r}/r)d\Phi(r)/dr$ is the electrostatic potential. Combining the above equations, Eq.1.15 becomes:

$$H_{\mathrm{SO}} = \frac{2\mu_{\mathrm{B}}\hbar}{c^2}\frac{d\Phi(r)}{dr}\boldsymbol{S}\cdot\boldsymbol{L} = \zeta(r)\boldsymbol{S}\cdot\boldsymbol{L} \tag{1.16}$$

where $\zeta(r)$ is the spin-orbit coupling parameter. In a many electron system, $\lambda = \pm\zeta/2S$

is used instead, and the negative and positive signs are used for shells with less or more than half-filling, respectively. As an energy scale, λ is directly proportional to the fourth power of the effective nuclear charge. This highlights that spin-orbit coupling becomes more relevant for heavier $4d$ and $5d$ transition metal ions, where $\lambda \gtrsim 0.1$ eV.

1.1.2 Crystalline Electric Field

For d-electron systems described by $l = 2$, the probability density of the valence shell electrons within the spherical electrostatic field of the nucleus can be approximated with the familiar $2l + 1 = 5$ degenerate d-orbitals (Fig. 1.3(a)). Given the anistropic nature of d-orbitals, the electrostatic potential of a ligand that coordinates a magnetic ion can split the orbital degeneracy depending on the relative spatial distance between the electron probability densities of the interacting ions and on the symmetry of the arrangement of the ligands. As shown in Fig. 1.3(b), this can be demonstrated for an octahedral coordination environment where the five-fold orbital degeneracy is split into a triply degenerate lower lying t_{2g} manifold and a higher-energy doubly degenerate e_g state depending on whether the orbitals contain components overlapping with the electron density of the ligand (Fig. 1.3(a)). Other patterns of splitting are observed depending on the local symmetry; in the case of ligands like O^{2-} and Cl^{-}, the splitting is typically associated with an energy scale of $\Delta \gtrsim 1$ eV.

The interplay of the crystalline electric field (CEF) and spin-orbit coupling can be highlighted by considering the $4d^1$ and $4d^5$ electron configurations of the Mo^{5+} (Chapter 3) and Ru^{3+} (Chapter 4) ions examined in this study. For a $4d$ electron system in an octahedral symmetry, the crystal field splitting separating the t_{2g} and e_g manifolds ranges from $\Delta_o = 1.5 - 3$ eV and is larger than $J_H < 0.6$ eV[16]. This stabilizes a "low-spin" configuration for $4d^5$ ions where the 5 electrons are filled according to Hund's rules thus leaving one unpaired electron within the t_{2g} manifold. As λ ranges from $0.1 - 0.2$ eV and

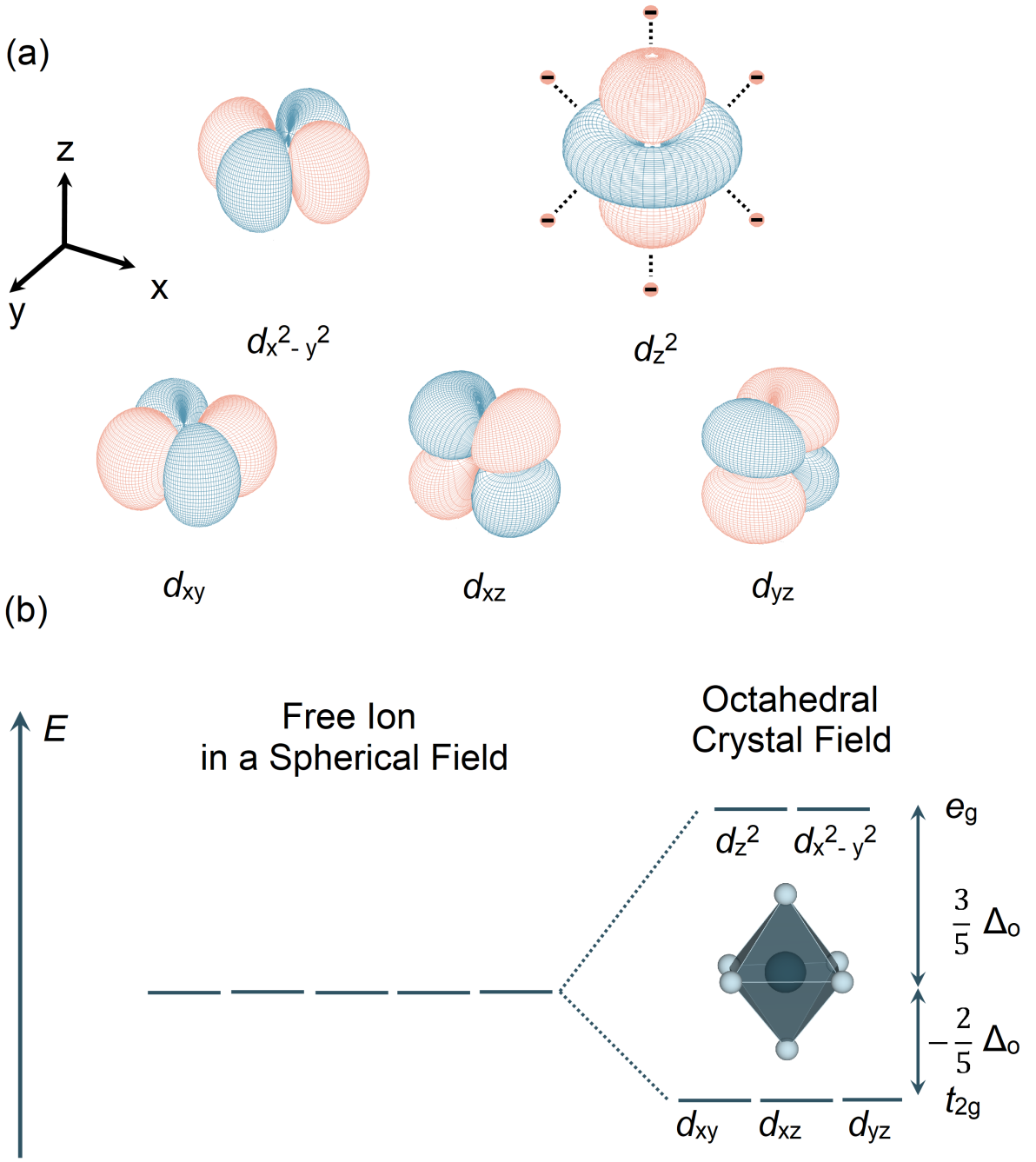

Figure 1.3: (a) Illustrations of the five d-orbitals for $n = 3$. (b) In the spherical potential of a free ion, the orbitals have a five-fold degeneracy. In the presence of an octahedral crystalline electric field, these orbitals are split into two manifolds containing a triply degenerate lower lying t_{2g} state and a higher energy e_g manifold. The isosurfaces of the d-orbitals were calculated and the figures were generated with permission using data from reference[15]. Copyright 2014 American Chemical Society.

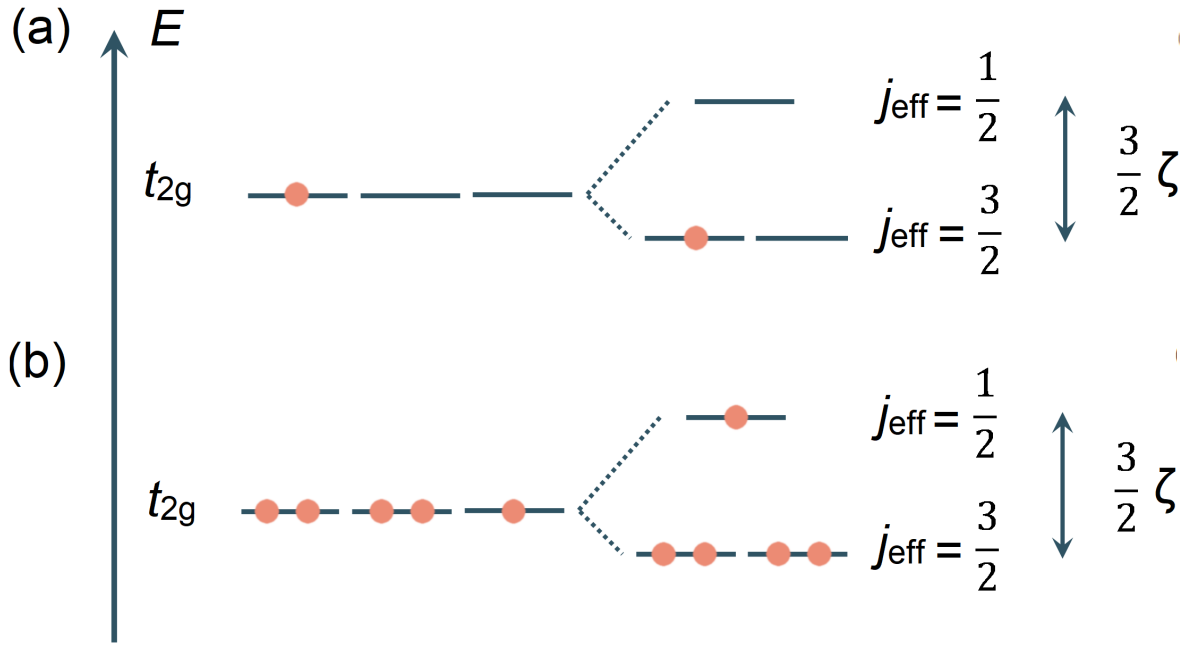

Figure 1.4: Multiplet splitting diagrams of the t_{2g} manifold for (a) d^1 and (b) d^5 electron systems in the presence of an octahedral crystal field and spin-orbit coupling, ζ.

is smaller than J_H, the LS coupling scheme can be used, and hence the total spin quantum number is $S = 1/2$ and is equivalent for both the d^1 and d^5 configurations. Meanwhile, the orbital component is three-fold degenerate within the t_{2g} symmetry which leads to an effective orbital angular momentum of $l_{\text{eff}} = 1$. As thoroughly described elsewhere[17,16], by considering the action of the $\boldsymbol{L}$ operator within the t_{2g} manifold, one finds the relation $\boldsymbol{L} = -\boldsymbol{L}_{\text{eff}}$. When substituting this expression into Eq.1.16, $H_{\text{SO}} = -\lambda \boldsymbol{S}.\boldsymbol{L}_{\text{eff}}$ results, and the signs in Hund's third rule are reversed to positive and negative for less and more than half-filled orbitals, respectively. The total effective angular momentum ground states are hence the psuedospin $J = 3/2$ and $J = 1/2$ states for d^1 and d^5 systems, respectively, with the splittings seen in Fig. 1.4. Following literature nomenclature, these will be described hereafter using the pseudospin $j_{\text{eff}} = J$. Hence, in the case of a $j_{\text{eff}} = 3/2$, the total magnetic moment vanishes as $\boldsymbol{M} = 2\boldsymbol{S} - \boldsymbol{L} = 2(1/2) - 1$[16]. For d^5 electrons, the effective moment is equivalent to that of a $S = 1/2$ system[18] as $\boldsymbol{L} = -1$ and is of dominant orbital character with $\boldsymbol{L} = (4/3)\boldsymbol{J}$ and $\boldsymbol{S} = (-1/3)\boldsymbol{J}$[16].

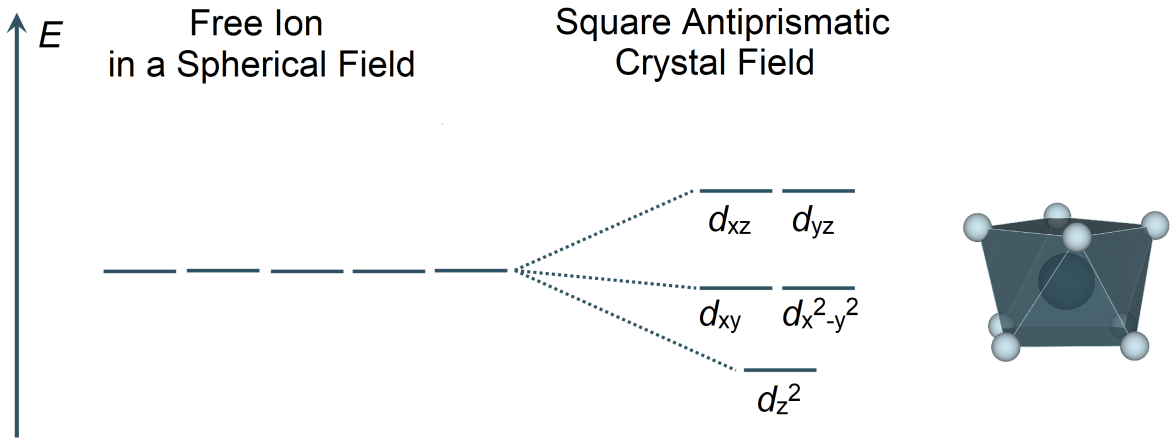

Figure 1.5: Multiplet splitting diagram of a d-electron system in a square antiprismatic crystalline electric field.

It should be noted that within the LS coupling framework, Δ_o is assumed to be infinitely large. In actual materials where $\Delta_o = 1.5 - 3$ eV and $\lambda = 0.1 - 0.2$ eV, finite admixtures of the t_{2g} and e_g states can further alter the multiplet structure[19,20]. Similarly, materials can feature some distortions to the coordination environment that can also modify the electronic structure. An example of this is seen in the materials studied in Chapter 3 where a distortion to the octahedral CEF of the $4d^1$ Mo^{5+} ions lifts the t_{2g} degeneracy and quenches the orbital contribution to result in a $S = 1/2$ ground state. In the square antiprismatic coordination geometry of the $3d^1$ Ti^{3+} systems discussed in Chapter 5, the orbital contribution is also quenched as the non-cubic crystal field splitting favors the L_z magnetic orbital for the ground state (Fig. 1.5). These electronic structures and their resulting effects on the ground state properties of the systems examined in this thesis are further discussed in their respective chapters.

1.1.3 Single Ion Magnetism in an Applied Field

We now turn to the responses of a magnetic atom to an external magnetic field, $\boldsymbol{H}$. This consists of diamagnetism and paramagnetism, where the former is a property of closed shell electron configurations—$\boldsymbol{S} = \boldsymbol{L} = 0$—and is inherent to all atoms. Its effect

corresponds to a temperature independent negative contribution to the magnetization, $\boldsymbol{M} = d\boldsymbol{\mu}/dV$, which describes the distribution of the magnetic moment $\boldsymbol{\mu}$ within a volume, V. Paramagnetism, on the other hand, is present for systems with unpaired electrons and contributes a temperature-dependent positive $\boldsymbol{M}$ that is relatively larger than the diamagnetic contribution. These effects can be illustrated by considering the decrease or increase of the total magnetic flux density, $\boldsymbol{B} = \mu_0(\boldsymbol{H} + \boldsymbol{M})$, where μ_0 is the permeability of free space, in the presence of a dia- or para-magnetic atom, respectively. For paramagnetic materials, the increase in $\boldsymbol{M}$ (and hence $\boldsymbol{B}$) corresponds to an alignment of the magnetic moments with respect to the direction of $\boldsymbol{H}$. Detailed derivations of these phenomena are presented in Khomskii [12].

The response of the magnetization to an applied magnetic field is commonly reported using the molar magnetic susceptibility,

$$\chi_{\mathrm{m}} = \frac{d\boldsymbol{M}}{n\boldsymbol{dH}} \tag{1.17}$$

where n is the number of moles. Within the limit of a linear $M(H)$, the magnetic susceptibility can be approximated as:

$$\chi_{\mathrm{m}} \approx \frac{\boldsymbol{M}}{n\boldsymbol{H}}. \tag{1.18}$$

Hence, across the experimental chapters, unless $M(H)$ is non-linear within the applied magnetic field, M/H will be reported as the magnetic susceptibility, χ. To a first approximation, the temperature dependence of a non-interacting paramagnet (*i.e.* each atom is isolated) takes on the form of the Curie law,

$$\chi = \frac{C}{T}, \tag{1.19}$$

which highlights the role of thermal fluctuations in destabilizing the alignment of magnetic

moments in an applied magnetic field. Here, $C = 3N_A\mu_{eff}^2/3k_B$ where N_A is Avogardro's number and k_B is the Boltzmann constant. The Curie law, however, does not take into account any electron-electron interactions which, as described below, are crucial for describing the collective phenomena arising in magnetic solid-state materials.

1.2 Collective Phenomena: Interactions, Dimensionality, and Competition

The phenomena we have examined so far have focused on the electron and its role in determining the magnetic properties of a single ion. In the crystalline solids we are interested in, these magnetic ions interact to exhibit collective phenomena that are dependent on the type and range of the interactions and the host lattice geometry.

1.2.1 Exchange Interactions

Cornerstone to correlated magnetism is the exchange interaction which is a phenomenon associated with the electrostatic interactions between overlapping wave functions of identical particles. The derivation of the exchange interaction between electrons in overlapping orbitals is well documented in Stöhr[10] and Sakurai[13], and can be understood as a direct consequence of the symmetrization postulate for fermions. The energy scale associated with this interaction is described by the exchange interaction parameter, J, that is often within the range of $0 < |J/k_B| < 1000$ K. Beyond this point and within the experimental chapters, J/k_B will be presented as J. Here, negative and positive values of J denote interactions favoring the parallel or antiparallel alignment of neighboring spins, which are named ferro- (FM) or antiferromagnetic (AFM) interactions, respectively.

As we have alluded to while discussing crystalline electric fields, magnetic materials are commonly comprised of transition metal ions that are in the presence of coordinating ligands. In this case, exchange interactions are not limited to the direct orbital overlap between neighboring magnetic ions. In fact, except for $5d$ electron systems, the spatial extent of the active magnetic d-orbitals is generally much too small in comparison to the crystallographic metal-metal distances of transition metal oxides to result in an appreciable direct exchange interaction. Instead, indirect exchange through non-magnetic ions such as O^{2-} or even longer multi-atom pathways can mediate "superexchange" interactions between neighboring magnetic ions.

The reasoning behind superexchange interactions can be understood within the context of the Hubbard model, first introduced in Eq.1.1, and repeated here for convenience as:

$$H = -t \sum_{<i,j>} \sum_{\sigma} (c^{\dagger}_{i\sigma} c_{j\sigma} + c^{\dagger}_{j\sigma} c_{i\sigma}) + U \sum_{i} n_{i\uparrow} n_{i_{\downarrow}} + \lambda \sum_{i} \boldsymbol{S}_i \cdot \boldsymbol{L}_i \tag{1.20}$$

Within this framework, the magnetic ground state is dependent on the hopping energy of electrons of the same spin states between atoms, t, and the Coulomb repulsion between these electrons, U. Given that the hopping energy is proportional to the kinetic energy, $-t \propto E_{\mathrm{K}}$, and that $E_{\mathrm{K}} \propto 1/r^2$, where r is the distance between particles, delocalizing the electrons across the multiple atoms involved in superexchange increases t and, in turn, minimizes the total energy of the system [10]. As t only involves the hopping of electrons of the same spin states, and in accordance with the Pauli exclusion principle, the resulting exchange favors antiferromagnetic interactions. (Fig. 1.6) [12]. In reality however, the Hubbard model is only an approximation, and the strength and type of superexchange interactions cannot be simply rationalized. Instead, they are highly dependent on the M-L-M bond angle and the M-L orbital overlap, where M and L are the metal and ligand, respectively [21,22].

Using the Hubbard model, one can arrive at a familiar description of the ground state Hamiltonian of magnetically interacting particles[10], the Heisenberg Hamiltonian,

$$H = J \sum_{<i,j>} \boldsymbol{S}_{\mathrm{i}} \cdot \boldsymbol{S}_{\mathrm{j}}, \tag{1.21}$$

where the summation runs over the nearest neighboring i and j spins defined by the spin operator, $\boldsymbol{S}$, and the exchange interaction is $J = 4t^2/U$. However, the Heisenberg Hamiltonian is a limiting case, and in the presence of spin-orbit coupling, exchange interactions do not necessarily need to be isotropic. An exchange tensor, $\mathbb{J}$, for a symmetric anistropic interaction can be described by:

$$H = \sum_{<i,j>} \boldsymbol{S}_i \mathbb{J} \boldsymbol{S}_j \tag{1.22}$$

where

$$\mathbb{J} = \begin{pmatrix} J_{\mathrm{x}} & 0 & 0 \\ 0 & J_{\mathrm{y}} & 0 \\ 0 & 0 & J_{\mathrm{z}} \end{pmatrix}.$$

Depending on the relative strength of the different $\eta = x, y, z$ components of J_η, the dimensionality of the interaction, D, can be one- (Ising), two- (XY), or three-dimensional (Heisenberg) when, for example, $J_{\mathrm{z}} \gg J_{\mathrm{x}} + J_{\mathrm{y}}$, $J_{\mathrm{x}} = J_{\mathrm{y}} \gg J_{\mathrm{z}}$, and $J_{\mathrm{x}} = J_{\mathrm{y}} = J_{\mathrm{z}}$, respectively.

Such exchange anisotropy stems from the interplay of the single ion physics of the magnetic ion and the exchange pathway. Depending on the crystal symmetry, terms beyond those on the diagonal can appear in the exchange tensor. An example is the antisymmetric or Dzyaloshinskii–Moriya (DM) exchange interaction, $\boldsymbol{D}$, defined as:

$$H = \sum_{<i,j>} \boldsymbol{D}_{ij} \cdot \boldsymbol{S}_i \times \boldsymbol{S}_j \tag{1.23}$$

where

$$\boldsymbol{D}_{ij} = \begin{pmatrix} 0 & D^z & -D^y \\ -D^z & 0 & D^x \\ D^y & -D^x & 0 \end{pmatrix}.$$

DM interactions arise in the absence of a center of inversion in the middle of the bond linking the interacting magnetic ions, amongst other symmetry requirements. More complex structures for the exchange tensor can appear, and one such example is presented for the Kitaev model in Chapter 4.

1.2.2 Long-Range Magnetic Order

At this point, let us consider some of the practical aspects highlighted by the discussion of the electronic structure of a single ion, its magnetic moment, and the interactions between them. At high temperatures and in no applied magnetic field, the Curie law suggests that atomic magnetic moments are paramagnetic—randomly aligned due to thermal fluctuations—such that the spins are invariant under symmetry operations. In an extended solid, depending on the type and energy scale of the interactions between the magnetic ions, the magnetic moments could align below some critical temperature where the interactions dominate over thermal fluctuations. The result of this is what is called symmetry breaking; within the paramagnetic regime, the randomly aligned magnetic moments are characterized by a rotational symmetry that is broken as the system undergoes long-range magnetic order[14]. When approximating such interactions using a mean-field approach—all interactions are generalized to one effective interaction—the onset of long-range magnetic order can be illustrated using the Curie-Weiss (CW) law:

$$\chi = \frac{C}{T - \theta_{\mathrm{CW}}}. \tag{1.24}$$

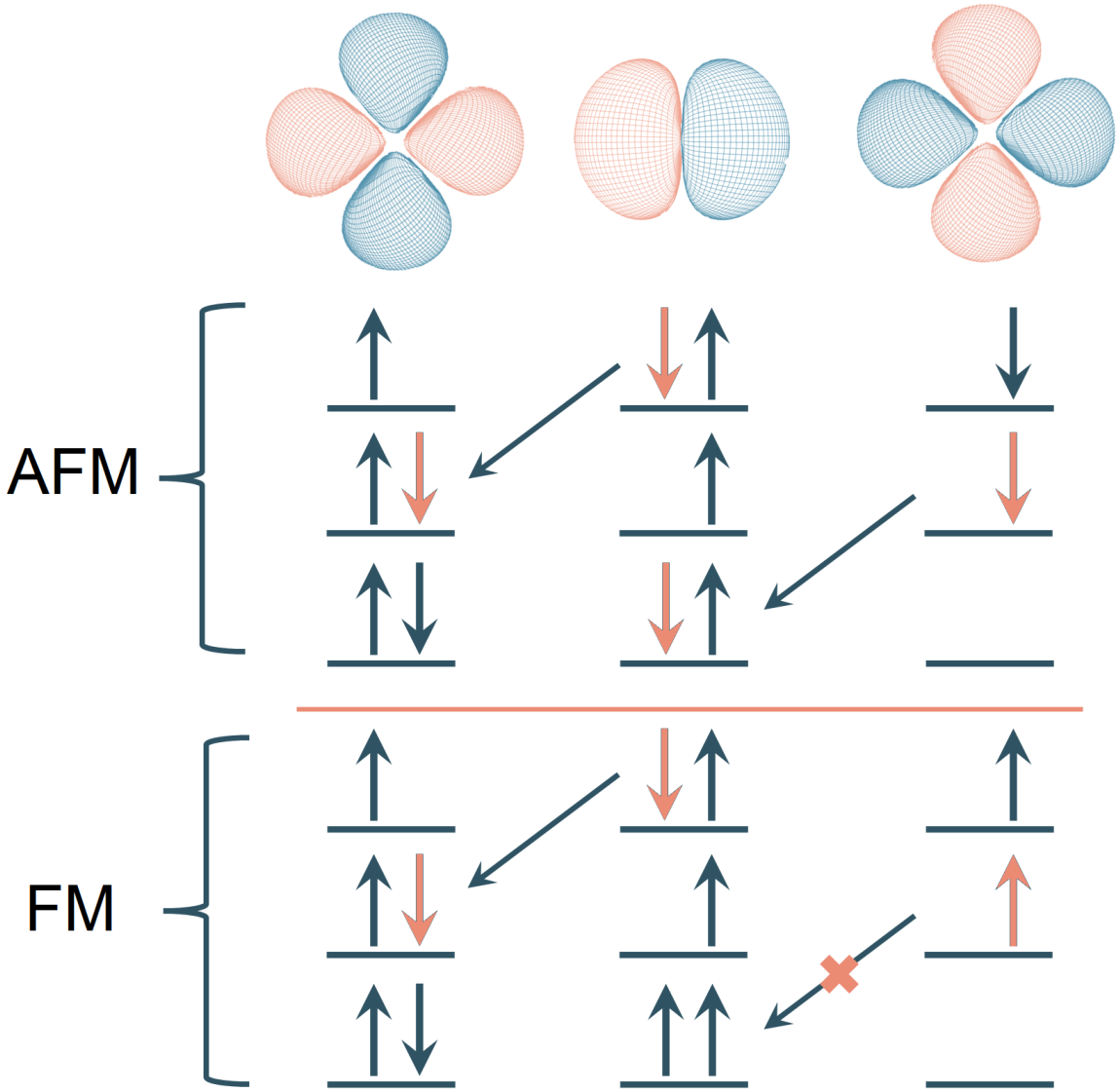

Figure 1.6: Schematic diagram for a superexchange interaction involving a d^1 electron system mediated by a fully occupied p atomic orbital of a ligand. (b) The Pauli exclusion principle favors antiferromagnetic interactions as electron hopping for a ferromagnet is not allowed. Moving electrons are denoted in red. The isosurfaces of the atomic orbitals were calculated and the figures were generated with permission using data from reference [15]. Copyright 2014 American Chemical Society.

Here, the Weiss field, θ_{CW}, characterizes the strength of this effective interaction and can take on negative or positive values that describe dominant antiferro- and ferromagnetic interactions, respectively. Within this approximation, the system can undergo ferro- or antiferromagnetic order where the moments align parallel or antiparallel to one another, respectively, beyond a critical temperature θ_{CW} such that[14]:

$$|\theta_{\mathrm{CW}}| = T_{\mathrm{x}} = \frac{n|\lambda|\mu_{\mathrm{eff}}^2}{3k_{\mathrm{B}}} = -\frac{2zS(S+1)}{3k_{\mathrm{B}}}\sum_i z_i J_i. \tag{1.25}$$

Here, $\mathrm{x} = \mathrm{C}, \mathrm{N}$ so that T_{C} and T_{N} are the Curie and Néel ordering temperatures for ferro- and antiferromagnets, respectively, λ is strength of the mean-field, z is the number of interactions per site i, J is the exchange interaction, and n is the number of magnetic moments per unit volume. Illustrations of FM and AFM orders are shown in Figs. 1.7(a,b).

In real materials, however, the assumptions underlying the CW law render it valid only for temperatures much larger than θ_{CW}, except for simple (*e.g.* cubic) spin models at lower temperatures. As shown in Figs. 1.7(c,d), more complex spin models containing multiple exchange interactions and magnetic sites can result in a diverse set of magnetic orders ranging from, amongst others, ferrimagnetic[23] to helical structures[24,25]. Additionally, true long-range magnetic order (*i.e.* fully ordered magnetic moment) is only an approximation as, even in the absence of thermal fluctuations (*i.e.* $T = 0$), quantum fluctuations can introduce disorder to the system. This is especially true for antiferromagnetic systems where antiferromagnetic order is not the true eigenstate of the spin Hamiltonian and where quantum corrections can play a large role in determining the ground state energy[12]. More complex approximations such as linear spin wave theory (LSWT) are thus necessary for a more accurate description of such effects, as well as for describing the dynamics of the ordered state.

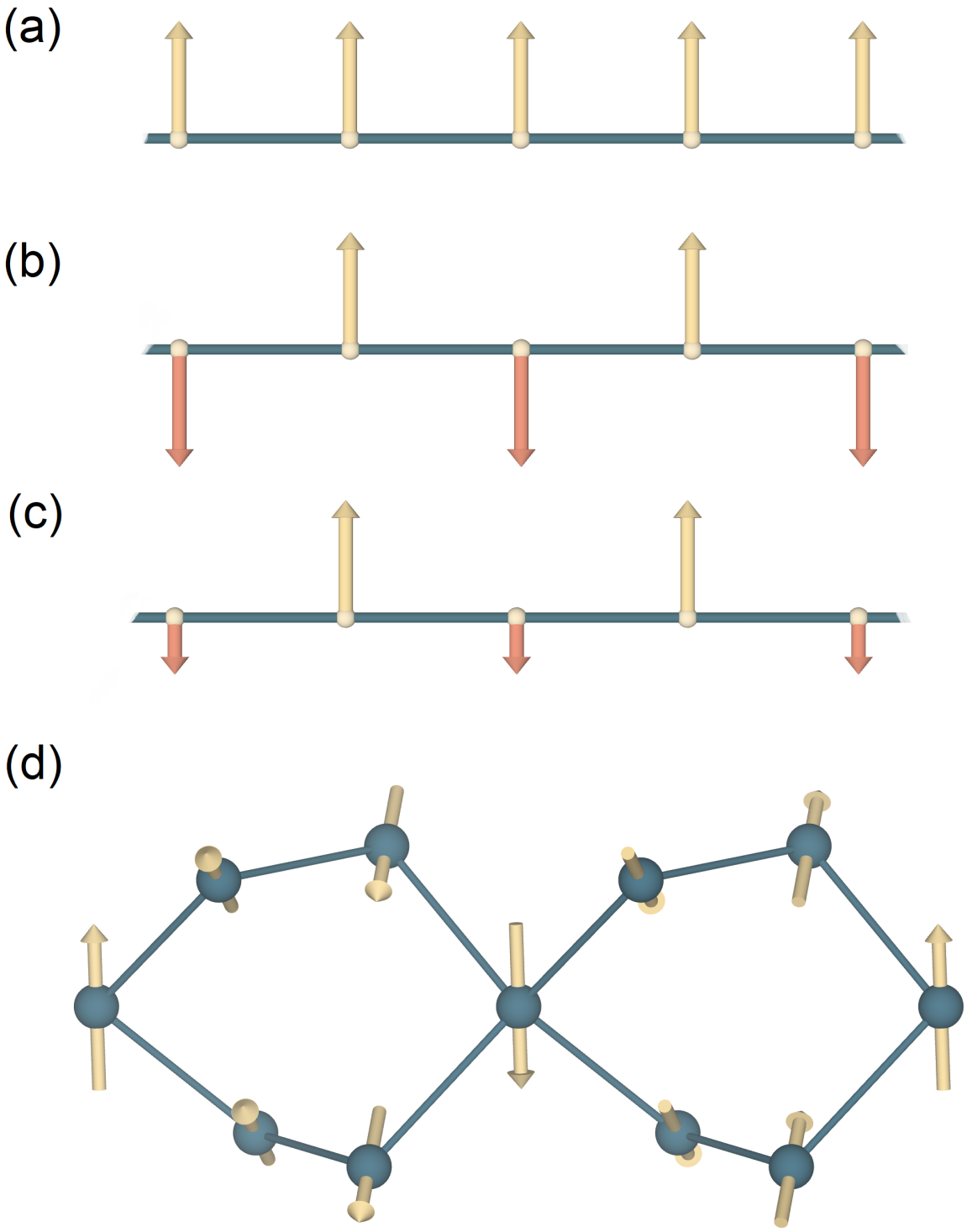

Figure 1.7: Schematic of (a, b) ferro- and antiferromagnetic order on a one-dimensional chain. (c) Ferrimagnetic order where $J_{\mathrm{AFM}} \neq J_{\mathrm{FM}}$ so that the relative moment sizes can vary. (d) One illustration of helical order on a diamond lattice where the moments are rotated according to a certain periodicity. Figures are generated using the `VESTA` visualization software[26].

1.2.3 Linear Spin Wave Theory

The familiar schematic of the static alignment of spins for magnetically ordered structures is only an approximation. In real correlated electron systems, thermal and quantum fluctuations can locally perturb the spins from their average direction to result in collective excitations that are termed spin waves for magnetically ordered systems. This collective behavior can be described by dispersion relations that are dependent on the spin degree of freedom and the type and strength of the exchange interactions characterizing the system. One approach for identifying such dispersion relations and for determining the ground state energy is the semi-classical linear spin wave theory (LSWT). The formalism of LSWT is well documented in Toth[27] and Khomskii[12] where the diagonalization of the spin Hamiltonian is broken down into several steps:

- The spin operators are expressed in terms of creation and annihilation operators for $S = 1$ bosons using the Holstein-Primakoff transformation[28].
- Assuming that quantum fluctuations are minimal—*i.e.* $S^z \approx S$ and $S^x, S^y \ll S$—, the Hamiltonian can be Fourier transformed.
- For AFM systems, an additional step prior to the diagonalization of the spin Hamiltonian is necessary to account for the effects of quantum fluctuations. This is done using the Bogoliubov transformation[29].

For example, the dispersion relations for Heisenberg one-dimensional ferro- and antiferromagnetic spin chains, described by the Hamiltonian,

$$H = J \sum_i \boldsymbol{S}_i \cdot \boldsymbol{S}_{i+1}, \tag{1.26}$$

are, respectively, given by[12]:

$$\hbar\omega(\boldsymbol{k}) = 4JS(1 - \cos(\boldsymbol{k}a)) \tag{1.27}$$

and

$$\hbar\omega(\boldsymbol{k}) = 4JS|\sin(\boldsymbol{k}a)|. \tag{1.28}$$

Here, $\omega(\boldsymbol{k})$ is the spin wave dispersion, a is the spacing between the spins, and $\boldsymbol{k}$ is the wave vector. The resulting spin waves are considered as $S = 1$ quasiparticles termed magnons which correspond to spin excitations delocalized across the system with a total spin change, $\Delta S = 1$.

A few assumptions underlie the formalism of LSWT as it considers spin waves in a harmonic oscillator approximation and leaves out any anharmonic contributions—*i.e.* magnon-magnon interactions[30]. Within this framework, corrections for quantum effects are treated as perturbations[30]. This deems LSWT a reasonable approximation for systems with $S > 1$ and where deviations in the expectation value of the ordered moment, δS, and the associated quantum fluctuations are minimal[27].

1.2.4 Dimensionality, Frustration, and Unconventional Magnetism

1.2.4.1 Low Dimensionality

One example where LSWT fails to predict the ground state is the one-dimensional Heisenberg spin model presented in the previous section. Indeed, low dimensional magnets, which are systems characterized by dominant interactions in only one- or two dimensions, cannot undergo long-range magnetic order at finite temperatures for Heisenberg spins[31].

An exact solution for the $S = 1/2$ Heisenberg chain antiferromagnet model (HAF) confirms this[32]. Yet, this solution demonstrates a few curious aspects as, while the $S = 1/2$ HAF model does not undergo long-range magnetic order, unlike paramagnets where spin-spin correlations exponentially decay over distance, the spins are still long-range or "algebraically" correlated with a spin-spin correlation function $\langle S_0 S_n \rangle \propto r^{-1}$, where r is the distance between the spins, and form a macroscopic spin singlet—$\langle S^{x,y,z} \rangle = 0$. Additionally, unlike the $S = 1$ magnons describing the excitations of long-range ordered systems, the excitations of the $S = 1/2$ HAF model are characterized by gapless fractionalized $S = 1/2$ particle-like excitations termed spinons[33–35]. The differences between these excitations are illustrated in Fig. 1.8 where magnons are classically pictured as local precessions about the mean spin direction in the ordered state. Spinons, on the other hand, are most easily pictured for Ising spins and correspond to two domain walls propagating independently across the chain upon a spin flip excitation. For the Heisenberg case, each spin flip decays into an even number of spinons, with a pair being the most common[36]. Owing to its long-range spin entanglement, this ground state is often called an algebraic spin liquid and it presents a canonical example of unconventional magnetic ground states beyond the paradigm of symmetry breaking.

Low dimensional magnets carrying quantum spins hence appear as a natural starting point to seek out unconventional magnetic ground states. Underlying these phenomena are quantum fluctuations which can more easily perturb static orders as the number of interaction pathways between neighboring magnetic ions, z, decreases[37]. For the HAF model, $z = 2$, and other geometries that manifest similarly small z values range from honeycomb networks ($z = 3$), corner sharing triangles ($z = 4$), to square geometries ($z = 4$), amongst many others.

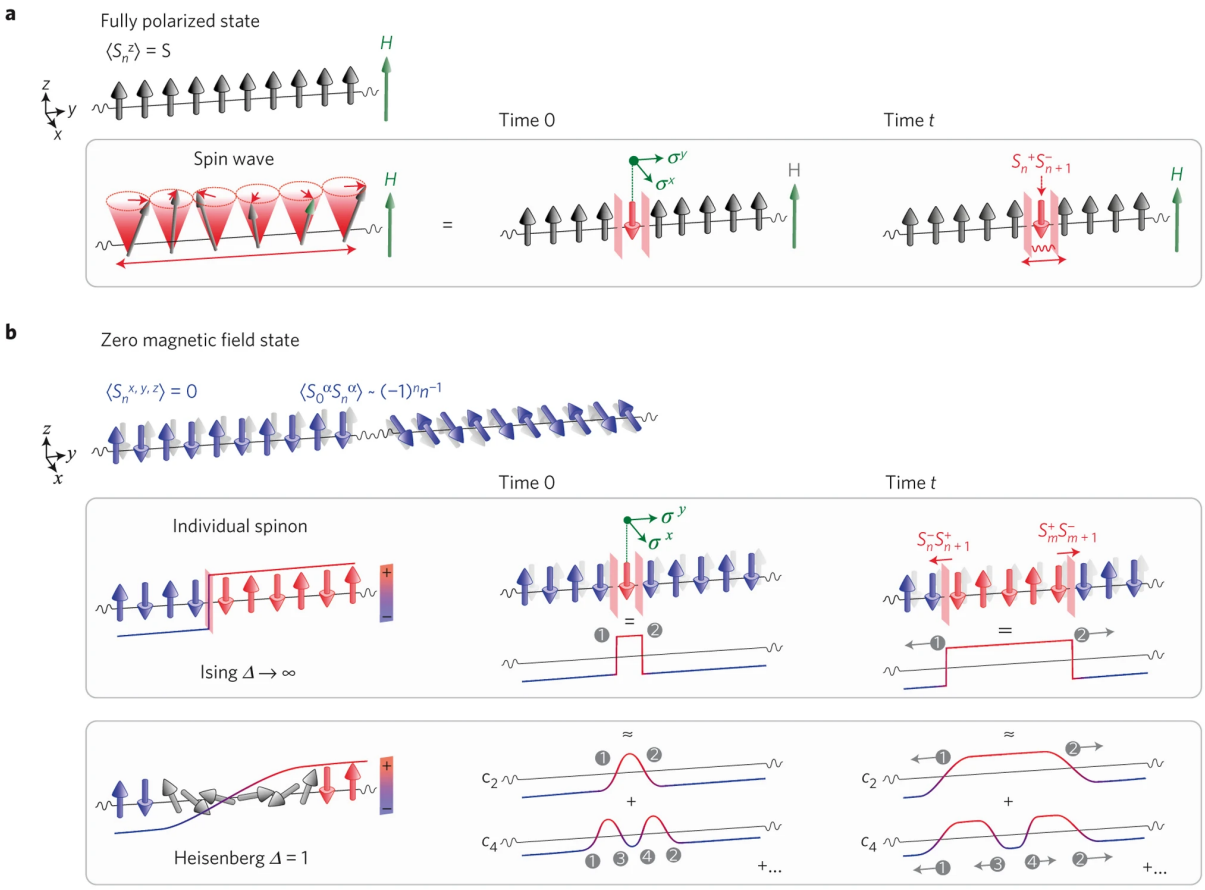

Figure 1.8: (a) A fully polarized static ferromagnetic chain in an applied magnetic field, H. A perturbation to this state, in the form of a spin flip event, travels as a single entity across the chain, and can be classically pictured as a precession of the spins about their mean value. (b) For the $S = 1/2$ Heisenberg one-dimensional antiferromagnet model, the long-distances covered by algebraic correlations are illustrated as antiferromagnetic regions on a chain as the expectation value of the spin-spin correlation function, $\langle S_0^\alpha S_n^\alpha \rangle \propto (-1)^n n^{-1}$, where n is the distance between the atoms. In the Ising limit ($\Delta \to \infty$, $S_n S_{n+1} = S_n^x S_{n+1}^x + S_n^y S_{n+1}^y + \Delta S_n^z S_{n+1}^z$), a spin flip excitation can be pictured as two domain walls propagating across the chain. For Heisenberg spins ($\Delta = 1$), a higher order of even numbers of spinons form a series of such domain walls[36]. Figures adapted with permission from reference[36]; copyright Springer [Nature Physics], 2013

.

1.2.4.2 Competing Interactions

An additional parameter for destabilizing long-range magnetic order can be identified when examining the structures mentioned in the previous section. Specifically, the concept of competing interactions can be introduced by placing antiferromagnetically interacting Ising spins on a triangular plaquette. As seen in Fig. 1.9(a), the AFM constraints cannot be simultaneously satisfied for all bonds, and the spin interaction is deemed "frustrated"[38]. The magnetic ground state hence fluctuates between the six degenerate states describing the possible configurations for two parallel and one antiparallel aligned spins[39,4]. Competing interactions, however, do not only arise in low dimensional magnets and for AFM interactions. Indeed, another canonical example of a spin liquid is the spin ice model. The spin ice model is archetypal for the cubic pyrochlore lattice, which is comprised of corner linked tetrahedra, and arises in the presence of ferromagnetically interacting Ising spins with an easy axis pointing towards the centers of the tetrahedra. As shown in Fig. 1.9(b), the resulting spin configuration is frustrated, and as experimentally demonstrated in $Ho_2Ti_2O_7$[40,41], the ground state instead adopts a degenerate manifold of six possible two-in and two-out spin configurations and exhibits unconventional magnetic excitations that can be approximated as magnetic monopoles[42]. Both of these ground states, however, are classical spin liquids as they require thermal fluctuations for the persistence of the spin liquid behavior. For example, for the spin ice systems, as $T \rightarrow 0$, there exists a critical temperature below which the spin dynamics can freeze[42].

It should also be noted that frustration is not exclusive to the geometry of the magnetic sublattice. As illustrated in Fig. 1.9(c), for a square lattice antiferromagnet model, the presence of AFM exchange interactions along the sides (J_1) and across the diagonal (J_2) of the square can also result in competition. In fact, when $J_1 = 2J_2$, this model is also theorized to evade long-range magnetic order and favor an entangled spin liquid state instead[43].

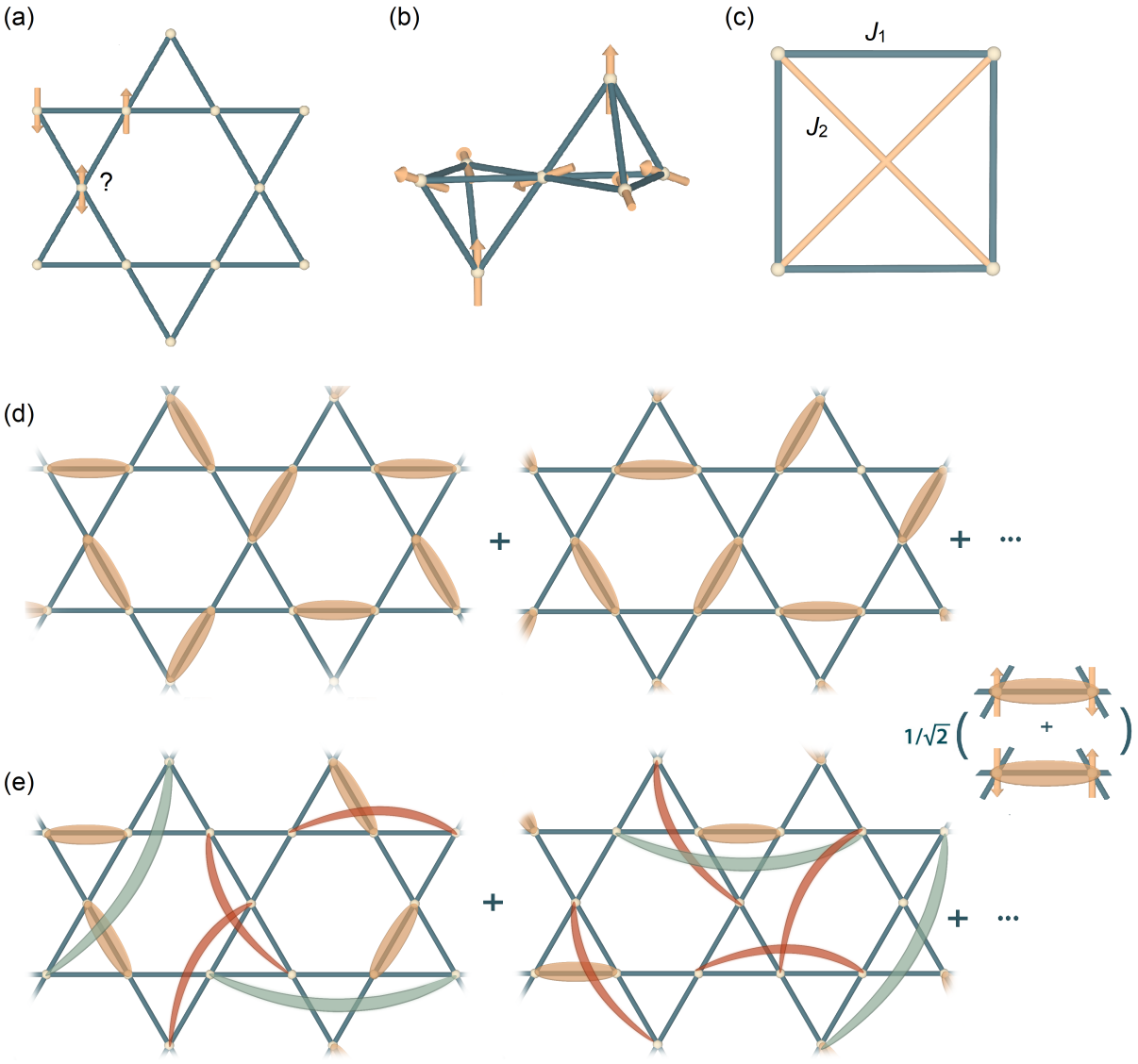

Figure 1.9: (a) Schematic of Ising spins with AFM interactions on a corner-linked triangular network where geometric frustration can arise. This is denoted by the spin up and down state and the question mark. (b) One of the possible two-in and two-out configurations for a classical spin ice. (c) Competing interactions on a square plaquette. (d) Short-range RVB state illustrating some of the possible configurations for the dimer singlet states denoted by the orange ovals. (e) Long-range RVB state where singlets can form beyond the nearest neighboring spins. Figures (a), (b), and (d) are adapted with permission from reference[9]; copyright Annual Reviews 2021. All figures are generated using the `VESTA` visualization software[26].

When considering the Heisenberg analogues of both the triangular and Ising pyrochlore spin models, quantum fluctuations can theoretically stabilize a variety of dynamic spin ground states that persist down to $T = 0$ while evading symmetry breaking[9]. This framework describes quantum spin liquid (QSL) ground states which are characterized by long-range entangled spins and a macroscopic ground state degeneracy that can be robust against perturbations[4]. Key to the difference between paramagnets and QSLs is the former property as, unlike the randomly oriented spins in paramagnets, QSL ground states can be highly correlated[9]. Associated with these correlations are a wide variety of unconventional excitations ranging from spinons as in the HAF model[35], Majorana fermions for the Kitaev model[6], to photon-like quasiparticles in quantum spin ice[44].

A fundamental example for demonstrating the structure of such QSL states of matter is the resonating valence bond (RVB) state[45]. As illustrated on the corner sharing triangular "Kagomé" network in Fig. 1.9(d), this ground state is described by a superposition of all possible spin singlet dimer configurations that can populate the underlying magnetic sublattice. These dimers, however, do not necessarily need to form between neighboring spins, and other long-ranged RVB state flavors can arise with different excitations (Fig. 1.9(e)). Yet, QSL states do not exclusively form in this RVB-like picture. In fact, a classification of QSL symmetries predicts hundreds of unique spin liquid classes[46]. As we have established throughout this chapter, promoting the emergence of such unconventional magnetic ground states in spin models will hence depend on the interplay of parameters like S and z values, anistropy, low dimensionality, and frustration[9].

A wide array of spin models have been theorized to host a variety of such spin liquid symmetries. This allows for the material chemist to seek out realizations in different material classes that can host frustrated and low-dimensional interactions such as in the square, honeycomb, triangular, square, and diamond structures, amongst many others. Some famous examples of such materials that have been extensively studied include, but are not limited to, $YbMgGaO_4$ for the Heisenberg triangular AFM[47], $ZnCu_3(OH)_6Cl_2$

for the Heisenberg Kagomé AFM[48], and $H_3LiIr_2O_6$ on the honeycomb lattice[49]. Yet, these studies and others highlight the inevitable complexities present in real materials where structural disorder and perturbing terms in the spin Hamiltonian can drive such systems towards more classical ground states[9,47,50,51].

The identification of novel material realizations that can better map spin models predicted to host unconventional ground states is thus fundamental for gaining a better understanding of the quantum properties associated with these states. This thesis hence attempts to contribute to this effort by examining the ground state properties of systems related to such spin models. This includes:

- Chapter 3: A family of $S = 1/2$ Mo^{5+}-containing materials, $A MoOP_2O_7$ (A = Li, Na, K, Cs), where the latter three are related to the Heisenberg spin chain antiferromagnet model, whereas $LiMoOP_2O_7$ involves three-legged spin ladders.
- Chapter 4: A study of a novel $j_{\text{eff}} = 1/2$ Ru^{3+} honeycomb system, RuP_3SiO_{11}, follows, and its relevance to the Kitaev model is examined.
- Chapter 5: An investigation of the Heisenberg square and diamond lattice antiferromagnet α and β pseudo-polymorphs of the $S = 1/2$, Ti^{3+}-based coordination framework material, $KTi(C_2O_4)_2{\cdot}xH_2O$, then concludes the results chapters.

The literature relevant to these spin models will be presented in their respective chapters.

Chapter 2

Experimental Methods

As we have established throughout the previous chapter, the emergence of quantum ground states in magnetic materials is dependent on an interplay of a wide range of structural and electronic properties. Identifying or designing materials relevant to such spin models is thus a challenging task that requires one to consider the choice of the transition metal ion, the underlying magnetic sublattice, and the amenability of the proposed material to a variety of synthetic techniques. While *ab-initio* crystal structure prediction tools have seen promising advances in recent years, the possibility of synthesizing the output structures has yet to reach a consistency that is translatable to chemistry laboratories[52–54]. Hence, sources for material realizations of quantum magnets, whether inorganic, hybrid, or organic, heavily rely on identifying or modifying previously reported materials that can host the ingredients necessary for realizing the spin model of interest. All of the materials discussed in this study have been identified through this method.

The characterization of the magnetic ground state properties of material realizations of spin models involves a varied range of complementary experimental and *ab-initio* techniques that probe the crystallographic structure, hierarchy of the exchange interaction

energy scales, and the spin dynamics and excitations[9]. As many quantum magnetic ground states are characterized by a lack of long-range magnetic order and small exchange interaction energies, most experiments are carried out as close as possible to $T = 0$ K. The lack of long-range magnetic order does not act as a sole signature for identifying quantum magnets, however, as structural disorder[50] and hidden order[55,56] can mask the true nature of the magnetic ground state of a particular model. The identification of quantum magnetic ground states hence involves combining multiple experimental and *ab-initio* techniques, particularly spectroscopic ones, that reveal the signature spin excitations of the states. This chapter will cover the subset of these techniques that is relevant to the experimental chapters. As many excellent resources containing detailed descriptions of the physics underlying these techniques exist in the literature, many of the discussions in this chapter will focus on examining the physical interpretation of the resulting data sets and the analysis tools available to the experimentalist.

2.1 Synthetic Methods

Deciding on the most suitable synthetic method for the preparation of crystalline materials is reliant on the class, ranging from inorganic, hybrid to organic, and state, whether single- or polycrystalline, of the target material. For both single- and polycrystalline inorganic oxides, many of the precursor transition metal oxides and salts are water insoluble. Hence, one of the most commonly utilized techniques for these materials is the solid state method which has been used across Chapters 3 and 4 of this study. This procedure is facilitated by the atomic diffusion of precursors towards an interface at which a reaction can occur[57]. Typical reactions begin by homogenizing the particle sizes of the solid state precursors through either manual or automated pulverization, done using mortars and pestles or ball-mills. To reduce diffusion distances and to bring interfaces closer to one another, the following step involves pressing the homogeneous powder into a pellet, typically using

a hydraulic press, with pressures reaching up to 10 tonnes. The pellet is subsequently transferred to a non-reactive crucible, commonly made out of alumina or platinum, and is finally heated for extended periods to increase the atomic diffusion rate to the interfaces.

Solid state reactions are complex and are dependent on a large number of interdependent variables[58]. While a few parameters, such as the starting materials and stoichiometries, can sometimes be rationalized, the reaction scheme is generally phenomenologically devised and involves a large parameter space that includes the number of heating stages, reaction temperatures, dwelling times, and the heating and cooling rates, amongst many others. The temperature, for example, is decided based on the melting points of the starting materials, T_{melt}, with $T_{\mathrm{dwell}} = 0.7T_{\mathrm{melt}}$ being a common starting point[59]. The number of heating stages can depend on the type of the precursors; for hygroscopic starting materials and for carbonates and nitrates, an additional initial decomposition heating stage is necessary for removing the volatile groups. Additional heating stages can also be required if the reaction time is insufficient for a complete reaction. Depending on the oxidation state of the ions in the target material, an inert, oxidizing, or reducing environment could be required. This approach has been applied for RuP_3SiO_{11} in Chapter 4, where the samples were reacted in evacuated sealed quartz tubes.

While versatile, a few limitations exist for the solid state method. First, "hidden" parameters arising from the interplay of the precursor type, homogeneity of the reaction mixture, and imperfections on the reaction crucibles, amongst many others, can influence the reaction. One example is the preparation of the archetypal superconducting material $YBa_2Cu_3O_{6+x}$[60], in which the reaction time can be reduced twenty-fold by changing one of the starting materials. The reduction in reaction time has been related to the formation of an intermediate product with a melting point close to that of the reaction temperature that only occurs when using a specific precursor. This results in a partial-liquid matrix within which the reaction can occur. Rationalizing intermediate products, however, is typically not obvious without challenging in-situ experiments. Also related to

this intricate interplay of the reaction conditions is the physical property variation across samples prepared using nominally the same precursors and conditions. This is seen across a variety of magnetic[61–63] and superconducting materials[64] and is commonly related to the formation of structural defects, strain, and domains. Another limitation involves the large thermal activation necessary for the formation of products using solid state reactions. At such high temperatures, which range from $500 - 2000$ °C in a typical reaction, only the most thermodynamically stable phases within a material's phase diagram are accessible[65]. This deems more complex reaction schemes involving other synthetic methods, as illustrated by $Sr_2MnO_2Cu_{1.5}S_2$[66] and Pb_2NaIO_6[67], as necessary for the isolation of meta-stable compounds.

For soluble precursors, a variety of synthetic tools are available to the chemist. Of these, one of the simplest is the hydrothermal method where reactions proceed in an aqueous solution of starting materials. While seemingly facile, this technique involves many parameters that begin with the reactor type and include pressure, solution pH, stoichiometric ratios of the starting materials, reaction times, temperature, and type of environment, amongst many others. In the simplest case, which is applied for the preparation of the hybrid materials discussed in Chapter 5, the reaction proceeds under constant stirring in a beaker filled with an aqueous solution of the starting materials that is sparged with an inert gas.

2.2 Bulk Magnetism

2.2.1 Magnetic Susceptibility

Examining the magnetic properties of a newly discovered material often begins by measuring the magnetic susceptibility. This is due to several factors including the ease of

access to magnetometers in many laboratories, the small sample volumes ($30 - 100$ mg) used for the measurements, the relatively short collection times ($\approx 1 - 6$ hours), and most importantly, the broad range of information that can be inferred about the static and dynamic behavior of the magnetic moments from data sets collected in direct- (DC) or alternating current (AC) magnetic fields, respectively[68].

In this study, DC magnetic susceptibility $\chi(T)$ and isothermal magnetization $M(H)$ measurements were conducted on a Quantum Design Magnetic Property Measurement System (MPMS3) utilizing a Superconducting QUantum Interference Device (SQUID) magnetometer. The principles underlying SQUID magnetometry are reliant on the physical properties of its superconducting components and are thoroughly examined in Clarke[69] and Fagaly[70]. In essence, a DC-SQUID magnetometer is an extremely sensitive linear current-to-voltage transducer. First, an electromagnetic current is induced in the detection coils through the sinusoidal movement of a sample in an applied magnetic field. The detection coils are connected to the DC-SQUID within which the sample dependent current generates a voltage gradient by biasing the pre-existing current. The resulting voltage gradient can then be transformed back into the magnetic moment of the sample, and from which the magnetic susceptibility can be calculated.

The analysis of magnetic susceptibility data is highly sample dependent yet, some aspects can be generalized. In zero applied magnetic field, symmetry breaking is associated with a divergence in the order parameter, here the magnetization. Hence, the onset of long-range magnetic order for three-dimensional magnetic sublattices in small applied magnetic fields can be evidenced by sharp features in $\chi(T)$. Examples of this are shown in Figs. 2.1(a, b) where the onset of FM and AFM order in $Ni_{0.68}Rh_{0.32}$[71] and $Gd_2Pt_2O_7$[72] is associated with sharp anomalies followed by an increase or decrease in $\chi(T)$, respectively. In the absence of long-range magnetic order, a Curie-Weiss-like description of $\chi(T)$ is seen instead (Fig. 2.1(c)[73]). It should be noted that the lack of any features in $\chi(T)$, does not conclusively demonstrate the absence of long-range magnetic order, and other

complementary techniques (*e.g.* neutron diffraction, muon spectroscopy) must be used to confirm this.

To determine the nature of the magnetic moments and interactions and to ultimately quantify the exchange parameters of the spin Hamiltonian, $\chi(T)$ can be fitted to analytical and numerical models. The simplest model used is the CW law (Eq.1.24) where the effective magnetic moment can be calculated as $\mu_{\text{eff}} = \sqrt{8C}\mu_{\text{B}}$, and the type and strength of the exchange energy can be approximated through the Weiss constant, θ_{CW}. Care must be taken when using the CW model, however, as it is only valid for $T \gg \theta_{CW}$. As done in Chapters 3 and 5, if the spin Hamiltonian is known, better approximations of the exchange parameters can be extracted by fitting a broader range of $\chi(T)$ to a magnetic susceptibility that is calculated for the specific spin model, $\chi^{\text{model}}(T)$. Software packages, applying different tools including high-temperature series expansions[76,77], exact diagonalizations of the spin Hamiltonian for a finite number of spins[78,79], and quantum Monte Carlo techniques[78,79], have been developed for this purpose.

For lower-dimensional and magnetically frustrated materials, features in $\chi(T)$ can be broad or even nonexistent. One example is shown in Fig. 2.1(d) for the one dimensional magnet $BaMo(PO_4)_2$[74] where the the development of antiferromagnetic short range correlations is suggested by a broad maximum that is centered around 50 K. Finally, the magnetic susceptibilty of some quantum magnets do not even contain maxima despite strong interactions. This can be demonstrated by examining the magnetic susceptibility of the $S = 1/2$ Kagomé system, $Zn_xCu_{4-x}(OH)_6FBr$[75]. On increasing x, the magnetic sublattice becomes more quasi-two-dimensional as a Zn^{2+}-containing layer separates the Kagomé sheets. For $x = 1$, a seemingly paramagnetic susceptibility is found despite a large $\theta_{CW} \approx -200$ K. This behavior is characteristic of frustrated magnets where long range magnetic order is suppressed.

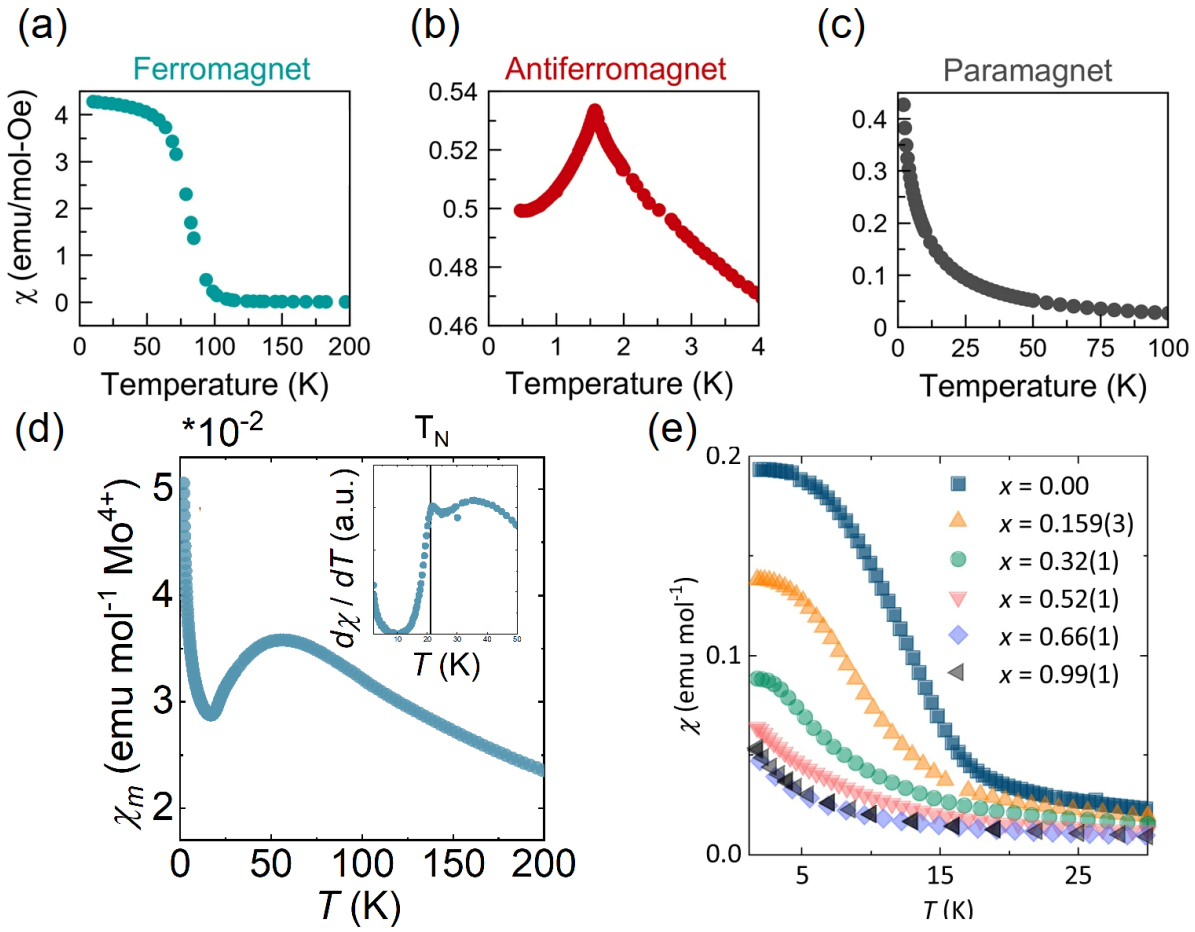

Figure 2.1: The temperature dependence of the magnetic susceptibility, $\chi(T)$, of (a) $Ni_{0.68}Rh_{0.32}$ [71],(b) $Gd_2Pt_2O_7$ [72], and (c) $SrMn_{0.5}Te_{1.5}O_6$ [73] highlighting the onset of ferromagnetic, antiferromagnetic, and paramagnetic behavior, respectively. Figures adapted from reference [68]; copyright 2022 CC BY 4.0. (d) For low dimensional magnets such as the $S = 1$ one-dimensional system $BaMo(PO_4)_2$, the development of short range correlations is evidenced by a broad feature in $\chi(T)$. Figure generated using data from reference [74], copyright 2018 by the American Physical Society. (e) The suppression of long range magnetic order in the $S = 1/2$ Kagomé system, $Zn_xCu_{4-x}(OH)_6FBr$, with increasing Zn^{2+} doping. Figure adapted from reference [75]; copyright 2020 CC BY 4.0.

2.2.2 Specific Heat

Specific heat measurements are commonly utilized for examining the magnetic properties of a system and can be complementary to magnetometry measurements. Underlying the importance of the specific heat, $C_{\mathrm{p}}(T) = dQ/dT$, where Q is heat, is its relation to the entropy S of a system,

$$S = \int_0^T \frac{C}{T} dT, \tag{2.1}$$

through which the evolution of the entropy, and accordingly information on phase transitions and excited states, can be inferred. In this study, zero-field specific heat (C_{p}) measurements were conducted on a Quantum Design Physical Property Measurement System (PPMS) that uses relaxation calorimetry. A detailed description of the methodology underlying relaxation calorimetry, which involves measuring the thermal relaxation rate of a sample after heating with a known ΔT, can be found in Ventura[80].

The total specific heat is comprised of contributions from lattice, nuclear, electronic, and magnetic states. For insulating transition-metal-based materials, the most relevant contributions to the total specific heat are those related to the lattice- and spin degrees of freedom, $C_{\mathrm{p,\ phonon}}$ and $C_{\mathrm{p,\ mag}}$:

$$C_{\mathrm{p,\ total}} = C_{\mathrm{p,\ phonon}} + C_{\mathrm{p,\ mag}}. \tag{2.2}$$

The magnitude of the contributions to $C_{\mathrm{p,\ total}}$ are temperature dependent; $C_{\mathrm{p,\ phonon}}$ is typically larger and dominates at high temperatures, whereas $C_{\mathrm{p,\ mag}}$ is often smaller and is associated with the energy scale of the exchange interactions in the system and only becomes comparable to $C_{\mathrm{p,\ phonon}}$ at lower temperatures.

The onset of long range magnetic order is associated with an entropy release, $\Delta S =$

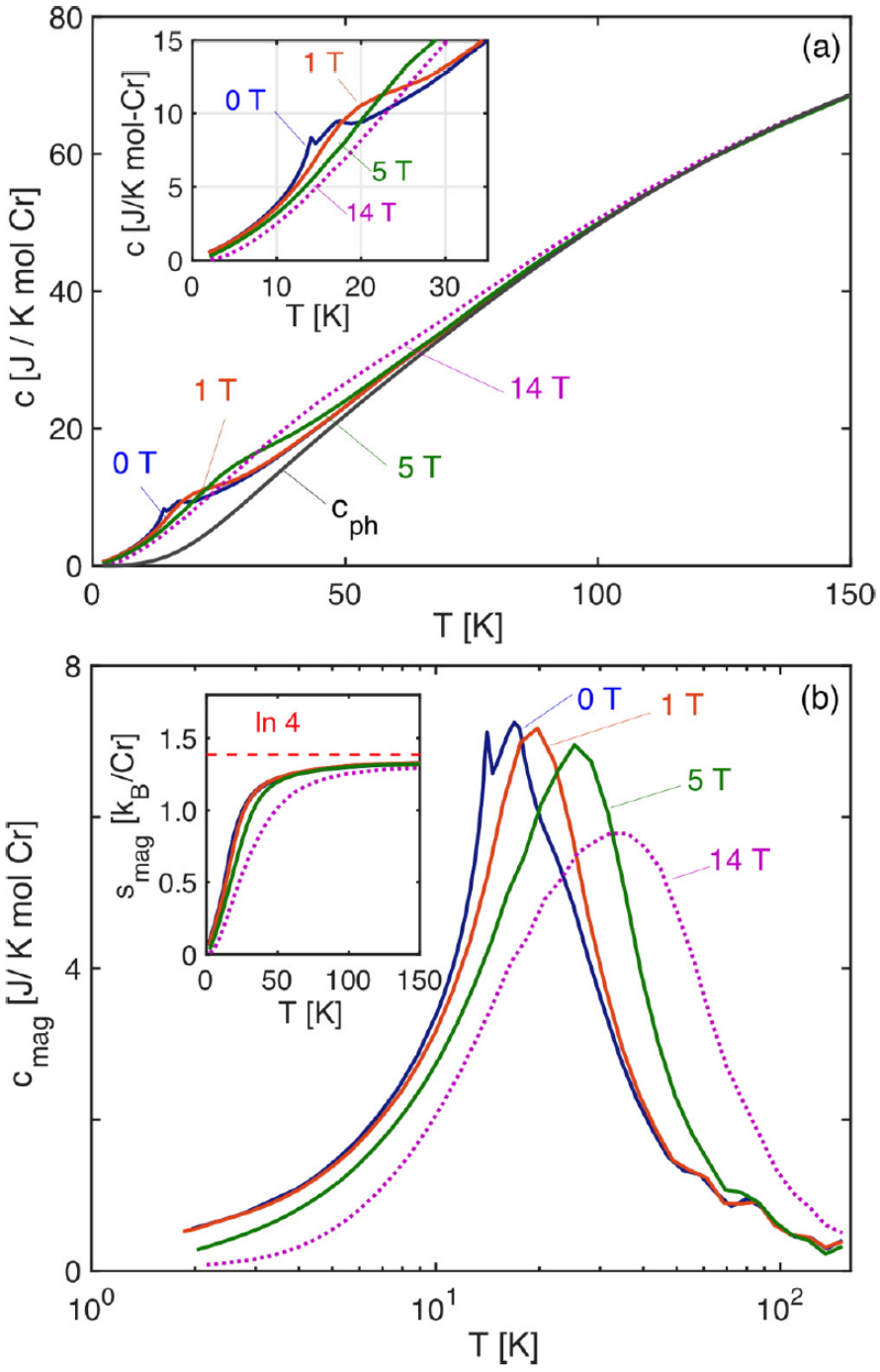

Figure 2.2: The temperature dependence of the specific heat, $C_{\mathrm{p}}(T)$ of (a) the honeycomb-based material, CrI_3, in different applied magnetic fields. The phonon contribution to the specific heat, $C_{\mathrm{p,\,ph}}$ (black line), is estimated by fitting a Debye model to data collected for the diamagnetic isotypic analogue, ScI_3. (b) Subtracting $C_{\mathrm{p,\,ph}}$ from $C_{\mathrm{p}}(T)$ results in the magnetic contribution to the specific heat, $C_{\mathrm{p,\,mag}}(T)$, from which (inset) the entropy release can be calculated. Figure reproduced from reference[81]; copyright 2020 CC BY 4.0.

$R\ln(\omega)$, that can be observed as an anomaly in $C_{\text{p, mag}}(\text{T})$. Here, ω defines the number of states which take on a value of $(2j_{\text{eff}} + 1)$. However, for low-dimensional magnets, the development of short range correlations corresponds to a gradual entropy release that often manifests as a broad feature in the magnetic specific heat. In this case, an anomaly denoting long range magnetic order can be smaller than that predicted. Additionally, for frustrated systems, some excited states can be allowed with little to no entropy release [4]. Hence, magnetic features in $C_{\text{p, total}}$ are often subtle, and $C_{\text{p, mag}}$ must be isolated to avoid any masking effects from $C_{\text{p, phonon}}$.

One of the most commonly used methods for modelling $C_{\text{p, phonon}}$ is combining the Debye ($C_{\text{D}}(\theta_{\text{D}}, T)$) and Einstein ($C_{\text{E}}(\theta_{\text{E}}, T)$) approximations of the specific heat. This method is used to model $C_{\text{p, phonon}}$ in Chapter 3. Such a model is defined as:

$$
\begin{aligned}
C_{\text{p, phonon}}(T) &= \sum_{i}^{k} f_{\text{D}_\text{i}} C_{\text{D}_\text{i}}(\theta_{\text{Di}}, T) + \sum_{j}^{l} f_{\text{E}_\text{j}} C_{\text{E}_\text{j}}(\theta_{\text{E}_\text{j}}, T), \\
C_{\text{D}}(\theta_{\text{D}}, T) &= 9nR(\frac{T}{\theta_{\text{D}}})^3 \int_0^{\frac{\theta_{\text{D}}}{T}} \frac{x^4 e^x}{(e^x - 1)^2}\, dx, \\
C_{\text{E}}(\theta_{\text{E}}, T) &= 3nR(\frac{T}{\theta_{\text{E}}})^2 \frac{e^{\theta_{\text{E}}/T}}{(e^{\theta_{\text{E}}/T} - 1)^2},
\end{aligned}
\tag{2.3}
$$

where, f_{D} and f_{E_i} are weighting factors, θ_{D} and θ_{E} are the Debye and Einstein temperatures, respectively, for a linear combination of a number of k and l terms, n is the number of atoms per formula unit, and R is the universal gas constant. Both models, however, stem from a highly simplified physical theory for the specific heat. Indeed, the Einstein model approximates atomic vibrations as non-interacting harmonic oscillators of a single frequency defined by θ_{E} [82]. Meanwhile, the Debye model approximates atomic vibrations as acoustic phonons with frequency θ_{D} [82]. Although combining these terms can approximate the phonon density of states, assigning meaning to the number of terms used for each model and to the resulting frequencies is questionable, and care must be taken when using this approach.

Alternatively, given that $C_{\text{p, phonon}}$ stems from lattice atomic vibrations, it follows that the specific heat of an isotypic diamagnetic analogue of the material can be used as an approximation of the lattice dynamics. An example of this is shown in Fig. 2.2 for the honeycomb-based material, CrI_3 [81]. Here, $C_{\text{p, phonon}}$ was estimated by fitting $C_{\text{p, total}}$ of the diamagnetic isotypic compound, ScI_3, to a Debye model through which the features present in $C_{\text{p, mag}}$ could be isolated (Fig. 2.2(b)). This approach, however, assumes that the phonon spectrum and atomic masses, on which the phonon frequencies are dependent, are equivalent between both materials. In reality, and as seen in Chapter 3, this is not always the case, and even this approach cannot precisely approximate $C_{\text{p, phonon}}$.

On isolating $C_{\text{p, mag}}$, some information can be inferred about the magnetic properties of the system. For example, the exchange parameters of the spin Hamiltonian can be approximated by fitting $C_{\text{p, mag}}$ to models calculated using similar approaches to those presented in the previous section. An example of this is seen in Chapter 5 where $\chi_{\text{m}}(\text{T})$ and $C_{\text{p, mag}}(\text{T})$ are simultaneously fitted to models calculated using a high temperature series expansion approach. Additionally, the type of the spin excitations present in the system can be probed from the temperature dependence of $C_{\text{p, mag}}$ [4,83,84]. Whilst versatile, care must be taken when interpreting specific heat data as such measurements only probe the temperature dependence of the magnetic density of states, and these results should be used as complementary to other techniques instead.

2.3 Neutron Scattering – Theory

As we have alluded to in the introduction, the relevance of a material to a quantum spin model can be probed by examining the presence, or indeed absence, of unconventional long range magnetic orders and, crucially, spin excitations. In this regard, neutron scattering techniques are a cornerstone for examining both the static and dynamic nuclear

and magnetic responses of a system. Underlying the importance of this technique to condensed matter systems are the thermal neutron's characteristic wavelength and kinetic energy, which are compatible with the inter-atomic distances and excitation energies in crystalline solids[85]. The neutron is furthermore an uncharged particle with an intrinsic spin degree of freedom which allows for probing both the nuclear crystal structures and lattice excitations along with the magnetic structures and spin excitations through the short-ranged strong nuclear force and dipole-dipole interactions, respectively. As detailed derivations of neutron scattering theory are available in Boothroyd[86] and Squires[85], this section will focus on the measurable quantities in a neutron experiment along with descriptions of the instruments used in this study.

In a typical scattering experiment, incident neutrons of momentum $\hbar\boldsymbol{k}_i$ and energy E_i are scattered by a sample at a certain angle, 2θ, to result in neutrons with final momentum and energy transfers of $\hbar\boldsymbol{k}_f$ and E_f. The kinematics of a neutron scattering event can be described by the conservation of total momentum and energy,

$$\begin{aligned} \boldsymbol{Q} &= \boldsymbol{k}_i + \boldsymbol{k}_f, \\ \hbar\omega &= \Delta E = E_i - E_f, \end{aligned} \tag{2.4}$$

where $\boldsymbol{Q}$ is the scattering vector. The measurable quantity in a neutron experiment is the double differential scattering cross section, which defines the number of neutrons scattered into a small solid angle $d\Omega$ with an energy in a narrow range around E_f:

$$\frac{d^2\sigma}{d\Omega dE_f} = \frac{k_f}{k_i} S(\boldsymbol{Q}, \hbar\omega). \tag{2.5}$$

Here, $S(\boldsymbol{Q}, \hbar\omega)$ is the dynamical structure factor which contains all of the sample-dependent physical information and can be defined by time Fourier transform of the correlation func-

tion of a physical property presented by an operator, $\hat{A}$, $\langle \hat{A}^{\dagger}\hat{A}(t)\rangle$, such that:

$$S(\boldsymbol{Q},\hbar\omega) = \frac{1}{2\pi\hbar}\int_{-\infty}^{\infty} \langle \hat{A}(\boldsymbol{Q},t=0)^{\dagger}\hat{A}(\boldsymbol{Q},t)\rangle exp(-i\omega t)\ dt. \tag{2.6}$$

In practical terms, the dynamical structure factor is the time Fourier transform of the correlation function which defines the space and time evolution of a physical property, $\hat{A}$ [86]. It is this physical property, defined through a Fermi pseudopotential $\hat{V}(\boldsymbol{r})$ of the strong nuclear force for nuclear scattering, or a component of a spin operator S^{η} through the dipole-dipole magnetic potential $\hat{V}_{\mathrm{M}}(\boldsymbol{r})$ for magnetic scattering, along with ΔE, that determines the type of a neutron experiment and the information accessible through it [86].

2.3.1 Diffraction

Let us begin by considering an elastic scattering event such that $E_i = E_f$ and $|\boldsymbol{Q}| = 4\pi\sin(\theta)/\lambda$. For a crystalline solid with a periodic arrangement of atoms, this denotes a diffraction experiment in which a neutron wave incident on an atom is diffracted with no change in energy. This type of scattering can be described by Bragg's law which states that the scattered neutron can constructively interfere with others such that the interplanar distances, d_{hkl}, between the hkl crystallographic planes, can be calculated through knowledge of the wavelength of the incident neutrons λ and the scattering angle 2θ when the diffraction order n is an integer such that $n\lambda = 2d\sin(\theta)$. As E does not vary, one finds that the double differential cross section simplifies to the differential cross section, $d\sigma/d\Omega$. When considering the action of the nuclear scattering pseudopotential

$\hat{V}(\boldsymbol{r})$, one finds:

$$\begin{aligned}
&\frac{d\sigma}{d\Omega} = \frac{d\sigma_{\text{coherent}}}{d\Omega} + \frac{d\sigma_{\text{incoherent}}}{d\Omega}, \\
&\frac{d\sigma_{\text{coherent}}}{d\Omega} \propto |F_{\text{N}}(\boldsymbol{Q})|^2, \\
&F_{\text{N}}(\boldsymbol{Q}) = \sum_j \bar{b}_j \exp\left(i\boldsymbol{Q}\cdot\boldsymbol{R}_j\right)\exp\left(-W_j\right).
\end{aligned} \tag{2.7}$$

The first equation demonstrates that two components, namely coherent and incoherent, comprise the nuclear scattering cross section. The incoherent cross section is associated with a (mostly) flat contribution to the intensity defined by the differential cross section and does not contain any structural information [86]. Meanwhile, the coherent contribution to the differential cross section is dependent on the nuclear structure factor, $F_{\text{N}}(\boldsymbol{Q})$. The definition of the structure factor shows that the scattering depends on the average over all scattering nuclei j with scattering length b at position $\boldsymbol{R}$ and that the scattering will be attenuated by a factor W. Here, b defines the effective extent of the Fermi pseudopotential of the interaction between the neutron and an atomic nucleus and is characterized by the nuclear and spin structure of the nucleus [86]. Consequently, b is element and isotope specific and varies considerably and randomly across the periodic table [85]. The Debye-Waller factor, W, introduces an intensity reduction that is due to the displacement of atoms from their average positions.

When the Laue condition—*i.e.* when $\boldsymbol{Q}$ corresponds to a reciprocal lattice point $\boldsymbol{G}$—, and hence Bragg's law, is met, the resulting diffraction pattern will be comprised of Bragg peaks with intensities that are modulated by the structure factor [87]. The diffraction peaks and intensities will contain all of the information necessary for identifying the parameters that describe the average crystal structure of a material; through the peak positions, one can identify the interatomic distances of the smallest repeating unit within a crystal (*i.e.* the unit cell), and through the intensities, the atomic types, positions, thermal motion, and other crucial information can be identified [85].

If the system contains a magnetic atom, a neutron can also scatter from the electron probability density of the unpaired electrons through the magnetic dipole-dipole potential, $\hat{V}_m(\boldsymbol{r})$, which results in:

$$\begin{aligned}
&\frac{d\sigma}{d\Omega} \propto |F_{M_\perp}(\boldsymbol{Q})|^2 \\
&F_{M_\perp}(\boldsymbol{Q}) = \hat{\boldsymbol{Q}} \times (F_M(\boldsymbol{Q}) \times \hat{\boldsymbol{Q}}), \\
&F_M(\boldsymbol{Q}) = p \sum_j \boldsymbol{\mu}_j f_j(Q) \exp(i\boldsymbol{Q} \cdot \boldsymbol{R}_j) \exp(-W_j).
\end{aligned} \tag{2.8}$$

Here, p is a constant, $\boldsymbol{\mu}$ is the magnetic moment, $f(Q)$ is the magnetic form factor, and $\hat{\boldsymbol{Q}}$ is a unit vector. In a similar vein to nuclear scattering, the scattered intensity depends on the magnetic structure factor, $F_M(\boldsymbol{Q})$. The second equation, however, states that neutrons can only probe the component of $F_M(\boldsymbol{Q})$, and hence the magnetization, that is perpendicular to $\boldsymbol{Q}$[85]. Additionally, unlike nuclear scattering, the intensity of magnetic scattering has an angular dependence through $f(Q)$ which decreases with increasing Q and arises from the fact that the probability density of the valence shell electrons is extended in space.

As described in the Chapter 1, a magnetic system can undergo long range magnetic order below a critical temperature. The magnetic order can be related to the crystal structure through the propagation vector, $\boldsymbol{\kappa}$. Here, $\boldsymbol{\kappa}$ describes the periodicity of the directions and magnitudes of $\boldsymbol{\mu}$ with respect to the crystallographic unit cell[86]. Thus, when $\boldsymbol{Q}$ is equivalent to a magnetic reciprocal lattice point $\boldsymbol{G}_M = \boldsymbol{G} \pm \boldsymbol{\kappa}$, and when $T < T_{\text{critical}}$, the diffraction pattern will contain magnetic Bragg peaks with positions and scattered intensities that define $\boldsymbol{\kappa}$ and $\boldsymbol{\mu}$.

All neutron experiments conducted in this thesis were carried out on polycrystalline materials. As the name suggests, a polycrystalline sample is comprised of many micro-sized or smaller crystallites so that, on average, every possible crystal orientation is present in the bulk. In a diffraction experiment, this results in a loss of all orientational informa-

tion as an incident beam can be diffracted by all crystallites satisfying Bragg's law. The diffraction pattern thus appears as Debye-Scherrer cones where each cone at a particular 2θ angle represents a set of hkl crystallographic planes with the same d_{hkl}.

It should be noted that this discussion does not consider aspects of scattering theory that are not pertinent to the current study. Indeed, the nuclear differential cross section can also contain information about the local structure within the static structure factor, $S(\boldsymbol{Q})$, which is probed in total scattering experiments. Additionally, given that a neutron is characterized by an intrinsic spin degree of freedom, controlling its spin angular momentum quantum number m_s or "polarizing" the beam, gives access to an additional probe which can separate the directional components of the magnetic cross section as well as separate nuclear coherent scattering from spin incoherent. The interested reader can follow these in Squires[85] and Boothroyd[86].

2.3.2 Spectroscopy

So far, we have considered the limiting case of elastic scattering which allows for probing the "static" or ordered nuclear and magnetic structures of a material. To examine the spin dynamics in the materials investigated in this study, inelastic neutron scattering is used. In this case, we return to the double differential cross section as the measured quantity (Eq.2.5). For nuclear scattering, the dynamics probed are those associated with collective or atomic vibrations. For the systems examined here, those are termed phonons and have an intensity that is typically proportional to Q^2—*i.e.* the intensity of phonon scattering is largest at high Q-values[85]. As discussed in Chapter 1, for inelastic magnetic scattering, the investigated spin dynamics in an ordered periodic magnet are those related to perturbations to the spin average direction. Considering the formalism of the double differential cross section (Eq.2.5), such excitations are measured by the dynamical structure factor, $S(\boldsymbol{Q}, \hbar\omega)^{\alpha\beta}$, through the associated time Fourier transform of the spin-spin correlation

function, $\langle \boldsymbol{S}^{\alpha}_{\boldsymbol{R}}(0)\boldsymbol{S}^{\beta}_{\boldsymbol{R'}}(t)\rangle$. Here, $\alpha, \beta = (x, y, z)$ are components of the spin operator $\boldsymbol{S}$ at positions $\boldsymbol{R}$ and $\boldsymbol{R}^{'}$. For the measured polycrystalline samples here, all orientational information is lost as the measured dynamical structure factor is powder averaged.

2.4 Neutron Scattering – Instrumentation

All neutron experiments presented in this study were conducted at the ISIS Neutron and Muon Source and the Institut Laue Langevin (ILL). These are examples of spallation and neutron reactor sources, respectively. For a spallation source, a polychromatic beam of neutrons, typically pulsed with a particular frequency, is first moderated to energies that correspond to wavelengths which are compatible with the materials that a particular instrument is specialized for. For diffraction beamlines such as the WISH and HRPD instruments used in this study, the moderated polychromatic beam is scattered from a sample into fixed angle detector banks. By measuring the time taken by the neutrons from the moderator, through the sample, and to the fixed angle detector banks, the wavelengths of the neutrons can be calculated, and a Q-dependent diffraction pattern can be generated[86]. This method is known as time-of-flight diffraction. What determines the choice of diffractometer is the interplay between the flux, wavelength range, and resolution of the instrument; the WISH diffractometer has a high cold neutron flux that allows for the investigation of the small magnetic moments and large unit cells associated with ordered states in quantum magnets, meanwhile the HRPD diffractometer has a higher resolution which aids in crystallography studies.

For time-of-flight-based direct geometry neutron spectrometers such as the IN5 and the LET instruments used here, the polychromatic beam must first be monochromated prior to scattering. This is achieved through a series of choppers which are neutron absorbing rotating discs with slots that allow neutrons of a particular velocity, and hence

energy, to pass through. The resulting pulsed monochromatic beam is scattered from a sample into a large array of time and position sensitive detectors. Through conservation of momentum and energy, the final scattered neutron energies and momentum transfer can be calculated.

At a reactor source like the ILL, the neutron beam is typically continuous. Diffractometers here, such as the D20 and D2B instruments used in this study, define the incident wavelength through a monochromator. The monochromatic beam is then scattered by a sample into a large array of detector banks covering a wide 2θ angular range to generate the diffraction pattern

2.5 Neutron Scattering – Analysis

2.5.1 Nuclear Diffraction

Analysis of neutron diffraction data is dependent on the phase of the material—single- or polycrystalline—and the goal of the experiment. As the crystal structures of all samples investigated in this thesis have been previously established, the goal of the experiments conducted here was to determine the validity of these structural models for describing the new samples. One of the most commonly used tools in this regard is the Rietveld method[88]. In the Rietveld method, the full profile of the diffraction pattern is calculated using the structure factors and other intrinsic properties, as well as the instrumental resolution, and compared to the measured diffraction pattern. A variety of parameters, including those defining the structure factor (atomic positions, Debye-Waller factor), peak positions (unit cell parameters), and peak shapes (instrumental parameters, crystallinity), amongst many others that characterize the sample texture and instrumental geometry, can then be "refined" to fit the experimental data. The refinement is done through a least

squares minimization of the difference in the measured and calculated intensities, y_{obs} and y_{calc}, respectively, such that

$$Y = \sum_i w_i (y_{\text{i, obs}} - y_{\text{i, calc}})^2, \tag{2.9}$$

where $w_i = 1/y_{\text{i, obs}}$. The quality of the refinement is then investigated by examining the goodness-of-fit parameters, R_{p} and χ^2:

$$\begin{aligned} R_{\text{p}} &= \sqrt{\frac{Y}{\sum_i w_i y_{\text{i, obs}}^2}}, \\ \chi^2 &= \left(\frac{R_{\text{p}}}{R_{\text{e}}}\right). \end{aligned} \tag{2.10}$$

Here, R_{e} is a data quality parameter dependent on the statistics of the measured data and the refined model[89]. The Rietveld method can be applied through several software packages, and the ones used in this study are the `Fullprof`[90], `GSAS`[91], and `GSASII`[92] packages.

2.5.2 Magnetic Diffraction

The determination of magnetic structures is heavily reliant on neutron diffraction methods. In a typical experiment, temperature dependent neutron diffraction measurements are carried out beginning in the paramagnetic regime, across the transition temperature, and towards a base temperature that is well within the magnetically ordered phase. For a second order magnetic transition, the temperature dependence can reveal Bragg peaks, in addition to the nuclear ones, that correspond to the magnetic structure. An example of this is shown in Fig. 2.3 for the $S = 2$ hybrid magnetic material, $KFe(C_2O_4)F$[93]. The position of the magnetic Bragg peaks will depend on the relation of the magnetic structure to the crystal structure and, through their positions, one can identify the propagation vector(s), $\boldsymbol{\kappa}$. This can be done by first considering high-symmetry positions in

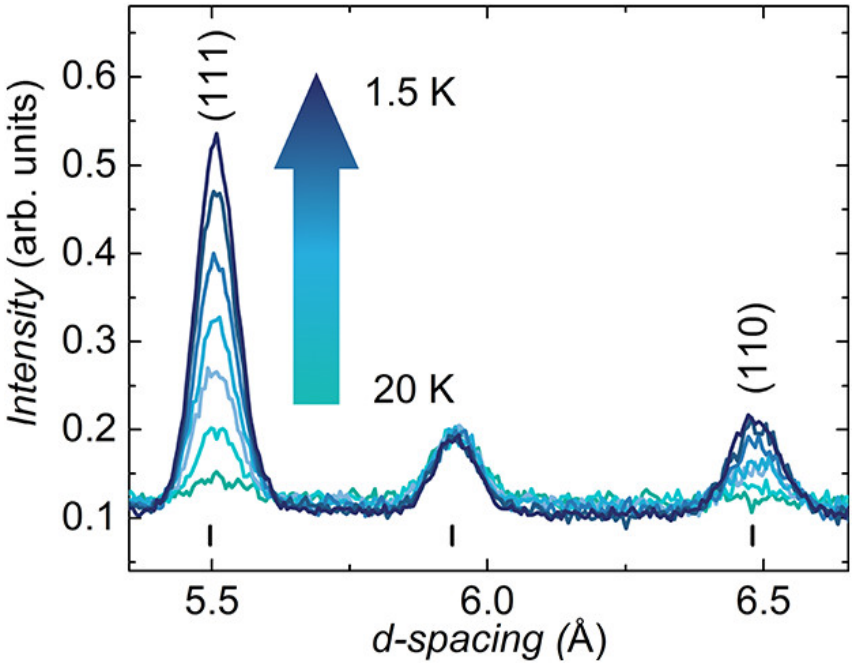

Figure 2.3: The temperature evolution of magnetic Bragg peaks for the hybrid material, $KFe(C_2O_4)F$. Figure reprinted from reference[93]; copyright 2019 American Chemical Society.

the Brillouin zone, then, by using software packages like `K-search` in `Fullprof`[90] suite. If the positions of the magnetic Bragg peaks are not evident, or are commensurate with the nuclear peaks, it is common to subtract a diffraction pattern collected within the paramagnetic regime from one that is collected in the ordered regime. This is especially relevant to quantum magnets where the intensity of magnetic Bragg peaks can be orders of magnitude smaller than the nuclear peaks.

Information on the nature of the magnetic structure can then be gleaned through the $\boldsymbol{\mu}$ vector in the magnetic structure factor (Eq.2.8) which defines the modulation of the magnetic moment across the structure with respect to $\boldsymbol{\kappa}$ such that[94]:

$$\boldsymbol{\mu}_{jd} = \sum_{\boldsymbol{\kappa}} \boldsymbol{m}_{\boldsymbol{\kappa},d} \exp(-i\boldsymbol{\kappa} \cdot \boldsymbol{R}) \tag{2.11}$$

Here, $\boldsymbol{\mu}_{jd}$ defines the magnetic moment on site d and in unit cell j, $\boldsymbol{m}_{\boldsymbol{\kappa},d}$ is a complex Fourier component vector containing all information on the phases and sizes of the or-

dered moment, and $\boldsymbol{R}$ is a lattice vector[86]. To then identify the magnetic structure that is compatible with the symmetry of the paramagnetic group and $\boldsymbol{\kappa}$, one can use either magnetic space groups[95–97] or representational analysis[98]. The latter of these is applied here, and its detailed formalism can be found in Bertaut[98] and Qureshi[94]. In summary, through representational analysis, one can identify the irreducible representations which are the transformations under the symmetry operations applicable to $\boldsymbol{\mu}$ that are concomitant with the paramagnetic space group and that leave $\boldsymbol{\kappa}$ unchanged. Within this framework, the Fourier components of $\boldsymbol{m}_{\boldsymbol{\kappa},d}$ can then be described by the basis vectors of the irreducible representations[86]. It is through fitting the coefficients of these basis vectors that the values and phases of the ordered magnetic moment can be identified. As representational analysis can be quite complex, this method is typically done computationally using software packages like `SARAh`[99], `BASIREPS` in `Fullprof` suite[90], and `Mag2Pol`[100].

As seen in Chapter 5, the symmetry of the magnetic space group does not necessarily need to follow that of the paramagnetic space group. In this case, the paramagnetic space group can be deconstructed to examine all of the possible lower symmetry space groups using software packages like `ISODISTORT`[101].

2.5.3 Spectroscopy

The analysis tools used for inelastic neutron scattering data are highly varied and dependent on the material of interest. In a typical single crystal inelastic neutron scattering experiment with the aim for examining the spin excitations, one begins by investigating the temperature dependence of the measured spectra. For example, and as shown in the dynamical structure factor of yttrium iron garnet ($Y_3Fe_5O_{12}$)[102] Fig. 2.4(a), for non-frustrated classical systems and below the transition temperature, sharp features can suggest a magnon spin wave dispersion. In this case, and as described in Chapter 1

(Sec.1.2.3), linear spin wave theory (LSWT) can be used to calculate the spin-spin correlation function, and hence the dynamical structure factor, for the spin Hamiltonian. This is commonly done using the `SpinW`[27] software package through which the exchange parameters describing the spin Hamiltonian can be determined by fitting the calculated model to the experimental data.

If broader features appear, such excitations can often be associated with low-dimensional and frustrated materials. In such cases, LSWT is no longer a good approximation, and other approaches must be used. One example is shown in Fig. 2.4(b) for the $S = 1/2$ one-dimensional Heisenberg antiferromagnet, $Cu(SO_4)\cdot 5D_2O$, where the spin Hamiltonian was modelled using the numerically evaluated dynamical structure factor of the 2+4 spinon continuum[36]. For experiments on powder samples, such distinct features are typically smeared by powder averaging. In this case, a priori detailed knowledge of the relevant spin Hamiltonian, determined by combining other experimental and *ab-inito* techniques, must be in place prior to modelling to the experimental data.

2.6 X-ray Diffraction

Diffraction experiments are not limited to neutron scattering. In fact, other particles with wavelengths that are comparable to the interatomic distances in crystalline solids, such as X-rays and electrons, can also be used. For X-rays, a slight variation to the formalism of the nuclear diffraction of particles presented above applies. This variation stems from the properties of the incident beam as X-rays are electromagnetic waves with no spin component. X-rays hence mainly interact with the electron density of atoms in crystalline solids through electromagnetic interactions.

In a similar vein to magnetic neutron scattering, the structure factor associated with

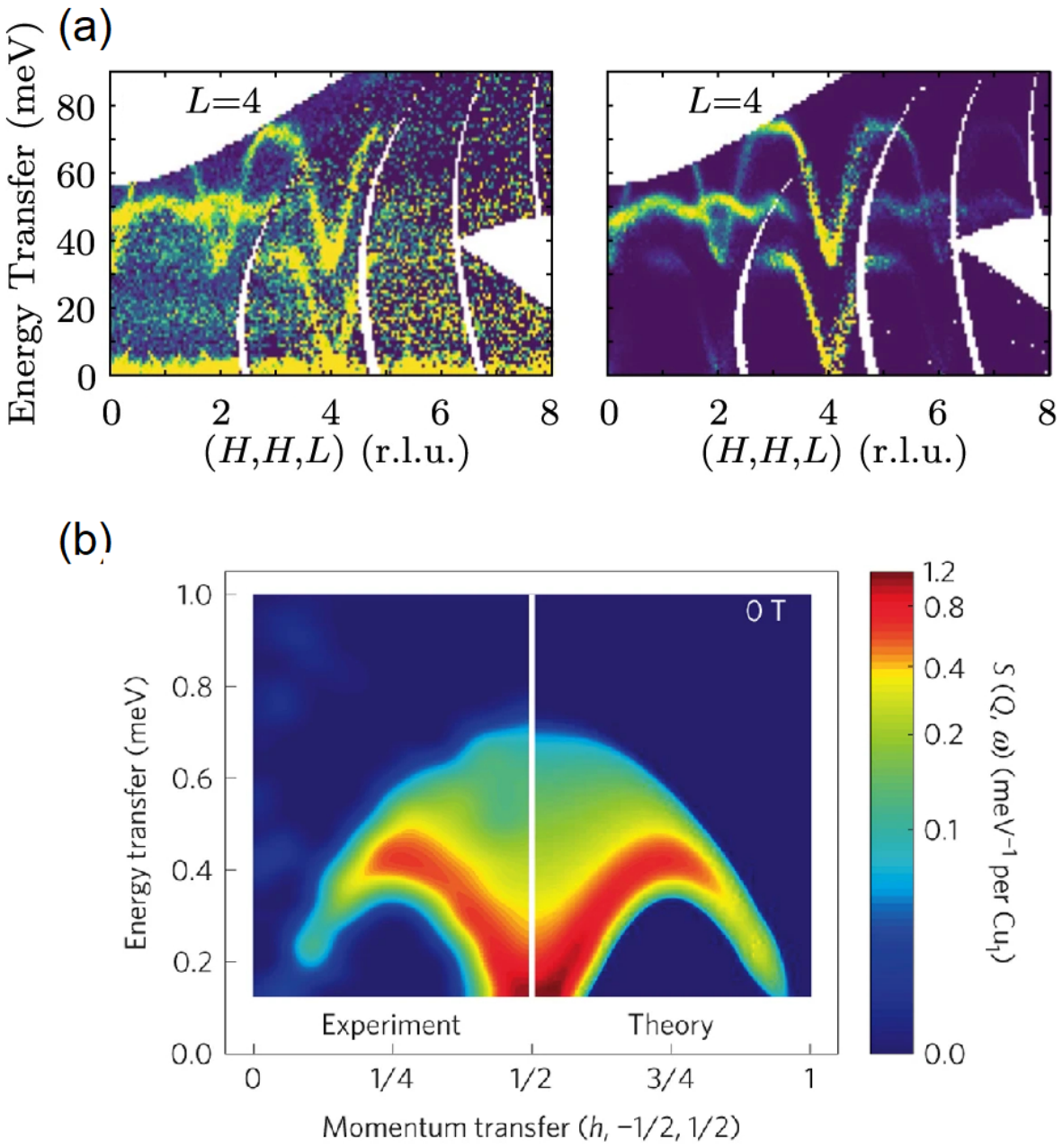

Figure 2.4: (a, left) The experimental dynamical structure factor of a single crystal of $Y_3Fe_5O_{12}$ as viewed along the (H,H,L) direction[102]. (a, left) Energy-convoluted SpinW simulated spectrum for a best fit model. Figure reproduced from reference[102]; copyright 2020 CC BY 4.0. (b, left) The single-crystal experimental dynamical structure factor of the one-dimensional Heisenberg antiferromagnet, $Cu(SO_4)\cdot 5D_2O$, as viewed along the $(h, -1/2, 1/2)$ direction[36]. (b, right) Best simulated model using the numerically evaluated dynamical structure factor of the 2+4 spinon continuum. Figures adapted with permission from reference[36]; copyright Springer [Nature Physics], 2013

X-ray scattering involves a form factor. The form factor, f, increases with the atomic electron count. Additionally, as the electron density is extended, the structure factor will vary depending on the scattered wave vector and decrease as Q increases.

The appeal of X-ray scattering stems from the ease through which X-rays can be generated. Indeed, laboratory X-ray sources are commonplace in most solid state laboratories. This allows for in-house structural confirmation and determination. Additionally, due to the higher fluxes of X-ray sources, collection times for diffraction patterns are typically shorter than those of neutrons. For even shorter collection times and better resolutions, synchrotron X-ray diffraction beamlines, such as the I11 beamline at Diamond used here, are available.

In comparison to neutron diffraction, a downside of using X-rays is its form factor dependence. Indeed, this complicates the structural analysis of materials containing neighboring elements in the periodic table as their form factors are difficult to distinguish. Additionally, as the scattering power is dependent on the number of electrons, smaller atoms such as the oxides and hydrogens that are present in the materials examined are difficult to locate. Hence, X-ray and neutron scattering techniques are commonly used as complementary for a full characterization of the crystal structure of a system.

Chapter 3

Exploring the Magnetic Properties of the Spin Chain Mo(V) Pyrophosphate Family of Materials, AMoOP$_2$O$_7$ (A = Li, Na, K, Cs)

3.1 Introduction

The one-dimensional chain spin model has long served as a canonical example of the fascinating emergent properties of low-dimensional many-body electron systems. Such systems can manifest correlated ground states characterized by a continuous symmetry that is maintained by quantum fluctuations at all temperatures[103,9]. Antiferromagnetically interacting $S = 1/2$ Heisenberg spin chains, for instance, host an analytically-tractable entangled spin singlet ground state[32,104]. Termed the $S = 1/2$ Heisenberg chain antiferromagnet model (HAF), the ground state of this model is described by algebraically

decaying spin correlations that are entangled across the system[4]. One of the intriguing properties of this model is its gapless collective excitations; the $S = 1/2$ HAF model famously hosts spinons which are $S = 1/2$ fractionalized particle-like excitations that, for Ising spins, can be pictured as domain walls propagating in opposing directions.

From a materials perspective, an approximation of this one-dimensionality can arise in a variety of material classes where magnetic ions are connected such that exchange interactions are strongest in one spatial crystallographic dimension. Hence, the ground state of the HAF model has been extensively experimentally investigated and the emergence of spinons has been conclusively identified in a variety of materials[105,106]. Examples of such materials span a few magnetic ions within the $3d$ electronic configuration limit and most notably include Cu^{2+} as the $S = 1/2$ spin source as in Sr_2CuO_3[107,108] and $Cu(SO_4)\cdot 5H_2O$[36]. With a few exceptions such as $KTi(SO_4)_2$[109] and $YbAlO_3$[110], amongst others, comprehensive studies on material realizations of the HAF model containing rare earth or other transition metal ions are scarce.

Typically, however, many materials can include additional perturbative terms in the spin Hamiltonian that can expand the magnetic phase diagram to include a variety of interesting ground states. A prototypical example of this is the $S = 1/2$ Heisenberg frustrated chain model (FCM), which hosts a rich magnetic phase diagram that is dependent on the strength of the frustrating interchain exchange coupling, J_1, with respect to the linear intrachain interaction, J_2, such that $\alpha = J_1/J_2$. For example, at $\alpha = 0.5$, this model provides another exactly solvable point with the Majumdar-Ghosh solution[111,112] that describes a ground state characterized by a superposition of doubly degenerate spin singlets with a spin gap to the first excited state. Later reports identified a critical point $\alpha \geq 0.2411$ beyond which this dimer-like spin liquid regime is maintained up to $\alpha \approx 4$ and after which long range magnetic order ensues[113–116].

Although this dimer-fluid ground state persists in a broad region of the phase diagram,

candidate materials relevant to this model are scarce, and the presence, or indeed absence, of the spin gap has yet to be experimentally verified. A recent investigation of a system pertaining to this model is the Cu^{2+}-based mineral szenicsite, $Cu_3(MoO_4)(OH)_4$ [117,118]. Curiously, while similar copper minerals such as lindgrenite, $Cu_3(MoO_4)(OH)_2$, can be prepared [119], no synthetic procedure is known for szenicsite, and all experimental studies were conducted on mined mineral samples. Hence, while a combination of experimental and *ab-initio* calculations place this material within the right region of the phase diagram, an experimental verification via inelastic neutron scattering is hindered by a lack of a suitable deuterated sample. A similar issue arises in $KTi(SO_4)_2{\cdot}H_2O$ [120,121] where the unreliability of the synthetic procedure has hampered a more detailed experimental verification of its relevance to the dimerized region of the FCM. The discovery of new materials related to the FCM is hence crucial for elucidating the true ground state of the dimerized region of the phase diagram. In this vein, phosphate and pyrophosphate linkers, $(PO_4)^{3-}$ and $(P_2O_7)^{4-}$, respectively, offer an abundance of structural topologies in which to explore a variety of spin models when they connect magnetic ions. Depending on the interplay of the ionic radii of the metal sites, these linkers bridge architectures ranging spin chains [122], triangular networks [74], and square plaquettes [123], amongst many others [124–126]. Additionally, the three fold symmetry of $(PO_4)^{3-}$ linkers naturally lends itself to frustrated frameworks in some bridging geometries.

One particular example is the $A\mathrm{MoOP_2O_7}$ family of materials which, depending on the ionic radius of the alkali metal A-site, forms a magnetic sublattice comprised of either pairs of $S = 1/2$ Mo^{5+} chains for A = Na-Cs [127–129] or a three-legged spin ladder for A = Li [130]. Those will henceforth be referred to as LMP, NMP, KMP, and CMP for A = Li, Na, K, or Cs, respectively. More broadly, this family of materials also offers a platform for the examination of the ground state properties of spin chain-related compounds containing a $4d$ transition metal ion. Hence, this chapter will present an experimental and *ab-initio* investigation of the ground state properties of the $A\mathrm{MoOP_2O_7}$ family of materials. This

chapter will begin with a comprehensive investigation describing the spin Hamiltonian of KMP. The results of this, which have been submitted for publication in Physical Review B[106], reveal dominant one-dimensional correlations and minimal frustration. This one-dimensional behavior will be discussed through the lens of the structural-property relations in KMP and will be compared across the series with NMP and CMP. Beyond this, a study demonstrating the magnetic ground state of the three-legged spin ladder compound, LMP, will be presented.

3.2 Methods

3.2.1 Synthesis

Polycrystalline samples of $A\mathrm{MoOP_2O_7}$ (A = Li, Na, K, Cs) were prepared following modified versions of previously published solid state methods[127–130]. All temperatures, heating times, and molar ratios are summarized in Table 3.1. In a typical reaction, $\mathrm{MoO_3}$ (Alfa Aesar, 99.998%), Mo (Alfa Aesar, powder, <150 μm, 99%), and $(\mathrm{NH_4})_2\mathrm{HPO_4}$ (Alfa Aesar, 98%+) were combined with the respective $\mathrm{Li_2O}$ (Alfa Aesar, 99.5%), $\mathrm{Na_2CO_3}$ (Alfa Aesar, 99.6% anhydrous), $\mathrm{K_2CO_3}$ (Sigma Aldrich, 99.995%), or $\mathrm{Cs_2CO_3}$ (Sigma Aldrich, 99.5%) source and wet ground for 30 minutes in a Retsch planetry ball mill using an isopropyl alcohol medium. The resulting powder was then heated at a rate of Q_H = 3 K min^{-1} to the respective temperature, held for 12 hours, before cooling down to room temperature at a rate of Q_C = 3 K min^{-1}. This formed dark blue (A = Li) or dark green (A = Na–Cs) powders that were retrieved, manually reground, pressed, and heated at a rate of 3 K min^{-1} under flowing argon gas. An additional final heating stage involved washing the sample with acetone before being reground, pelletized, and sealed in an evacuated quartz ampoule with 300 mbar of argon gas. It should be noted that the

final products were brightly colored and any darker colored samples included amorphous paramagnetic impurities. A similar darkening of the samples reveals their deterioration in air over extended periods of time. All attempts at synthesizing $RbMoOP_2O_7$, which, interestingly, unlike the rest of the series, is reported [127] to be isotypic with the anisotropic triangular yavapaiite crystal structure, were unsuccessful.

The preparation of the diamagnetic analogue $KNbOP_2O_7$ (KNP) followed a newly developed nitrate-citrate combustion procedure. Here, a stirred 2 M nitric acid aqueous solution of Nb_2O_5 (Sigma Aldrich, 99.99%), K_2CO_3 (Sigma Aldrich, 99.995%), $(NH_4)_2HPO_4$ (Alfa Aesar, 98%+), and citric acid, combined in the molar ratio 1:1:4:9, was evaporated at 410 K for 24 hours. This results in a brown resin that can be transferred to an alumina crucible and heated to 873 K for 24 hours to form a grey-colored powder. Grinding, pressing, and sintering this powder at 1073 K for another 24 hours burns the citrate matrix and forms the white-colored final product.

3.2.2 Diffraction

Neutron powder diffraction (NPD) data were collected between 200 K and 300 K in 10 K steps on a 5 g sample of KMP using the HRPD diffractometer. At lower temperatures, the same powder sample was measured on both the WISH and D20 neutron diffractometers. Here, two measurements were collected on each instrument with temperatures of 20 K and 1.8 K on WISH and 1.8 K and 0.05 K on D20, respectively.

As for NMP, CMP, and KNP, X-ray powder diffraction measurements were performed on the Miniflex, D8, and D2 diffractometers, respectively. Room temperature NPD data were collected for a 5 g sample of ^7Li enriched LMP sample on the D2B diffractometer. Finally the same 5 g LMP sample was measured on the D20 diffractometer at 1.8 K and 10 K. Rietveld analysis of crystal structures was performed using the `GSAS-II` [92] software

Table 3.1: Synthetic routes for the preparation of $A\mathrm{MoOP_2O_7}$ (A = Li, Na, K, Cs) and $\mathrm{KNbOP_2O_7}$. Here, the cooling and heating rates for all $A\mathrm{MoOP_2O_7}$ reactions are Q_H = 3 K/min and Q_C = 3 K/min, respectively. P_Ar refers to the argon gas pressure used in an evacuated quartz ampoule.

Composition	Reaction	Thermal treatment
$\mathrm{LiMoOP_2O_7}$	$\mathrm{Li_2O}$ + 1.68 $\mathrm{MoO_3}$ + 0.32 Mo + 4 $\mathrm{(NH_4)_2HPO_4}$	623 K, 12 h 833 K, 24 h, Ar flow 833 K, 12 h, P_Ar = 300 mbar
$\mathrm{NaMoOP_2O_7}$	$\mathrm{Na_2CO_3}$ + 1.44 $\mathrm{MoO_3}$ + 0.56 Mo + 4 $\mathrm{(NH_4)_2HPO_4}$	673 K, 12 h 853 K, 24 h, Ar flow 853 K, 12 h, P_Ar = 300 mbar
$\mathrm{KMoOP_2O_7}$	$\mathrm{K_2CO_3}$ + 1.68 $\mathrm{MoO_3}$ + 0.32 Mo + 4 $\mathrm{(NH_4)_2HPO_4}$	773 K, 12 h 873 K, 24 h, Ar flow 973 K, 12 h, P_Ar = 300 mbar
$\mathrm{CsMoOP_2O_7}$	$\mathrm{Cs_2CO_3}$ + 1.76 $\mathrm{MoO_3}$ + 0.24 Mo + 4 $\mathrm{(NH_4)_2HPO_4}$	673 K, 12 h 863 K, 24 h Ar flow 863 K, 12 h, P_Ar = 300 mbar
$\mathrm{KNbOP_2O_7}$	$\mathrm{K_2CO_{3(aq)}}$ + $\mathrm{Nb_2O_{5(aq)}}$ + 2 $\mathrm{(NH_4)_2HPO_{4(aq)}}$ + 9 $\mathrm{C_6H_8O_{7(aq)}}$	410 K, 24 h, 2M Nitric acid 873 K, 24 h 1073 K, 24 h

package. Magnetic structure refinements were conducted using both the `FullProf`[90] and the `Mag2Pol`[100] suites.

3.2.3 Magnetometry and Specific Heat

All DC temperature dependent magnetic susceptibilities were measured in applied fields of 1000 Oe between 1.8 K and 300 K in DC mode using the Quantum Design Magnetic Property Measurement System (MPMS3) with both zero-field cooled and field cooled protocols. As no bifurcation is observed, generally suggestive of the formation of transitions to magnetically ordered or spin-freezing like states, the zero-field cooled measurements are reported here. For LMP, NMP, KMP, and CMP, the measured samples weighed 17.47 mg, 27.78 mg, 22.25 mg, and 30.58 mg, respectively. As for preparation, all samples were packed into gelatin capsules, secured using teflon tape, and inserted into plastic straws. Exact diagonalization calculations of the Heisenberg frustrated chain model were performed on a chain of 18 sites using the `ALPS` software package[78,79]. When fitting using non-linear least squares regression, further neighbor coupling parameters were fixed in 0.01 increments of the leading intrachain exchange parameter, J_2. A temperature independent background term, χ_0, was used, and its value was fixed to that obtained via Curie-Weiss fitting.

The temperature dependence of the specific heat was measured in zero applied field for all samples on the DynaCool Quantum Design Physical Property Measurement System (PPMS). Here, measurements were carried out between 1.8 K and 300 K on pressed powder samples weighing 2.69 mg, 7.32 mg, 5.58 mg, and 3.29 mg for A = Li-Cs, respectively. Measurements were also recorded between 0.08 K and 1.8 K using a dilution fridge insert.

3.2.4 Inelastic Neutron Scattering

The dynamical structure factors, $S(Q, E = \hbar\omega)_{\text{exp}}$, of 5 g samples of LMP, KMP, and KNP were measured at 1.8 K on the direct geometry time-of-flight spectrometer IN5. An incident energy of $E_{\text{i}} = 14.2$ meV was used for both KMP and its diamagnetic analogue, KNP. Three spectra were collected for LMP with $E_{\text{i}} = 3.55$ meV, 5.11 meV, and 14.2 meV.

3.3 $KMoOP_2O_7$

3.3.1 Crystal Structure

The reported monoclinic $P2_1/n$ structural model of $KMoOP_2O_7$ [128] was confirmed between 200 K and 300 K through Rietveld analysis of NPD data. The refinements are summarized for the 300 K model in Table 3.2 with the fit shown in Fig. 3.1. Here, all lattice parameters, atomic positions, and displacement parameters were refined. An additional minor (3.3(1)% wt.) Mo metal impurity was found to account for the extra peaks not described by KMP. The structural model of the isotypic diamagnetic analogue $KNbOP_2O_7$ was similarly confirmed at room temperature using powder X-ray diffraction data and is summarized in Table A.1 (Fig. A.1).

Focusing on the magnetic sublattice, the structural model can be described as forming infinite chains of octahedrally coordinated Mo^{5+} ions propagating along the *a*-axis, that are psuedo-edge sharing within the *ab*-plane through tetrahedral phosphate bridges (Fig. 3.2(a,b)). Each Mo octahedron is coordinated by five pyrophosphate groups (Fig. 3.2(d)) thus leaving a short apical bond to O^{2-} (O7), which is also bound to two K^+, that distorts

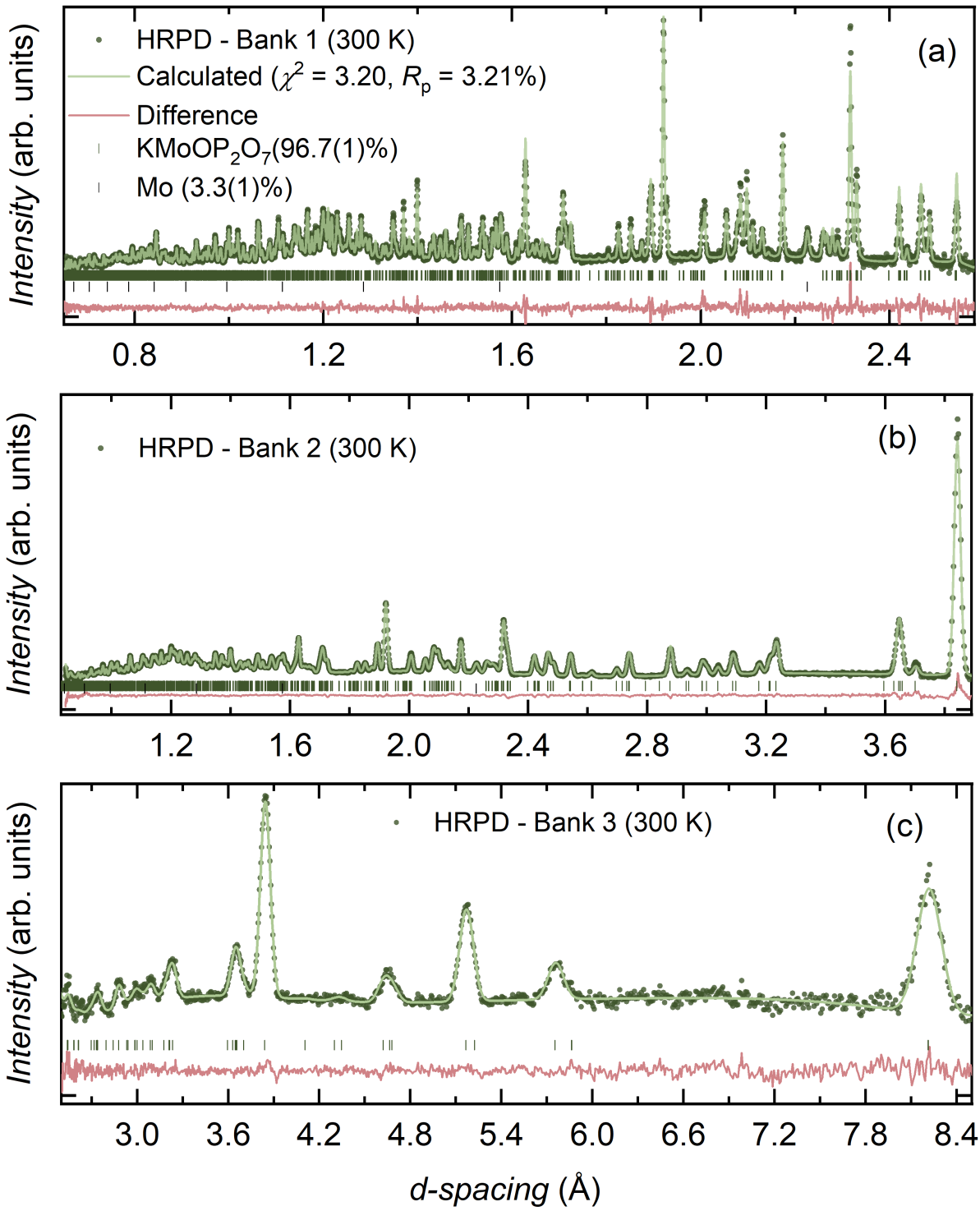

Figure 3.1: (a-c) Neutron powder diffraction data collected at 300 K on the HRPD diffractometer for $KMoOP_2O_7$. Rietveld analysis using the $P2_1/n$ model across all three detector banks resulting in goodness-of-fit parameters $\chi^2 = 3.20$ and $R_p = 3.21\%$

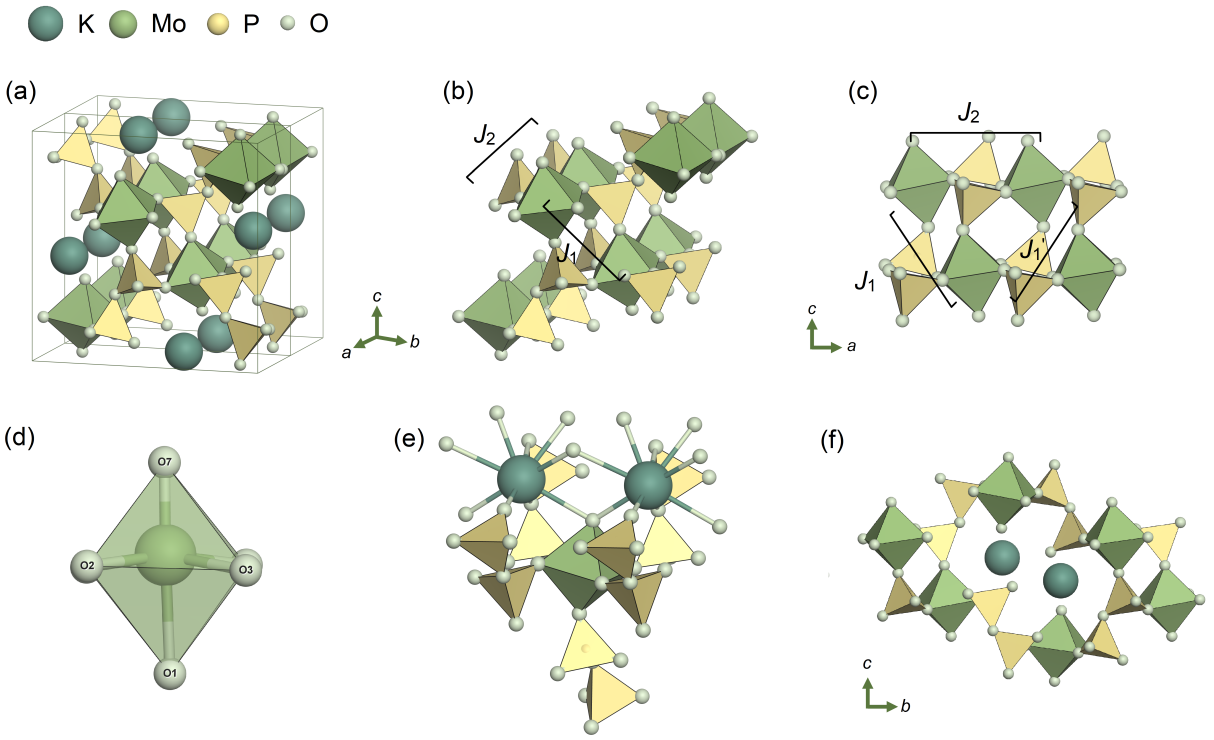

Figure 3.2: The crystal structure of $KMoOP_2O_7$. (a) The magnetic sublattice is comprised of infinite Mo^{5+}-containing chains running along the crystallographic a axis. (b, c) The possible leading superexchange pathways run through pseudo-edge sharing PO_4 tetrahedra along the intrachain direction, denoted J_2, and an interchain exchange interactions, J_1 and J_1'. (d) The octahedral geometry of Mo^{5+} which is distorted by a short Mo-O apical bond. This distortion arises from the (e) coordination of the octahedra which coordinate five pyrophosphate molecules leaving an apical oxygen shared with K^+ ions. (f) This coordination forms a tunnel-like structure which the K^+ ions occupy. Figures generated using the `VESTA` visualization package[26].

Table 3.2: Structural parameters of $KMoOP_2O_7$ as obtained through Rietveld refinement of the $P2_1/n$ model using powder neutron diffraction data measured at 300 K on the HRPD diffractometer. The resulting unit cell parameters are a = 5.0850(1) Å, b = 11.729(2) Å, c = 11.508(2) Å, and β = 90.975(1)° with goodness-of-fit parameters χ^2 = 3.20 and R_p = 3.21%.

Atom	x	y	z	U_{iso}(Å^2)
Mo	0.2606(4)	0.1203(2)	0.1658(1)	0.0080(6)
K	0.2742(8)	0.3686(3)	0.9437(3)	0.0102(2)
P1	0.2650(5)	0.1949(2)	0.6493(2)	0.0011(7)
P2	0.2468(5)	0.0643(2)	0.8648(2)	0.0065(8)
O1	0.1820(5)	0.1058(2)	-0.0177(2)	0.0057(7)
O2	-0.0659(5)	0.0290(2)	0.1852(2)	0.0059(6)
O3	0.0490(5)	0.2600(2)	0.1413(2)	0.0081(7)
O4	0.2179(5)	0.1762(2)	0.7851(2)	0.0034(7)
O5	0.4651(5)	-0.0262(2)	0.1496(2)	0.0050(6)
O6	0.2310(6)	0.0892(2)	0.5783(2)	0.0116(7)
O7	0.3201(5)	0.1372(2)	0.3079(2)	0.0113(8)
O8	0.5699(5)	0.2123(2)	0.1132(2)	0.0050(6)

the local geometry by off-centering the Mo from the basal-plane (Figs. 3.2(c, d)). This behavior is in accordance with other materials containing similarly coordinated Mo^{5+} and V^{4+} geometries[125,131,132]. Another consequence of this coordination is the presence of two distinct pathways connecting the chains to neighboring chains. In the first, a pseudo-edge sharing geometry forms a link to the nearest neighboring chain through phosphate groups. Meanwhile, further neighboring chains are linked by P_2O_7 groups through the corner shared Mo-octahedra. As depicted in Fig. 3.2(e), these form tunnel like structures along the a-axis that are occupied by the nine-fold coordinated K^+ ions.

To construct the relevant spin model, the most probable leading superexchange interaction pathways can be gleaned from the structural model. Similar to other phosphate containing materials, intra- and inter-chain exchange interactions could be mediated through phosphate links[133,134]. These form Mo-O-P-O-Mo pathways corresponding to an intrachain Mo-Mo distance of $d_{\text{Mo-Mo}}$ = 5.085(1) Å and interchain distances of

$d_{\text{Mo-Mo}} = 5.360(5)$ Å and 5.401(5) Å, respectively. Further neighbour couplings, running through pyrophosphate bridges, propagate along either the crystallographic *b*- or *c*-axes with distances ranging between $d_{\text{Mo-Mo}} = 6.180(1)$–$7.053(3)$ Å. When considering the strength of these interactions, the short apical bond distorting the Mo octahedra can split the degenerate t_{2g} orbitals into a lower-lying d_{xy} level, perpendicular to the shortest bond, and higher-energy d_{xz} and d_{yz} orbitals. Such a splitting would favor interactions along the crystallographic chain direction thus suggesting the FCM as a natural starting point for describing $KMoOP_2O_7$. Following the model's nomenclature, intrachain exchange interactions will be denoted J_2, whereas the nearest-neighbor interchain couplings will be described by J_1.

3.3.2 Magnetometry

The zero-field cooled temperature dependent magnetic susceptibility $\chi_m(T)$ of $KMoOP_2O_7$, measured in an applied field of 1000 Oe, is shown in Figs. 3.3(a). No sharp anomalies consistent with the onset of long-range magnetic order are present down to 2 K. Instead, there is a broad symmetrical feature, characteristic of low-dimensional magnetism, and suggestive of the development of short-range magnetic correlations, located around 21 K. To investigate the energy scale and sign of the dominant interaction, the Curie-Weiss behavior of $\chi_m(T)$ was examined above 160 K. This minimum fitting temperature was selected as the temperature beyond which the model parameters begin to plateau (Fig. A.2). The resulting CW model yields $\theta_{\text{CW}} = -16.9(1)$ K, $C = 0.341(1)$ emu K mol^{-1} ($g = 1.91$), $\mu_{\text{eff}} = 1.65(1)$ μ_B, and $\chi_0 = 2.51 \times 10^{-5}$ emu mol^{-1}, suggesting dominant antiferromagnetic interactions and an effective magnetic moment close to the expected full spin-only $S = 1/2$ magnetic moment of 1.73 μ_B. Accordingly, any contribution from the orbital moment is unlikely as μ_{eff} does not strongly deviate from its spin-only value as seen in other Mo^{5+} containing materials[135,136]. This spin-only behavior is also con-

comitant with the expected crystal field splitting which breaks the triple degeneracy of the low-lying t_{2g} orbitals.

To estimate the leading magnetic exchange parameters, an exact diagonalization of the $S = 1/2$ Heisenberg FCM with an interchain exchange parameter, J_1, and an intrachain exchange interaction, J_2, was calculated using the `ALPS`[78] software package on a chain of $L = 18$ spins. When fitting above 15 K (Fig. 3.3(b)), where the fitting range was determined by increasing the minimum temperature until the parameters were stable (Fig. A.2), χ_{m} is well described by a model with minimal frustration and dominant antiferromagnetic one-dimensional correlations as $J_2 = 35.2(1)$ K and $J_1/J_2 = -0.01$ ($g = 1.96$) are obtained. These parameters are broadly consistent with the CW model ($\theta_{\mathrm{CW}} = -16.9$ K) where the expected $\theta_{\mathrm{CW}} = -\frac{1}{4}(z_1 J_1 + z_2 J_2) \approx -17.4$ K when z_{i} defines the number of interactions per site. However, as the effects of a small J_1 manifest in the lower temperature region of the calculated magnetic susceptibility curve where finite size effects play the largest role, obtaining a reliable estimate of J_1 is beyond the scope of this model. Instead, this model highlights the dominant one-dimensional character of the magnetism in $KMoOP_2O_7$. Moreover, reflecting on the crystal structure where the chain propagates within the *ab*-plane, the resulting microscopic model is generally consistent with the assumed active d_{xy} magnetic orbital. Finally, assuming that $KMoOP_2O_7$ lies within the one-dimensional limit of the FCM, a saturation field of $H_{\mathrm{sat}} = \frac{2J_2}{g\mu_{\mathrm{B}}} \approx 53$ T can be estimated.

3.3.3 Specific Heat

To further examine the validity of the unfrustrated one-dimensional model, the zero-field temperature dependence of the specific heat, $C_{\mathrm{p,\ total}}$, was measured between 0.08-300 K (Fig. 3.4). Assuming that $KMoOP_2O_7$ is insulating, the total specific heat can be defined with respect to the lattice- and spin dynamics, $C_{\mathrm{p,\ phonon}}$ and $C_{\mathrm{p,\ mag}}$, respectively, where

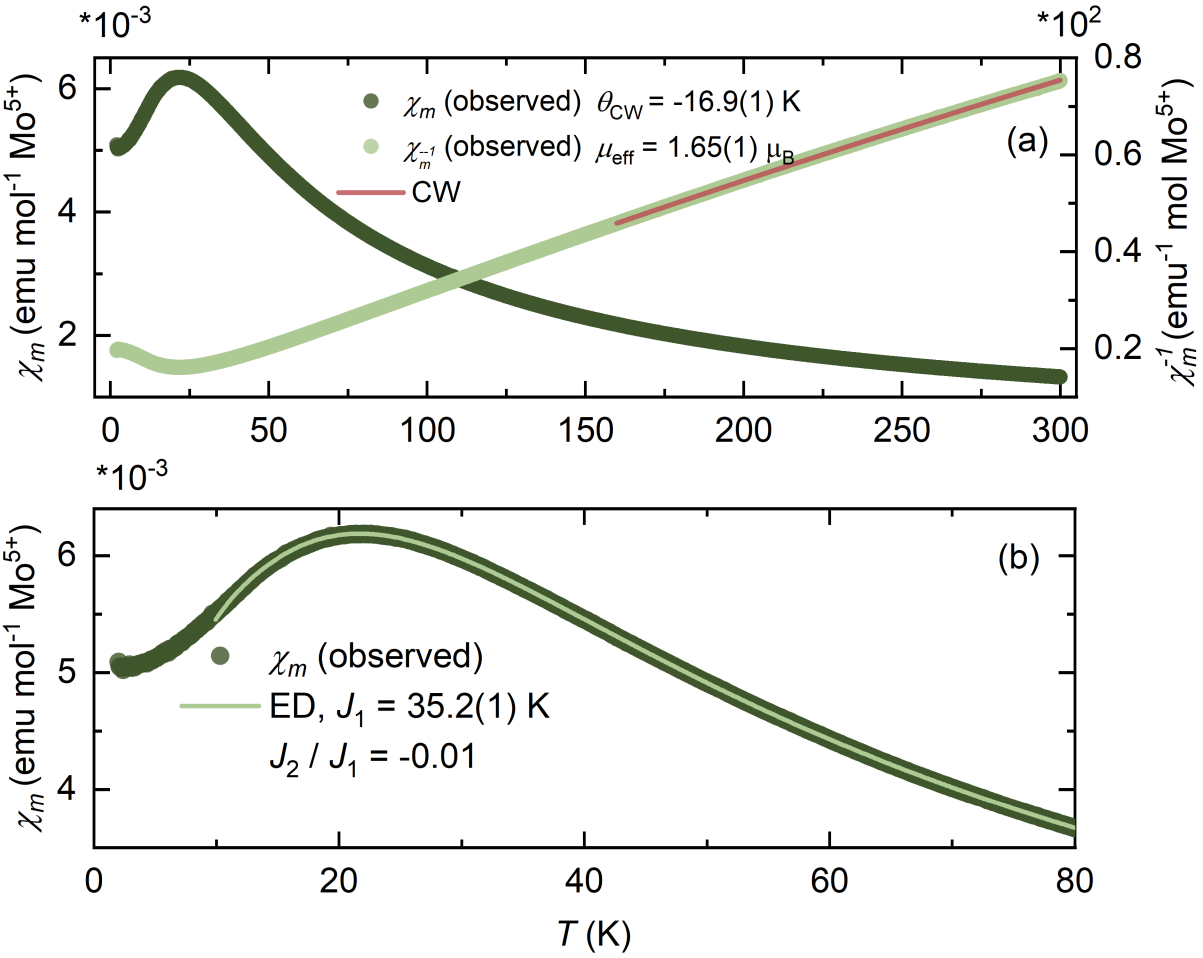

Figure 3.3: (a) Temperature dependent magnetic susceptibility, $\chi_{\rm m}(T)$, of $KMoOP_2O_7$ measured using a zero-field cooled protocol in an applied field of 1000 Oe. Above 160 K, $\chi_{\rm m}^{-1}$(T) is well described by the Curie-Weiss law with model parameters $\theta_{\rm CW} = -16.9(1)$ K, $C = 0.341(1)$ emu K mol^{-1} ($g = 1.91$), $\mu_{\rm eff} = 1.65(1)$ $\mu_{\rm B}$, and $\chi_0 = 2.51(1) \times 10^{-5}$ emu mol^{-1}. (b) Estimating the leading magnetic exchange interactions by fitting an exact diagonalization of the $S = 1/2$ Heisenberg frustrated chain antiferromagnet model above 15 K yields a dominant intrachain exchange interaction $J_2 = 35.2(1)$ K and an interchain exchange interaction $J_1/J_2 = -0.01$.

$C_{\text{p, total}} = C_{\text{p, phonon}} + C_{\text{p, mag}}$. To isolate $C_{\text{p, mag}}$, $C_{\text{p, phonon}}$ can be approximated using a linear combination of Debye (C_{D}) and Einstein (C_{E}) terms such that

$$
\begin{aligned}
C_{\text{p, phonon}}(T) &= f_{\text{D}} C_{\text{D}}(\theta_{\text{D}}, T) + \sum_{i=1}^{3} f_{\text{E}_i} C_{\text{E}_i}(\theta_{\text{E}_i}, T), \\
C_{\text{D}}(\theta_{\text{D}}, T) &= 9nR(\frac{T}{\theta_{\text{D}}})^3 \int_0^{\frac{\theta_{\text{D}}}{T}} \frac{x^4 e^x}{(e^x - 1)^2}\, dx, \\
C_{\text{E}}(\theta_{\text{E}}, T) &= 3nR(\frac{T}{\theta_{\text{E}}})^2 \frac{e^{\theta_{\text{E}}/T}}{(e^{\theta_{\text{E}}/T} - 1)^2},
\end{aligned}
\tag{3.1}
$$

where f_{D} and f_{E_i} are weighting factors, θ_{D} and θ_{E} are the Debye and Einstein temperatures, respectively, n is the number of atoms per formula unit, and R is the universal gas constant. Here, the number of C_{E} terms was based on the number of peaks in the phonon density of states observed in the measured dynamical structure factor, $S(Q, E)$ (Sec.3.3.5). On fitting down to 40 K (Fig. 3.4(a)), $C_{\text{p, total}}$ is found to be well described by $\theta_{\text{D}} \simeq 550$ K, $f_{\text{D}} \simeq 0.58$, $\theta_{\text{E}_1} \simeq 90$ K, $f_{\text{E}_1} = 0.11$, $\theta_{\text{E}_2} \simeq 115$ K, $f_{\text{E}_2} = 0.13$, $\theta_{\text{E}_3} \simeq 460$ K, and $f_{\text{E}_3} = 0.18$. Additional terms did not improve the quality of the fit. Upon subtracting the estimated phonon contribution, a broad anomaly, centered about 18 K, is revealed in the magnetic specific heat (Fig. 3.4(b)). Assuming dominant one-dimensional interactions as indicated through the exact diagonalization model describing $\chi_{\text{m}}(T)$ with $J_{\text{1D}} = 35.2(1)$ K, the temperature at which this feature is centered is in agreement with the expected $0.48 J_{\text{1D}} \approx 17$ K for the $S = 1/2$ Heisenberg one-dimensional chain antiferromagnet model[137]. Similarly, the maximum specific heat which this peak occurs, $C^{\text{max}}_{\text{p, mag}} \approx 3.1$ J mol^{-1} K^{-1}, is compatible with the predicted[138] $C^{\text{max}}_{\text{p, mag}} = 0.3497 \times R \approx 2.9$ J mol^{-1} K^{-1} for the $S = 1/2$ HAF model. Estimating the entropy release, S_{mag} (Fig. 3.4(b)), using $S_{\text{mag}}(T) = \int_{0.5\text{ K}}^{100\text{ K}} C_{\text{p, mag}}/T = 4.15$ J mol^{-1} K^{-1} reveals that only $\approx 70\%$ of the predicted $R\ln(2)$ spin entropy is recovered across this feature. This discrepancy most likely stems from an overestimation of the phonon contribution. On cooling, an anomaly, most likely associated with the onset of long-range magnetic order, is seen at $T_{\text{N}} = 0.52$ K. Using $|J_1| \simeq T_{\text{N}}/1.28\sqrt{\ln(5.8 J_2/T_{\text{N}})}$[139], interchain interactions can be estimated as $J_1 \lesssim 0.19$ K. Similarly, an upper limit on the

ordered moment is calculated as $\mu_{\rm ord} \lesssim 0.08$ $\mu_{\rm B}$ using $\mu_{\rm ord} \simeq 1.017\sqrt{|J_1|/J_2}$ [139].

3.3.4 Long Range Magnetic Order

To examine the origin of the features observed at 18 K and 0.52 K, NPD data were collected on the D20 and WISH diffractometers. The validity of the $P2_1/n$ structural model was first confirmed at all measured temperatures (Fig. 3.5). This was done through Rietveld analysis where lattice parameters and atomic positions were allowed to vary whereas the isotropic thermal parameters of like-atoms were constrained to the same value. Additional phases, on the other hand, which include a minor Mo metal impurity in all datasets and Cu phase from the sample can in the D20 datasets, were modeled using the LeBail method. The resulting models render an isotropic reduction in the lattice parameters upon cooling down to 0.04 K, an example of which is summarized in Table 3.3

For each feature seen in $C_{\rm p,\ mag}$(T), two datasets, one above and another below the temperature of interest, were measured. Given the small ordered magnetic moment expected for a $S = 1/2$ system, and hence the relatively weak expected intensities of the corresponding magnetic Bragg scattering, the paramagnetic data are subtracted from the low temperature data to isolate any magnetic scattering. No features consistent with magnetic Bragg peaks were observed in the $1.8 - 20$ K data. The $0.04 - 1.8$ K dataset, revealed several peaks alongside a broad feature around 3 Å (Fig. 3.6). At first glance, this type of diffuse scattering may suggest the possibility of correlated disorder. The position of this feature, however, could not be reproduced by any physical combination of short-range correlations. Instead, this feature most likely corresponds to the structure factor of liquid helium [140] which originates from exchange gas introduced into the sample can to thermalize the sample. Similarly, simulated models for the commensurate propagation vector $\kappa = 0$ confirm that the sharper peaks observed, which occur at positions

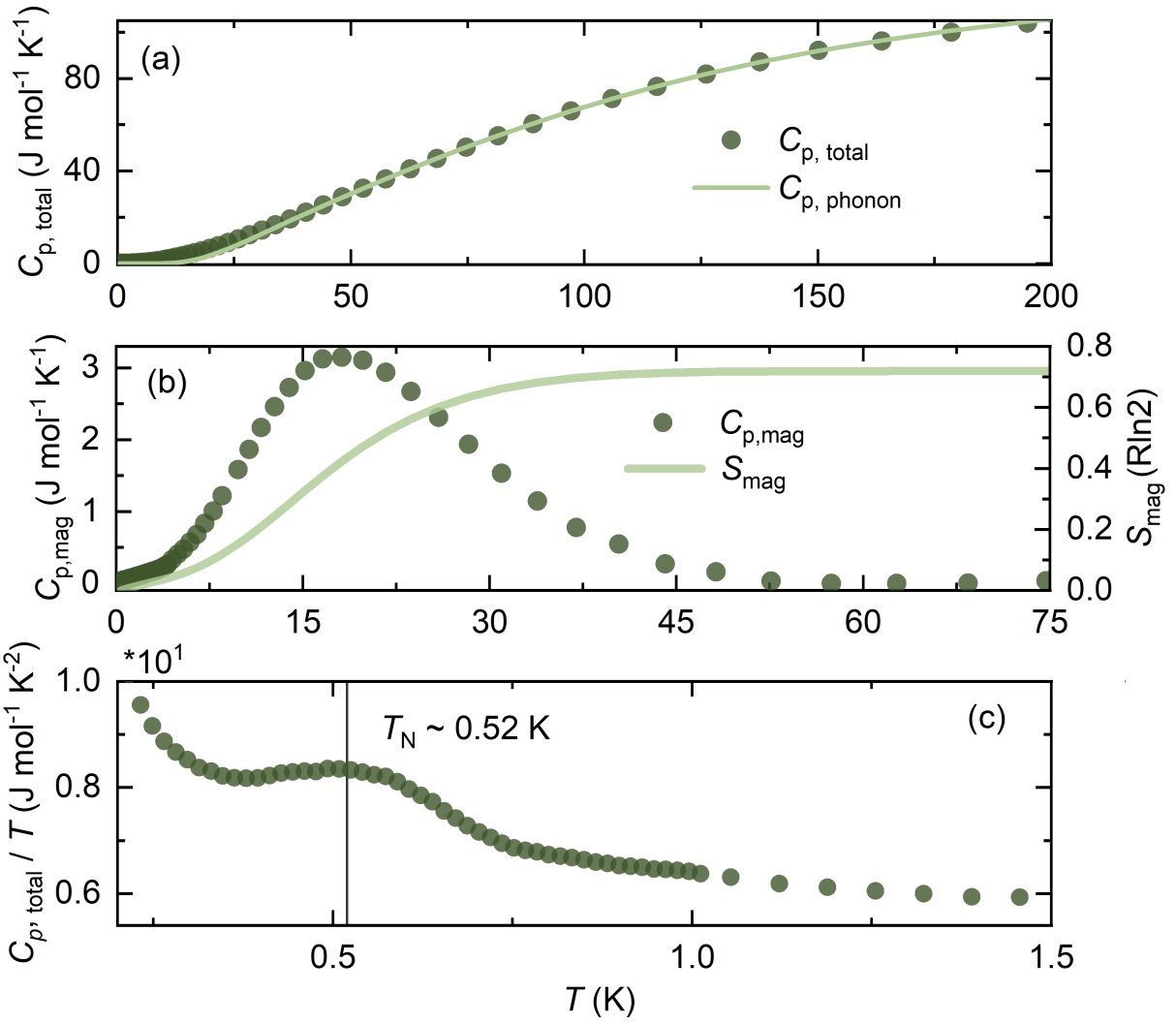

Figure 3.4: (a) Zero field measured temperature dependent specific heat, $C_{\mathrm{p,\ total}}$, fit to a Debye-Einstein model down to 40 K. (b) Subtracting the phonon contribution described by the Debye-Einstein model results isolates the magnetic contribution to the specific heat, $C_{\mathrm{p,\ mag}}$, through which the total entropy can be calculated. (c) A relatively broad feature, likely associated with the onset of long-range magnetic order is seen in C_{p}/T at 0.52 K.

Table 3.3: Structural parameters of $KMoOP_2O_7$ as obtained through Rietveld refinement of the $P2_1/n$ model using powder neutron diffraction data measured at 0.04 K on the D20 diffractometer. The resulting unit cell parameters are $a = 5.058(2)$ Å, $b = 11.645(5)$ Å, $c = 11.390(5)$ Å, and $\beta = 90.818(6)°$ with goodness-of-fit parameters $\chi^2 = 1.38$ and $R_p = 3.86\%$.

Atom	x	y	z	U_{iso}(Å^2)
Mo	0.234(3)	0.121(1)	0.1655(6)	0.008(3)
K	0.281(3)	0.359(1)	0.939(1)	0.011(4)
P1	0.241(2)	0.1921(7)	0.6457(7)	0.0014(2)
P2	0.218(2)	0.0659(6)	0.8681(8)	0.0014(2)
O1	0.195(1)	0.1001(6)	-0.0116(7)	0.002(1)
O2	-0.076(2)	0.0248(8)	0.1960(7)	0.002(1)
O3	0.020(2)	0.2662(7)	0.1310(7)	0.002(1)
O4	0.222(2)	0.1763(6)	0.7850(7)	0.002(1)
O5	0.447(2)	-0.0239(6)	0.1478(6)	0.002(1)
O6	0.215(2)	0.0879(6)	0.5720(5)	0.002(1)
O7	0.309(2)	0.1370(1)	0.3028(7)	0.002(1)
O8	0.559(2)	0.2089(9)	0.1200(9)	0.002(1)

corresponding to strong nuclear reflections, are artifacts from the subtraction (Fig. A.4). Hence, no magnetic scattering is observed down to 0.04 K.

Alternatively, an upper limit on the ordered magnetic moment can be predicted by simulating the most probable magnetic structures. Assuming antiferromagnetic interactions along the chain direction as inferred through the structural and microscopic models, a propagation vector of $\kappa = (1/2, 0, 0)$ can be assumed, and an upper estimate of $\mu_{ord} \lesssim 0.15\ \mu_B$, which would be difficult to experimentally detect, is obtained (Fig. 3.6). In comparison to the full ordered moment of $gS = 1$ for a $S = 1/2$ system, the reduction of μ_{ord} observed here is characteristic of lower dimensional materials[141,109] and is consistent with one-dimensional correlations in $KMoOP_2O_7$.

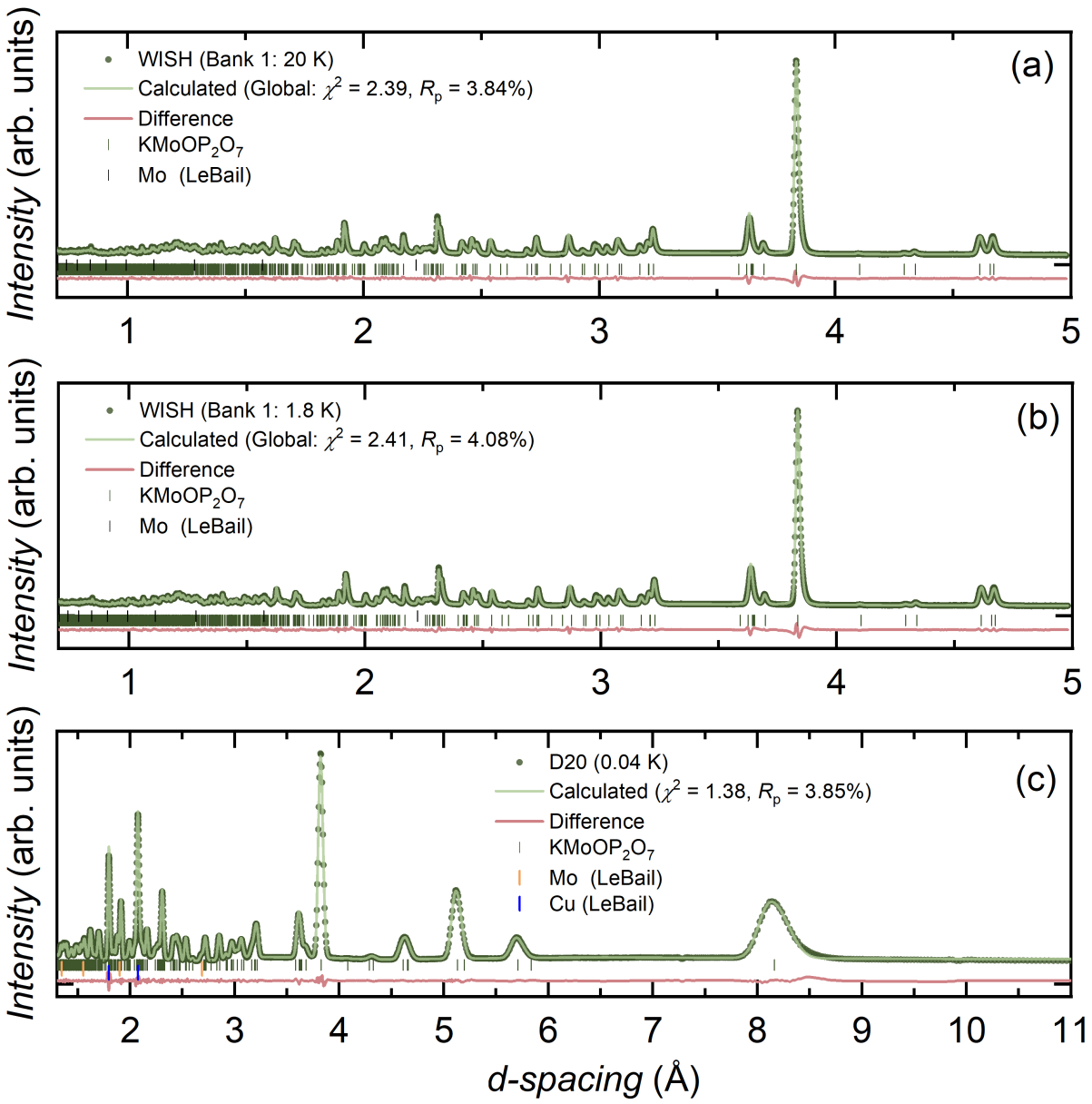

Figure 3.5: (a-c) Neutron powder diffraction data collected at 20 K, 1.8 K, and 0.04 K. Rietveld analysis confirms the $P2_1/n$ model across all measured temperatures.

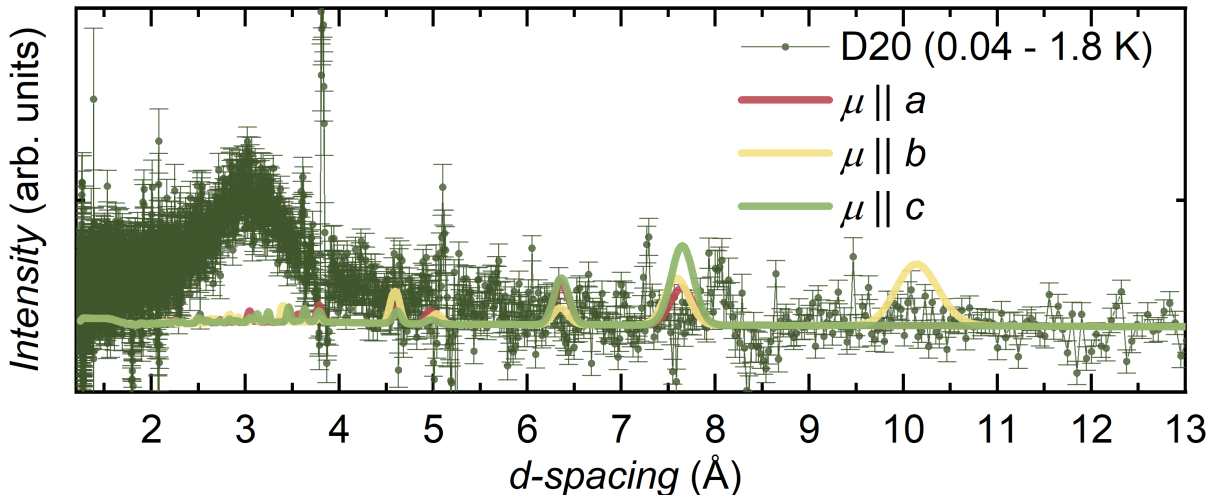

Figure 3.6: Neutron powder diffraction 0.04-1.8 K subtracted data collected on the D20 diffractometer at the ILL. By simulating an assumed magnetic structure with a propagation vector of $\kappa = (1/2, 0, 0)$, an upper limit on the ordered magnetic moment can be estimated as $\mu_{\text{ord}} \lesssim 0.15$ for all moment directions.

3.3.5 Ground State: Elucidating the Spin Hamiltonian

To gain insight into the electronic structure of $KMoOP_2O_7$, fully relativistic density functional theory (DFT) calculations were performed in the `FPLO`[142] code by Prof. Alexander Tsirlin at the University of Leipzig. Here, the exchange-correlation potential was approximated using the generalized gradient approximation[143] (GGA) and a k-mesh of 152 irreducible k-points was used. In the absence of correlations, the GGA density of states (Fig. 3.7) reveals a d_{xy} band near the Fermi level that is well separated from the near degenerate d_{xz} and d_{yz} bands. When considering the crystal field splitting of the strongly distorted Mo-octahedra, the observed splitting is consistent with the predicted active d_{xy} magnetic orbital and hence confirms the Heisenberg character of the spins.

By taking the effects of correlations into consideration, the exchange parameters of the spin Hamiltonian

$$\mathcal{H} = \sum_{i,j} J_{i,j} S_i \cdot S_j \tag{3.2}$$

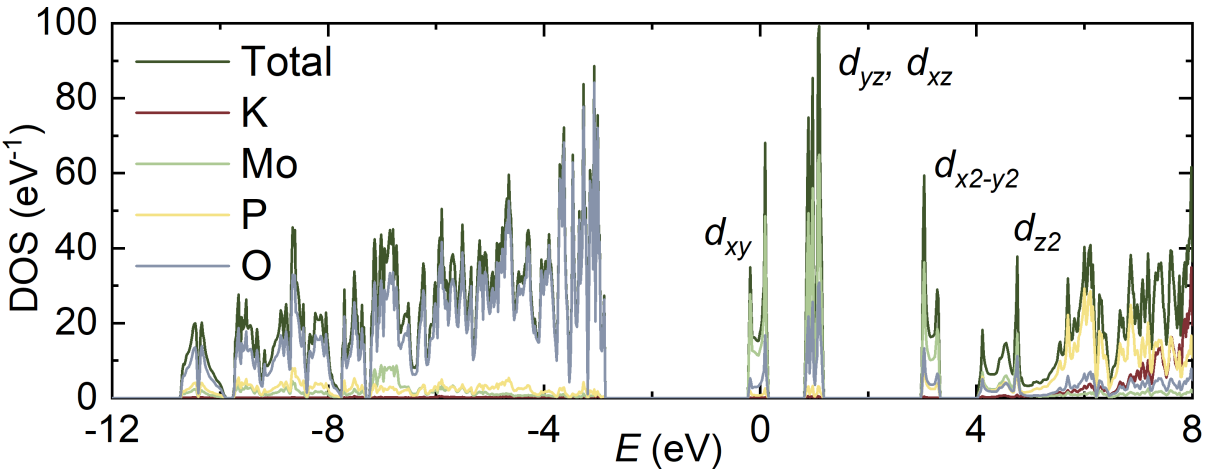

Figure 3.7: GGA density of states (DOS) for $KMoOP_2O_7$ highlighting the crystal-field splitting of the Mo $4d$ states. Here, the energy spectrum is metallic as electronic correlations are not accounted for.

were evaluated. Here, DFT+U was used and correlations were described on a mean-field level using an on-site Coulomb repulsion, $U = 4$ eV, and a Hund's coupling parameter, $J_{\mathrm{H}} = 0.5$ eV. Exchange parameters were evaluated using a procedure mapping out the energies of various collinear spin configurations[144,145]. The resulting model reveals dominant antiferromagnetic interactions along the chain direction with $J_2 = 34$ K, ferromagnetic interchain couplings $J_1 = -1.8$ K, $J_1^{'} = -1.4$ K, and negligible contributions from any further neighbour exchange interactions.

Having found a consistent description of the magnetic Hamiltonian through *ab-initio* calculations and bulk measurements, we now turn to an experimental investigation using neutron spectroscopy. The dynamical structure factors, $S(Q, E = \hbar\omega)_{\mathrm{exp}}$, of both $KMoOP_2O_7$ and $KNbOP_2O_7$, measured at 1.8 K with an incident energy of $E_{\mathrm{i}} = 14.2$ meV, are shown in Fig. 3.8. When compared to its diamagnetic analogue (Fig. 3.8(b)), several features are apparent in the spectrum of $KMoOP_2O_7$ (Fig. 3.8(a)). Firstly, an accumulation of inelastic spectral weight is observed below 2.5 meV and up to at least 2 Å^{-1}. Given the presence of this feature in both spectra, it can be associated with scattering from the instrument and sample environment. To correct for the masking effects of this spurious scattering, we thus subtract the empirically scaled spectrum of $KNbOP_2O_7$ from that of

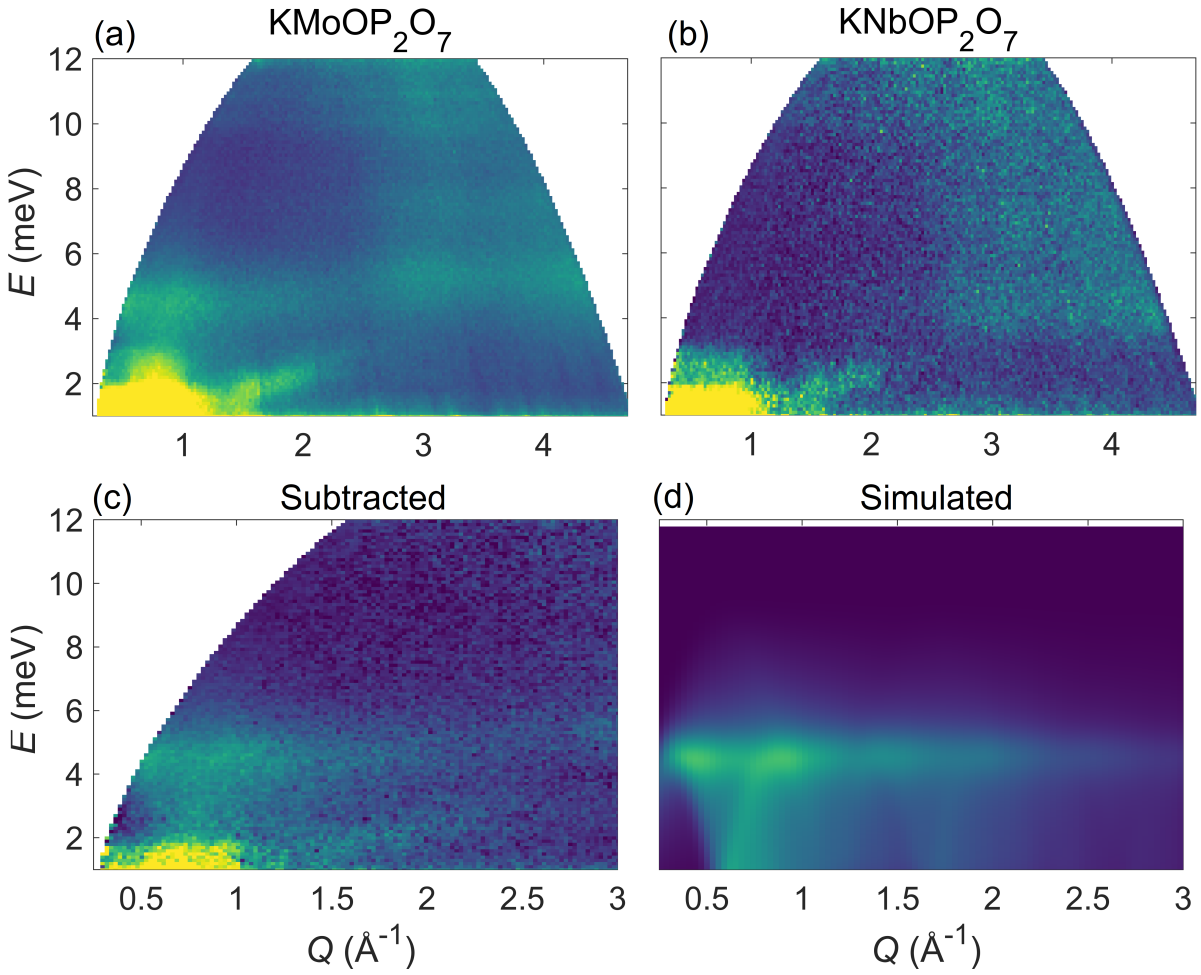

Figure 3.8: (a-b) The experimental dynamical structure factor, $S(Q, E = \hbar\omega)_{\text{exp}}$, measured at 1.8 K with an incident neutron energy of $E_{\text{i}} = 14.2$ meV for $KMoOP_2O_7$ and its diamagnetic analogue $KNbOP_2O_7$, respectively. (c-d) Comparison of the phonon subtracted $S(Q, E)_{\text{exp}}$ with the powder averaged and energy convoluted dynamical structure factor, $S(Q, E)^{\text{FCM}}_{2+4}$, simulated for the best fit model described by $J_1 = -1.8$ K and $J_2 = 34.4$ K.

$KMoOP_2O_7$. However, as differences in multiple scattering events and attenuation most likely modify this spurious scattering, remnants of these features are still apparent in the subtracted spectrum (Fig. 3.8(c)). While similarities are apparent in the phonon spectra of both materials, a phonon branch, centered about 5.5 meV, also remains. This could be related to differences in the bonding geometries with K^+. Hence, the analysis is confined within the least contaminated regions above 2.5 meV and below 3 $Å^{-1}$.

The subtracted $S(Q, E = \hbar\omega)_{\text{exp}}$ shows an accumulation of spectral weight peaked about 4.5 meV (Fig. 3.8(c)). On account of its absence from the spectrum of the diamagnetic analogue, we assign this feature to the magnetic response of $KMoOP_2O_7$. Whilst the spurious scattering masks any low-E features revealing the details of the spin Hamiltonian, both the exact diagonalization and *ab-initio* models establish the $S = 1/2$ Heisenberg frustrated chain model as a valid starting point to describe $KMoOP_2O_7$. Hence, the magnetic scattering could possibly be associated with a powder averaged spinon spectrum. Consequently, when using $J_{1\text{D}}$ from the DFT model, the peak of this scattering, centered about 4.5 meV, is consistent with the expected $\pi J_{1\text{D}}/2 \approx 4.6$ meV amplitude for the lower bound of the spinon continuum[33].

The full spin Hamiltonian described in Eqn. 3.2 was modeled by including the effects of an interchain interaction to the numerically evaluated dynamical structure factor of the two- and four-spinon continuum[146], $S(Q, E)^{1\text{D}}_{2+4}$, calculated by Prof. J.-S. Caux at the University of Amsterdam. This was done following the random phase approximation (RPA)-style approach pioneered by Kohno et al.[147] where the dynamical structure factor of Eqn. 3.2 is described as

$$S(Q, E)^{\text{FCM}}_{2+4} = \frac{S^{1\text{D}}_{2+4}(Q, E)}{[1 + J'(Q)\pi S^{1\text{D}}_{2+4}(Q, E)]^2 + [J'(Q)\chi''_{1\text{D}}(Q, E)]^2}. \tag{3.3}$$

Here, $J'(Q)$ is the Fourier transform of the interchain coupling $J_1 = J'_1$ whereas $\chi''_{1\text{D}}(Q, E) = \int_0^\infty S^{1\text{D}}_{2+4}(Q, E')/(E' - E)\ dE'$. Prior to any analysis, the resulting expression was powder

averaged by selecting random coordinates from a Gaussian distribution on a constant-Q sphere and convolved with the instrumental resolution. Using a particle swarm algorithm, $S(Q,E)^{\mathrm{FCM}}_{2+4}$ was then optimized to four E cuts that are centered about 0.9, 1.1, 1.4, and 1.6 Å^{-1} and integrated over $\delta Q = 0.1$ Å^{-1}. The best fit model, shown in Fig. 3.9, was found for $J_2 = 34.4$ K (2.95 meV) and a ferromagnetic $J_1 = -1.8$ K (-0.16 meV). Given the slight contamination of the data in regions where the redistribution of spectral weight resulting from J_1 would be most pronounced, however, this model should be treated as confirming the dominance of one-dimensional correlations in KMP rather than describing the exact value of J_1. As previously discussed and as expanded upon in the following section, this one dimensionality appears to stem from the distorted Mo-octahedral environment. The resulting d_{xy} active magnetic orbital, lying within the plane of the one-dimensional chains, favors one-dimensional interactions, and results in relatively small further neighbor interactions. Hence, the resulting model is consistent overall with KMP being a nearly ideal realization of the $S = 1/2$ Heisenberg chain antiferromagnet model echoing the exact diagonalization fit to $\chi_{\mathrm{m}}(T)$ and the DFT+U calculations.

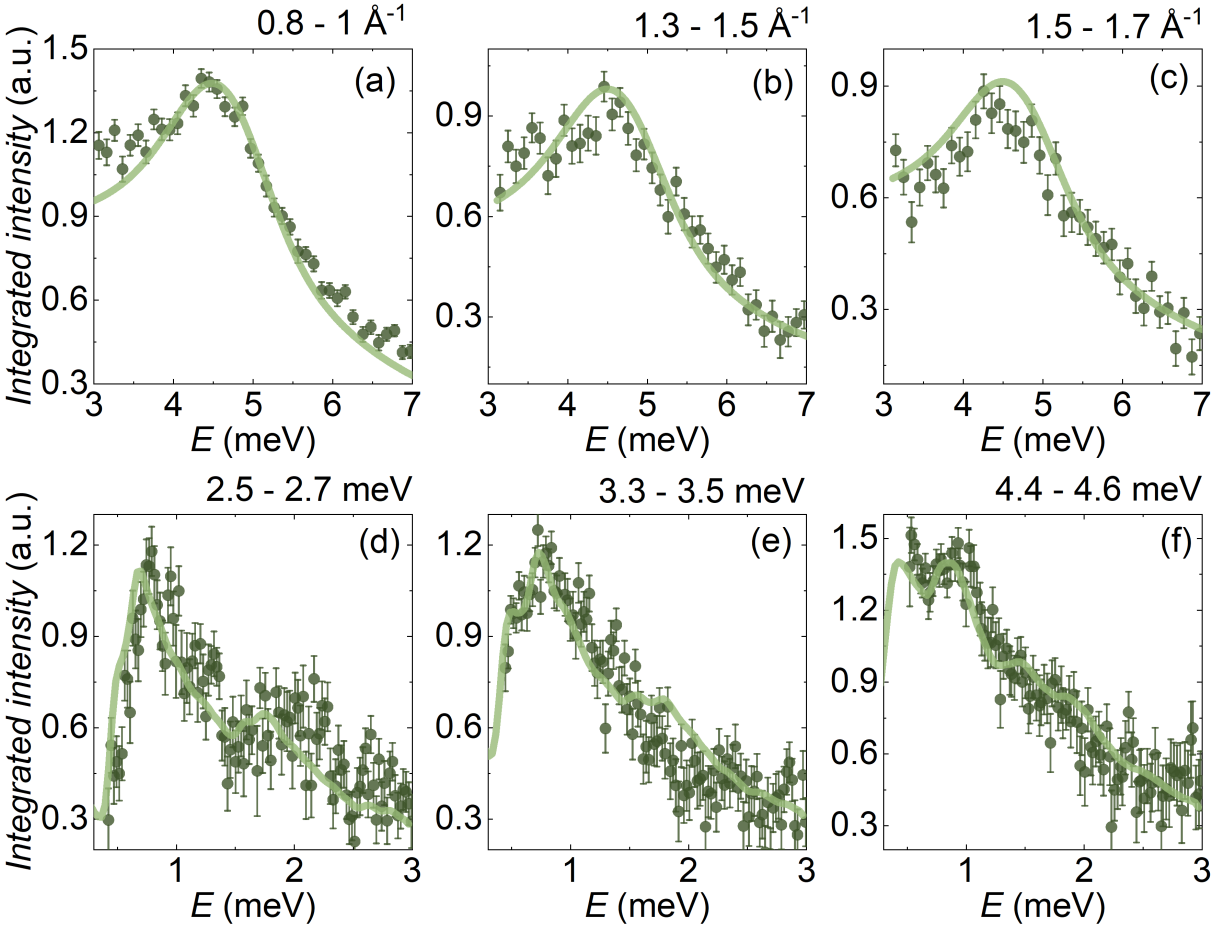

Figure 3.9: Best fit model resulting from a particle swarm optimization of $S(Q,E)^{\mathrm{FCM}}_{2+4}$ and yielding $J_1 = -1.8(2)$ K and $J_2 = 34.4(1)$ K fitted to selected (a-c) constant-Q and (d-f) constant-E cuts.

3.4 Investigating the Effects of Alkali Metal Substitution: AMoOP$_2$O$_7$ (A = Na, Cs)

The one-dimensional character of the correlations in KMoOP$_2$O$_7$ largely stems from the structural distortion of the octahedra (Fig. 3.2(c)). It would thus follow that the strength of the interchain couplings could be tuned by altering the crystal field splitting to favor either a degenerate t_{2g} manifold or a different magentic orbital. Several approaches could be taken, and a systematic tuning of the physical properties of the system could result from the application of pressure, magnetic fields, strain, or chemical pressure[9]. Given the versatility of the phosphate ligand in coordinating pentavalent transition metal ions[148,125,149,150], however, a natural starting point for this investigation is tuning through chemical substitution. Indeed, the pyrophosphate family of materials, AMOP$_2$O$_7$, where A^+ is an alkali metal ion and M^{5+} is a pentavalent transition metal cation, provides an extensive source of candidate materials as many structural studies have already been conducted on materials ranging from A^+ = Li-Cs[125] and M^{5+} = Mo[130,128,129,127], W[148,149], Nb[150], and Ta[151]. For this purpose of this study, given that it is the A^+-O^{2-}-Mo^{5+} bonding that distorts the metal containing octahedra, we shall examine the structural-property behavior of this system by substituting the alkali metal position with A^+ = Na, Cs.

3.4.1 Crystal Structure

The reported structural models of both NMP[127] and CMP[129] were confirmed at 300 K through analysis of powder X-ray diffraction data. As data were collected for NMP on the bench-top Miniflex diffractometer which does not separate Kα_1 and Kα_2 radiation, a LeBail profile fit of the orthorhombic $P2_12_12_1$ model was used to determine the lattice

Table 3.4: Structural parameters extracted from analysis of powder diffraction data at 300 K for the $A\mathrm{MoOP_2O_7}$ series.

A-site	Na	K	Cs
Space Group	$P2_12_12_1$	$P2_1/n$	$P2_1/n$
a (Å)	11.364(1)	5.0850(1)	5.1386(1)
b (Å)	5.1345(3)	11.729(2)	11.702(2)
c (Å)	10.683(5)	11.508(2)	12.059(3)
β (°)	90	90.975(1)	91.774(2)
V (Å^3)	627.3(2)	685.7(1)	724.8(1)

Table 3.5: Key structural distances resulting from Rietveld analysis of powder diffraction data for $A\mathrm{MoOP_2O_7}$ A = K, Cs at 300 K. Distances for $\mathrm{NaMoOP_2O_7}$ are obtained from a reported structural model[127]. Here, the subscript J_1 and J_2 represent the respective interchain and intrachain superexchange pathways, whereas J_b describes the non-frustrating coupling through $\mathrm{P_2O_7}$ bridges along the b-direction.

A-site	Na[127]	K	Cs
Mo-Mo$_{J_2}$ (Å)	5.146(11)	5.085(1)	5.138(1)
Mo-Mo$_{J_1}$ (Å)	5.334(3)	5.360(5)	5.251(2)
Mo-Mo$_{J_1'}$ (Å)	5.334(3)	5.401(5)	5.508(1)
Mo-Mo$_{J_b}$ (Å)	6.004(3)	6.171(1)	6.023(1)
Mo-O, short apex (Å)	1.643(9)	1.675(4)	1.670(3)
Mo-O, long apex (Å)	2.099(8)	2.140(1)	2.242(5)

parameters (Fig. 3.10(a)) which are consistent with the previously published structural model[127] (Table 3.4). The monoclinic $P2_1/n$ structural model of CMP, was confirmed at 300 K using Rietveld analysis of powder X-ray diffraction data and is summarized in Table 3.6. A Mo impurity accounts for 1.3(1)% of the bulk weight of the sample and a few unidentified minor impurity peaks, highlighted in Fig. 3.10(b), are observed. Here, the lattice parameters, atomic positions, and displacement parameters were refined. The relevant atomic distances across the series are summarized in Table 3.4 and Table 3.5. As expected, both the unit-cell volumes and the c lattice parameters increase monotonically with increasing A-site ionic radius.

In comparison to its monoclinic K and Cs analogues, NMP adopts an orthorhombic structure. The Mo-octahedral geometry is also significantly distorted in comparison to other members of the series. Indeed, while the apical Mo-O bond distances remain consistent for all three analogues (Table 3.5), O-O distances within the basal plane significantly vary between 2.38-3.39 Å in NMP while only ranging from 2.74-2.89 Å for both KMP and CMP. The underlying magnetic sublattice, however, is consistent across the series, with infinite Mo^{5+}-chains propagating through phosphate tetrahedra along either the *b*- or *a*-crystallographic axes for A = Na and A = K, Cs, respectively. Despite this similarity, differences in the conformation of the pyrophosphate groups across the series introduce subtle differences between the structures. While each Mo-octahedron remains coordinated by five P_2O_7 groups, the conformation of these, as highlighted in Figs. 3.11(d-f), is staggered in the Na and K analogues and instead eclipsed in CMP. This change in conformation alters the shape of the A-site-containing tunnel structures as reflected in Figs. 3.11(g-i) and most likely stems from the increase in ionic radius[127].

3.4.2 Magnetometry and Specific Heat

The zero-field cooled temperature dependent molar magnetic susceptibilities of NMP and CMP, measured in applied fields of 1000 Oe, are shown in Figs. 3.12 and 3.13. Both contain features comparable to those seen in KMP (Fig. 3.3); broad anomalies are seen in both at about 23 K and no features consistent with the onset of long range magnetic order are evident. Curie-Weiss fitting reveals dominant antiferromagnetic interactions and effective moments comparable to those expected for $S = 1/2$ systems. Given the similar distortion observed across the series and the Curie tails present in the data sets, the slight reduction in μ_{eff} for the Na and Cs analogues most likely arises from the presence of minor impurity phases rather than from an orbital contribution. Estimating exchange interactions by fitting an exact diagonalization of the $S = 1/2$ Heisenberg frustrated

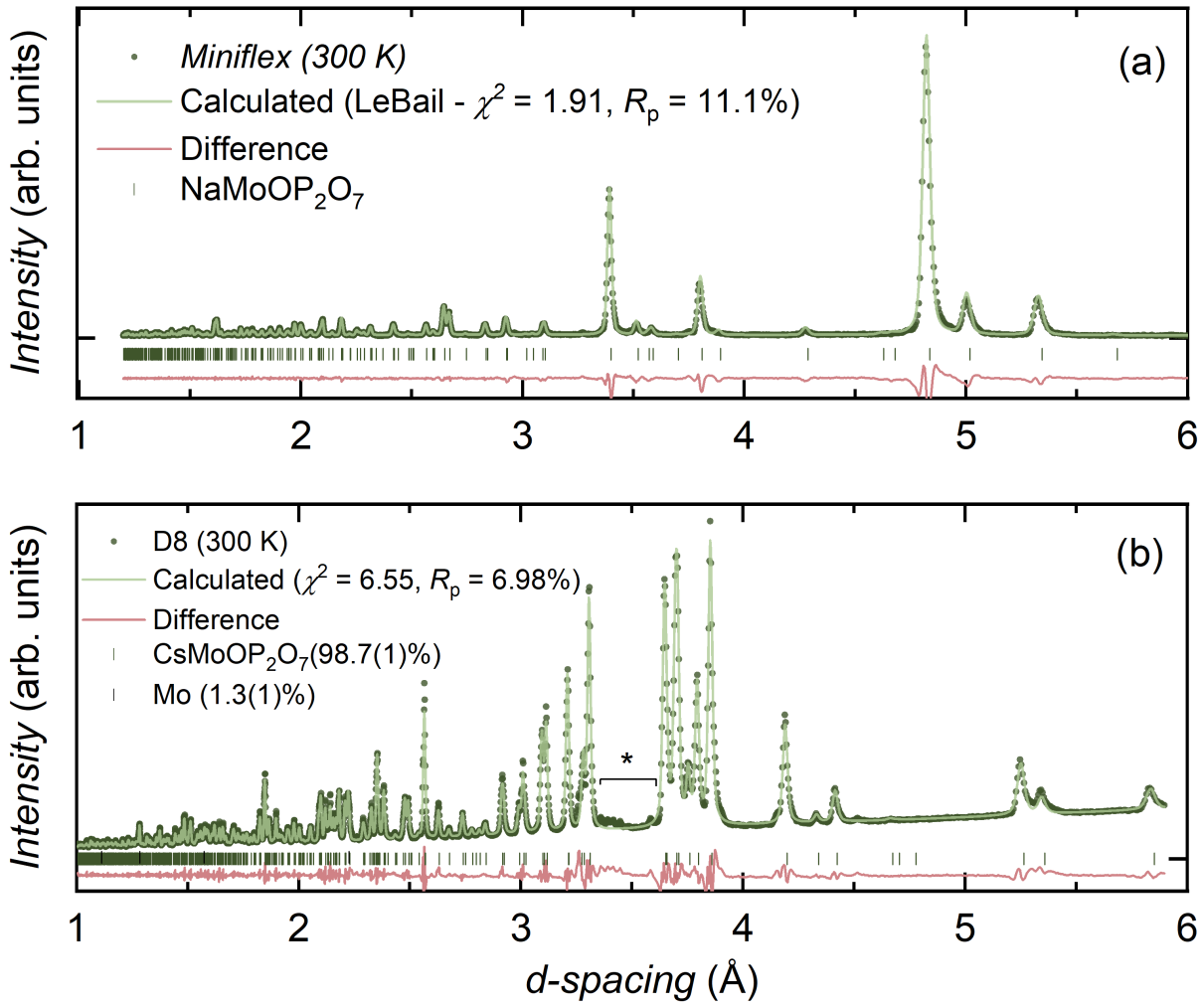

Figure 3.10: (a) LeBail fit of the $P2_12_12_1$ model for $NaMoOP_2O_7$ to PXRD data collected at 300 K. (b) Rietveld analysis of PXRD data collected at 300 K for the $P2_1/n$ model for $CsMoOP_2O_7$. The asterisk highlights several impurity peaks.

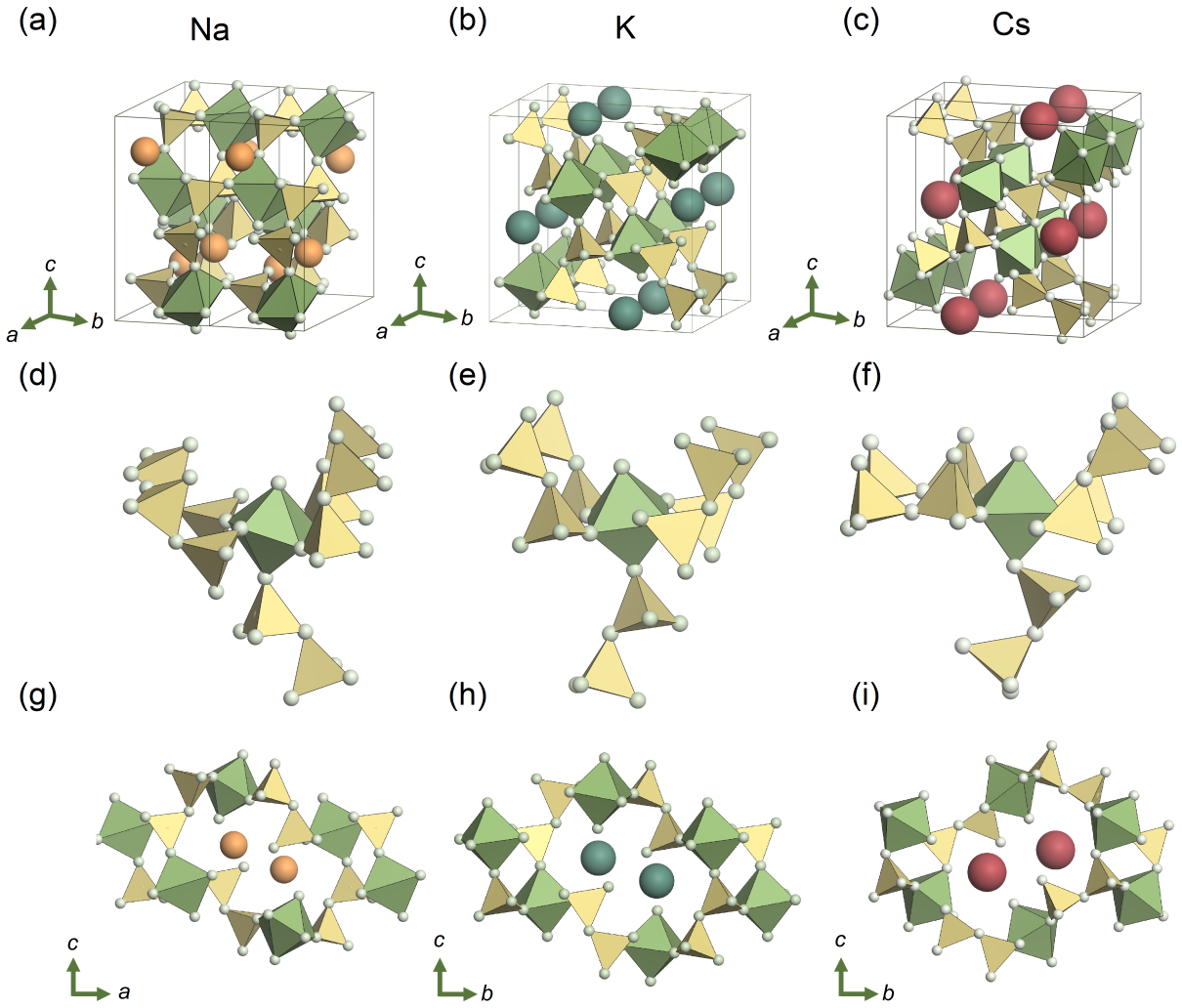

Figure 3.11: Comparison of structural models for the A = Na, K, and Cs alkali metal analogues of the pyrophosphate family of materials, $A\mathrm{MoOP_2O_7}$. (a) The $P2_12_12_1$ crystal structure of $\mathrm{NaMoOP_2O_7}$ alongside the $P2_1/n$ structural models of (b) $\mathrm{KMoOP_2O_7}$ and (c) $\mathrm{CsMoOP_2O_7}$ as viewed along the [111] direction. The main structural differences associated with the orientation of the pyrophosphate molecules and the tunnel-like structures are highlighted across (d-i) panels. Figures generated using the `VESTA` visualization package[26].

Table 3.6: Structural parameters of $CsMoOP_2O_7$ as obtained through Rietveld refinement of the $P2_1/n$ model using powder X-ray diffraction data measured at 300 K on a Bruker D8 diffractometer. The resulting unit cell parameters are $a = 5.1386(1)$ Å, $b = 11.702(2)$ Å, $c = 12.059(3)$ Å, and $\beta = 91.774(2)^\circ$ with goodness-of-fit parameters $\chi^2 = 6.55$ and $R_\mathrm{p} = 6.98\%$.

Atom	x	y	z	U_iso(Å^2)
Mo	0.2377(9)	0.0449(2)	0.1909(4)	0.014(1)
Cs	0.7687(6)	0.3361(2)	0.0515(2)	0.030(1)
P1	0.758(2)	0.164(1)	0.309(1)	0.020(3)
P2	0.776(2)	0.397(1)	0.418(1)	0.018(4)
O1	0.247(4)	-0.039(1)	0.302(2)	0.028(8)
O2	0.020(3)	0.165(2)	0.255(1)	0.018(7)
O3	0.540(4)	0.130(1)	0.219(1)	0.006(8)
O4	-0.073(4)	-0.003(1)	0.120(2)	0.029(8)
O5	0.438(4)	-0.073(2)	0.104(1)	0.014(8)
O6	0.259(7)	0.153(2)	0.038(2)	0.051(8)
O7	0.750(6)	0.100(2)	0.427(2)	0.01(1)
O8	0.700(5)	0.301(2)	0.339(2)	0.07(1)

chain antiferromagnet model yields dominant antiferromagnetic intrachain exchange interactions that are slightly larger than that of KMP and minimal interchain exchange as summarized in Table 3.7.

Given the small extracted interchain coupling parameters, the effect of J_1 most likely manifests within the low temperature regions of $\chi_\mathrm{m}(T)$ which are masked by the presence of large Curie tails in both NMP and CMP. Hence, an attempt at subtracting the Curie tails was undertaken. This was done by fitting $\chi_\mathrm{m} = C/T$ between 2 K and 8 K to result in $C = 0.007(1)$ emu K mol^{-1} and $C = 0.02(1)$ emu K mol^{-1} for NMP and CMP, respectively. This procedure was unsuccessful for KMP where the impurity paramagnetic contribution is minimal and the fitting overestimates the Curie tail. The difference in the values of C reflect the larger Curie tail that is related to the larger paramagnetic impurity phase in CMP as evidenced by the powder X-ray diffraction data. The Curie tail corrected χ_m(T) curves are shown in Fig. 3.14 and reflect over- and under-subtracted curves for NMP

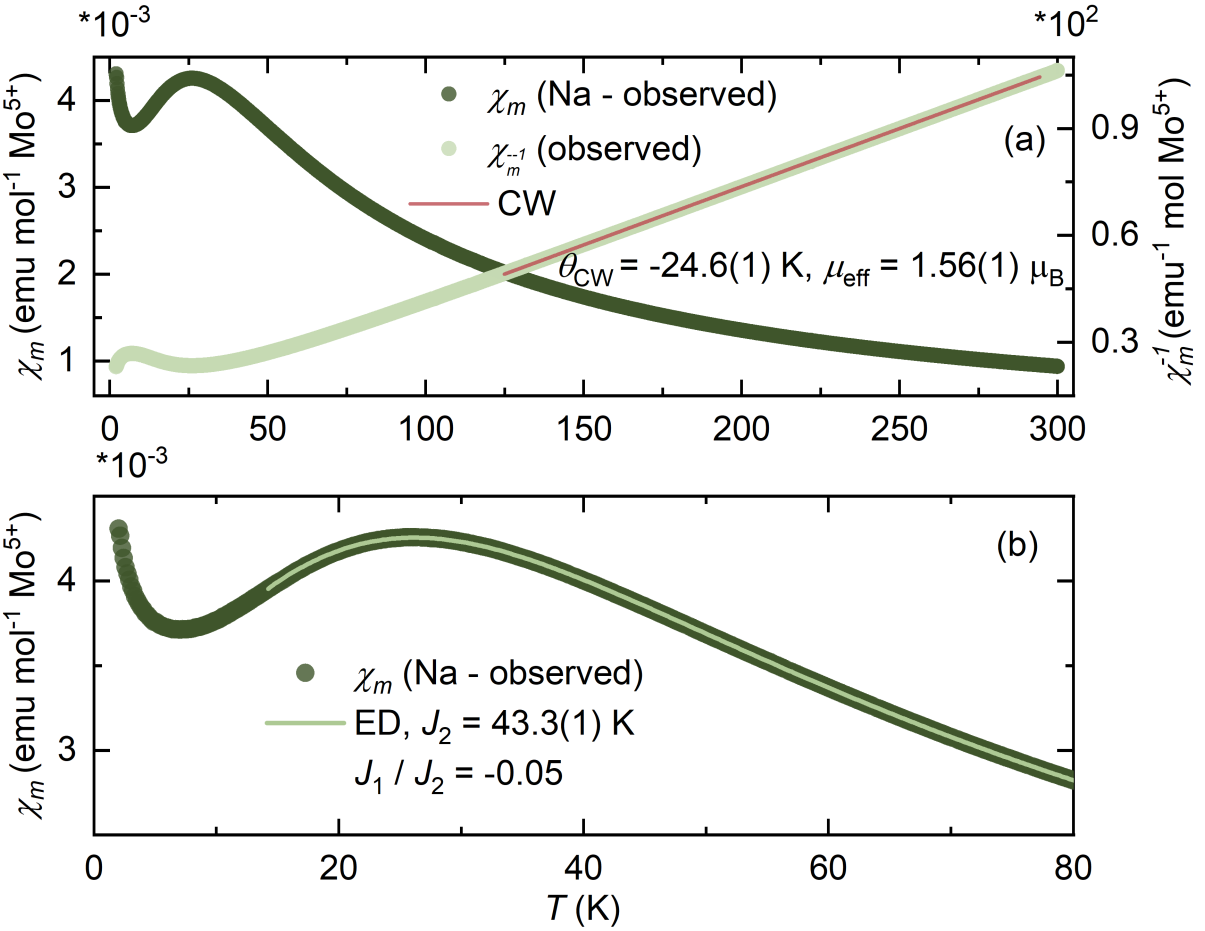

Figure 3.12: (a) Temperature dependent magnetic susceptibility, $\chi_{\rm m}(T)$, of $NaMoOP_2O_7$ measured using a zero-field cooled protocol in an applied field of 1000 Oe. Above 180 K, $\chi_{\rm m}^{-1}$(T) is well described by the Curie-Weiss law with model parameters $\theta_{\rm CW} = -24.6(1)$ K, $C = 0.303(1)$ emu K mol^{-1} ($g = 1.80$), $\mu_{\rm eff} = 1.56(1)$ $\mu_{\rm B}$, and $\chi_0 = 6.96(1) \times 10^{-5}$ emu mol^{-1}. (b) Estimating the leading magnetic exchange interactions by fitting an exact diagonalization of the $S = 1/2$ Heisenberg frustrated chain antiferromagnet model above 15 K yields a dominant intrachain exchange interaction $J_2 = 43.3(1)$ K ($g = 1.82$) and an interchain exchange interaction $J_1/J_2 = -0.05$.

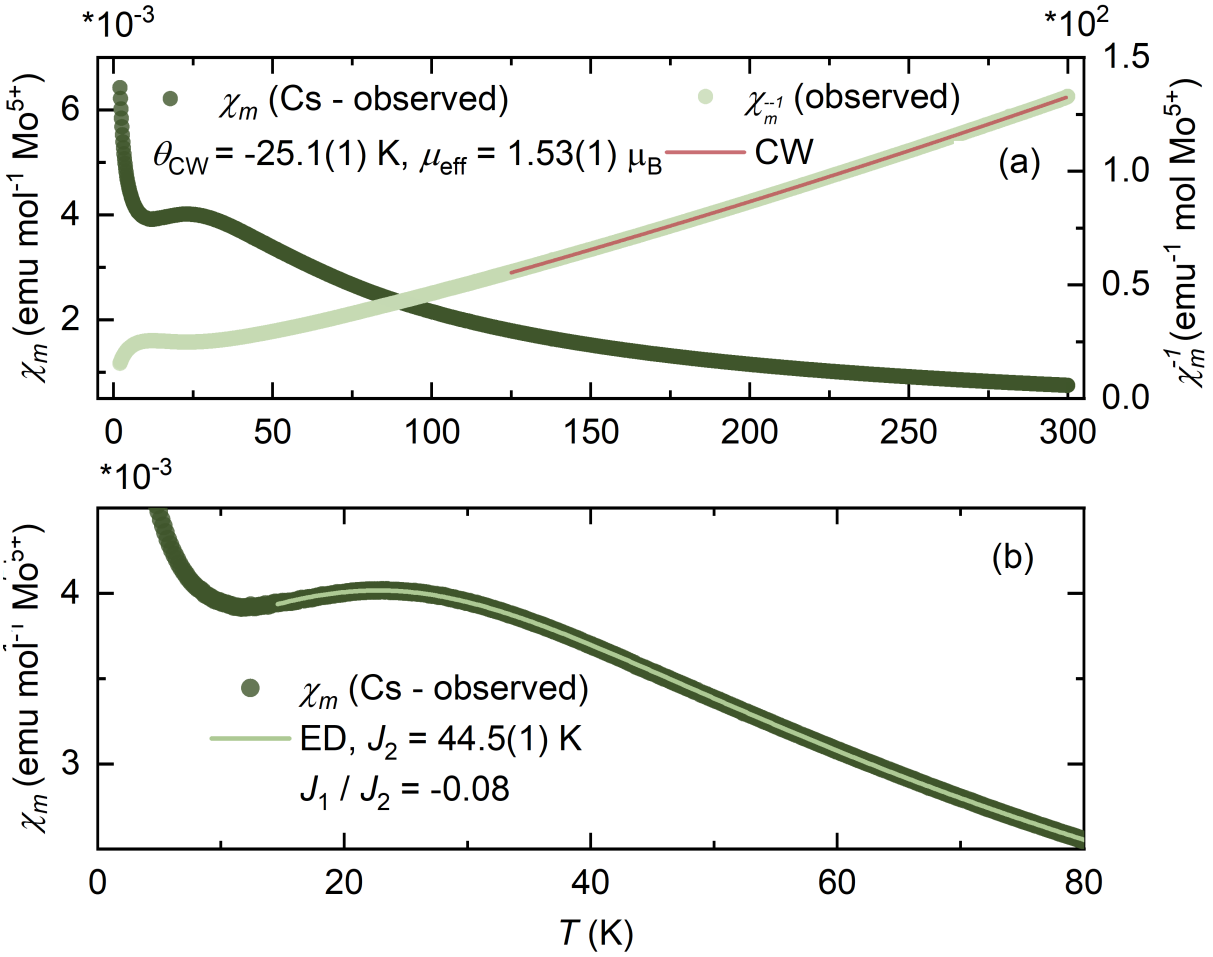

Figure 3.13: (a) Temperature dependent magnetic susceptibility, $\chi_{\rm m}(T)$, of $CsMoOP_2O_7$ measured using a zero-field cooled protocol in an applied field of 1000 Oe. Above 180 K, $\chi_{\rm m}(T)$ is well described by the Curie-Weiss law with model parameters $\theta_{\rm CW} = -25.1(1)$ K, $C = 0.341(1)$ emu K mol^{-1} ($g = 1.76$), $\mu_{\rm eff} = 1.53(1)$ $\mu_{\rm B}$, and $\chi_0 = -1.48(1) \times 10^{-5}$ emu mol^{-1}. (b) Estimating the leading magnetic exchange interactions by fitting an exact diagonalization of the $S = 1/2$ Heisenberg frustrated chain antiferromagnet model above 15 K yields a dominant intrachain exchange interaction $J_2 = 44.5(1)$ K ($g = 1.83$) and an interchain exchange interaction $J_1/J_2 = -0.08$.

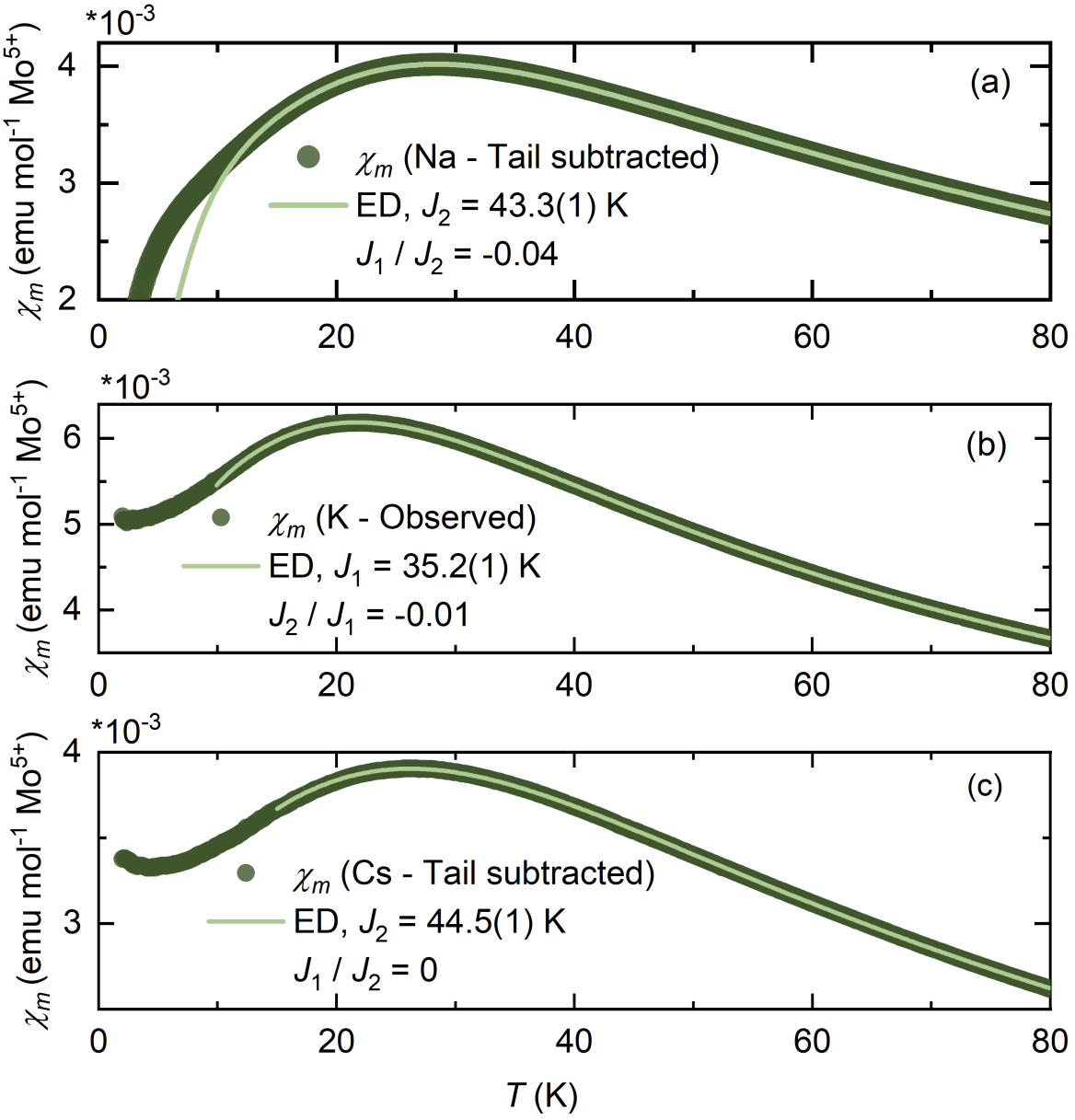

Figure 3.14: Temperature dependent magnetic susceptibility, $\chi_{\mathrm{m}}(T)$, of (a) $NaMoOP_2O_7$, (b) $KMoOP_2O_7$, and (c) CMP fit above 20 K to an exact diagonalization of the $S = 1/2$ Heisenberg frustrated chain antiferromagnet model. Here, the Curie tails present in the data collected for NMP and CMP were subtracted.

Table 3.7: Summary of the CW models and exchange parameters for AMoOP$_2$O$_7$ (A = Na, K, Cs) as obtained through fitting $\chi_{\mathrm{m}}(T)$ using exact diagonalization of the $S = 1/2$ FCM and T_{N} as obtained from $C_{\mathrm{p}}(T)$.

A-site	Na	K	Cs
J_1/J_2	-0.05	-0.01	-0.08
J_2 (K)	43.3(1)	35.2(1)	44.5(1)
θ_{CW} (K)	-24.6(1)	-16.9(1)	-25.1(1)
μ_{eff} (μ_{B})	1.56(1)	1.65(1)	1.53(1)
χ_0 (emu mol^{-1} $\times 10^{-5}$)	6.96(1)	2.51(1)	-1.48(1)
T_{N} (K)	0.52	0.52	0.65

and CMP, respectively. Fitting the same exact diagonalization model, while examining the effect of varying the minimum fitting temperature (Figs. A.2, A.5, A.6), reveals that subtracting the Curie tails does not alter the interchain exchange parameters. Instead, and as expected, J_1/J_2 changes and significantly decreases for CMP. This highlights the uncertainty associated with fitting magnetic susceptibility curves, and confirms the importance of complimentary analytical and experimental techniques for determining the spin Hamiltonian.

Despite the similarities in the magnetic susceptibility curves, the zero-field temperature dependent specific heat displays varying behavior across the series (Fig. 3.15). In comparison to KMP where the presumed onset of long range magnetic order is described by a broad anomaly in $C_{\mathrm{p,\ total}}$ (Fig. 3.15(b)), sharper features are observed for both NMP and CMP. The source of this difference is not clear, but could be related to differences in the sample quality. Interestingly, T_{N} remains comparable across the series despite the stronger J_1 and J_2 interactions in NMP and CMP. This again reflects that the exact diagonalization extracted J_1 parameters are inconclusive as stronger intrachain interactions would have presumably increased the ordering temperature.

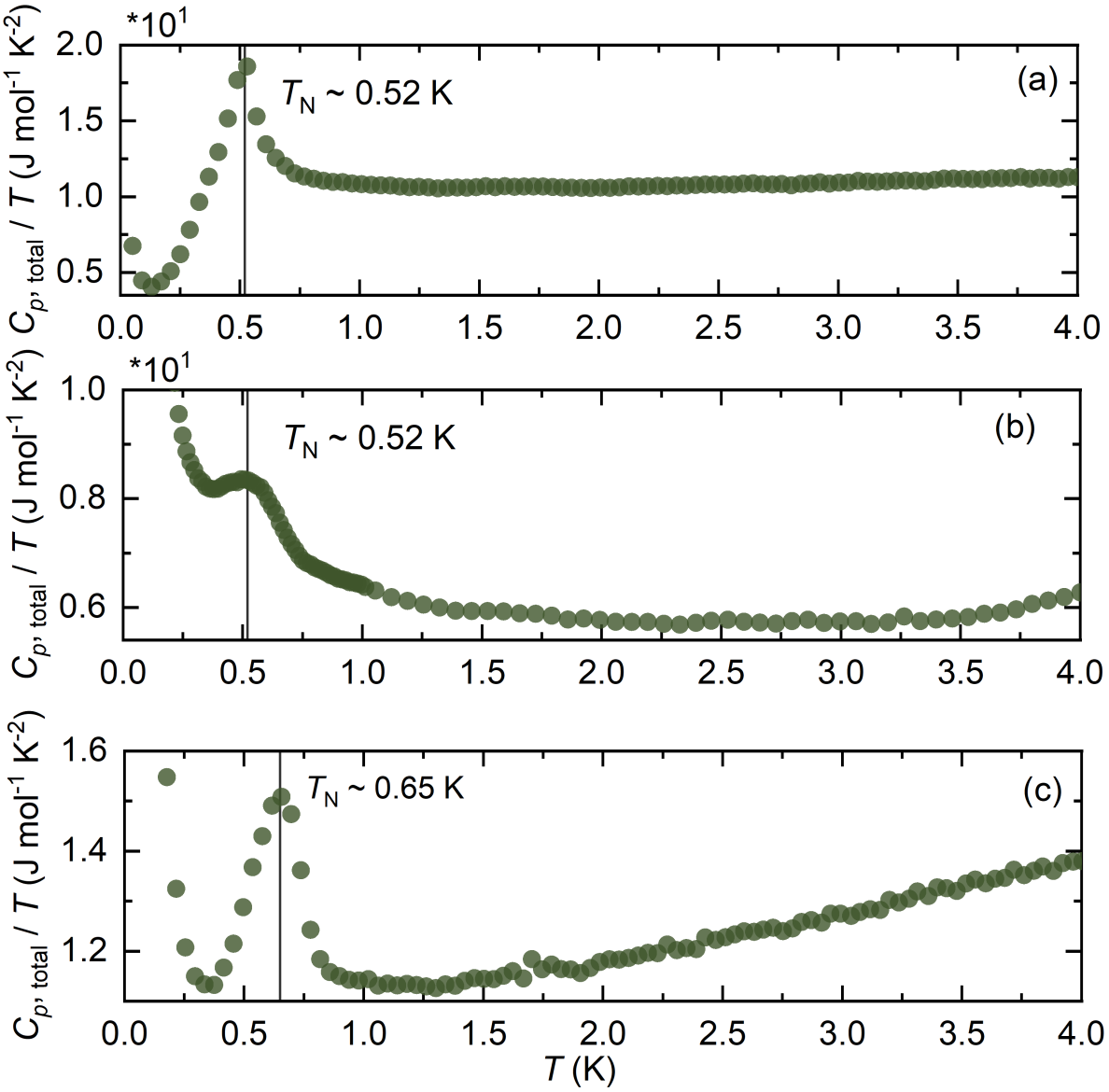

Figure 3.15: Zero-field temperature dependent specific heat, C_{p}/T, measured for (a) $NaMoOP_2O_7$, (b) $KMoOP_2O_7$, and (c) $CsMoOP_2O_7$.

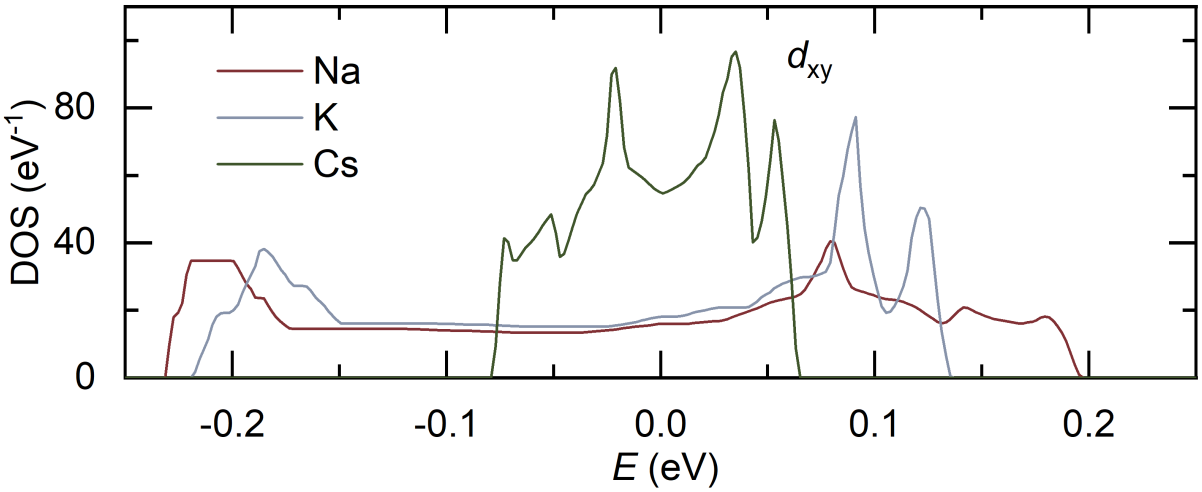

Figure 3.16: GGA density of states (DOS) highlighting the Mo d_{xy} band for the AMoOP$_2$O$_7$ series. Here, the spectrum is metallic as electronic correlations are not accounted for.

3.4.3 Microscopic Model

Given the structural differences, one of the interesting observations made in comparing members across the series is the similarities in the strength of the exchange interactions and ordering temperatures. To identify the source of these similarities, density functional theory calculations were performed by Prof. Alexander Tsirlin using a gradient generalized approximation (GGA) of the exchange-correlation potential within the `FPLO`[142] and `VASP`[152,153]. As expected, the uncorrelated GGA band structures of the Na and Cs analogues reveal similar level schemes, albeit with large differences in the bandwidths, and yield a d_{xy} active magnetic orbital (Fig. 3.16).

The leading exchange parameters were approximated through the same DFT+U approach used for KMP from which the resulting model parameters are summarized in Table 3.8. As discussed in the context of V^{4+}-containing systems that are similarly bridged by phosphate groups through pseudo-edge sharing geometries, the strength of the resulting exchange correlates with the relative positions of the interacting octahedra. Here, these are defined based on the lateral (L) and vertical (V) displacements with respect to the

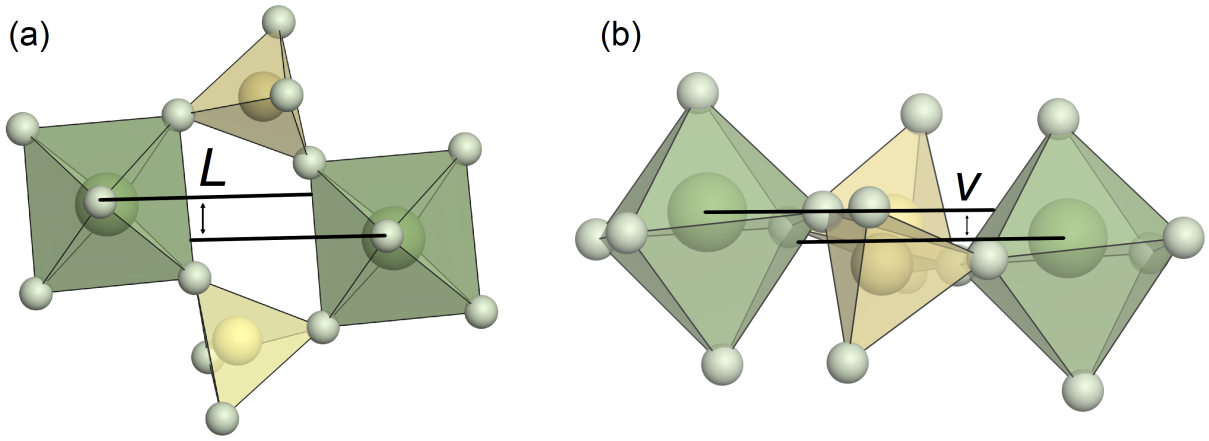

Figure 3.17: (a) Lateral and (b) vertical displacements of the MoO_6 octahedra.

shortest Mo-O bond as highlighted in Fig. 3.17 and are summarized in Table 3.8. The enhancement of the intrachain interactions in CMP, as consistently shown through the DFT+U model and by fitting $\chi_{\mathrm{m}}(T)$, could thus be understood through the lens of the reduced vertical displacement of the octahedra in comparison to KMP. Similarly, the same explanation could be considered for NMP where, instead, the lateral displacement is significantly smaller than in the rest of the series. Interestingly, however, the DFT+U model predicts a sizable reduction of all exchange parameters in NMP and does not corroborate the experimental data or the exact diagonalization model obtained from $\chi_{\mathrm{m}}(T)$. This discrepancy most likely stems from the deformation that buckles the octahedra in NMP which can affect the orbital overlap. Hence, an accurate determination of the exchange parameters must await a more detailed crystallographic study combined with a measurement of the spin excitations. Regardless, despite the subtle structural differences, both systems appear to host ground states that are quite similar to that of KMP. Hence, it can be concluded that the chemical substitution of the alkali metal site most likely does not tune the exchange parameters enough to enter a significantly frustrated region of the $S = 1/2$ FCM.

Table 3.8: Summary of the exchange parameters of AMoOP$_2$O$_7$ (A = Na, K, Cs) as calculated using DFT+U alongside the lateral (L) and vertical (V) displacement parameters of the octahedra.

A-site	Na	K	Cs
J_1 (K)	-2	-1	-2
J_1' (K)	-2	-2	-6
J_2 (K)	-2	34	49
L (Å)	0.05	0.95	0.92
V (Å)	0.53	0.69	0.11

3.5 Investigating the Effects of Alkali Metal Substitution: LiMoOP$_2$O$_7$

The Li analogue of the AMoOP$_2$O$_7$ series was also identified as part of the broader study to examine the effects of altering the A-site cation on the magnetic properties of the system. It was found, however, that upon reaching the smallest alkali metal, the structure type changes, and instead forms—from the perspective of the magnetic sublattice—a three-dimensional framework containing multiple unique Mo-sites[130]. To identify the source of this change, and to more broadly examine the magnetic ground state properties of the system, an experimental and computational study was carried out.

3.5.1 Crystal Structure

The reported $P2_1/n$ structural model[130] of LiMoOP$_2$O$_7$ was confirmed at 300 K using Rietveld refinement of neutron powder diffraction data collected on the D2B diffractometer (Fig. 3.18). Here, the lattice parameters and all atomic coordinates were refined. Given the large number of atoms in the unit cell, however, allowing the isotropic thermal

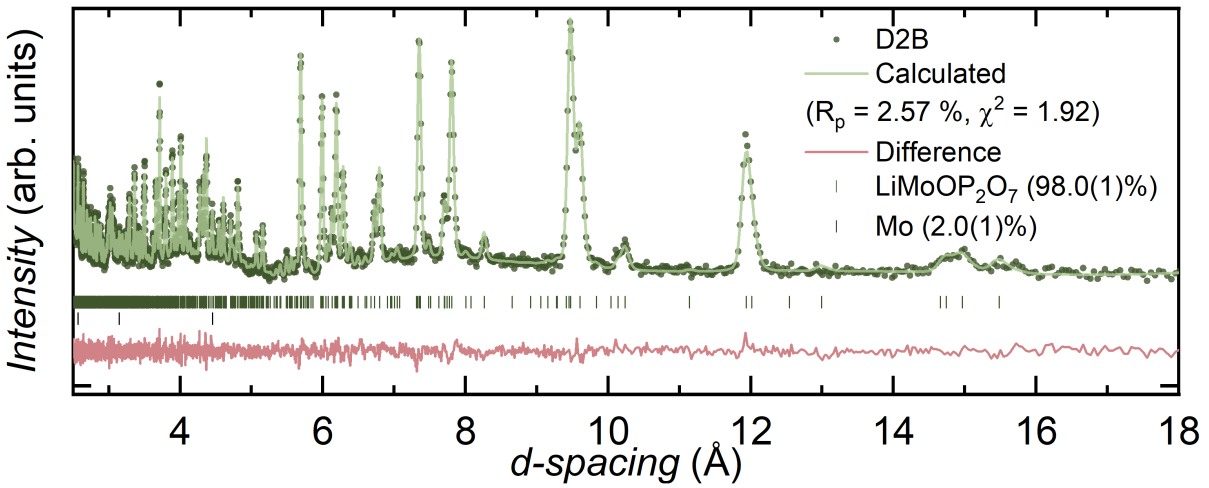

Figure 3.18: Rietveld refinement of neutron powder diffraction data collected at 300 K on the D2B diffractometer using the reported $P2_1/n$ structural model[130].

diplacement parameters to vary rendered the refinement unstable. Hence, the thermal displacement parameters reported for analysis of single-crystal data measured at 300 K were used as an approximation[130]. The resulting model is summarized in Table 3.9.

In comparison to the rest of the AMoOP$_2$O$_7$ series, LiMoOP$_2$O$_7$ adopts a completely different structure with three unique Mo crystallographic sites[130] (Fig. 3.19(a)). As depicted in Fig. 3.19(b), all Mo sites form octahedral geometries coordinated by four P$_2$O$_7$ groups alongside an edge-sharing LiO$_4$ tetrahedron. Three of the P$_2$O$_7$ groups corner-share one of their apices with the octahedron whereas one forms an edge-sharing geometry instead. This coordination leaves an unshared apex which forms the characteristic short Mo-O bond (1.65(1) Å) observed across the AMoOP$_2$O$_7$ family of materials. Empty pores form along these unshared apices and propagate along the crystallographic a-axis (Fig. 3.19(c)). Another tunnel-like structure, occupied by three unique Li cation sites, forms along the a-axis.

When considering the magnetic sublattice, LMP could be described as a three-legged-spin ladder propagating in the [401] direction (Fig. 3.19(d-e)). These ladders are then bridged by phosphate groups within the ac-plane, forming a three-dimensional framework

(Fig. 3.19(e)). Finally, in accordance with the rest of the alkali metal series, and as confirmed through DFT+U calculations (Sec.3.5.4), the shortest Mo-O bond breaks the degeneracy of the t_{2g} manifold into a lower-lying d_{xy} active magnetic orbital and higher-energy d_{xz} and d_{yz} orbitals. The leading magnetic exchange interactions, as such, are most likely those with components in the [401] direction as depicted in Fig. 3.19(e).

3.5.2 Magnetometry and Specific Heat

The zero field-cooled temperature dependence of the magnetic susceptibility measured in an applied field of 1000 Oe is shown in Fig. 3.20(a). Above 100 K, $\chi_{\mathrm{m}}(T)$ is well described by the Curie-Weiss law and yields $C = 0.349(1)$ emu K mol^{-1} ($g = 1.93$), $\mu_{\mathrm{eff}} = 1.67(1)$ μ_{B}, $\theta_{\mathrm{CW}} = -8.9(3)$ K, and $\chi_0 = 7.64(1) \times 10^{-4}$ emu mol^{-1}. The model parameters are suggestive of dominant antiferromagnetic interactions and an effective magnetic moment comparable to the 1.73 μ_{B} expected for a $S = 1/2$ system. Upon cooling, an anomaly is observed around 45 K. This feature could be assigned to the presence of minor amounts of oxygen in the measurement chamber as it is concomitant with the paramagnetic transition for solid O_2 [154]. It is furthermore inconsistent with the interaction energy scale as estimated through CW analysis, and also does not correspond to any structural transitions as described later. This also explains the relatively large temperature-independent background term χ_0. Consistent with the CW constant ($\theta_{\mathrm{CW}} = -8.9(3)$ K), at lower temperatures, a broad feature, centered about 9.5 K, marks the development of short-range correlations. This is followed by an inflection point at about 3.45 K at which the system is presumed to undergo long-range magnetic order. As seen in Fig. 3.20(b), this ordering transition also features in the temperature dependence of the zero-field measured specific heat.

To further examine the low-temperature magnetic properties of LMP, the field dependence of the magnetization, M, is shown in Fig. 3.21(a). No magnetic hysteresis is

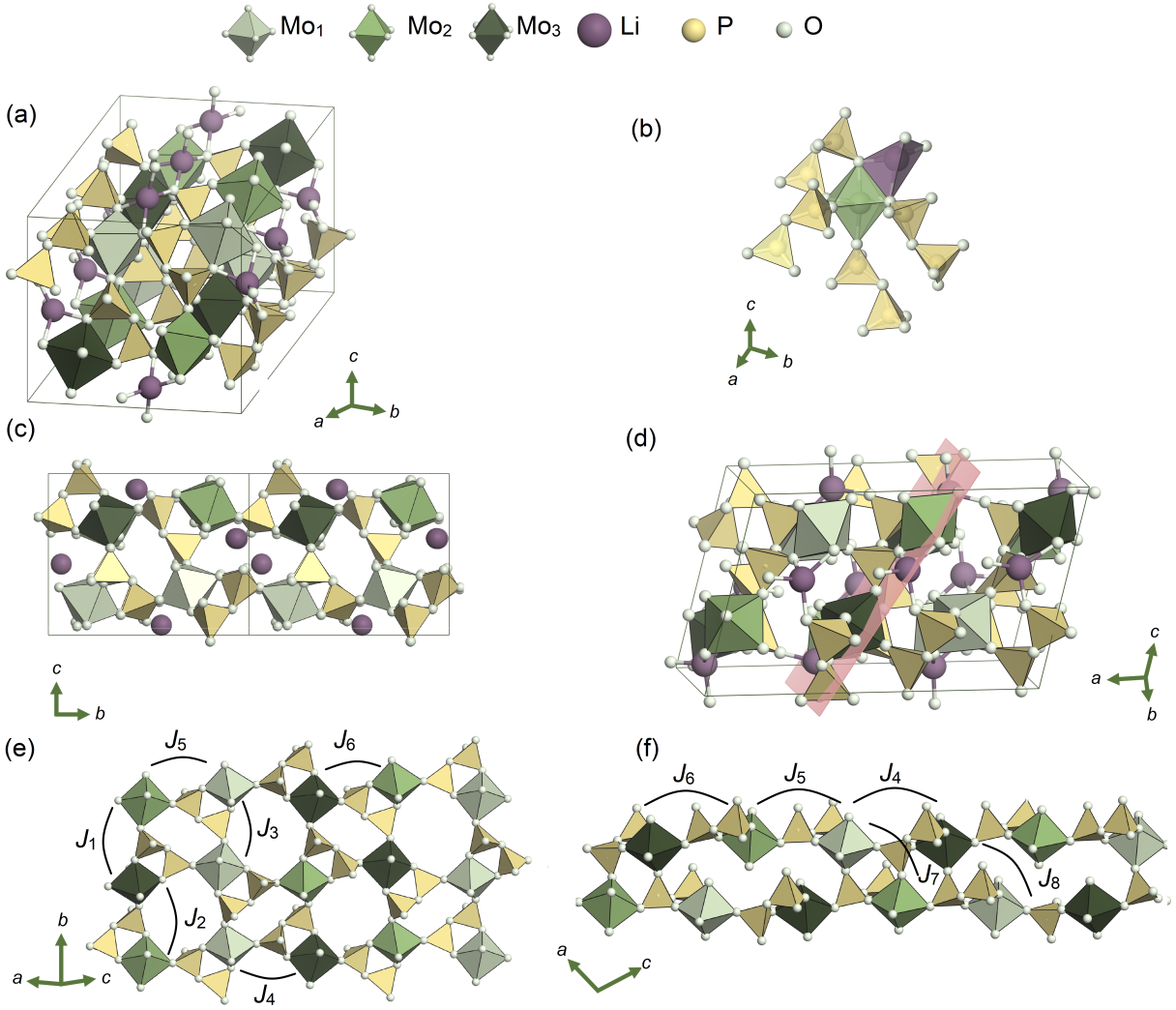

Figure 3.19: (a) Crystal structure of $LiMoOP_2O_7$ viewed along the [111] direction. (b) All Mo positions coordinate four P_2O_7 groups and edge share with a LiO_4 tetrahedron leaving one free apex that (c) points towards an empty tunnel like structure that runs along the a-axis. Another type of tunnel forms in which the Li cations run along the a-axis. The magnetic sublattice of $LiMoOP_2O_7$ is comprised of (d) three-legged ladders that propagate along the (e) [401] direction and are (f) coupled to the rest of the framework within the ac-plane. Figures generated using the `VESTA` visualization package[26].

Table 3.9: Structural parameters of $LiMoOP_2O_7$ as obtained through Rietveld refinement of the $P2_1/n$ model using powder neutron diffraction data measured at 300 K on the D2B diffractometer. The resulting unit cell parameters are $a = 16.015(2)$ Å, $b = 11.9453(5)$ Å, $c = 9.9374(9)$ Å, and $\beta = 104.688(4)°$ with goodness-of-fit parameters $\chi^2 = 1.92$ and $R_p = 2.57\%$.

Atom	x	y	z	U_{iso}(Å^2)
Mo1	0.229(2)	0.191(2)	0.182(3)	0.005
Mo2	0.583(1)	0.207(2)	0.210(3)	0.005
Mo3	0.910(2)	0.214(2)	0.194(3)	0.006
P1	0.122(1)	0.304(2)	0.384(2)	0.005
P2	0.155(1)	0.459(2)	0.190(2)	0.004
P3	0.482(1)	0.449(2)	0.185(2)	0.006
P4	0.437(1)	0.303(2)	0.385(2)	0.009
P5	0.342(8)	0.043(2)	0.720(2)	0.008
P6	0.381(2)	0.174(2)	0.972(3)	0.006
Li1	0.016(4)	0.461(5)	0.924(8)	0.016
Li2	0.194(3)	0.102(5)	0.417(7)	0.016
Li3	0.375(1)	0.447(2)	0.908(2)	0.016
O1	0.137(2)	0.152(3)	0.082(4)	0.022
O2	0.309(2)	0.201(2)	0.053(2)	0.022
O3	0.278(2)	0.060(2)	0.295(3)	0.011
O4	0.184(1)	0.209(3)	0.359(3)	0.009
O5	0.215(2)	0.364(2)	0.155(3)	0.014
O6	0.351(2)	0.274(3)	0.311(4)	0.013
O7	0.683(2)	0.257(3)	0.311(3)	0.025
O8	0.634(2)	0.188(3)	0.047(2)	0.005
O9	0.506(1)	0.222(2)	0.346(3)	0.006
O10	0.595(1)	0.059(2)	0.265(3)	0.014
O11	0.536(2)	0.359(3)	0.126(3)	0.009
O12	0.470(2)	0.133(3)	0.068(3)	0.011
O13	0.831(2)	0.136(3)	0.097(3)	0.015
O14	0.980(2)	0.183(3)	0.047(3)	0.009
O15	0.955(1)	0.051(2)	0.273(2)	0.009
O16	0.872(1)	0.225(2)	0.366(2)	0.008
O17	0.868(2)	0.356(3)	0.136(3)	0.010
O18	0.023(1)	0.281(2)	0.317(2)	0.025
O19	0.159(2)	0.418(2)	0.344(2)	0.004
O20	0.069(1)	0.477(2)	0.077(2)	0.009
O21	0.461(1)	0.420(2)	0.329(2)	0.011
O22	0.409(1)	0.487(2)	0.119(2)	0.025
O23	0.327(1)	0.069(2)	0.868(2)	0.009
O24	0.250(1)	0.012(2)	0.634(2)	0.013

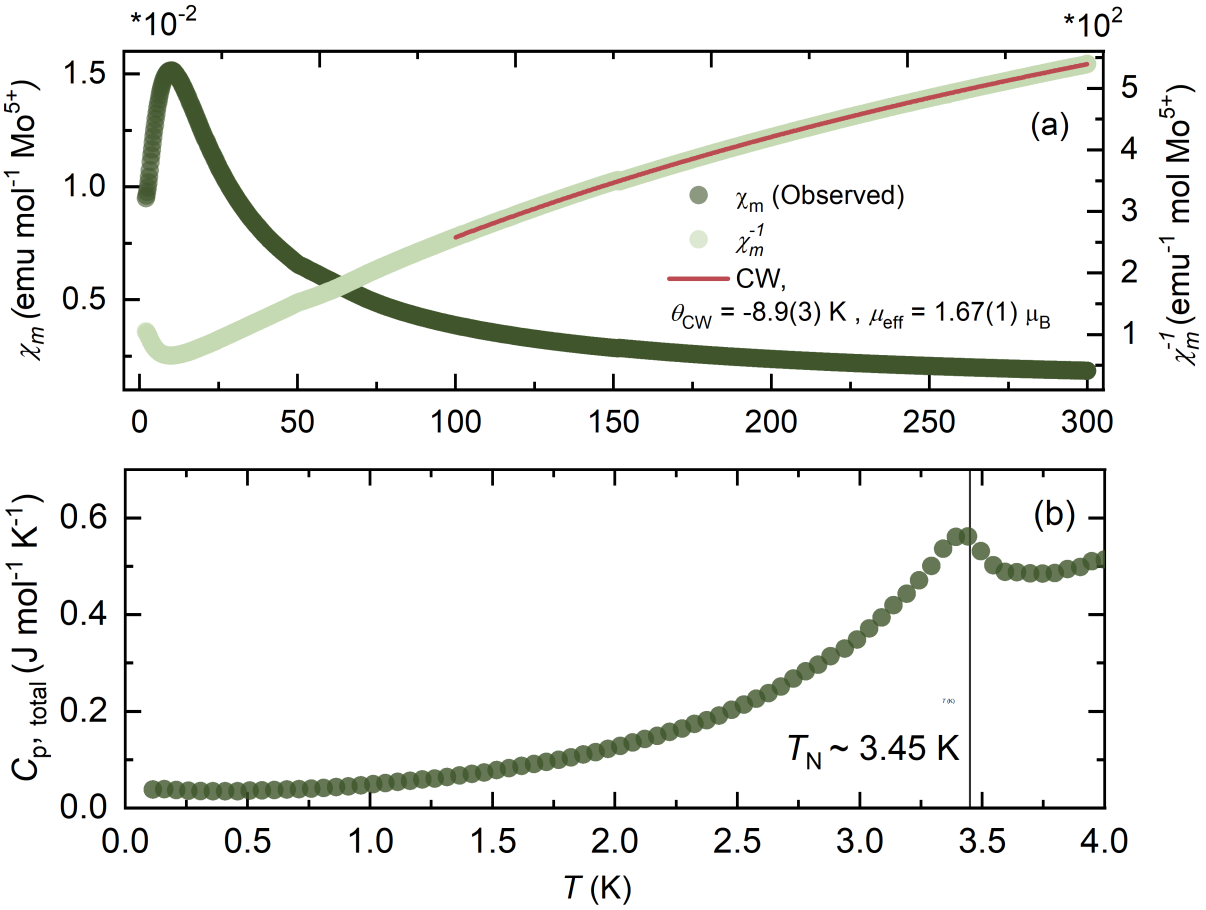

Figure 3.20: (a) Temperature dependent magnetic susceptibility, $\chi_{\mathrm{m}}(T)$, of $LiMoOP_2O_7$ measured using a zero-field cooled protocol in an applied field of 1000 Oe. Above 100 K, χ_{m}^{-1}(T) is well described by the Curie-Weiss law with model parameters $\theta_{\mathrm{CW}} = -8.9(1)$ K, $C = 0.349(1)$ emu K mol^{-1}, $g = 1.93$, $\mu_{\mathrm{eff}} = 1.67(1)$ μ_{B}, and $\chi_0 = 7.64(1) \times 10^{-4}$ emu mol^{-1}. (b) Temperature dependent zero-field measured specific heat.

observed, suggesting antiferromagnetic ordering without spin-canting, and the moment does not saturate up to an applied field of 7 T. At around 1 T, however, an anomaly is observed in the field derivative of the magnetization (Fig. 3.21(b)). To examine its effect on the temperature dependence, M was measured at 4 T. When compared to the curve measured below the critical field, $H_c = 1$ T, $M(T)/H$ at 4 T increases at temperatures below T_N (Fig. 3.21(c)). As this is currently beyond the scope of the current study, future investigations will examine the properties of this magnetic field dependence.

3.5.3 Magnetic Structure

To examine the nature of the feature at 3.5 K, neutron powder diffraction data were collected at 10 K and 1.7 K on the D20 diffractometer. At 1.7 K, the $P2_1/n$ structural model was confirmed through Rietveld analysis (Fig. 3.22(a)). Given the large number of atoms in the unit cell and the poor resolution of the D20 diffractometer, however, it was not possible to refine all atomic positions and isotropic thermal parameters independently. Hence, bond-length restraints of 1.54 Å and 2.1 Å were used for all P-O and Li-O bonds, respectively, which were defined based on the structural model obtained at 300 K on D2B and other P_2O_7 and LiO_4 containing materials[125,155]. The isotropic thermal parameters, on the other hand, were refined while constrained across like-atoms. The resulting model is consistent with an isotropic contraction of the lattice parameters with respect to temperature and the atomic positions and displacement parameters are summarized in Table 3.10. Here, the covalent form factor of Mo^{5+}, as calculated by Dr. Danis Badrtdinov at Radboud University using density functional theory, is used.

Subtracting the 10 K data from that collected at 1.7 K yields two magnetic Bragg peaks the that are indexed by the commensurate propagation vector, $\kappa = 0$ (Fig. 3.22(b)). Symmetry analysis using `BasiReps`[90] and `MAXMAGN`[156] results in four irreducible representations, $m\Gamma_{2+}$, $m\Gamma_{2-}$, $m\Gamma_{1+}$ and $m\Gamma_{1-}$ in Miller-Love notation[157], that are compatible with

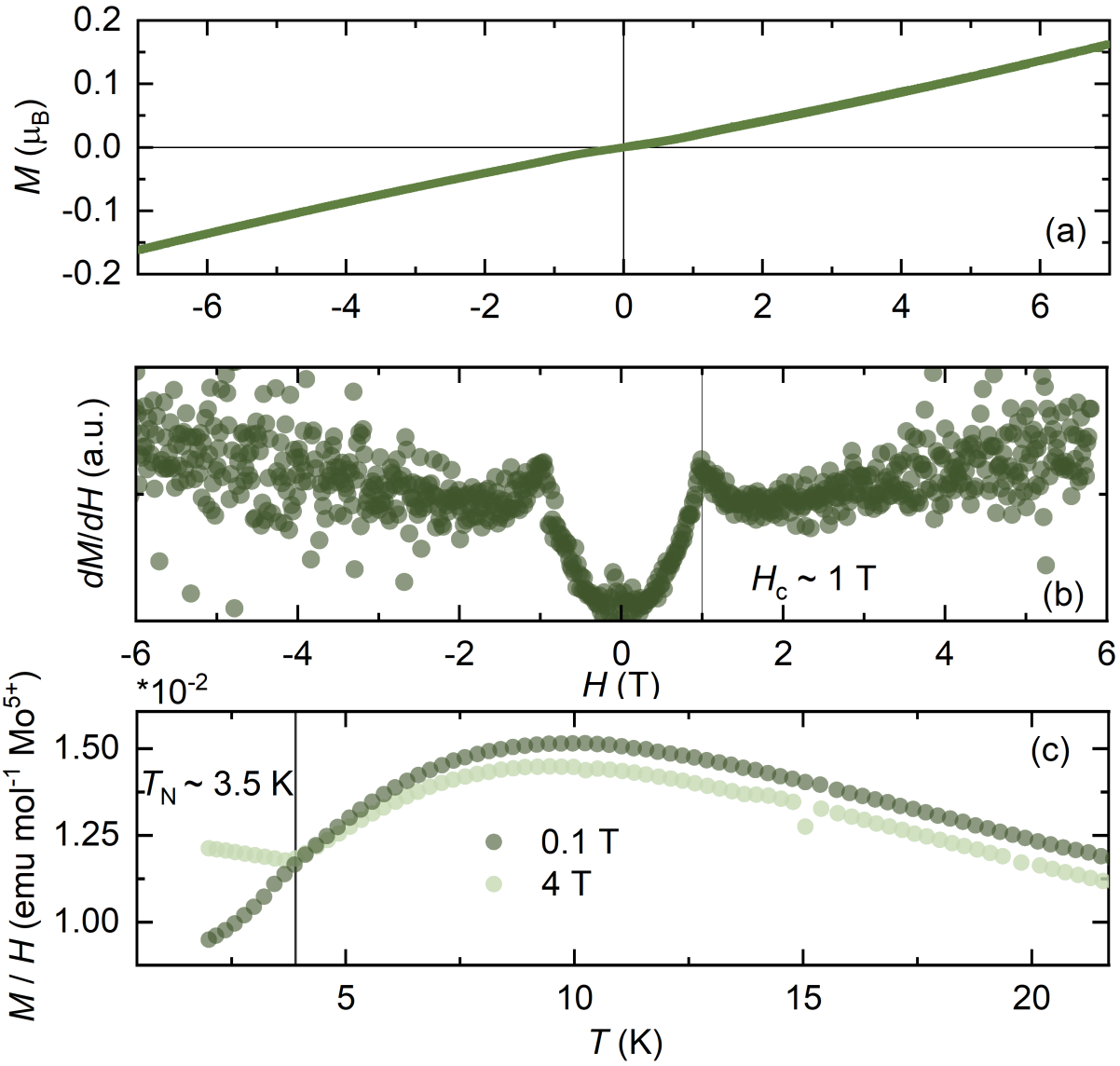

Figure 3.21: (a) Field dependence of the magnetization of $LiMoOP_2O_7$. (b) Field derivative of the magnetization marking a critical field $H_c = 1$ T. (c) Temperature dependent M/H curves measured at applied fields of 0.1 T and 4 T.

Table 3.10: Structural parameters of $LiMoOP_2O_7$ as obtained through Rietveld refinement of the $P2_1/n$ model using powder neutron diffraction data measured at 1.7 K on the D20 diffractometer. The resulting unit cell parameters are $a = 15.978(3)(2)$ Å, $b = 11.930(1)$ Å, $c = 9.916(2)$ Å, and $\beta = 104.686(5)°$ with goodness-of-fit parameters $\chi^2 = 13.5$ and $R_p = 1.38\%$.

Atom	x	y	z	U_{iso}(Å^2)
Mo1	0.236(1)	0.181(1)	0.204(2)	0.028(4)
Mo2	0.577(1)	0.213(1)	0.182(2)	0.028(4)
Mo3	0.908(1)	0.217(2)	0.203(2)	0.028(4)
P1	0.124(1)	0.299(2)	0.394(2)	0.044(3)
P2	0.161(1)	0.444(2)	0.166(2)	0.044(3)
P3	0.498(1)	0.454(2)	0.221(2)	0.044(3)
P4	0.435(1)	0.275(1)	0.366(2)	0.044(3)
P5	0.314(1)	0.063(2)	0.700(2)	0.044(3)
P6	0.403(1)	0.138(1)	0.981(2)	0.044(3)
Li1	0.048(1)	0.447(2)	0.931(1)	0.047(6)
Li2	0.188(1)	0.072(1)	0.413(2)	0.047(6)
Li3	0.377(1)	0.450(1)	0.890(2)	0.047(6)
O1	0.129(1)	0.171(1)	0.072(2)	0.009(2)
O2	0.313(1)	0.206(1)	0.048(2)	0.009(2)
O3	0.276(1)	0.043(2)	0.295(2)	0.009(2)
O4	0.189(1)	0.234(1)	0.355(2)	0.009(2)
O5	0.196(1)	0.355(2)	0.141(1)	0.009(2)
O6	0.336(1)	0.288(1)	0.302(2)	0.009(2)
O7	0.683(1)	0.248(1)	0.304(1)	0.009(2)
O8	0.637(1)	0.193(1)	0.058(2)	0.009(2)
O9	0.512(1)	0.208(2)	0.338(2)	0.009(2)
O10	0.609(1)	0.058(2)	0.268(2)	0.009(2)
O11	0.539(1)	0.346(1)	0.101(1)	0.009(2)
O12	0.476(1)	0.118(1)	0.086(2)	0.009(2)
O13	0.832(1)	0.147(1)	0.109(2)	0.009(2)
O14	0.964(1)	0.182(2)	0.027(1)	0.009(2)
O15	0.963(1)	0.051(1)	0.265(2)	0.009(2)
O16	0.865(1)	0.223(1)	0.365(2)	0.009(2)
O17	0.886(1)	0.369(1)	0.157(2)	0.009(2)
O18	0.021(1)	0.292(2)	0.332(2)	0.009(2)
O19	0.145(1)	0.419(1)	0.346(2)	0.009(2)
O20	0.079(1)	0.497(1)	0.141(1)	0.009(2)
O21	0.478(1)	0.391(1)	0.352(2)	0.009(2)
O22	0.408(1)	0.459(1)	0.107(2)	0.009(2)
O23	0.328(1)	0.075(2)	0.864(1)	0.009(2)
O24	0.244(1)	0.009(1)	0.608(1)	0.009(2)

κ and the crystal symmetry. Of those, only the magnetic space group $P2_1/n'$, in Belov-Neronova-Smirnova notation[97], belonging to the $m\Gamma_{1-}$ representation, is consistent with the observed peaks. However, because this model allows for three Fourier components on each Mo site, and because there are only two experimental observations, the direction of the magnetic moment could not be conclusively estimated. Indeed, the point group symmetry of the Mo sites allows for the presence of Dzyaloshinskii–Moriya interactions which in turn allow for spin-canting. Nevertheless, an estimate of the ordered magnetic moment could be obtained as 0.62(1) μ_B, 0.95(1) μ_B, and 0.4(1) μ_B for the Mo1, Mo2, and Mo3 sites, respectively, when refining this model while constraining the moment to lie along an arbitrary direction. When allowing all (m_x, m_y, m_z) sites to vary, instead, one solution yields averaged moments of 0.70 μ_B, 0.85 μ_B, and 0.53 μ_B for Mo1, Mo2, and Mo3, respectively. Both solutions, amongst others, result in the goodness-of-fit parameters $\chi^2 = 2.59$ and $R_p = 6.48\%$. Consistent amongst these solutions are the relative intensities of the magnetic moments across the three sites with Mo2 being the closest to the expected single ion moment of $gS = 1$ followed by Mo1 and Mo3, respectively. The discrepancy between the ordered moments could be associated with both the different crystal field splittings arising from the subtle differences in the distortions of the octahedra between the three sites and, more likely, differences in the superexchange pathways between the six different P sites.

One of the possible magnetic moment arrangements for the magnetic structure where the moments are constrained along the crystallographic c-axis is shown in Fig. 3.22(c). Here, the moments align antiferromagnetically along the b-axis and are instead oriented ferromagnetically within the ab-plane. This is consistent with the expected d_{xy} active magnetic orbital and the crystal structure where interactions are expected to be strongest for exchange parameters with components in along the [401] direction. Regardless, an unambiguous determination of the magnetic ground state must await a single-crystal study.

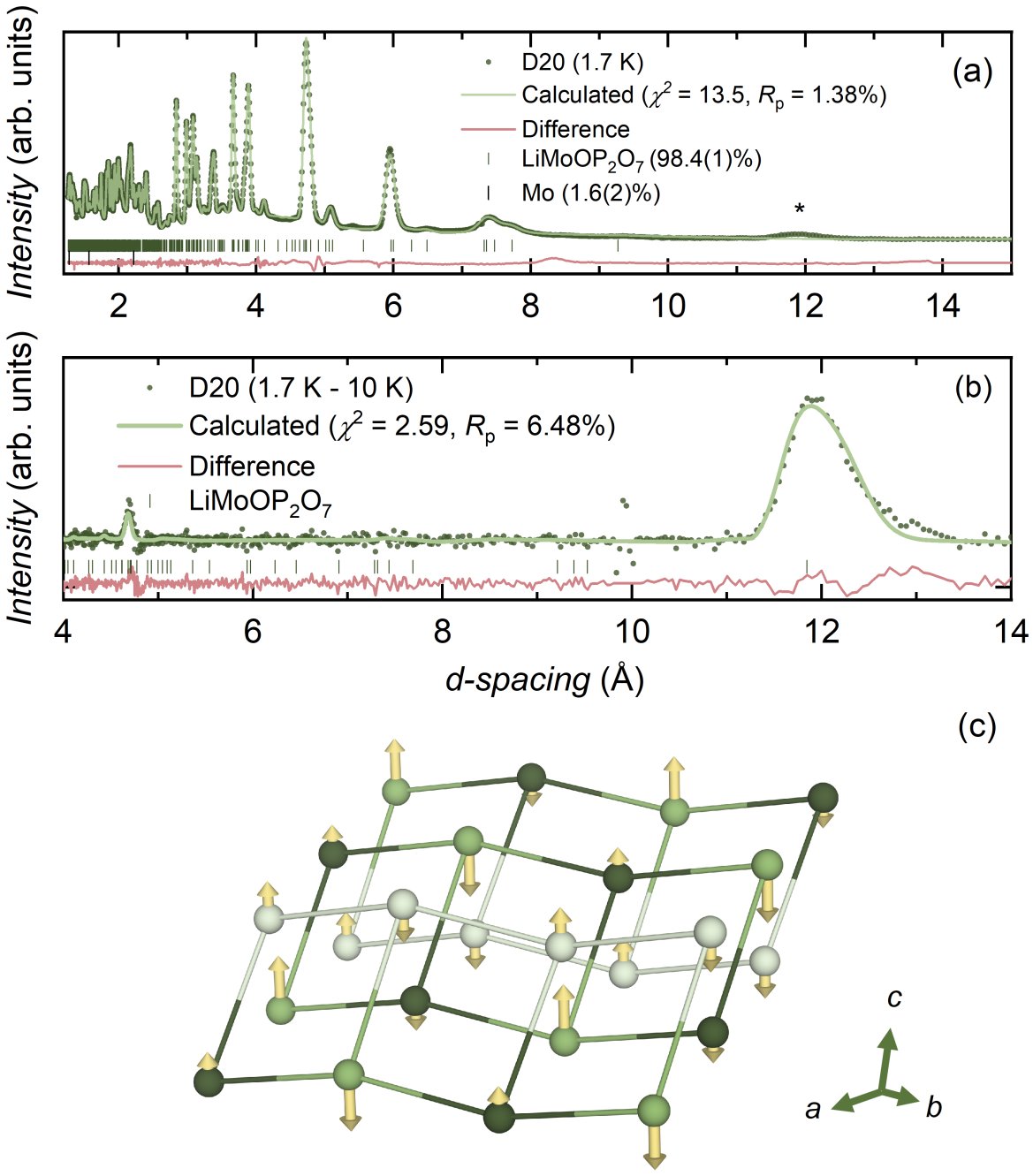

Figure 3.22: (a) Rietveld analysis of neutron powder diffraction data measured at 1.7 K using the $P2_1/n$ structural model. The asterisk identifies magnetic scattering. (b) Rietveld refinement of magnetic only-scattering using the $P2_1/n'$ magnetic space group model. (c) Magnetic structure of $LiMoOP_2O_7$ depicting one of the possible arrangements of the magnetic moments.

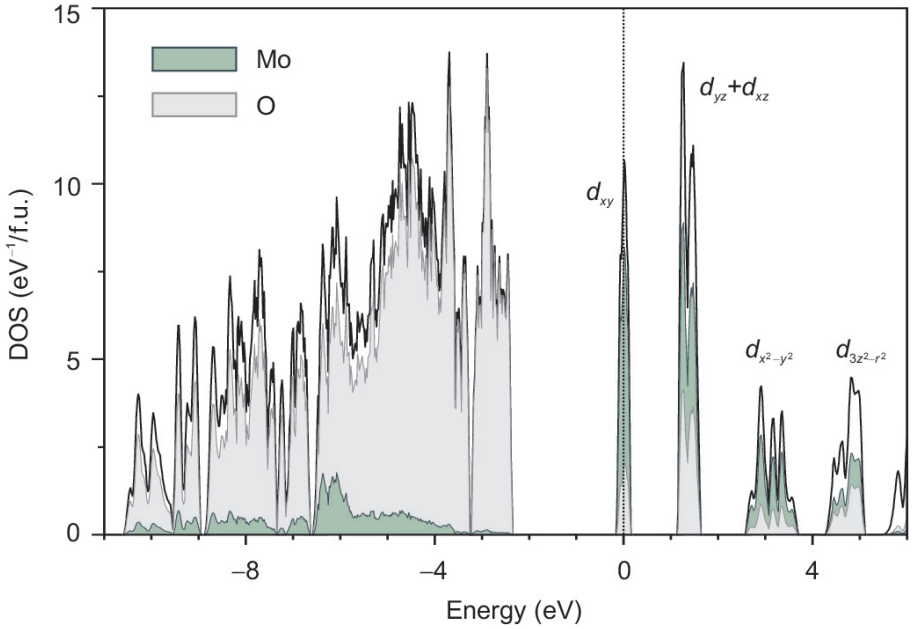

Figure 3.23: PBE density of states (DOS) highlighting the crystal-field splitting of the Mo $4d$ states. Here, the energy spectrum is metallic as electronic correlations are not accounted for.

3.5.4 Ground State: Elucidating the Spin Hamiltonian

To clarify the leading superexchange parameters, density-functional theory band-structure calculations were performed by Prof. Alexander Tsirlin at the University of Leipzeg using the `FPLO`[142] and `VASP`[152,153] codes while applying the Perdew-Burke-Ernzerhof[143] (PBE) flavor of the exchange-correlation potential.

As depicted in Fig. 3.23, examining the non-correlated PBE density of states reveals a band structure with a strong resemblance to that of $KMoOP_2O_7$. Indeed, as predicted by the crystallographic model, a tight-binding model fit to the band structure yields energies that are consistent with an active d_{xy} magnetic orbital that is well separated from the nearly degenerate d_{xz} and d_{yz} orbitals. As summarized in Table 3.11, similar crystal-field splittings are found across all three Mo sites.

Next, estimates of the leading exchange couplings were evaluated by mapping the total

Table 3.11: Orbital energies (in eV) extracted from Wannier fits to the PBE band structure of $LiMoOP_2O_7$.

	xy	yz	xz	x^2-y^2	$3z^2-r^2$
Mo1	0.07	1.43	1.39	3.08	4.73
Mo2	0.08	1.43	1.34	3.10	4.73
Mo3	0.02	1.28	1.36	3.13	4.76

energies of collinear spin configurations[145,144] within the DFT+U limit. Here, correlation effects were treated using a mean-field approach where the on-site Coulomb repulsion and Hund's coupling were $U = 4$ eV and $J_{\mathrm{H}} = 0.5$ eV, respectively, and double-counting correction is treated on the atomic-limit. The resulting spin Hamiltonian is summarized in Table 3.12 and describes a model in which dominant antiferromagnetic interactions, $J_1 - J_3$, run along the legs of the spin-ladders and ferromagnetic interactions, described by J_4 and J_5, constitute the rungs (Fig. 3.19(e,f)). A ferromagnetic exchange, J_6, connects the spin ladders and relatively weak ferromagnetic interlayer interactions, J_7 and J_8, bridge the layers within the *ac*-plane. These include all possible nearest neighbor pairs of Mo^{5+} in the structure and none of these generate exchange frustration. When comparing the relative strength of these interactions, the differences most likely arise from the varying geometries of the Mo-octahedra and their respective Mo-O-P-O-Mo superexchange pathways. This is seen in V^{4+} phosphates where the strength of the couplings is usually determined by the positions of d_{xy} orbitals with respect to the O-P-O links through the PO_4 tetrahedra[158]. Indeed, the interactions in the plane defined by the d_{xy} orbitals on all sites are dominant, despite the Mo-Mo bond lengths being longer than between the planes. Finally, the calculated microscopic model reproduces the $\kappa = 0$ magnetic order and returns Curie-Weiss temperatures of $\theta_{\mathrm{Mo1}} = -1.5$ K, $\theta_{\mathrm{Mo2}} = -5.2$ K, and $\theta_{\mathrm{Mo3}} = -4.4$ K that average -3.7 K and are roughly comparable with the experimental $\theta_{\mathrm{CW}} = -8.9(3)$ K and $T_{\mathrm{N}} = 3.45$ K.

To examine the validity of this model, and to more broadly determine the spin Hamiltonian, we now turn to the experimental dynamical structure factor $\left(S(Q, E = \hbar\omega)_{\mathrm{exp}}\right)$ as

Table 3.12: Summary of exchange couplings in $LiMoOP_2O_7$ obtained by the DFT+U mapping analysis. The couplings are labeled with $J_1 - J_8$ (Fig. 3.19) in the order of decreasing magnitude, and are presented in order of increasing Mo-Mo bond distance.

	$d_{\mathrm{Mo-Mo}}$ (Å)		J_{ij} (K)
J_8	5.299	Mo1–Mo3	−1.4
J_7	5.527	Mo1–Mo2	−3.2
J_1	6.021	Mo2–Mo3	17.7
J_3	6.033	Mo1–Mo1	13.2
J_2	6.106	Mo2–Mo3	15.8
J_4	6.366	Mo1–Mo3	−11.8
J_6	6.463	Mo2–Mo3	−4.0
J_5	6.407	Mo1–Mo2	−5.6

measured on the IN5 spectrometer at 1.8 K with incident energies of $E_\mathrm{i} = 3.55$, 5.11 meV, and 14.2 meV. As depicted in the inelastic spectra (Fig. 3.24(a-c), at low energies and angles, spurious scattering arising from the sample environment and the instrument contaminates both the E_i =3.55 meV and 5.11 meV spectra below energies of 0.4 meV and 0.8 meV. Otherwise, dispersive spin waves arise from the elastic line at a wave vector, $Q \simeq 0.5$ Å, which corresponds to that of the (010) magnetic Bragg peak seen using neutron diffraction. These excitations extend up to around 3 meV, peak at about 0.65 Å, and decrease in intensity with increasing Q as expected for a magnetic scattering (Fig. 3.25). More scattering appears at longer wave vector transfer and above 5 meV which, given its Q-dependence, we assign to scattering from phonons (Fig. 3.24). Hence, aside from the spurious scattering, and given the energy scale of the lower energy scattering, we assume that the low-Q dispersive features represent the magnetic response of the system.

Next, to model the observed magnetic scattering, spin wave spectra were calculated using linear spin wave theory as applied using the `SpinW` library[27]. We begin by constructing a magnetic Hamiltonian with the six exchange parameters, $J_1 - J_6$, describing the interactions within the three-legged spin ladders alongside the interlayer interactions J_7 and J_8. Using the DFT calculated exchange parameters results in the simulated spec-

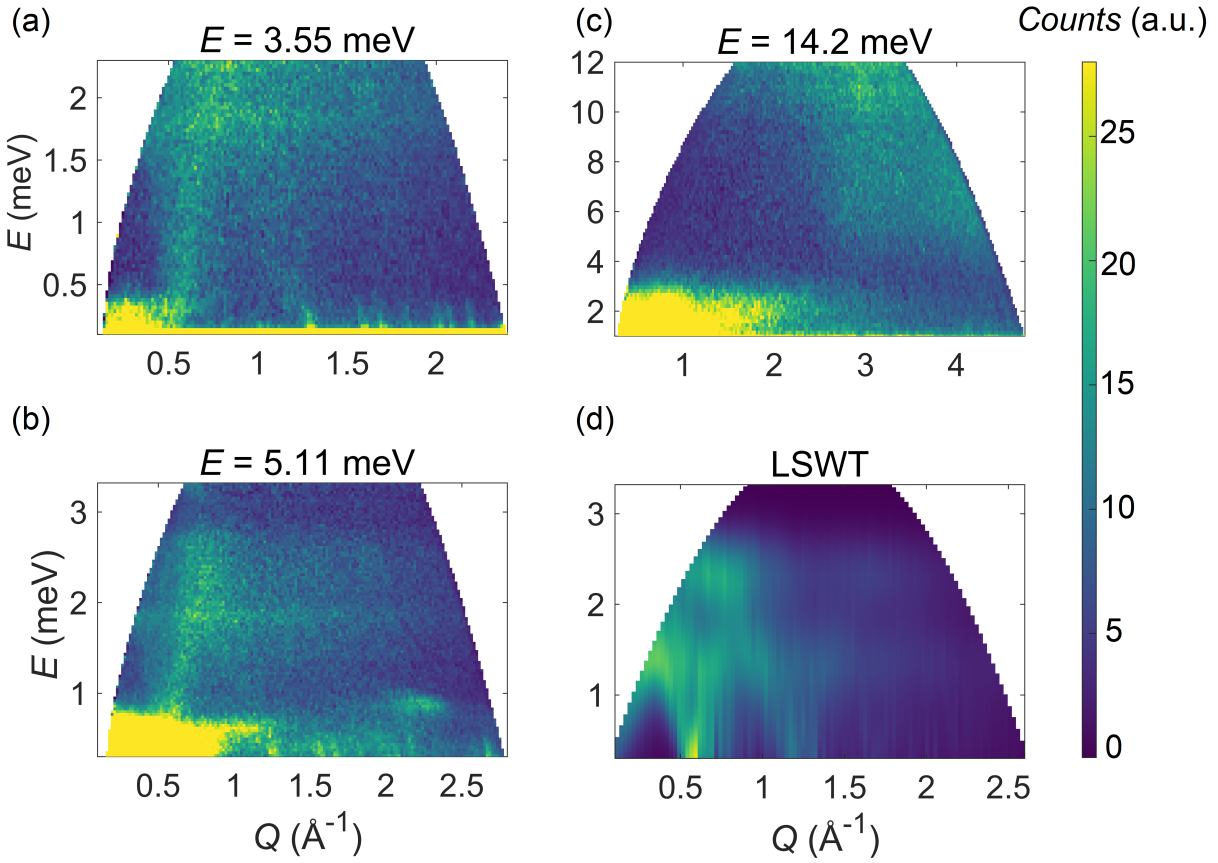

Figure 3.24: (a-c) Experimental dynamical structure factor measured on the IN5 spectrometer at 1.8 K with incident neutron energies of E_i = 3.55 meV, 5.11 meV, and 14.2 meV. (d) Linear spin wave theory simulated spectrum using the DFT calculcated exchange parameters.

trum displayed in Fig. 3.24(d) which, at first glance, accurately describes the general features and bandwidth of the magnetic excitations. Upon closer examination, however, the energy dependence of these features are slightly mismatched. Hence, a more rigorous optimization, starting with the DFT model parameters, will be necessary for a detailed determination of the magnetic Hamiltonian.

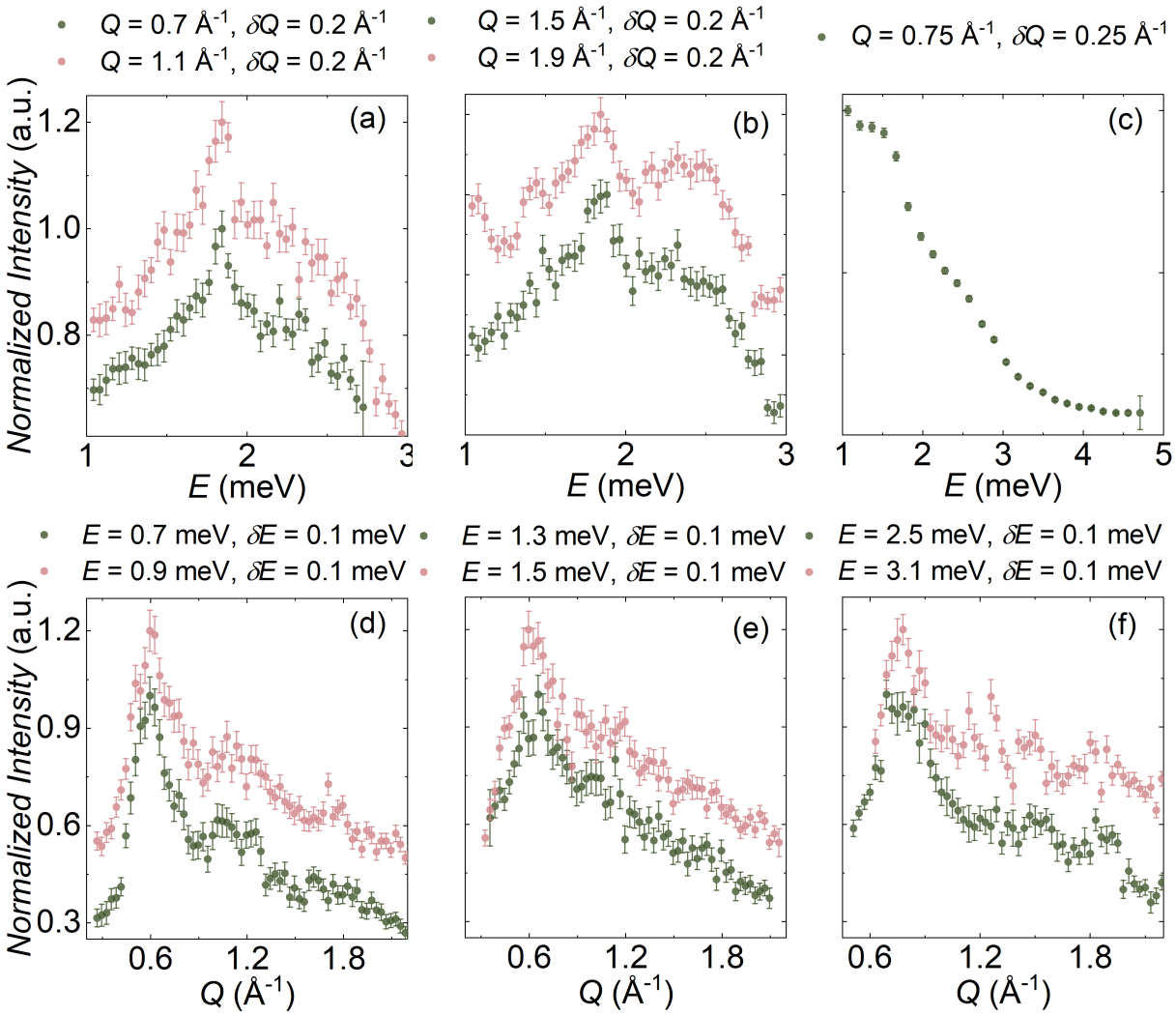

Figure 3.25: (a-c) E- and (d-f) Q-integrated cuts of $S(|Q|, E)$ as measured for $LiMoOP_2O_7$ on the IN5 spectrometer at 1.8 K.

3.5.5 Conclusions

This chapter presents a comprehensive experimental and *ab-initio* study on a family of $S = 1/2$ Mo^{5+}-containing systems described by the chemical formula $A\mathrm{MoOP_2O_7}$. The magnetic model relevant to the A = Na, K, and Cs members was found to be the Heisenberg antiferromagnet chain model through analysis of neutron powder diffraction, magnetometry, specific heat, and inelastic neutron scattering data alongside DFT+U calculations. The key findings can be summarized as follows:

- A comparative crystallographic investigation using Rietveld analysis of powder neutron and X-ray diffraction data indicates that the K and Cs members adopt a monoclinic $P2_1/n$ space group as opposed to the orthorhombic $P2_12_12_1$ structure of $\mathrm{NaMoOP_2O_7}$. While subtle differences associated with the conformation of the pyrophosphate groups arise across the series, the magnetic sublattice, comprised of pairs of octahedrally coordinated Mo^{5+} spin chains, remains the same. Similarly consistent is the presence of short Mo-O apical bonds that distort the Mo-octahedral geometries along the c-direction.

- Across the series, temperature dependent magnetic susceptibility measurements reveal broad symmetric features, characteristic of low-dimensional magnets, at relatively similar temperatures. Curie-Weiss analysis yields almost complete $S = 1/2$ spin-only effective moments suggesting no contribution from the orbital moment. Extracting the leading magnetic exchange interactions by fitting $\chi_\mathrm{m}(T)$ to an exact diagonalization of the $S = 1/2$ frustrated Heisenberg chain model suggests dominant antiferromagnetic one-dimensional correlations and negligible interchain interactions for all three members.

- Around 0.6 K, the temperature dependence of the specific heat shows anomalies consistent with the onset of long-range magnetic order. Interestingly, while T_N

remains relatively similar across the series, the sharpness of these features vary depending on the material.

- Reasons for this variation are discussed through the microscopic magnetic models derived from DFT+U calculations. Here, the lifting of the orbital degeneracy of the $4d^1$ electronic configuration of Mo^{5+} due to a short Mo-O bond results in an active d_{xy} magnetic orbital that is well separated from other levels. Similar to the magnetic susceptibility fits, the resulting spin Hamiltonian reveals dominant antiferromagnetic interactions and negligible frustrating couplings as favored by the d_{xy} orbital ground state. Small differences in the strength of these interactions across the series can be explained by subtle structural differences.

- To investigate these claims, neutron powder diffraction and spectroscopy measurements were carried out on $KMoOP_2O_7$. No magnetic Bragg peaks were observed down to 0.05 K, placing an upper limit of $\mu_{ord} \leq 0.15$ μ_B on the ordered moment. Analysis of the experimental dynamical structure factor identified a spin-Hamiltonian consistent with that obtained computationally.

- It is thus concluded that all three Na, K, and Cs members of the $A MoOP_2O_7$ family of materials realize the $S = 1/2$ Heisenberg antiferromagnet chain model and that chemical substitution of the A-site does not introduce any major differences in their ground states.

- Inelastic neutron scattering alongside neutron diffraction experiments should provide further insight into the ordered ground state of both NMP and CMP.

- Future work on this family of materials should aim to stabilize different active magnetic orbitals or maintaining the t_{2g} orbital degeneracy of the d^1 electronic configuration. Studying $A MoOV_2O_7$ [159] or $NaTiP_2O_7$ [160] could hence be fruitful as minimal distortions afflict the octahedral geometries of their transition metal ions.

Having examined the ground states of the Na, K and Cs members of the $A\mathrm{MoOP_2O_7}$ family of materials and established their relevance to the $S = 1/2$ Heisenberg antiferromagnet chain model, we then turned to the compositionally analogous yet structurally distinct Li analogue. Using a similarly extensive set of experimental and computational tools reveals the following:

- Unlike the other members of the series, $\mathrm{LiMoOP_2O_7}$ forms a three-dimensional magnetic framework comprised of three-legged spin ladders that run within the [401] plane and that are bridged across the the *ac*-plane through $\mathrm{PO_4}$ groups. Its monoclinic $P2_1/n$ symmetry which contains three unique Mo crystallographic sites has been confirmed using Rietveld analysis of neutron powder diffraction data. While structurally distinct, the characteristic short Mo-O bond similarly distorts the octahedral geometries of all Mo sites in LMP.

- Examining the Curie-Weiss behavior of the temperature dependence of the magnetic susceptibility yields dominant antiferromagnetic interactions and an effective moment concomitant with a spin only $S = 1/2$ system. The onset of long range magnetic order at $T_\mathrm{N} \simeq 3.5$ K is evidenced by an inflection point in the magnetic susceptibility and is confirmed as an anomaly in the temperature dependent specific heat.

- Interestingly, the field dependence of the magnetization indicates the presence of an anomaly at a critical field of $H_\mathrm{c} = 1$ T.

- NPD data reveals a long-range magnetically ordered ground state at 1.8 K adopting the $P2_1/n'$ magnetic structure described by an antiferromagnetic spin configuration along the *b*-axis and ferromagnetic interactions in all other directions. The strength of the ordered moment, however, could not be conclusively identified due to the presence of only two magnetic Bragg peaks in the experimental data.

- *Ab-initio* calculations shed light on the magnetic ground state and identify a d_xy ac-

tive magnetic orbital stemming from the Mo-octahedral distortion, again related to a short apical Mo-O bond. The leading exchange parameters were hence found to be those with superexchange pathways lying along the [401] direction where antiferromagnetic correlations dominate along the legs of the spin ladders and ferromagnetic interactions on the rungs.

- The relevance of this spin Hamiltonian was confirmed by comparing the experimental dynamical structure factor as measured using inelastic neutron scattering with spectra simulated using linear spin wave theory and the DFT parameters.

- While slight discrepancies exist between the simulated and experimental spectra, the simulated model captures the magnetic ground state and the general features of the spectrum, and this non-frustrated spin-model is concluded to describe the magnetic ground state of $LiMoOP_2O_7$.

- An accurate determination of the magnitude of the Hamiltonian parameters requires further optimization.

- Future measurements will also show the field dependence of the magnetic properties of the system using a combination of neutron scattering and bulk property measurement techniques.

Chapter 4

Exploring RuP_3SiO_{11} as a Novel Kitaev Spin Liquid Candidate

4.1 Introduction

Quantum spin liquid ground states are traditionally sought in frustrated magnets. Frustration, however, often compromises the analytical and numerical tractability of the diverse set of model Hamiltonians predicted to host such ground states[4,161]. Indeed, an unambiguous conclusion regarding the true nature of the spin liquid states emerging in many archetypal spin models is still outstanding; the character of the QSL describing the ground states of both the Heisenberg Kagomé and triangular antiferromagnet models, amongst others, are still hotly debated[4,9]. Accordingly, frustrated spin models with exactly solvable spin liquid ground states are highly attractive.

In this vein, the Kitaev model serves as a paradigmatic example of an exactly solvable frustrated model[6]. Conceptualized within the framework of a honeycomb geometry, but also accessible to any tri-coordinated lattice, the Kitaev model describes a spin sys-

tem comprised of ferromagnetically interacting spins that are frustrated by an easy-axis exchange anisotropy orthogonal to the pairing bond[162] (Fig. 4.1(a)). The resulting microscopic Hamiltonian is commonly represented in a cubic Cartesian frame of reference[161,163],

$$\mathcal{H} = \sum_{<i,j>_\gamma} K_{ij}^{\gamma} S_i^{\gamma} S_j^{\gamma}, \tag{4.1}$$

where the summation of the spin degrees of freedom, S, covers the $<i,j>$ nearest neighbor bonds along some $\gamma \in X, Y, Z$ direction and K is the Kitaev exchange interaction. The ground state of the Kitaev model is exactly solvable by fractionalizing the spin degrees of freedom into Majorana fermions and gauge fluxes[6]. A variety of topological spin liquid ground states can be adopted depending on the relative strength of the bond-dependent interaction parameters, K_{ij}^{γ}[161,164].

Although the model was formulated as a purely theoretical exercise, a superexchange theory that renders the Kitaev interaction possible has remarkably been formulated. This paradigm has been established by the Jackeli-Khaliullin (J-K) mechanism which sets several structural and electronic criteria for the formation of dominant Kitaev-like interactions in materials[165]. The first ingredient is a relativistic spin-orbit-entangled $j_{\text{eff}} = 1/2$ psuedospin that is responsible for the characteristically anistropic nature of the Kitaev interaction. Such an electronic configuration can arise in low spin $4d^5$ and $5d^5$ electron systems where an octahedral crystal field splits the degenerate d manifold into a low lying t_{2g} triplet and an empty higher energy e_g doublet. Within the large spin-orbit coupling limit of heavier transition metal ions, the degeneracy of the t_{2g} manifold is lifted, and the resulting states are composed of a fully occupied $j_{\text{eff}} = 3/2$ quartet and a half-filled ground state psuedospin $j_{\text{eff}} = 1/2$ doublet (Fig. 4.1(b)). An additional consideration is the bonding geometry of the transition metal octahedra; in the presence of an edge sharing bonding geometry, equal and opposing electron hopping processes inhibit any isotropic Heisenberg interactions. The resulting Hamiltonian is an exact mapping of the Kitaev

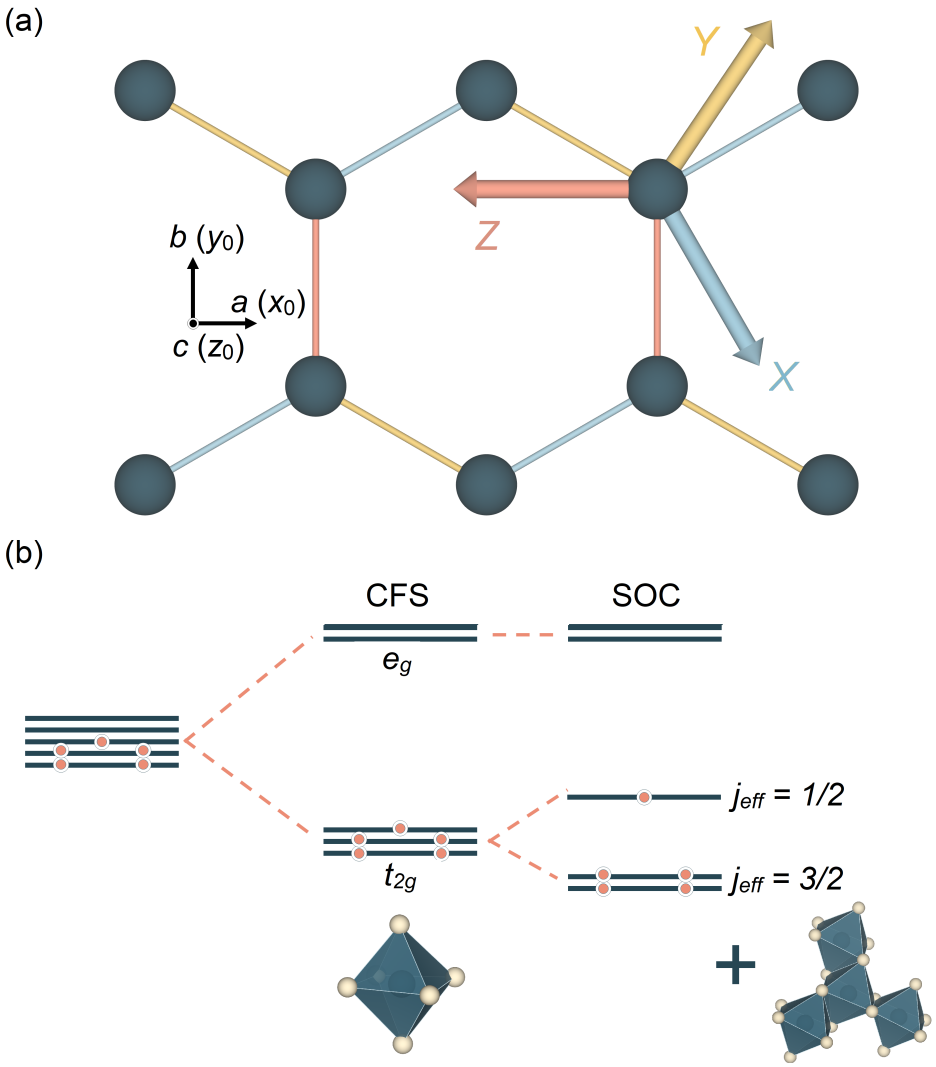

Figure 4.1: (a) The Kitaev model on a honeycomb lattice. Bond-dependent interactions are highlighted by different colored bonds and spins on cubic (X, Y, Z) axes that are different than the crystallographic coordinates, $(x_0, y_0, z)_0$). (b) Crystal field splitting (CFS) of the d^5 electronic configuration suggested by the J-K superexchange mechanism [165] where spin-orbit coupling (SOC) splits the degenerate t_{2g} manifold into $j_{\text{eff}} = 1/2$ and $j_{\text{eff}} = 3/2$ states. An edge-sharing bonding geometry for metal octahedra on a tri-coordinated lattice is further necessary to ensure dominant bond-directional interactions. Figure (a) is generated using the `VESTA` visualization software [26].

Table 4.1: Key model parameters for relevant material realizations of the Kitaev model. Here, ZZ and IS denote zigzag and incommensurate spin spiral structures, respectively, and $\theta_{\text{CW, iso}}$ is the isotropic Weiss constant. Table is adapted from multiple review articles[8,162,18].

Material	S.G.	$\theta_{\text{CW, iso}}$ (K)	μ_{eff} (μ_B)	T_N (K)	μ_{ord} (μ_B)	Order
α-$RuCl_3$	$C2/m$, $R\bar{3}$[169]	20–40	2–2.7	7–14	0.4–0.7	ZZ
Na_2IrO_3	$C2/m$	-125	1.8	13–18	0.22	ZZ
α-Li_2IrO_3	$C2/m$	-30–(-100)	1.8	13–18	0.4	IS
β-Li_2IrO_3	$Fddd$	40	1.6–2.0	37	0.4	IS
γ-Li_2IrO_3	$Cccm$	75	1.6–2.4	39	0.4	IS
Cu_2IrO_3	$C2/c$	-110	1.93	2.7	–	–
$H_3LiIr_2O_6$	$C2/m$	-105	1.60	–	–	–
$Ag_3LiIr_2O_6$[170,171]	$C2/m$	-140	1.79	8–14	–	–
$Cu_3LiIr_2O_6$	$C2/c$	-145	2.1	15	–	–

model (Eq.4.1). While this model has originally been reported for low spin d^5 electronic configurations, more recent reports have extended such predictions to include d^7 [166,167] and f-electron[168] systems.

The requirements of the J-K mechanism, however, introduce considerable synthetic challenges. When considering the originally defined d^5 electronic configuration, only five transition metal ions, with, typically, chemically inaccessible valencies, are available for study. As summarized in Table 4.1, the study of the Kitaev model has thus focused on only a handful of Ru^{3+}- and Ir^{4+}-containing materials, with the more synthetically challenging Re^{2+}, Os^{3+}, and Rh^{4+} remaining largely unexplored. Additionally, the proposed bonding geometry poses a stringent requirement that, typically, the structural complexity of many materials does not allow for. Hence, additional perturbative terms in the spin Hamiltonian are generally inevitable in material realizations.

One of the first and most extensively studied materials in relation to the Kitaev model is α-$RuCl_3$. Described by the monoclinic symmetry $C2/m$[172], the crystal struc-

ture of α-$RuCl_3$ is comprised of van der Waals stacked quasi-two-dimensional honeycomb sheets of edge-sharing trigonally distorted $RuCl_6$ octahedra. Large single crystalline samples can be prepared following various synthetic procedures[161]. The applicability of the pseudo-spin $j_{\text{eff}} = 1/2$ doublet was investigated through a combination of spectroscopic techniques[173–175] and confirmed by resonant inelastic X-ray scattering[176]. Long range magnetic order was found to set in at temperatures ranging from 7–14 K[172,177,178]. Given the van der Waals interaction between the honeycomb layers, this variation was assigned to stacking faults in lower quality samples, and $T_{\text{N}} = 7$ K was confirmed as the ordering temperature for pristine samples by elastic- and inelastic neutron scattering experiments[179]. Yet, Curie-Weiss analysis yields a strongly anisotropic Weiss constant, $\theta_{\text{in-plane}} \simeq 40$ K and $\theta_{\text{out-of-plane}} = -200$ K, with an energy scale that is at least an order of magnitude larger than T_{N}[172,180]. A similarly anisotropic effective moment ranging from 2–2.7 μ_{B} was found and is larger than the expected 1.73 μ_{B} for a $j_{\text{eff}} = 1/2$ doublet. This discrepancy was explained through resonant inelastic X-ray scattering data as an additional unquenched orbital contribution stemming from the non-cubic distortion of the Ru-containing octahedra[176]. Below T_{N}, single-crystal neutron diffraction[181] reveals a zigzag ordered structure described by ferromagnetic chains that are coupled antiferromagnetically (Fig. 4.2(e)). Inelastic neutron scattering data, on the other hand, show low energy spin-waves that are associated with the ordered phase alongside a non-dispersive higher energy continuum[182,183]. The relevance of this T_{N}-independent continuum to Kitaev physics has been scrutinized through a plethora of *ab-initio* and experimental studies[163,162,176,184–186]. While the ground state of α-$RuCl_3$ remains heavily debated[161,8,163], the excitation spectrum and magnetic order suggest that additional perturbative terms in the Hamiltonian, namely, isotropic Heisenberg (J) and off-diagonal exchange (Γ) parameters, are relevant. These expand the magnetic phase diagram of the Kitaev model as depicted in Fig. 4.2[187,164]. This model is further extended by additional off-diagonal exchange terms, Γ', and further intra- and interlayer exchange couplings[188]. Overall, while proximate to the Kitaev model, the structural complexities of α-$RuCl_3$ highlight

the material challenges of attaining the criteria described by the J-K mechanism.

Alongside α-$RuCl_3$, the Ir^{4+}-based A_2IrO_3 (A = Li[189–192], Na[193,194]) family of materials and its A = H[49,51,195], Ag[196,197], Cu[198] intercalated derivatives, $A_3LiIr_2O_6$, have been thoroughly studied in recent years. While varying widely in their ground state properties, of all its members, only $H_3LiIr_2O_6$ does not undergo long range magnetic order[49]. Reminiscent of the Kagomé lattice antiferromagnet mineral Herebertsmithite[50], however, the structure of $H_3LiIr_2O_6$ suffers from H-site-disorder that has been suggested to mask the true nature of its low temperature physics[51,195]. An additional difficulty arises from the presence of Ir which has a large neutron absorption cross section, and thus hinders an in-depth experimental verification of the ground state properties via inelastic neutron scattering.

Given the above complexities associated with the current set of material realizations, the identification of novel materials is crucial for approaching the KSL ground state. Within this framework, recent *ab-initio* calculations propose studying materials with longer metal-metal bond distances so that non-Kitaev terms arising from the overlap of the spatially extended $4d$ and $5d$ orbitals vanish[199,200]. Promising electronic structure calculations indicate that Kitaev-type interactions can be maintained through superexchange mechanisms involving multiple atoms.

Inspired by this proposal, this chapter presents a comprehensive experimental and *ab-initio* study of the honeycomb Ru^{3+}-based system, RuP_3SiO_{11} (Fig. 4.3). The chapter will begin by introducing a new synthetic procedure for the preparation of powder samples for which the quality is verified by synchrotron powder X-ray diffraction. The onset of long range magnetic order, and the field-temperature phase diagram are then examined using a combination of specific heat, field-dependent magnetometry, and neutron powder diffraction measurements. Electronic structure calculations then confirm the $j_{\text{eff}} = 1/2$ character of the psuedospin Hamiltonian, and the exchange Hamiltonian is discussed

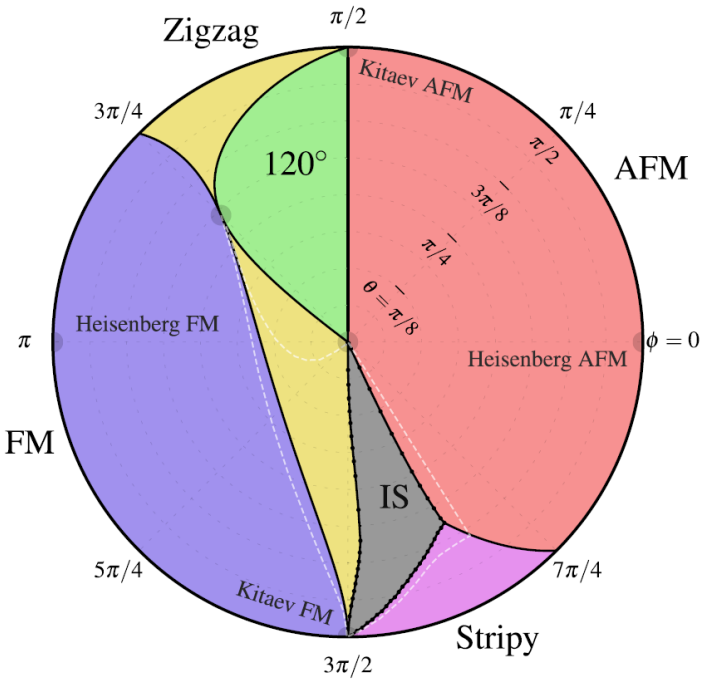

(a) Classical phase diagram with $\Gamma > 0$

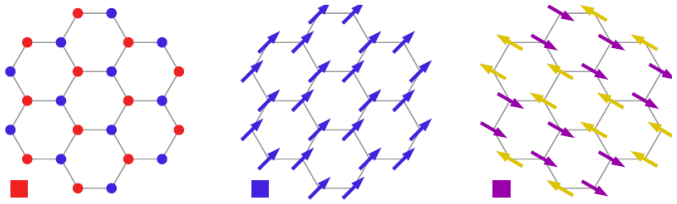

(b) AFM (c) FM (d) Stripy

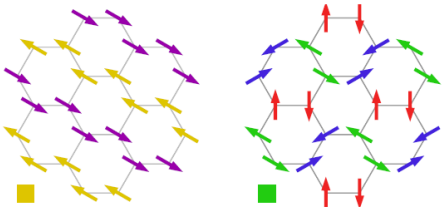

(e) Zigzag (f) 120°

Figure 4.2: (a) Extended magnetic phase diagram of the Kitaev model including an isotropic Heisenberg interaction, $J = \sin(\theta)\cos(\phi)$, a bond-directional Kitaev interaction, $K = \sin(\theta)\sin(\phi)$, and an off-diagonal exchange term, $\Gamma = \cos(\theta)$ shown for an antiferromagnetic $\Gamma > 0$ and calculated using a classical Luttinger-Tisza method. (b-f) Possible moment orientations depicted on the phase diagram. Here, IS indicates an incommensurate spin spiral structure. Figures adapted with permission from reference [164]; copyright APS 2014.

through the lens of inelastic neutron powder diffraction data.

4.2 Methods

4.2.1 Synthesis

Polycrystalline samples of RuP_3SiO_{11} were prepared following one of two synthetic procedures. Further details on the optimization of this synthesis are presented in the appendix (B.2). The first step of either reaction follows a modified version of the previously reported method for the preparation of the precursor $H_2RuP_3O_{10}$[201]. In a typical reaction, $RuCl_3{\cdot}xH_2O$ (Sigma-Aldrich, 99.98%) and H_3PO_4 (Sigma-Aldrich, 85 wt.% in H_2O, 99.99% trace metals basis) were combined in a round bottom flask in a 1:4 molar ratio, respectively, and heated in air at 350 K for 6 hours under constant stirring. The resulting viscous brown solution was transported to an alumina crucible and slowly heated (Q_H = 1 K/min) to 650 K under flowing Ar gas, held there for 168 hours, before being slowly cooled down to room temperature at a rate of Q_c = 1 K/min. This generally resulted in a light brown, water insoluble, and glass-like amorphous product which has been reported as $H_2RuP_3O_{10}$[201–203]. To prepare the final phase, $H_2RuP_3O_{10}$ is combined in stoichiometric amounts with SiO_2 (Alfa Aesar, 99.99%), pressed into a pellet, and heated at 1173 K for 168 hours in an evacuated sealed quartz tube refilled with 350 mbar of Ar. While reproducible, this method typically produced products with large ($\geq$10% wt.) RuO_2 impurity contents. These impurities likely stem from structural water in the precursor acting as an oxidizer. Indeed, both the Al and Fe analogues of $H_2RuP_3O_{10}$ have been known to form as hydrates[204,205].

The second method attempts to avoid the presence of water and involves an additional precursor, $Ru(PO_3)_3$[201], which forms upon heating a water washed and pressed powder

of $H_2RuP_3O_{10}$ for 168 hours in an evacuated sealed quartz tube refilled with 425 mbar of Ar. Temperature control at this stage is crucial as $Ru(PO_3)_3$[201] can adopt three polymorphs of which only the monoclinic cyclo-hexaphosphate ($Ru_2P_6O_{18}$), prepared by slow heating ($Q_H = 0.5$ K/min) and dwelling at 823 K, reacts to form the final product. Finally, RuP_3SiO_{11} could be prepared by combining the resulting pale orange product of $Ru(PO_3)_3$ in stoichimetric amounts with SiO_2 before sealing a pressed pellet of this mixture in an evacuated quartz tube refilled with 425 mbar of Ar that is subsequently heated at a rate of $Q_H = 3$ K/min to 1233 K and kept there for 72 hours before cooling to room temperature. The resulting final product is yellow colored, water insoluble, and stable in air for extended periods of time.

4.2.2 Diffraction

Synchrotron powder X-ray diffraction data were collected on the I11 beamline at Diamond Light Source using the MAC detector. The sample was densely packed in a 0.5 mm borosilicate capillary using sonication and measured at 300 K with an incident wavelength of $\lambda = 0.826015(5)$ Å. Neutron powder diffraction data were recorded on the time-of-flight WISH beamline at the ISIS Neutron and Muon Source. Here, a 1 g sample was packed in a cylindrical copper can and data sets were collected at 0.08 K and 2.5 K, respectively, with the former being measured with a dilution fridge insert. Nuclear structural refinements were conducted using the `GSASII`[92] software package. Representational analysis and magnetic refinements utilized the `MAXMAGN`[156] and `FullProf` suite[90], respectively.

4.2.3 Magnetometry and Specific heat

The temperature dependence of the magnetic susceptibility was measured in DC mode for a 28.01 mg sample in an applied field of $H = 0.1$ T between 0.4 K and 300 K using

both field-cooled and zero-field cooled protocols on a Quantum Design Magnetic Property Measurement System (MPMS3). A gelatin capsule was used as the container in which the sample was tightly packed with teflon tape and held in a plastic straw. No bifurication was observed, hence only the zero-field cooled measurements are shown here. Between 0.4 K and 1.8 K, more data sets were collected at applied fields of 1 T, 2 T, 3 T, 3.25 T, 3.5 T, 3.75 T, 4 T, 4.25 T, and 5 T. The magnetic field dependence of the magnetization was also measured in 0.06 K temperature steps between 0.4 K and 1.8 K usign the same MPMS3 system with an attached ^{3}He insert. At 0.4 K, a full loop, including all four quadrants between -7 T and 7 T, was measured, whereas all other data sets were recorded between 0 and 7 T.

The temperature dependent specific heat was measured on the Quantum Design Physical Property Measurement System (PPMS). A 2.6 mg sample prepared from a pressed pellet was used, and data were recorded in zero applied field between 0.1 K and 300 K. Each measurement was repeated three times and averaged to result in the data presented here.

4.2.4 Neutron Spectroscopy

The dynamical structure factor, $S(Q, E = \hbar\omega)_{\text{exp}}$, was measured on the direct geometry time-of-flight LET spectrometer at the ISIS Neutron and Muon Source using neutron incident energies of $E_{\text{i}} = 1.78$ meV, 3.14 meV, and 7 meV. Spectra were collected at 0.08 K, 2 K, 3 K, 4 K, 5 K, 10 K, and 15 K for the same 1 g sample packed in a cylindrical copper can. Temperatures below 2 K were reached using dilution refrigeration.

4.3 Results and Discussion

4.3.1 Crystal Structure

The reported $R\bar{3}c$ structural model[203] of RuP_3SiO_{11} was confirmed through Rietveld analysis of powder X-ray (300 K) and powder neutron (2.5 K, 0.08 K) diffraction data at all measured temperatures. At 300 K, all lattice parameters, atomic positions, and isotropic thermal parameters were refined, resulting in the model summarized in Table 4.2 (Fig. 4.4(a)). Additional impurity phases of RuO_2 and Ru metal were found to account for approximately 4.6% of the sample mass. For the neutron data collected at lower temperatures, a similar approach was taken. The additional Al and Cu phases from the instrument and sample can were modelled using the LeBail method. A summary of the model obtained at 2.5 K is given in Table 4.3. For the 0.08 K refinement, all structural and instrumental parameters, except for the lattice parameters, were constrained to their values at 2.5 K with two example refinement plots depicted in Figs. 4.4(b,c). This was done to refine magnetic only scattering (Sec.4.3.3). Overall, the unit-cell was found to isotropically contract with decreasing temperature and the lattice parameters are generally consistent with the isotypic compounds, MoP_3SiO_{11}[206] and FeP_3SiO_{11}[207].

The crystal structure of RuP_3SiO_{11} is comprised of quasi-two-dimensional buckled honeycomb sheets of octahedrally coordinated Ru^{3+} ions that are layered in an ABC stacking (Fig. 4.3). All apexes of the Ru-octahedra are coordinated by phosphate tetrahedra that form pseudo-edge sharing geometries between the octahedra within the *ab*-plane (Fig. 4.3(b,c)). As depicted in Fig. 4.3(d), the phosphate tetrahedra are part of P_2O_7 groups that connect the two-dimensional sheets along the crystallographic *c*-axis of which six of these interplane P_2O_7 groups surround Si_2O_7 groups sitting at the center of the honeycomb layers. Each P_2O_7 adopts a staggered conformation, hence slightly distorting the

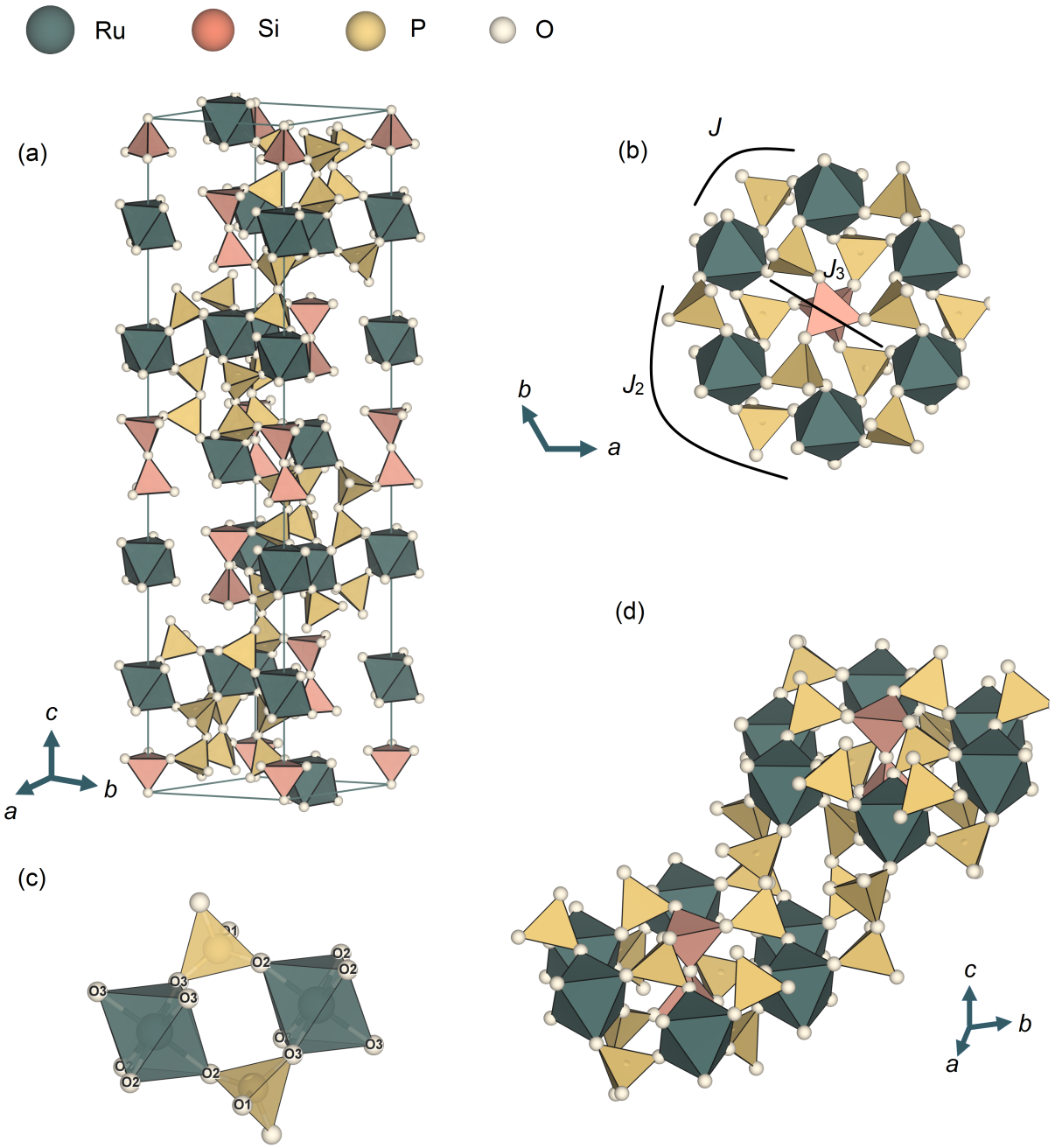

Figure 4.3: (a) Crystal structure of RuP_3SiO_{11} as viewed along the [111] direction. With respect to magnetic sublattice, RuP_3SiO_{11} can be described as forming (b) quasi-two-dimensional honeycomb sheets comprised of Ru^{3+}-octahedra that are (c) psuedo-edge shared through tetrahedrally coordinated phosphate groups. (d) These layers are connected along the crystallographic c-axis by pyrophosphate groups. Figures generated using the `VESTA` visualization software[26].

Table 4.2: Structural parameters of RuP_3SiO_{11} as obtained through Rietveld refinement of the $R\bar{3}c$ model using powder X-ray diffraction data measured at 300 K on the I11 power diffraction beamline. The resulting unit cell parameters are $a = b = 8.2410(1)$ Å and $c = 39.223(1)$ Å with goodness-of-fit parameters $\chi^2 = 3.55$ and $R_p = 8.06\%$.

Atom	Site	x	y	z	$U_{iso}((Å^2))$
Ru	12c	0	0	0.15858(1)	0.0058(1)
P	36f	0.3705(1)	0.0377(1)	0.11972(1)	0.0003(2)
Si	12c	0	0	0.04017(4)	0.0012(1)
O1	36f	0.122(1)	0.304(2)	0.384(2)	0.0001(1)
O2	36f	0.0440(3)	0.1929(3)	0.05235(5)	0.0037(6)
O3	36f	0.2233(3)	0.0829(2)	0.12706(5)	0.0043(5)
O4	18e	0.1374(3)	0.2322(3)	0.18896(5)	0.0097(6)
O5	6b	0.2094(3)	0	$\frac{3}{4}$	0.0027(7)

Ru-octahedra, with distances of $d_{\text{Ru-O2}} = 2.027(1)$ Å and $d_{\text{Ru-O3}} = 2.049(1)$ Å.

As summarized in Table 4.4, and in comparison to denser honeycomb frameworks where the metal containing octahedra are directly edge shared, the presence of the pseudo-edge-sharing geometry in RuP_3SiO_{11} results in larger metal-metal bond distances across the whole structure. Following the nomenclature of the extended Kitaev model, the leading isotopic in-plane superexchange interaction, J, most likely occurs through the two equivalent Ru-O-P-O-Ru pathways formed by the PO_4 tetrahedra as seen in the previous chapter and in other PO_4 containing magnetic materials[124,125]. The next nearest neighbor interaction, J_2, has no obvious superexchange mechanism. Further neighbor couplings, such as J_3, if present, require much longer pathways comprised of two PO_4 and one SiO_4 groups. Between the honeycomb layers, $J_\perp$ describes an exchange pathway formed by the pyrophosphates as Ru-O-P-O-P-O-Ru .

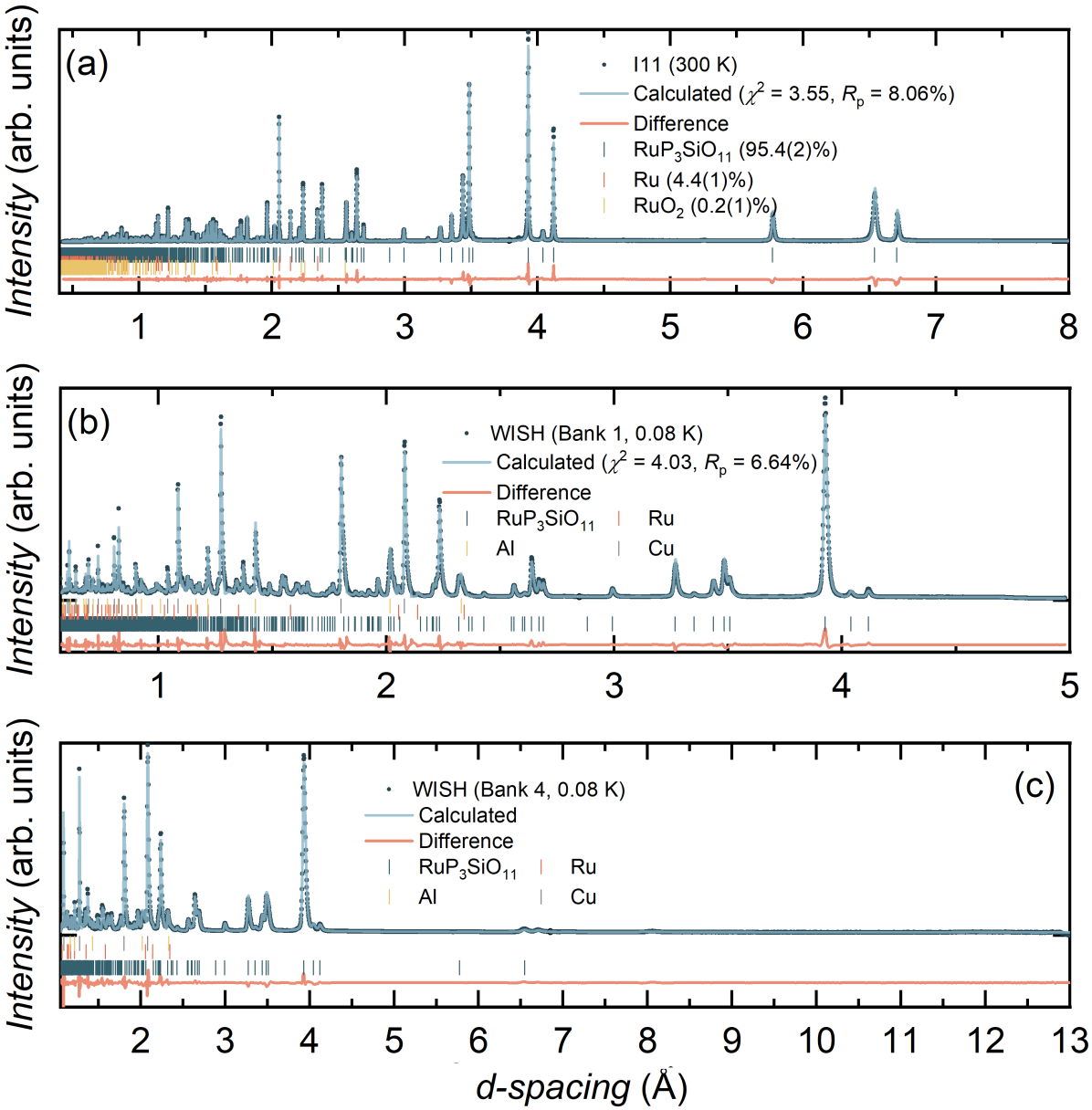

Figure 4.4: Rietveld analysis of powder (a) X-ray and (b-c) neutron diffraction data using the $R\bar{3}m$ structural model describing the crystal structure of RuP_3SiO_{11}. Data were collected at 300 K on the I11 beamline at Diamond Light Source using the MAC detector and at 0.08 K on the WISH diffractometer at the ISIS Neutron and Muon Source.

Table 4.3: Structural parameters of RuP_3SiO_{11} as obtained through Rietveld refinement of the $R\bar{3}c$ model using powder neutron diffraction data measured at 2.5 K on the WISH diffractometer. The resulting unit cell parameters are $a = b = 8.2282(5)$ Å and $c = 39.20(2)$ Å with goodness-of-fit parameters $\chi^2 = 3.23$ and $R_p = 5.97\%$.

Atom	Site	x	y	z	$U_{iso}((Å^2))$
Ru	$12c$	0	0	0.1586(1)	0.002(1)
P	$36f$	0.3731(8)	0.0391(8)	0.1192(1)	0.002(5)
Si	$12c$	0	0	0.0393 (3)	0.001(2)
O1	$36f$	0.0501(7)	0.2042(6)	0.0539(1)	0.016(3)
O2	$36f$	0.2245(7)	0.0872(7)	0.1273(1)	0.012(2)
O3	$36f$	0.1400(6)	0.2335(6)	0.1889(1)	0.009(3)
O4	$18e$	0.2080(8)	0	$\frac{3}{4}$	0.01(1)
O5	$6b$	0	0	0	0.02(3)

Table 4.4: Key distances and angles for RuP_3SiO_{11} and other materials relevant to the Kitaev model. All distances are reported in Å and refer to the exchange parameters described in Fig. 4.2(b), $J_\perp$ describes exchange between the honeycomb layers, and angles are reported in °.

Material	d_J	d_{J_2}	d_{J_3}	$d_{J_\perp}$	$\angle_{\text{M-O-M}}$
RuP_3SiO_{11}	4.800(1)	8.241(1)	9.702(1)	7.172(1)	94.36(3)
α-$RuCl_3$ [172]	3.454(1)	5.979(1)	6.905(3)	6.014(2)	93.93(7)
Na_2IrO_3 [208]	3.139(1)	5.426(1)	6.260(1)	5.606(1)	98.89(1)
$Ag_3LiIr_2O_6$ [196]	3.057(7)	5.284(1)	6.098(7)	6.503(1)	96.0(1)

4.3.2 Magnetometry and Specific Heat

The zero-field cooled temperature dependence of the magnetic susceptibility measured in an applied field of 0.1 T is shown in Fig. 4.5(a). The high-temperature data was fitted to the Curie-Weiss (CW) law where the fitting range was determined by increasing the minimum temperature until the parameters were stable (Fig. A.7). Above 140 K when this condition is met, the CW model yields the parameters $\theta_{\mathrm{CW}} = -17.6(1)$ K, $C = 0.381(1)$ emu K mol^{-1} ($g = 2.02$), $\mu_{\mathrm{eff}} = 1.75(1)$ μ_{B}, and $\chi_0 = 1.94(1) \times 10^{-4}$ emu mol^{-1}. This model suggests dominant antiferromagnetic interactions and an effective moment that is consistent with the expected $g\sqrt{j_{\mathrm{eff}}(j_{\mathrm{eff}}+1)}\mu_{\mathrm{B}} = 1.73$ μ_{B} for the $j_{\mathrm{eff}} = 1/2$ doublet describing the psuedospin Hamiltonian of RuP_3SiO_{11}. The paramagnetic temperature-independent background term χ_0, on the other hand, most likely stems from the Pauli paramagnetism of the Ru and RuO_2 impurities. Below 15 K, the development of short-range correlations is evidenced by the deviation of $\chi_{\mathrm{m}}(T)$ from its CW behavior and a broad anomaly in the temperature dependent zero-field specific heat (Fig. 4.5(b)). At lower temperatures still, the onset of long range magnetic order is marked by an inflection point in $\chi_{\mathrm{m}}(T)$ at $T_{\mathrm{N}} \simeq 1.3$ K and a λ-anomaly in the specific heat.

A similar two-peak structure consisting of a broad feature accompanied by a sharper one in $C_{\mathrm{p}}(T)$ appears in some samples of $RuCl_3$ [209]. These have been associated with the presence of two long-range ordered regimes that arise from the presence of stacking faults in powder samples [181]. The presence of some stacking faults have indeed been suggested for the isotypic compound MoP_3SiO_{11} [206], although, there is no evidence for that here. While the effect of such faults cannot be conclusively disregarded without a higher resolution low temperature powder and single-crystal structural study, only paramagnetic scattering is observed above $T_{\mathrm{N}} = 1.3$ K in the experimental dynamical structure factor as measured on the same powder sample (Sec.4.3.4). Furthermore, unlike the van der Waals layered nature of α-$RuCl_3$, the presence of the pillaring P_2O_7 groups between the

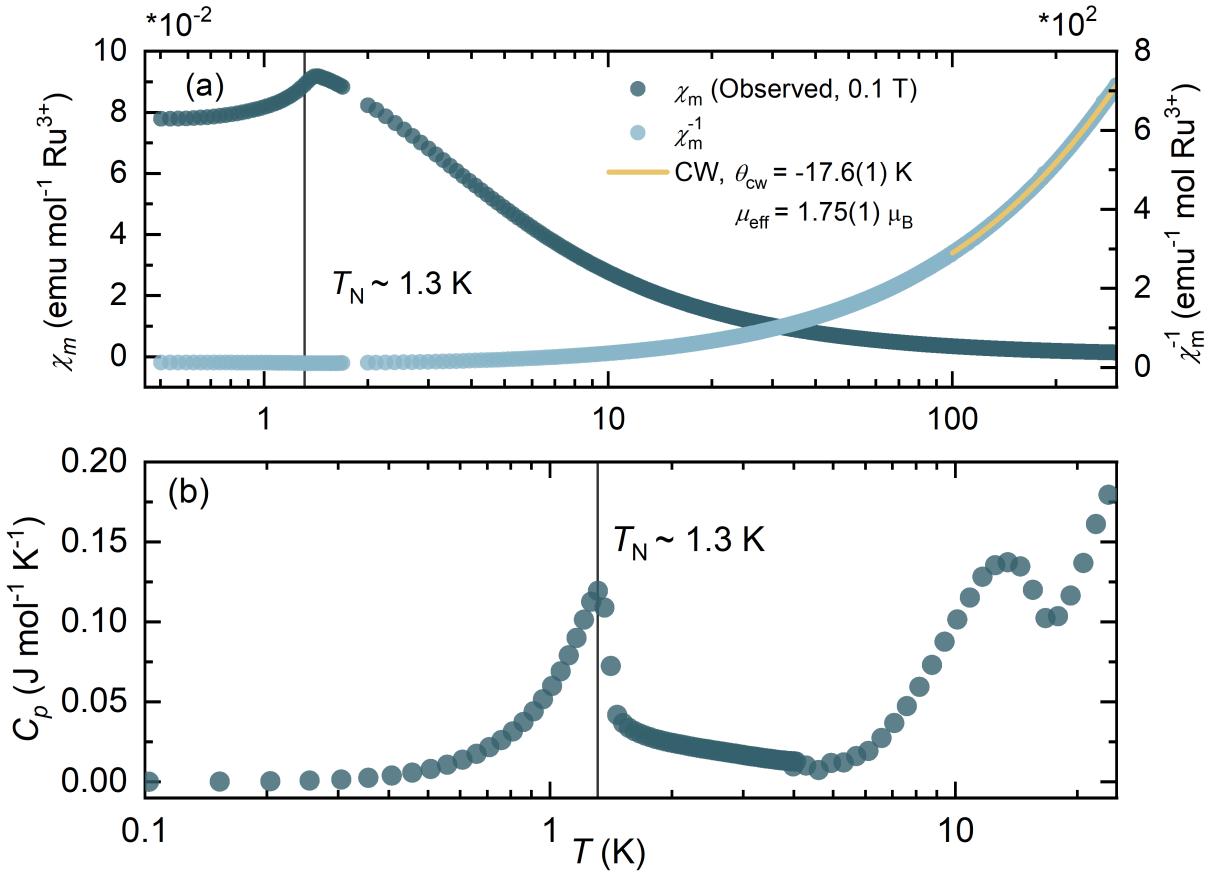

Figure 4.5: (a) Zero-field cooled temperature dependent magnetic susceptibility measured at 0.1 T. Above 140 K, χ_{m}^{-1}(T) is well described by the Curie-Weiss model with parameters $\theta_{\mathrm{CW}} = -17.6(1)$ K, $C = 0.381(1)$ emu K mol^{-1} ($g = 2.02$), $\mu_{\mathrm{eff}} = 1.75(1)$ μ_{B}, and $\chi_0 = 1.94(1) \times 10^{-4}$ emu mol^{-1}. (b) Zero-field temperature dependent specific heat highlighting the presence of a broad feature centered about 14 K and a sharper anomaly at 1.3 K.

honeycomb layers in RuP_3SiO_{11} should significantly reduce stacking faults. Hence, the presence of the feature, which coincides with $\theta_{CW} = -17.6(1)$ K, is more likely associated with the onset of short-range correlations. Conversely, it could be related to spin fractionalization as Monte Carlo calculations suggest this type of two-step entropy release for the Kitaev-Heisenberg model[210,211,161].

As summarized in Table 4.1, the powder averaged exchange in RuP_3SiO_{11} is similar to the in-plane exchange in $RuCl_3$. On the other hand, the out-of-plane exchange component in the latter is an order of magnitude larger[8,162,177,178]. Differences in the strength of the exchange energies are also reflected by the larger ordering temperature of α-$RuCl_3$ which varies between 7–14 K[162,8] depending on the quality of the sample[179]. The discrepancy most likely highlights the weaker orbital overlap that stems from the longer superexchange pathways in RuP_3SiO_{11}, and a suppression of the direct exchange component. Furthermore, unlike the current study, α-$RuCl_3$ consistently exhibits an effective moment that is larger than the expected 1.73 μ_B for a true $j_{eff} = 1/2$ psuedospin Hamiltonian. This is generally attributed to a small trigonal field splitting through which an additional orbital contribution arises[176]. In comparison to Ir^{4+}-containing materials, both T_N and $|\theta_{CW,\,iso}|$ are around an order of magnitude smaller in RuP_3SiO_{11}. Again, this most likely reflects the weaker orbital overlap, this time stemming from the larger $5d$-orbitals in the Ir-based compounds.

An interesting consequence of the relatively weaker exchange energies in RuP_3SiO_{11} is the possibility of tuning the physical properties of the system using smaller extrinsic perturbations. To examine this, the field dependence of $M(T)/H$ (Fig. 4.6), magnetization (Fig. 4.7(a,b), and the field-temperature phase diagram (Fig. 4.7(c)) are presented here. Beyond 0.1 T, the anomaly indicating the onset of long-range magnetic order broadens, and its temperature dependence decreases monotonically with increasing applied field (Fig. 4.6). Upon reaching 3.25 T, however, T_N is no longer observable within the measured 0.5 K–1.7 K temperature regime of the measurement.

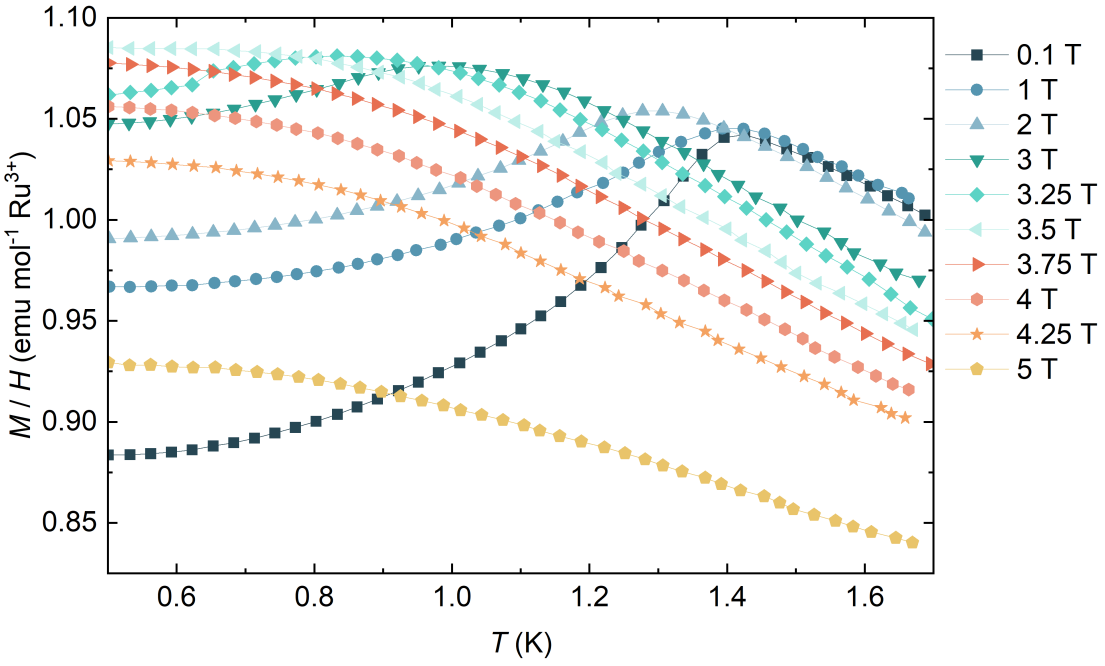

Figure 4.6: Field dependence of the zero-field cooled $M(T)/H$.

To investigate this further, the field dependence of the isothermal magnetization, $M(H)$, is presented in Fig. 4.7(a). At 0.4 K, $M(H)$ behaves linearly up to a field of 2 T, beyond which the the rate of increase rapidly becomes steeper, before reaching the critical field of $H_c \simeq 3.8$ T (0.72 μ_B). The magnetization then continues growing with a shallow slope but does not completely saturate and reaches a moment of 0.87 μ_B at 7 T. This type of field dependence is generally characteristic of a field-induced magnetic phase transition and can be more easily seen in the field derivative of the magnetization as depicted in Fig. 4.7(b). Interestingly, a similar behavior is observed for α-$RuCl_3$ in which a critical field of approximately 8 T marks the onset of a field induced paramagnetic regime[212]. The presence of this feature so close to the saturation field, however, complicates its interpretation. Indeed, unlike the characteristically sharp plateaus expected for saturation when isotropic interactions dominate, asymptotic approaches to saturation are instead more likely for highly anistropic interactions such as those related to the Kitaev model[181]. In the latter case, $M(H)$ never reaches its full $gS = 1$ value[181], which would

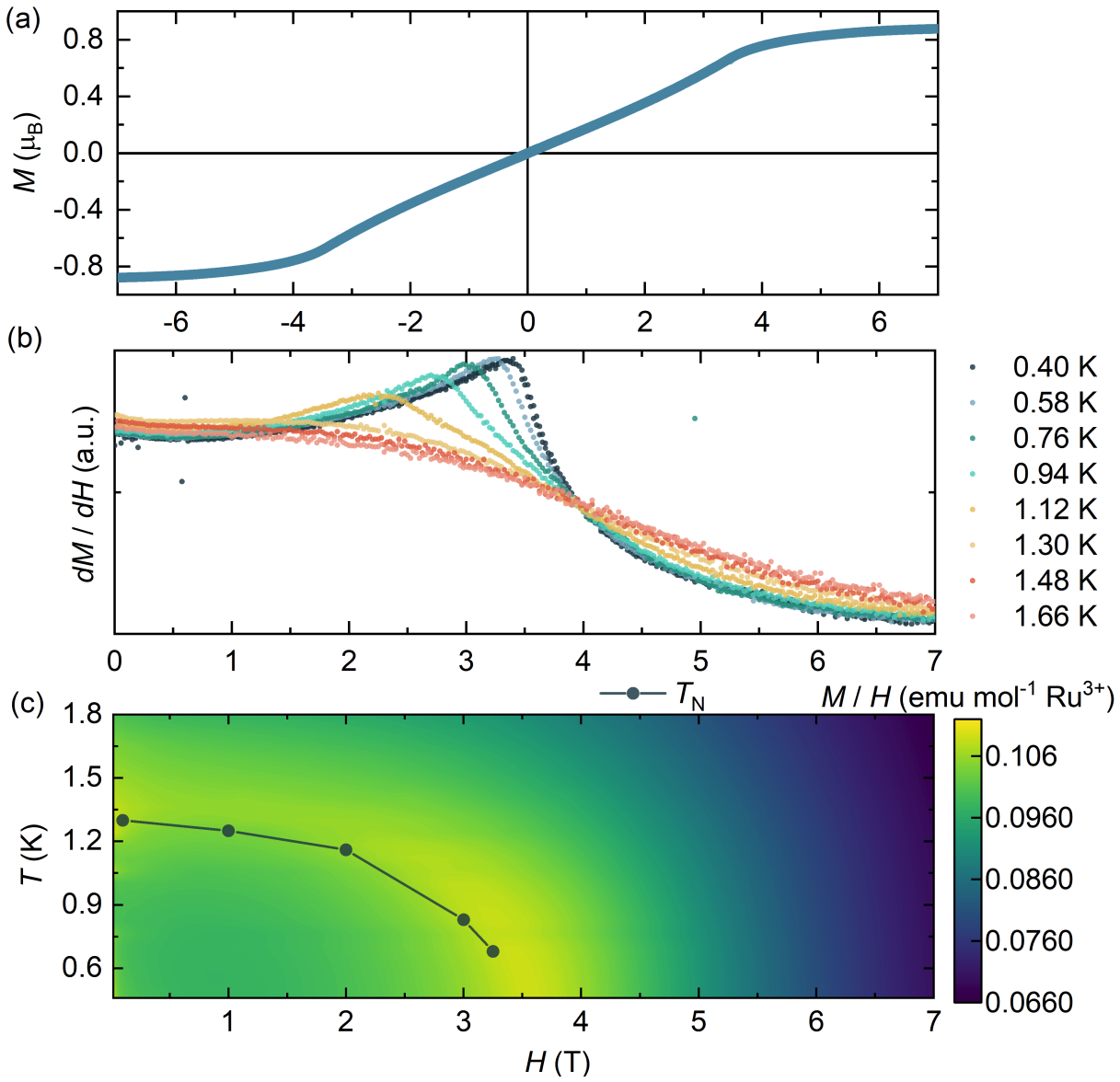

Figure 4.7: (a) Field dependent magnetization isotherm measured at 0.4 K. (b) The first derivative of the magnetization with respect to the applied field at multiple temperature points.(c) Magnetic field-temperature phase diagram prepared from magnetization data measured every 0.06 K. The solid line highlights the Néel temperature as obtained from the field dependence of the magnetic susceptibility.

then explain the slightly smaller 0.87 μ_B observed here at 7 T.

The temperature dependence of this feature, more easily seen in the field derivative of the magnetization, is depicted for selected temperatures in Fig. 4.7(b). Here, the peak broadens and H_c monotonically decreases with increasing temperature up until $T_N = 1.3$ K where it is no longer observable. The field-temperature phase diagram (Fig. 4.7(c)) reveals an M/H dependence that is consistent with the observed reduction in T_N with increasing field and is reminiscent of that seen for α-$RuCl_3$ [212]. Regardless, as these measurements are done on polycrystalline samples, no conclusion could be drawn on the nature of this critical field until a more detailed single-crystal field-dependence study could be performed. Finally, as no magnetic hysteresis is observed at any of the measured temperatures, and as implied by the negative θ_{CW}, antiferromagnetic ordering is to be expected.

4.3.3 Magnetic Structure

To examine the type of long range magnetic order in RuP_3SiO_{11}, the magnetic scattering was isolated by subtracting NPD data collected on the time-of-flight WISH diffractometer below (0.08 K) and above (2.5 K) T_N. As depicted in Fig. 4.8(a), the subtraction reveals three magnetic Bragg peaks corresponding to the (012), (104), and (018) nuclear reflections and hence suggest a commensurate propagation vector, $\kappa = (0, 0, 0)$. Symmetry analysis using `BasiReps` [90], `ISODISTORT` [101], and `MAXMAGN` [156] results in four irreducible representations, $m\Gamma_{2+}$, $m\Gamma_{2-}$, $m\Gamma_{1+}$ and $m\Gamma_{1-}$ in Miller-Love notation [157], that are compatible with κ and the crystal symmetry. Of these, $m\Gamma_{2+}$ corresponds to a ferromagnetically ordered structure, whereas the remaining $m\Gamma_{2-}$, $m\Gamma_{1+}$ and $m\Gamma_{1-}$ describe C-, A- and G-type Néel ordered states, respectively. When refining these models, only the $R\bar{3}'c'$ magnetic space group, in Belov-Neronova-Smirnova notation [97], which corresponds to the $m\Gamma_{1-}$ representation, is consistent with the data and yields goodness-of-fit param-

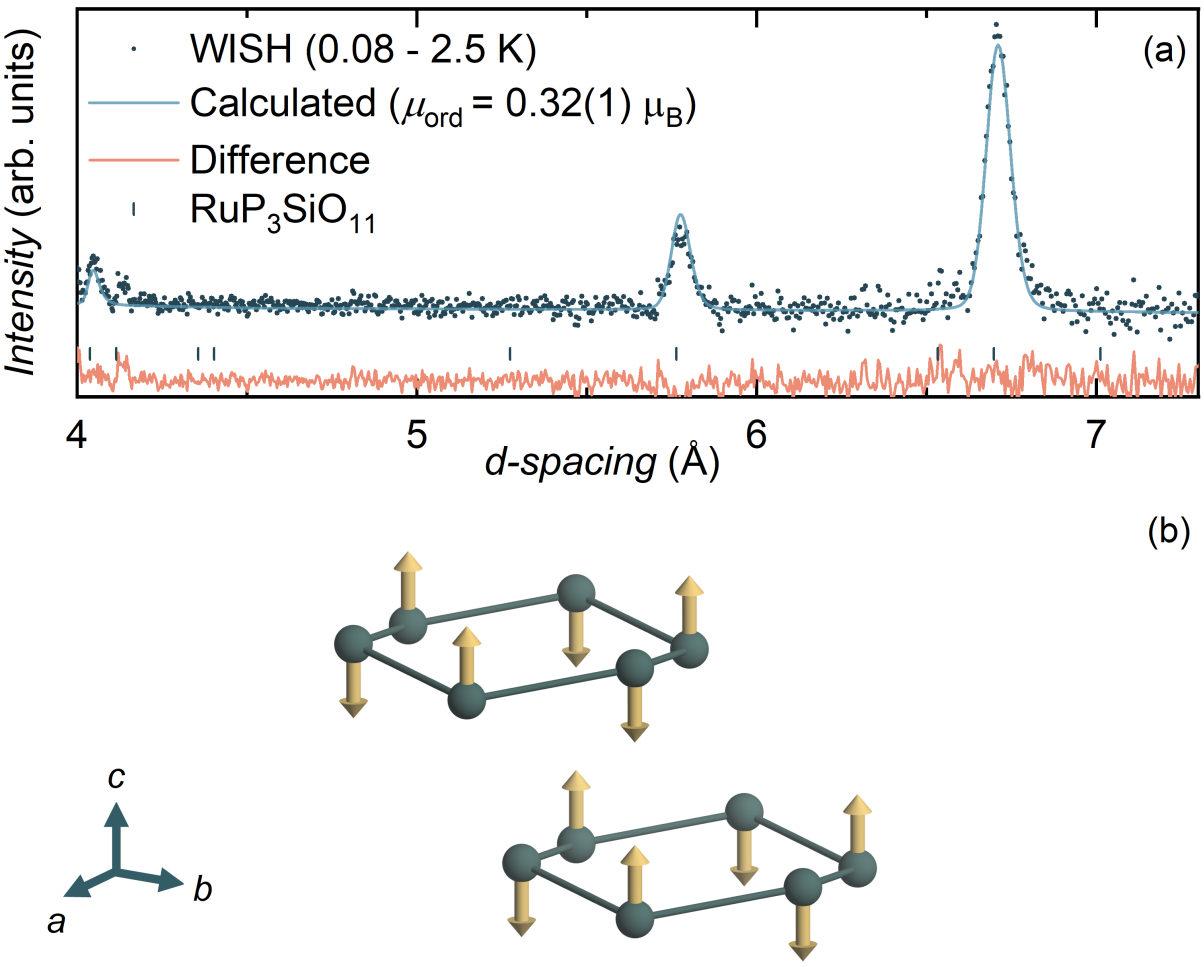

Figure 4.8: (a) Rietveld refinement of the $R\bar{3}'c'$ magnetic space group fit to subtracted (0.08-2.5 K) neutron powder diffraction data collected on the WISH diffractometer. The resulting goodness of fit parameters are $\chi^2 = 1.07$ and $R_{\text{mag}} = 10.2\%$, and the extracted ordered moment is $\mu_{\text{ord}} = 0.32(1)$ μ_B. (b) The resulting G-type Néel ordered structure with antiferromagnetic spins aligning parallel to the crystallographic c-axis.

eters $\chi^2 = 1.07$ and $R_{\text{mag}} = 10.2\%$. The resulting magnetic model is shown in Fig. 4.8(b) and describes a G-type Néel ordered structure where spins align antiferromagnetically along the crystallographic c-axis. When using the magnetic form factor of Ru^{3+}, as obtained by interpolating the parameters of a Dirac–Slater wave function approximation [213], an ordered magnetic moment of $\mu_{\text{ord}} = 0.32(1)$ μ_B is obtained. This is much reduced from its expected $gj_{\text{eff}} = 1$ value and is characteristic of lower-dimensional magnets and is consistent with the expected ordered moment of ≈ 0.3 μ_B [214] for a $S = 1/2$ honeycomb lattice. As summarized in Table 4.1, the extracted ordered moment is comparable to those of other Kitaev materials.

Through the lens of the Kitaev model, Néel-type magnetic order has yet to be experimentally observed in any material realization (Table 4.1). When considering the Kitaev-Heisenberg phase diagram, this type of long range magnetic order indicates an antiferromagnetic nearest neighbor Heisenberg exchange interaction, J, and either a ferromagnetic or an antiferromagnetic Kitaev-type interaction, K[187]. However, if the model is extended to incorporate the effects of off-diagonal Γ and Γ' terms, both ferro- and antiferromagnetic J interactions are allowed[188].

4.3.4 Ground State: Elucidating the Spin Hamiltonian

To investigate where RuP_3SiO_{11} lies on the extended Kitaev phase diagram, density functional theory (DFT) band-structure calculations were performed by Prof. Alexander Tsirlin at the University of Leipzig using the Perdew-Burke-Ernzerhof (PBE) flavor of the correlation-potential[215] as applied in the `FPLO`[142] and `VASP`[152,153] codes. The validity of the $j_{\text{eff}} = 1/2$ character of the spin-orbital degree of freedom was first examined. To pursue this, the density of states of RuP_3SiO_{11} was compared to that of α-$RuCl_3$ in which the $j_{\text{eff}} = 1/2$ state has been confirmed[173,216,217,176]. Furthermore, to ensure the validity of the comparison, the proposed rhombohedral $R\bar{3}$ low-temperature structure of α-$RuCl_3$[169], where the Ru^{3+} adopts a three-fold symmetry similar to in RuP_3SiO_{11}, was used.

In both compounds, the dominant octahedral crystal field term in the Hamiltonian of the Ru cations splits the degenerate $4d$ orbitals into a low lying t_{2g} manifold and a higher energy, doubly degenerate e_g^σ term. Trigonal distortions can then further split the t_{2g} manifold into the a_{1g} and e_g^π terms. Beginning with the uncorrelated PBE density of states (Fig. 4.9), similar orbital energies are obtained from Wannier projections as $\epsilon_{a_{1g}} = -0.08\,\text{eV}$, $\epsilon_{e_g^\pi} = -0.14\,\text{eV}$, and $\epsilon_{e_g^\sigma} = 2.40\,\text{eV}$ for RuP_3SiO_{11} and $\epsilon_{a_{1g}} = -0.38\,\text{eV}$, $\epsilon_{e_g^\pi} = -0.32\,\text{eV}$, and $\epsilon_{e_g^\sigma} = 2.08\,\text{eV}$ in α-$RuCl_3$. As for the octahedral splitting, Δ_{o}, as

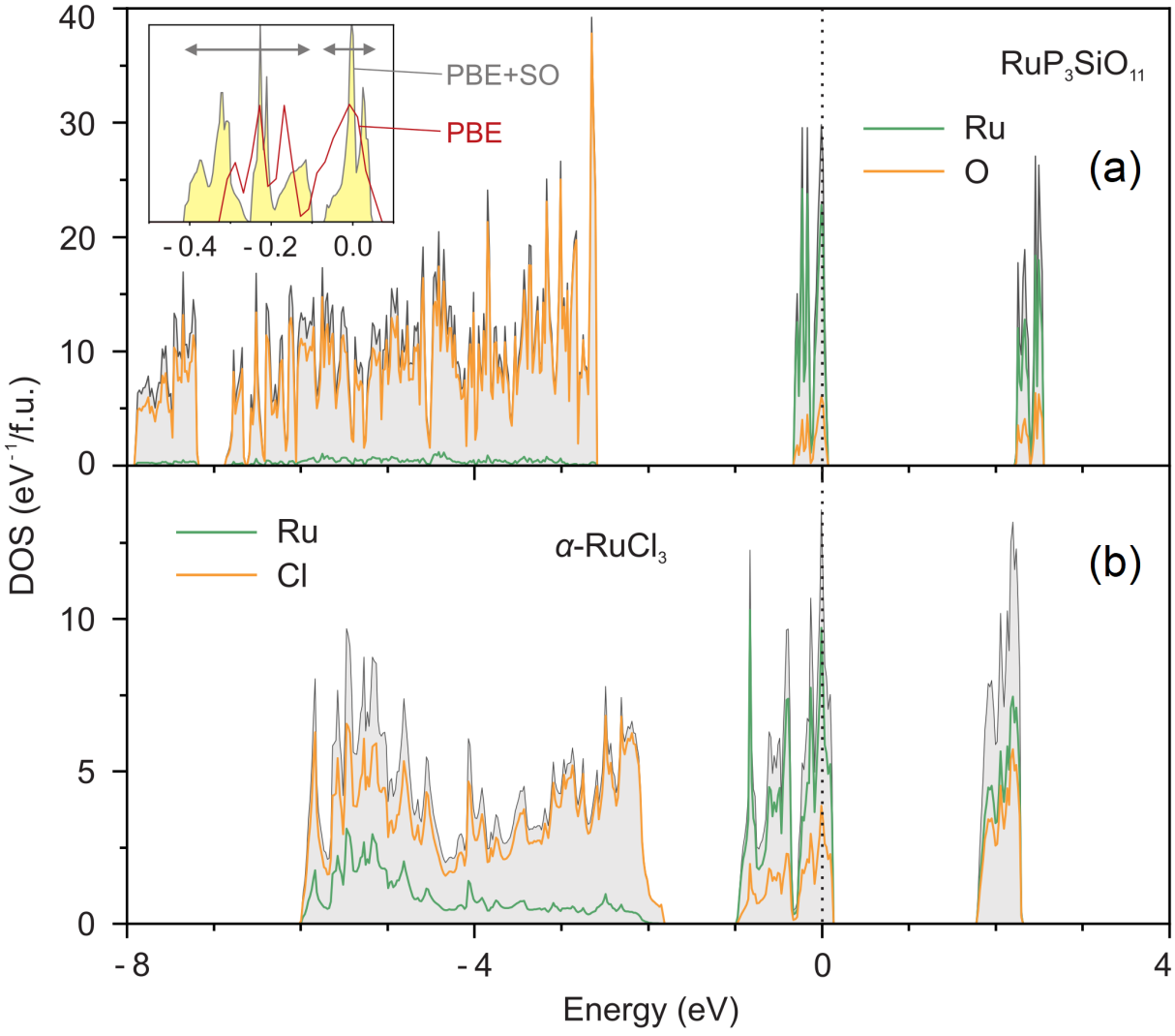

Figure 4.9: Perdew-Burke-Ernzerhof (PBE) density of states for $RuP_3SiO_{11}$and (b) α-$RuCl_3$. The Fermi level (E_F) is at zero energy. The inset shows a comparison of the PBE and PBE+SO density of states around E_F with arrows labeling the regions of $j_{eff} = \frac{3}{2}$ and $\frac{1}{2}$ states.

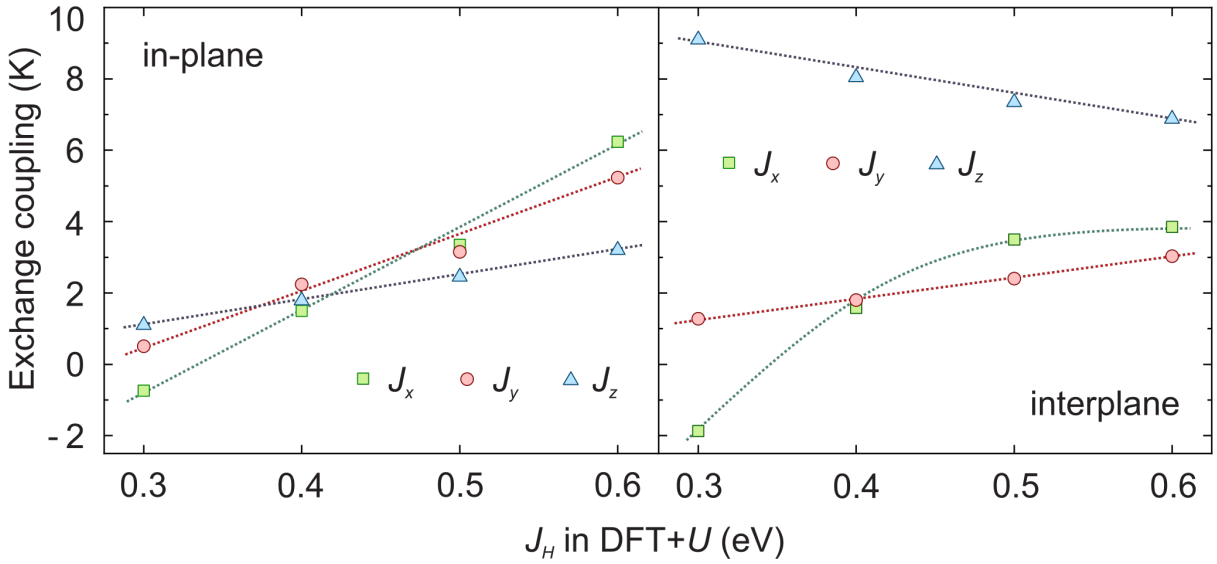

Figure 4.10: Exchange couplings calculated using the PBE+U+SO method with different values of the Hund's coupling parameter J_H.

expected for the more strongly interacting O^{2-} ligand, a relatively stronger $\Delta_o = 2.52$ eV is found for RuP_3SiO_{11} in comparison to 2.42 eV for the Cl^- ions in α-$RuCl_3$. The trigonal field splitting, on the other hand, was found to be equivalent, but opposing in signs, for both compounds, and is $|\Delta_t| = 0.06$ eV. Overall, all general prerequisites for the stabilization of a $j_{\text{eff}} = 1/2$ state are shared by both compounds.

To confirm this, the PBE+SO density of states of RuP_3SiO_{11}, where the effects of spin-orbit coupling are considered using a spin-orbit coupling constant $\lambda = 0.15$ eV[176], was calculated. The resulting density of states (Fig. 4.9(a, inset)) reveals a clear splitting of the t_{2g} manifold into lower and higher lying $j_{\text{eff}} = 1/2$ and $j_{\text{eff}} = 3/2$ states, respectively, as has also been seen in the PBE+SO density of states of Ir^{4+} compounds[218]. Regarding the exchanges, the effect of correlations was considered on a mean field level and calculated using PBE+U+SO using an on-site Coulomb repulsion $U_d = 3$ eV and a Hund's coupling $J_H = 0.6$ eV. A relatively isotropic magnetic moment, $\mu^x_{\text{spin}} = 0.19$ μ_B and $\mu^x_{\text{orb}} = 0.38$ μ_B vs. $\mu^z_{\text{spin}} = 0.20$ μ_B and $\mu^{'}_{\text{orb}} = 0.47$ μ_B, was found when the moment was constrained to be along the a- or c-axes, respectively. The formation of the $j_{eff} = 1/2$ state in RuP_3SiO_{11} is hence supported by the isotropic nature of the moments and the 1:2 ratio of the μ_{spin} and

μ_{orb} contributions to the magnetic moment.

Having established the validity of the $j_{eff} = 1/2$ state, we now turn to investigating the spin Hamiltonian. Depending on the frame of reference, the generalized Hamiltonian of the Kitaev model can be written in two forms[163]:

$$\mathcal{H}_{xxz} = \sum_{\langle ij \rangle} (J_{ij}^{x}(S_i^x S_j^x + S_i^y S_j^y) + J_{ij}^{z} S_i^z S_j^z) \tag{4.2}$$

and

$$\begin{aligned} \mathcal{H}_{JK\Gamma\Gamma'} = \sum_{\langle ij \rangle} [& J_{ij}\mathbf{S}_i\mathbf{S}_j + K_{ij}S_i^\gamma S_j^\gamma + \Gamma_{ij}(S_i^\alpha S_j^\beta + S_i^\beta S_j^\alpha) \\ & + \Gamma'_{ij}(S_i^\alpha S_j^\gamma + S_i^\gamma S_j^\alpha) + \Gamma'_{ij}(S_i^\beta S_j^\gamma + S_i^\gamma S_j^\beta)], \end{aligned} \tag{4.3}$$

for the cubic and XYZ frames of reference, respectively. Mapping the PBE+U+SO total collinear spin configuration energies onto the former model (Eqn. 4.2) yields a dominantly antiferromagnetic anisotropic spin Hamiltonian with relatively strong interplanar interactions such that $J^x = 0.44$ meV and $J^z = 0.28$ meV for the in-plane interactions and $J_\perp^x = 0.09$ meV and $J_\perp^z = 0.59$ meV between the planes. The extracted parameters reproduce the experimentally observed $\kappa = 0$ magnetic order and result in a Curie-Weiss temperature, $\theta_{\text{CW}}^\alpha = -\frac{1}{4}(3J^\alpha + J_\perp^\alpha)$, of -4.1 K for $\alpha = x, z$ that is relatively smaller than that obtained experimentally. As noncollinear spin configurations could not be stabilized in PBE+U+SO, however, none of the allowed off-diagonal terms, which have proved crucial for relevant Kitaev materials[163], could be calculated. Another issue with this approach is the strong energy dependence of the symmetric anisotropic exchange interactions on the Hund coupling parameter, J_H, as both the in-plane and interplane components significantly vary between antiferromagnetic to ferromagnetic regions (Fig. 4.10).

Hence, superexchange theory, as applied for d^5 electrons in the presence of spin-orbit coupling[219,164], was instead used to examine the extended Kitaev spin Hamiltonian de-

scribed in Eqn. 4.3. When considering the three-fold local symmetry of the nearest neighbor in-plane and interplane Ru–Ru bonds in RuP_3SiO_{11}, no symmetry operation constrains the form of the exchange tensor for each anisotropic X, Y, or Z bond. Thus, while the diagonalized values of the exchange parameters must be equivalent across all bonds, a non-trivial exchange tensor results such that

$$\begin{aligned}\mathcal{H}_{JK\Gamma\Gamma'} = \sum_{\langle ij \rangle} [& J_{ij}\mathbf{S}_i\mathbf{S}_j + K^x_{ij}S^\alpha_i S^\alpha_j + K^y_{ij}S^\beta_i S^\beta_j + K^z_{ij}S^\gamma_i S^\gamma_j \pm \Gamma_{ij}(S^\alpha_i S^\beta_j + S^\beta_i S^\alpha_j) \\ & \pm \Gamma'_{ij}(S^\alpha_i S^\gamma_j + S^\gamma_i S^\alpha_j) \pm \Gamma'_{ij}(S^\beta_i S^\gamma_j + S^\gamma_i S^\beta_j)], \end{aligned} \tag{4.4}$$

and

$$\mathbb{J}_X = \begin{pmatrix} J + K^Z & \Gamma' & \Gamma' \\ \Gamma' & J + K^X & \Gamma \\ \Gamma' & \Gamma & J + K^Y \end{pmatrix},$$

$$\mathbb{J}_Y = \begin{pmatrix} J + K^Y & \Gamma' & -\Gamma \\ \Gamma' & J + K^Z & -\Gamma' \\ -\Gamma & -\Gamma' & J + K^X \end{pmatrix},$$

$$\mathbb{J}_Z = \begin{pmatrix} J + K^X & -\Gamma & \Gamma' \\ -\Gamma & J + K^Y & -\Gamma' \\ \Gamma' & -\Gamma' & J + K^Z \end{pmatrix}$$

with respect to $[\alpha,\ \beta,\ \gamma] = [(y, z, x),\ (z, x, y),\ (x, y, z)]$ where the $\pm$ sign highlights the variation in the sign structure of the off-diagonal terms. This tensor structure is further complicated by allowed off-diagonal anisotropic terms, ϵ_n in the notation of Ref.[219], for both Γ and Γ'. Consequently, J and K^γ cannot be independently determined. When using $\lambda = 0.15$ eV[176], the calculated symmetrized parameters are summarized in Table 4.5 and their tensor form is:

$$\mathbb{J}_X = \begin{pmatrix} -1.22 & 0.83 & 0.71 \\ 0.83 & -0.29 & 0.47 \\ 0.71 & 0.47 & -0.39 \end{pmatrix},$$
$$\mathbb{J}_Y = \begin{pmatrix} -0.39 & 0.71 & -0.47 \\ 0.71 & -1.22 & -0.83 \\ -0.47 & -0.83 & -0.29 \end{pmatrix},$$
$$\mathbb{J}_Z = \begin{pmatrix} -0.29 & -0.47 & 0.83 \\ -0.47 & -0.39 & -0.71 \\ 0.83 & -0.71 & -1.22 \end{pmatrix}$$

with $\epsilon_n \approx 0.1$ meV. The interlayer coupling $J_\perp$ also features an anisotropic tensor in this coordinate frame:

$$\mathbb{J}_\perp = \begin{pmatrix} 0.20 & -0.09 & -0.09 \\ -0.09 & 0.20 & 0.09 \\ -0.09 & 0.09 & 0.20 \end{pmatrix}.$$

Unlike the PBE+U+SO calculated model, the resulting model reveals a significant contribution from off-diagonal terms and predicts a stronger tendency towards ferromagnetism, as well as a much weaker $J_\perp$. This model is also inconsistent with θ_{CW}. The nature of this discrepancy is unclear, but most likely stems from the differences in the computational approaches used; PBE+U+SO does not account for off-diagonal terms but, unlike the alternative method, considers e_g^σ orbital contributions and accounts for any residual t_{2g} crystal field splitting.

To differentiate between these scenarios, and to more broadly examine the spin Hamiltonian, the experimental dynamical structure factor of RuP_3SiO_{11}, $S(Q, E = \hbar\omega)_{\mathrm{exp}}$, was measured on the LET direct geometry time-of-flight neutron spectrometer using incident

Table 4.5: Exchange couplings (in meV) written in the Kitaev XYZ reference frame, Eq. (4.4), using superexchange theory with $U_d = 3$ eV, $J_d = 0.6$ eV, and spin-orbit coupling $\lambda = 0.15$ eV.

	$d_{\mathrm{Ru-Ru}}$	J_{ij}	K_{ij}	Γ_{ij}	Γ'_{ij}
J	4.800	-0.35	-0.96	0.47	0.78
$J_\perp$	7.172	0.20	0	0.09	-0.09

neutron energies of $E_\mathrm{i} = 1.78$ meV and 3.14 meV. Above T_N, and up to 10 K, the spectra are gapless and show low-Q scattering up to $E \simeq 0.7$ meV (Fig. 4.11). At 0.08 K, a gap of approximately 0.1 meV develops in the spectrum, and two clear bands, lying within a bandwidth of 0.1 – 0.8 meV, are observed (Fig. 4.12(a)). A closer look at the E-dependence of the scattering (Fig. 4.13(a-c)) reveals that the bands are almost separated in energy, that their intensities vary by at least a factor of two, and their energy scale is concomitant with both the experimental θ_CW and *ab-initio* models. The Q-dependence, on the other hand, confirms the spin-wave-like dispersive character of the inelastic spectral weight in which the lower band peaks at about 0.2 Å^{-1}, 0.6 Å^{-1}, and 0.8 Å^{-1} vs. 0.5 Å^{-1} and 1.2 Å^{-1} for the higher energy band (Fig. 4.13(d-e)). As confirmed through the spectra collected at $E_\mathrm{i} = 3.14$ meV, other than a superfluid ^{4}He roton[220] from exchange gas, no further excitations are present above 0.8 meV (Fig. 4.12(e)). Indeed, the phonon contribution to the spectra appears beyond 1.6 Å^{-1} and 1.5 meV (Fig. 4.12(g)).

To simulate the experimental dynamical structure factor, linear spin wave theory was performed using the `SpinW`[27] software package. When constructing the spin Hamiltonian following the $\mathcal{H}_{xxz}$ (Eq.4.2) *ab-initio* calculated model, the energy scale of the resulting spectrum is consistent with $S(Q, E = \hbar\omega)_\mathrm{exp}$, yet, its structure, consisting of only a single band, is incompatible with the the experimental data (Fig. 4.14(a)). A similarly incompatible spectrum results when using the parameters calculated for the $\mathcal{H}_{JK\Gamma\Gamma'}$ (Eq.4.4) model. However, the role of K and Γ is made clear as the resulting spectrum does reproduce the characteristic two-band structure observed in the experimental dynamical structure factor (Fig. 4.14(b)).

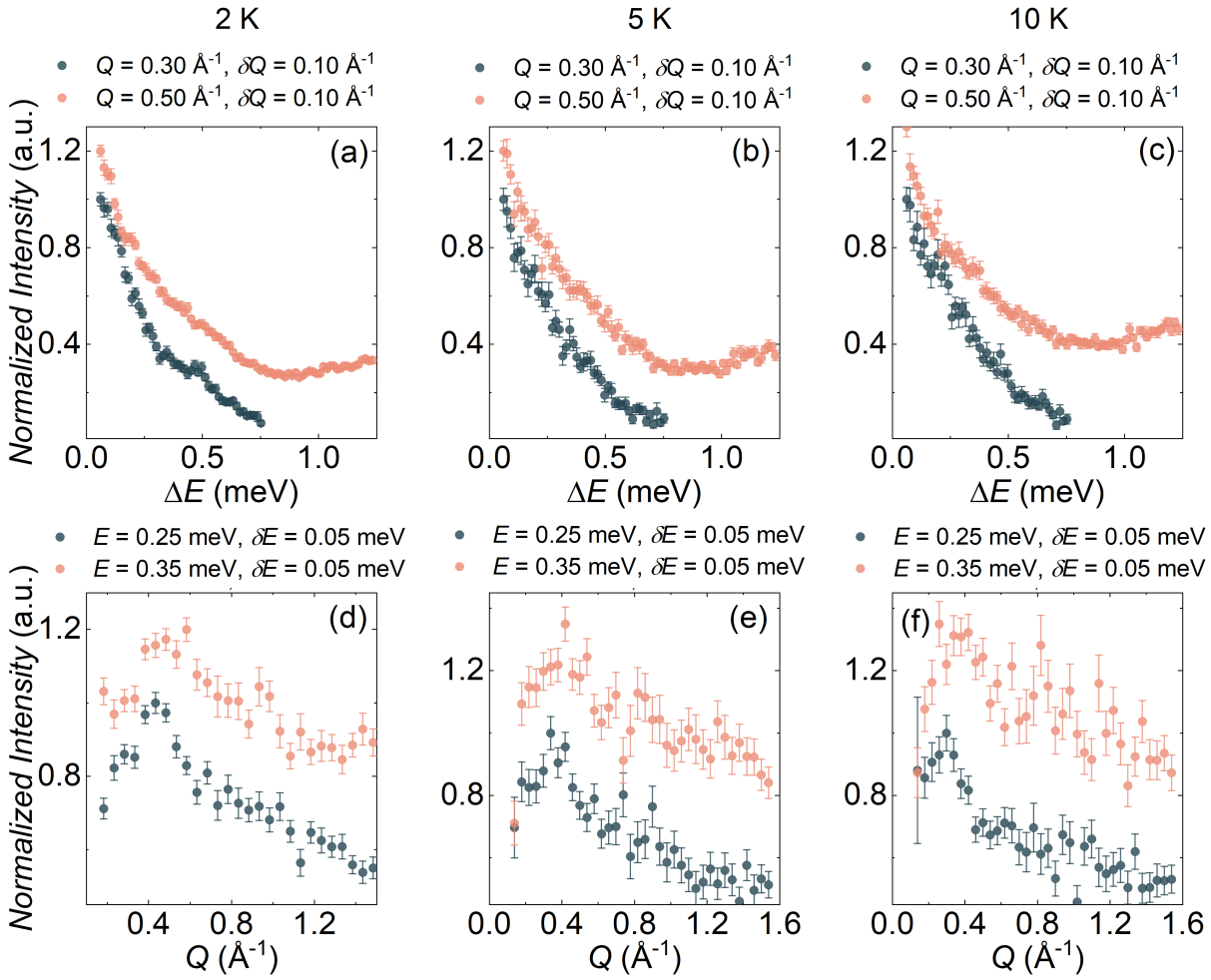

Figure 4.11: Examples of (a-c) E- and (d-f) Q-integrated cuts of $S(|Q|, E)$ as measured for RuP_3SiO_{11} on the LET spectrometer at the specified temperatures. All red colored points are offset for ease of visualization.

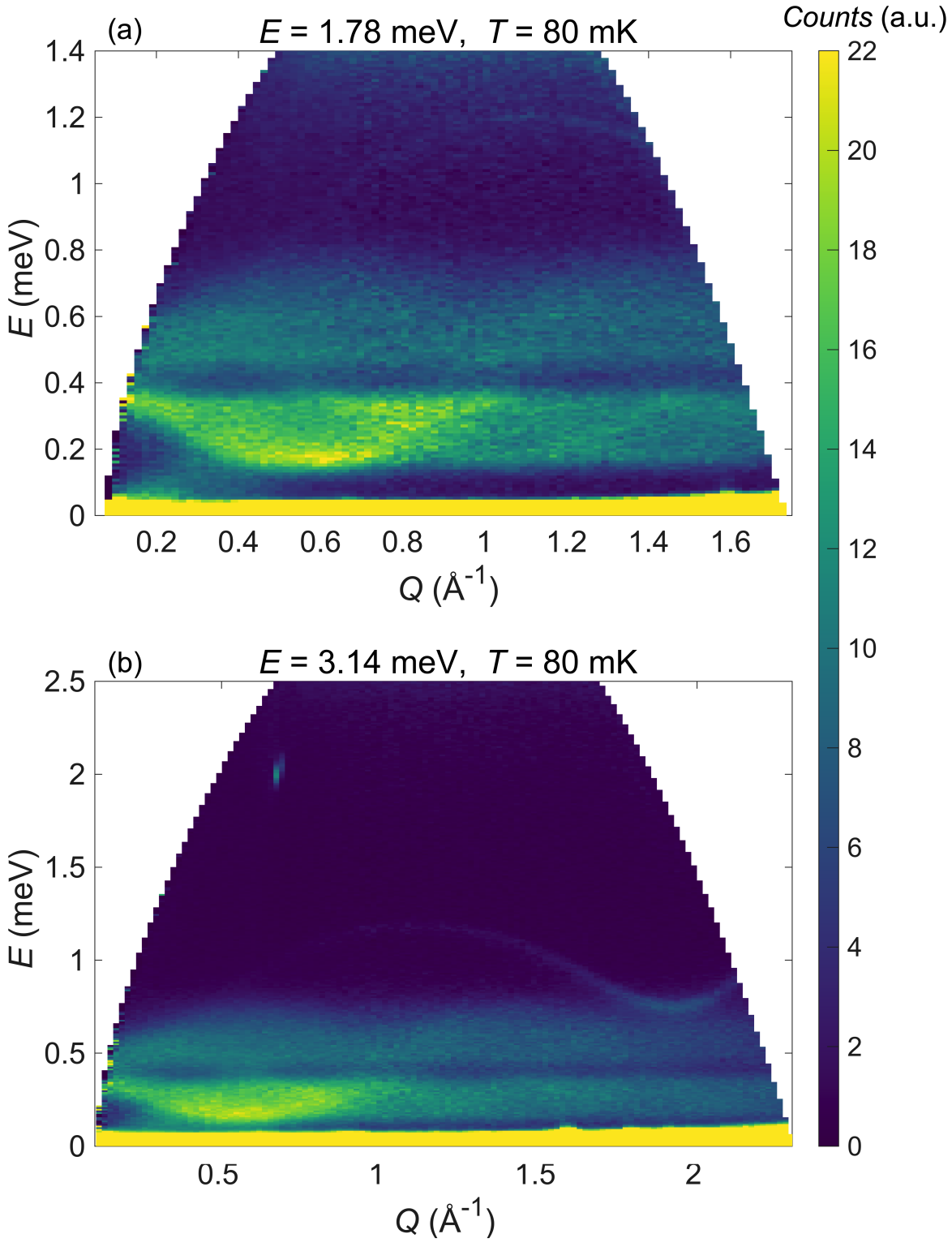

Figure 4.12: (a,b) Experimental dynamical structure factor, $S(Q, E = \hbar\omega)_{\text{exp}}$, measured on the direct geometry time-of-flight LET spectrometer at 0.08 K using neutron incident energies of $E_{\text{i}} = 1.78$ meV and 3.14 meV, respectively.

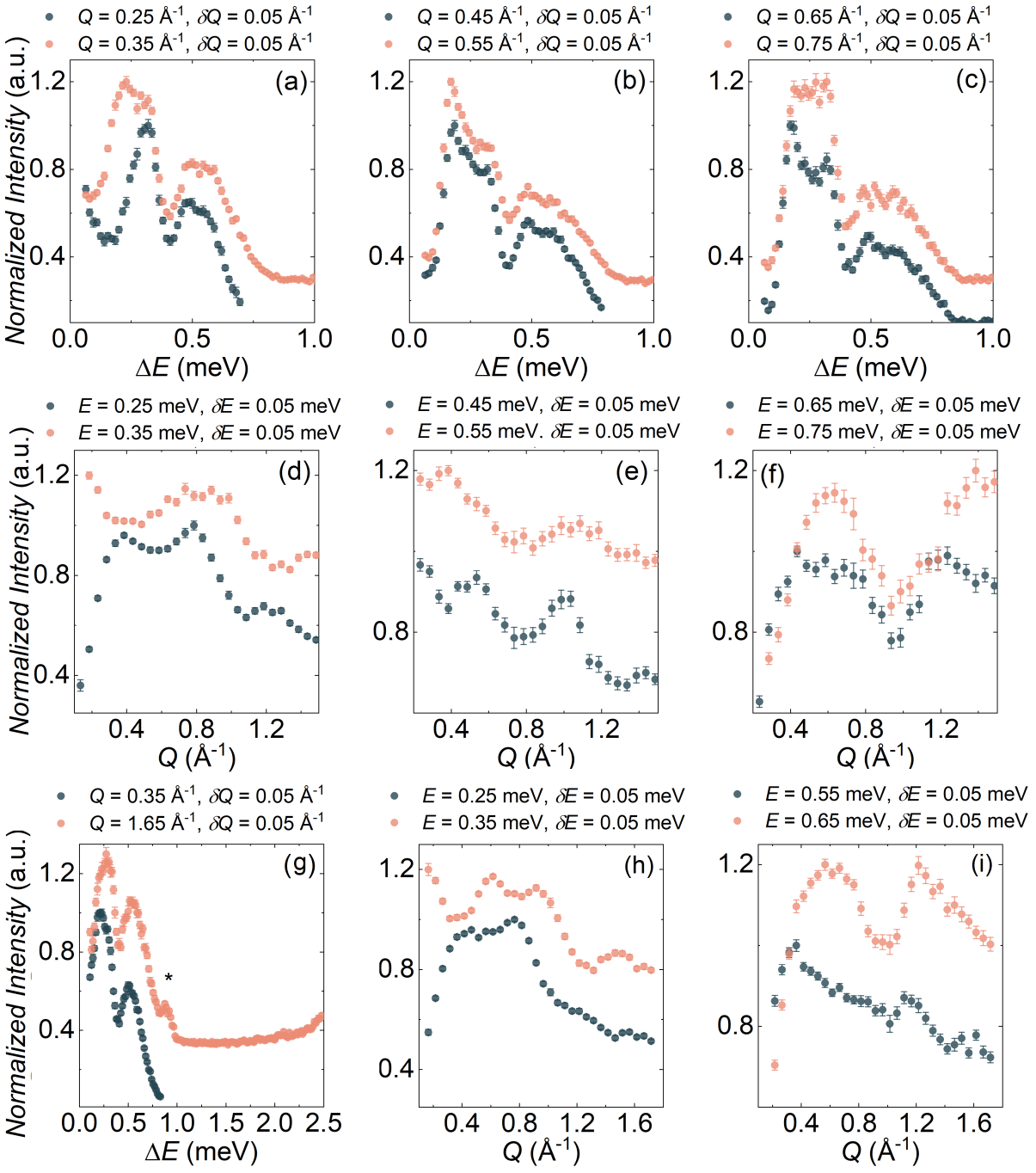

Figure 4.13: (a-c) E- and (d-f) Q-integrated cuts of $S(|Q|, E)$ as measured for RuP_3SiO_{11} on the LET spectrometer at 0.08 K with $E_i = 1.78$ meV. (g) E- and (h,i) Q-integrated cuts of $S(|Q|, E)$ measured with $E_i = 3.14$ meV. The asterisk in panel (e) highlights the contribution from the ^{4}He roton. All red colored points are offset for ease of visualization.

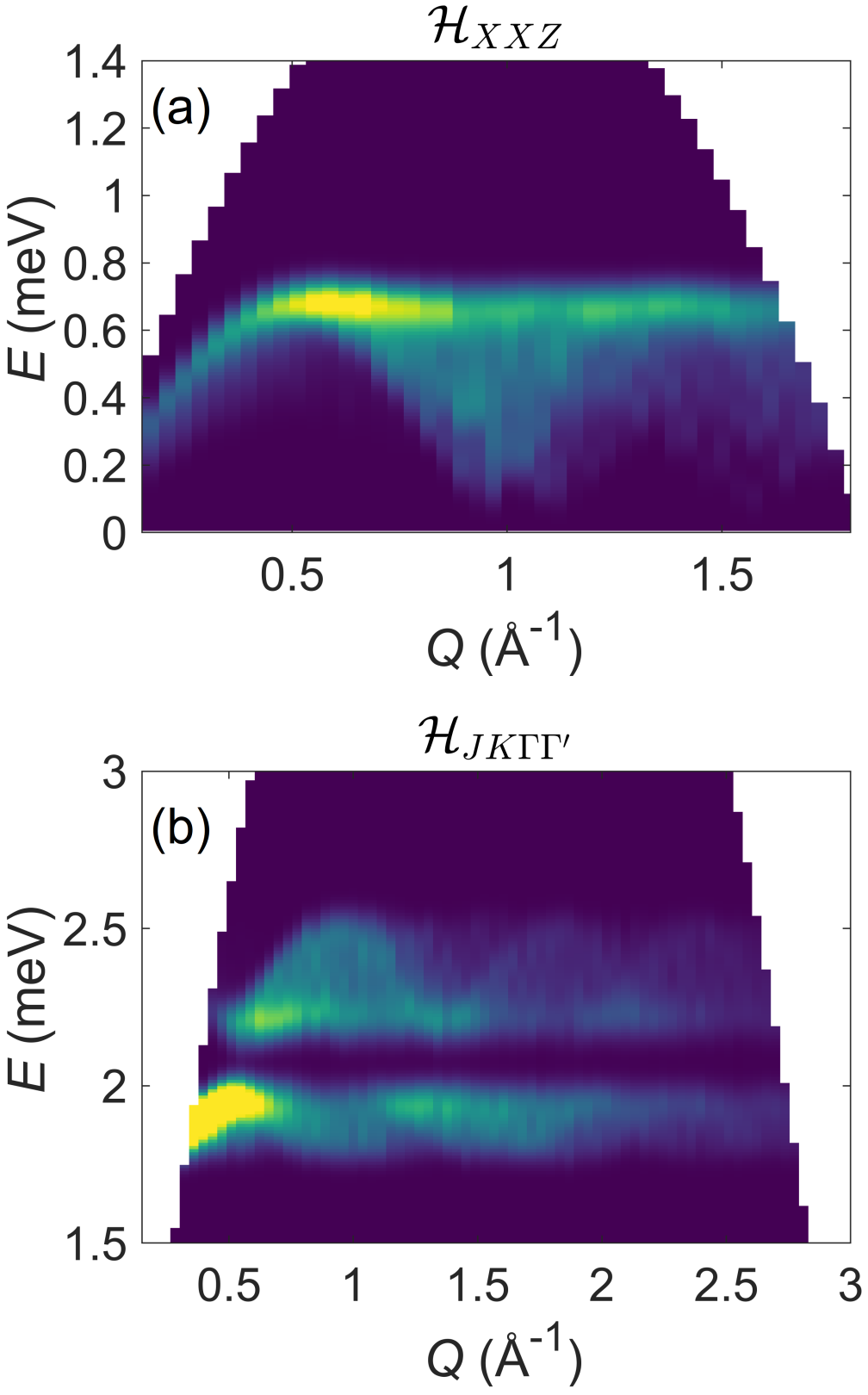

Figure 4.14: Linear spin wave theory simulations of the *ab-initio* calculated parameters for the (a) $\mathcal{H}_{XXZ}$ (Eq.4.2) and (b) $\mathcal{H}_{JK\Gamma\Gamma'}$ (Eq.4.4) spin Hamiltonians.

As neither *ab-initio* model captures the experimental spectra, an optimization of the parameters describing $\mathcal{H}_{JK\Gamma\Gamma'}$ is necessary. Given the large parameter space of the minimal model, however, narrowing down to a physical parameter space (*i.e.* one that reproduces the magnetic ground state and the structure of the excitation spectra) is crucial to avoid local minima. As a starting point towards this, a spin Hamiltonian including K^X, K^Y, K^Z, Γ, and Γ' will be used as J cannot be separated from the Kitaev terms. When varying each parameter in ± 0.05 meV steps, the best resulting model reveals a strongly anisotropic spin Hamiltonian with $K^X = 0.55$ meV, $K^Y = -0.15$ meV, $K^Z = 0.2$ meV, $\Gamma = 0.15$ meV, and $\Gamma' = 0$ meV (Fig. 4.15). It should be noted, however, that the parameters are strongly interdependent, and that further optimization, including $J_\perp$, is necessary. Regardless, it is evident that off-diagonal terms and exchange parameters beyond the Kitaev interaction are necessary to describe the Hamiltonian of RuP_3SiO_{11}.

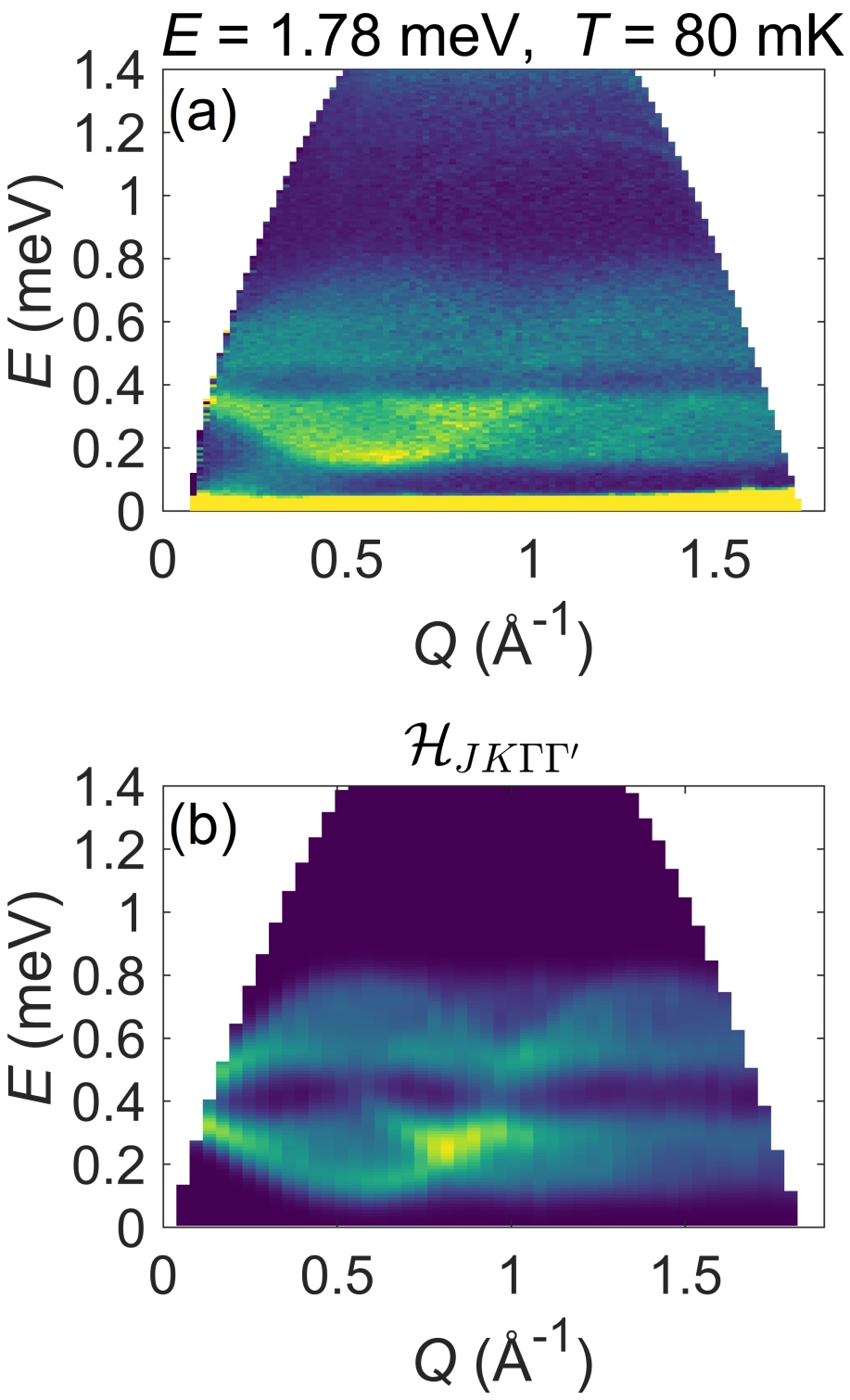

Figure 4.15: (a) Experimental dynamical structure factor of RuP_3SiO_{11} as measured at 0.08 K. (b) Linear spin wave theory simulations of the$\mathcal{H}_{JK\Gamma\Gamma'}$ (Eq.4.4) spin Hamiltonian with parameters $K^X = 0.55$ meV, $K^Y = -0.15$ meV, $K^Z = 0.2$ meV, $\Gamma = 0.15$ meV, and $\Gamma' = 0$.

4.4 Conclusions

This chapter presents a comprehensive study on the low-temperature magnetic properties of the honeycomb Ru^{3+}-based material, RuP_3SiO_{11}. Using a combination of scattering and magnetometry measurements, alongside electronic structure calculations, the relevance of RuP_3SiO_{11} to the extended Kitaev model is established, and the main findings are summarized as:

- A novel synthetic procedure for the preparation of polycrystalline samples was established for RuP_3SiO_{11}. Using Rietveld analysis of synchrotron powder X-ray diffraction and neutron powder diffraction data, minimal impurity phases were found, and the trigonal $R\bar{3}c$ symmetry of the system was confirmed. The resulting honeycomb magnetic sublattice is comprised of pseudo-edge-sharing Ru^{3+}-octahedra in the *ab*-plane that are separated by P_2O_7 and Si_2O_7 groups along *c*.

- Curie-Weiss analysis of the temperature dependent magnetic susceptibility suggests dominant antiferromagnetic interactions and yields an effective moment that is concomitant with the expected moment for a $j_{\text{eff}} = 1/2$ psuedospin Hamiltonian.

- The onset of long range magnetic order at 1.3 K is evidenced by an inflection point in the magnetic susceptibility and a sharp anomaly in the temperature dependent specific heat.

- Two features, one broad, and another sharp, are found in the temperature dependent specific heat. Such two-step behavior has been theorized for the Kitaev model and could suggest the relevance of RuP_3SiO_{11} to it. Similarly, it could also be related to the development of short-range correlations, that is then followed by long range magnetic order.

- Within the 0.5–1.8 K temperature regime, the magnetic field-temperature phase

diagram of the magnetization shows that long range magnetic order is suppressed beyond 3.25 T. At a critical field of 3.8 T, an anomaly appears in the magnetization. It was not possible to determine whether this represents saturation or a phase transition.

- Below 1.3 K, analysis of neutron powder diffraction data establishes a Néel ordered magnetic structure for RuP_3SiO_{11}. A much reduced ordered moment, consistent with the predicted moment for a $S = 1/2$ honeycomb lattice, is obtained.

- The relevance of the $j_{\text{eff}} = 1/2$ doublet in RuP_3SiO_{11} is confirmed through electronic structure calculations.

- Below T_{N}, the temperature dependence of the dynamical structure factor measured using inelastic neutron scattering shows a gapped spectrum comprised of two spin-wave-like bands with an overall energy scale of ≈ 0.8 meV.

- *Ab-inito* calculated model parameters are generally inconsistent with the observed spectra, and an initial model confirms the importance of exchange parameters beyond the Kitaev interaction.

To the author's knowledge, RuP_3SiO_{11} is the only Ru^{3+}-based honeycomb system aside from α-$RuCl_3$ that could be related to the Kitaev model[161,18,8]. Additionally, it is the first in which a Kitaev-type interaction involves a multi-atom superexchange mechanism. In comparison to other relevant Kitaev materials, it is also the first that Néel orders. Hence, this introductory study poses many interesting future directions through which the spin Hamiltonian could be revealed:

- Given the characteristic anistropy of the Kitaev model, single crystal samples would be crucial for a better understanding of the ground state properties of the system. Chemical vapor transport could prove fruitful in this direction as single crystal samples of the isotypic compound, VP_3SiO_{11}, have been prepared using this method[221].

- Preparing the diamagnetic InP_3SiO_{11} [222] analogue would allow for a subtraction of the phonon contribution from the specific heat. This could provide insight on the nature of the two step features seen in the total specific heat.

- Field dependent specific heat and inelastic neutron scattering measurements could shed light on the nature of the critical field observed in this study and establish whether it stems from critical behavior, as in α-$RuCl_3$, or simple moment saturation.

- The character of the pseudospin Hamiltonian and the hierarchy of the crystal field energies could be verified using resonant inelastic X-ray scattering data. This experiment has already been completed, and analysis is currently underway.

- Finally, a rigorous numerical optimization (*e.g.* Monte Carlo or other optimization methods for high-dimensional optimization problems) of the spin Hamiltonian parameters will provide, at least, the region within which RuP_3SiO_{11} falls on the extended Kitaev phase diagram and establish its relevance to the model.

Chapter 5

Realising Square and Diamond lattice $S = 1/2$ Heisenberg Antiferromagnet Models in the α and β Phases of the Coordination Framework, $KTi(C_2O_4)_2 \cdot xH_2O$

5.1 Introduction

Hybrid materials comprised of at least one molecular component alongside a magnetic transition metal, and which are generalized under the hypernym of coordination frameworks, provide an alternative chemical route to inorganic materials for the realization of unconventional magnetic ground states. In comparison to their oxide counterparts, the wide assortment of available organic ligands has generated considerable interest as

these may provide a more controlled route to map spin models onto material realizations[223]. This stems from the flexibility of organic ligands in producing a rich variety of magnetic structural topologies. Command over the interaction energy scales can also be achieved—large pillaring molecules, for example, can theoretically allow for the formation of quasi-low dimensional magnetic materials[224,225].

This low-dimensional behavior is exemplified by many metal-organic framework (MOF) materials containing a variety of coordinating ligands. Particular examples include the pyridyl- and benzenedicarboxylate-based MOFs, $Cu_3(CO_3)_2(x)_3{\cdot}2ClO_4$ (x = 1,2-bis(4-pyridyl)ethane and 1,2-bis(4-pyridyl)ethylene)[226] and Cu(1,3-bdc)[227,228], respectively, in which the large molecular groups pillar Cu-based Kagomé networks. These studies, however, highlight the complexity associated with the multi-atom superexchange pathways in molecular-based systems that can hinder attempts to favor particular types of spin interactions in MOFs. Indeed, despite Cu-Cu bridging geometries that are in accordance with antiferromagnetic interactions with respect to the Goodenough-Kanomari rules, ferromagnetic long range magnetic order develops in both materials, and the role of interlayer interactions in the ordering mechanism is yet to be concluded[226–228]. This is further complicated by their structural complexity as, for example, multiple symmetries have been reported for the $Cu_3(CO_3)_2(x)_3{\cdot}2ClO_4$ family of materials[226,229–231].

Given the highlighted complexities associated with the large bridging molecules in MOFs, simpler, shorter ligands can provide an intermediate avenue in which to pursue spin models in hybrid systems. Such simple ligands can include a range of molecules that have been experimentally demonstrated to host superexchange interactions such as in the thiocynate Cr^{3+}-based perovskite, $Cr[Bi(SCN)_6]{\cdot}xH_2O$[232], or the square lattice antiferromagnet Cu-formate, $Cu(DCOO)_2{\cdot}4D_2O$[233]. Similarly interesting are $(C_2O_4)^{2-}$ oxalate-based systems which can generate an abundance of low-dimensional geometries ranging honeycomb[234,235], triangular[93], and square lattice networks[236]. Of particular interest to this study is the $ATi(C_2O_4)_2{\cdot}xH_2O$ family of materials ($A^+ = (NH_4)^+$[237,238],

Na^{+} [239], K^{+} [240], and Cs^{+} [239]) which has been reported to adopt diamond- and square-planar magnetic sublattices of $S = 1/2$ Ti^{3+} ions which have yet to be examined for their magnetic properties.

Interest in the $S = 1/2$ frustrated square lattice (FSL) model stems from its rich magnetic phase diagram that depends on the dimensionality of the spin, the relative strength of the frustrating diagonal exchange interaction, J_2, in comparison to the nearest neighbor coupling, J_1, and the sign of these interactions. In the case of Heisenberg spins, the magnetic phase diagram presented in Fig. 5.1(a) describes diverse ordered magnetic ground states that neighbor quantum critical regimes between $0.4 \leq |J_2/J_1| \leq 0.6$ [43,241]. While the true nature of these ground states have yet to be conclusively established, the presence of a dynamic spin liquid ground state has been established in a variety of experimental realizations. Examples of this include the solid solution of $Sr_2Cu(Te_{1-x}W_x)O_6$ in which the chemical substitution of W^{6+} ions possibly, albeit in the presence of structural disorder [242], drives the system into the critical spin liquid regime of the FSL phase diagram [83]. Additionally, even in the limit of $J_2 = 0$, an inelastic neutron scattering study of $Cu(DCOO)_2 \cdot 4D_2O$ [233] suggests fractional excitations akin to those present in one-dimensional systems. New material realizations can hence help to explore the magnetic phase diagram of the FSL model and potentially even realize a disorder-free spin liquid state. Indeed, as shown by the extensive studies on the $S = 1/2$ V^{4+} system, $BaCdVO(PO_4)_2$ [241], a spin-nematic ground state has been found to manifest in the presence of an applied magnetic field which has led to new theoretical predictions for the FSL model [243,244].

Alternatively, the frustrated diamond lattice antiferromagnetic model (FDL) provides a means for accessing unconventional magnetic ground states in three-dimensions. In this bipartite structure, comprised of two interpenetrating face centered cubic sublattices (Fig. 5.1(b)), interactions between the same and different sublattices can generate frustration and produce degenerate ground states; beyond a critical point of $J_2/J_1 = 0.125$, where J_1

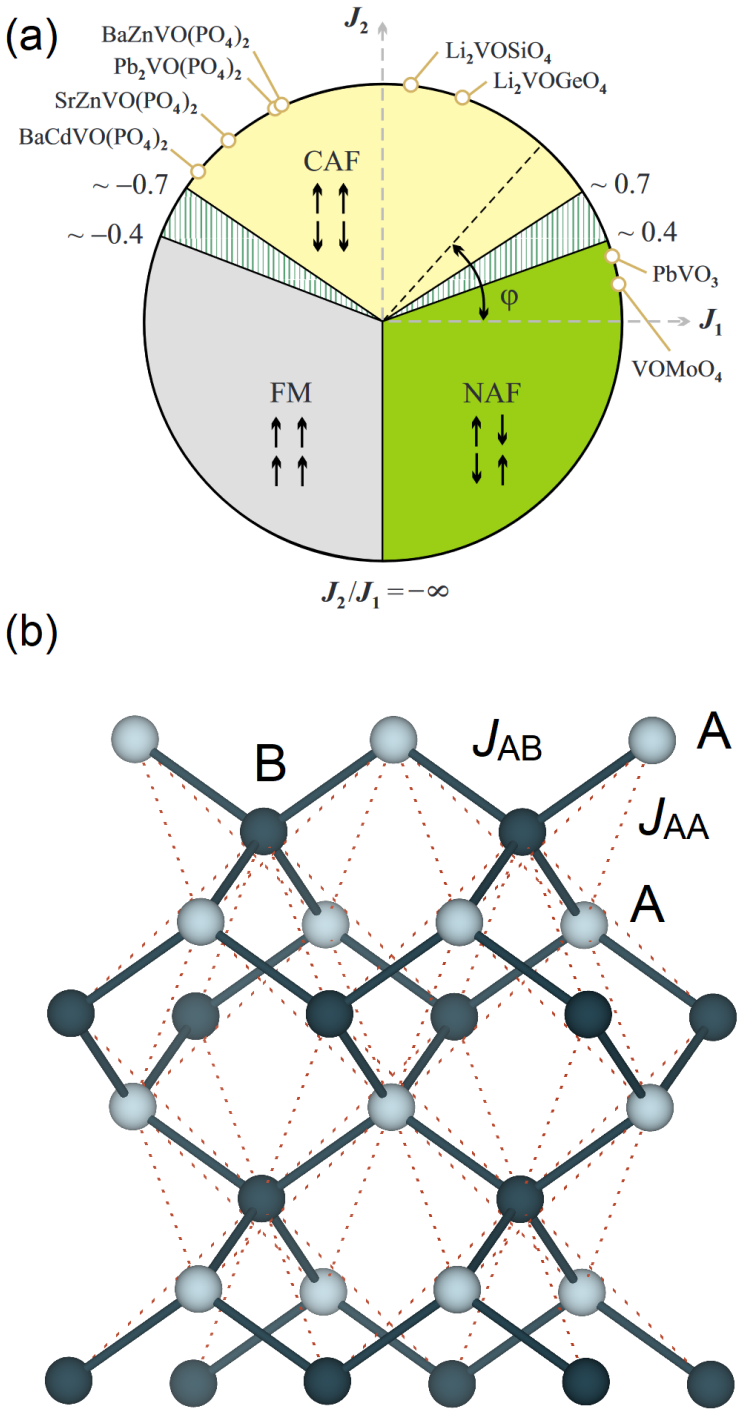

Figure 5.1: (a) Magnetic phase diagram of the $S = 1/2$ Heisenberg frustrated square lattice model including a nearest neighbor interaction, J_1, and a frustrating coupling across the diagonal of the square, J_2. CAF and NAF refer to canted- and Néel-ordered antiferromagnetic states, respectively. Figures adapted with permission from reference [241]; copyright APS 2008. (b) The two face centered cubic sublattices, highlighted by the different colored atoms, comprising the diamond lattice where solid bonds indicate nearest neighbor interactions and dotted bonds indicate frustrating couplings. Figure generated using the `VESTA` visualization software [26].

and J_2 denote nearest and next nearest-exchange interactions, respectively, the FDL model has been theorized to host a spiral spin-liquid ground state[245]. This dynamic behavior has been extensively studied in *A*-site spinels such as in $MnSc_2S_4$[246], $CuRh_2O_4$[247], and $CoAl_2O_4$[248,249], amongst others, where combined *ab-inito* and neutron scattering measurements confirm the role of a frustrating interaction in the development of spin-spiral ground states. Theoretical predictions for dynamic ground states beyond such spin spiral structures, including topological paramagnets, further expand the need for material realizations of the FDL model[250,251].

Whilst coordination framework material realizations of the FSL model have been previously investigated[233,252,253], the FDL model has yet to be examined in hybrid materials. This chapter presents an experimental and *ab-initio* study of the α and β psuedo-polymorphs of the $S = 1/2$ Ti^{3+} system, $KTi(C_2O_4)\cdot xH_2O$. The results presented here are published in Physical Review Materials[254]. Previous structural studies have identified $KTi(C_2O_4)\cdot 2H_2O$ (which will henceforth be dubbed β) as forming an oxalate bridged diamond-network of Ti^{3+} ions[237]. However, a structural study on the Na analogue of this compound, $NaTi(C_2O_4)\cdot xH_2O$, suggests a square-planar network of oxalate bridged Ti^{3+}-ions instead[239]. This will be called the α structure for the K-containing version discussed in this chapter. By analyzing a combination of single-crystal X-ray and neutron powder diffraction data alongside bulk property measurements, this chapter will show that these compounds are instead pseudo-polymorphs where α is a non-stoichiometric hydrate. The resulting models reveal that α and β pertain to the $S = 1/2$ Heisenberg square and diamond lattice antiferromagnet models, respectively. These results will be discussed in the context of *ab-initio* calculations which reveal the mechanism from which the difference in the observed magnetic exchange behavior across the pseudo-polymorphs stems.

5.2 Methods

5.2.1 Synthesis

The preparation of microcrystalline samples of α- and β-$KTi(C_2O_4)_2{\cdot}xH_2O$ followed revised versions of previously published methods[240,239]. These revisions were devised by Dr. Teng Li (University of St. Andrews) and Dr. Wenjiao Yao (Chinese Academy of Sciences). The molar ratios of the starting materials, K_2CO_3 (Sigma Aldrich, 99.99%), $H_2C_2O_4{\cdot}2H_2O$ (Sigma Aldrich, >99.5%), $TiCl_3$ (Sigma Aldrich, $\geq$ 12% $TiCl_3$ basis), and distilled water used were 1 : 3 : 5 : 227 and 2 : 6 : 1 : 1000 for α and β, respectively. In a typical reaction for either compound, a stirred aqueous solution of K_2CO_3 and $H_2C_2O_4{\cdot}2H_2O$ was heated in a round bottom flask to either 343 K (α) or 363 K (β) and sparged with N_2 gas for 1 hour to form an inert environment. The final orange (α) or maroon (β) colored polycrystalline product immediately formed upon introducing $TiCl_3$ into the solution. Microcrystalline samples were obtained when heating for an additional 30 minutes followed by an ice bath quench. The resulting samples were collected by vacuum filtration and washed with acetone to dissolve any impurity phases. Both time and temperature control were crucial for obtaining pure α samples as, if not quickly collected from the solution, α slowly recrystallized as β. Hence, β appears to be the thermodynamically stable product. Sample deuteration using D_2O was successful only for α. Both samples are stable for approximately one day when exposed to air, after which they quickly oxidize to form the anatase polymorph of TiO_2.

5.2.2 Diffraction

Neutron powder diffraction (NPD) data were collected by Mr. Lewis Farrar (University of Liverpool) and Dr. Katherine Tustain (University of Liverpool) at 1.8 K and 300 K on 2 g samples placed in vanadium-windowed flat plate containers on the HRPD diffractometer at the ISIS Neutron and Muon Source. At lower temperatures, NPD data were collected on the same 2 g samples placed in cylindrical vanadium canisters at 1.2 K and 15 K for α and 1.2 K and 35 K for β on the WISH diffractometer at the ISIS Neutron and Muon Source. Structural refinements were performed by the author using the `GSAS`[91] software package whereas the magnetic structure analysis utilized the `MAXMAGN`[156] and `FullProf`[90] suites.

Single crystal X-ray diffraction (SC-XRD) data were measured using Mo Kα radiation ($\lambda = 0.71013$ Å) on a Bruker D8 VENTURE diffractometer equipped with a PHOTON-II detector. Data were collected using ω-scans and reduced and integrated using the `APEX-III` software package. The structures were determined using `SHELLXT-2013`[255] and refinements were conducted using `SHELLXL-2013`[256] as applied in the `OLEX2`[257] software package. Initial structural models utilized previously published structures[239,240] and anisotropic displacement parameters were used to model all non-hydrogen atoms.

5.2.3 Magnetometry and Specific Heat

Temperature dependent magnetic susceptibility measurements were carried out on 13.21 mg and 38.09 mg samples of α and β, respectively, in applied fields of $H = 0.1$ T between 1.8 K and 300 K using both field-cooled and zero-field cooled protocols on a Quantum Design Magnetic Property Measurement System (MPMS3). Samples were placed in gelatin capsules, packed tightly with teflon tape, and placed in a plastic straw. No bifurcation

was observed between the zero field cooled and field cooled data, hence only the zero-field cooled data are presented here.

Specific heat measurements were carried out on pressed powder samples weighing 9.11 mg and 6.71 mg for α and β, respectively, in zero applied magnetic field between 1.8 K and 300 K on a Quantum Design Physical Property Measurement System (PPMS). Between 0.1 K and 1.8 K, measurements were carried on the same α sample using the DynaCool Quantum Design PPMS system equipped with a dilution fridge insert.

Tenth order high temperature series expansion calculations for both the FSL and FDL models were performed using the `HTE10`[76] code. When fitting using non-linear least squares regression, further neighbor coupling parameters were fixed in 0.01 increments of the leading exchange parameter of either model, J_1. A temperature independent background term, χ_0, was used, and its value was fixed to that obtained via Curie-Weiss fitting.

5.3 Square Lattice, α-$KTi(C_2O_4)_2{\cdot}xH_2O$

5.3.1 Crystal Structure

Rietveld analysis of single crystal X-ray diffraction data measured at 150 K confirms that the $I4/mcm$ structural model of α-$KTi(C_2O_4)_2{\cdot}xH_2O$ is isotypic with that which is predicted for the analogous compound, $NaTi(C_2O_4)_2{\cdot}xH_2O$[239]. The refined parameters are summarized in Table 5.1. Here, x highlights the possibility of an unconfirmed water-site structural disorder in $KTi(C_2O_4)_2{\cdot}xH_2O$[239]. To examine this, high-resolution neutron powder diffraction data were collected at 1.8 K and 300 K. The presence of the water site was first confirmed using Fourier difference maps, and refining the lattice parame-

ters, isotropic thermal parameters, and atomic positions of the SC-XRD model using a stoichiometric hydration level ($x = 2$) results in goodness-of-fit parameters $\chi^2 = 7.23$ and $R_p = 3.45\%$. A significant improvement to the fit was achieved when allowing the occupancy of the water site to vary; the goodness-of-fit parameters are reduced to $\chi^2 = 4.80$ and $R_p = 2.83\%$ (Fig. 5.3). The resulting model, which is summarized in Table 5.2 for data collected at 1.8 K, reveals a non-stoichiometric water occupancy of 0.37(1) that reflects a chemical formula of α-$KTi(C_2O_4)_2 \cdot 1.48(4)H_2O$. Allowing the occupancy parameters of the K^+ and Ti^{3+} ions to refine does not improve the quality of the fit ($\chi^2 = 7.13$ and $R_p = 3.23\%$) and results in a non-physical Ti^{3+} excess of 1.4(1)%.

The crystal structure of α can be described as a network of Ti^{3+} ions that are eight-coordinated by oxalate groups within the *ab*-plane (Figs. 5.2(a,b)). As depicted in Figs. 5.2(b,c), this configuration forms an unusual and perfect square antiprismatic geometry for the Ti^{3+} ions that are then psuedo-edge shared to form a square magnetic sublattice within the *ab*-plane. Hence, the most probable leading superexchange pathways are those highlighted in Fig. 5.2(b) with a nearest-neighbour interaction parameter, J_1, and another across the diagonal of the squares, J_2. Those correspond to Ti-Ti distances of 5.91(1) Å and 8.05(1) Å and superexchange pathways of Ti-C-O-C-Ti and Ti-C-O-C-Ti-C-O-C-Ti, respectively. Along the crystallographic *c*-axis, the square layers are separated by a disordered K^+ and H_2O containing layer with an interlayer distance of 7.36(1) Å, and correspond to an exchange parameter, $J_\perp$ (Fig. 5.2(d)). Finally, in the square antiprismatic geometry, the crystal field symmetry splits the degenerate *d* manifold into a low lying A_1 term and two higher energy E_2 and E_3 terms. Hence, the d_{z^2} orbital is expected to be the active magnetic orbital in the system.

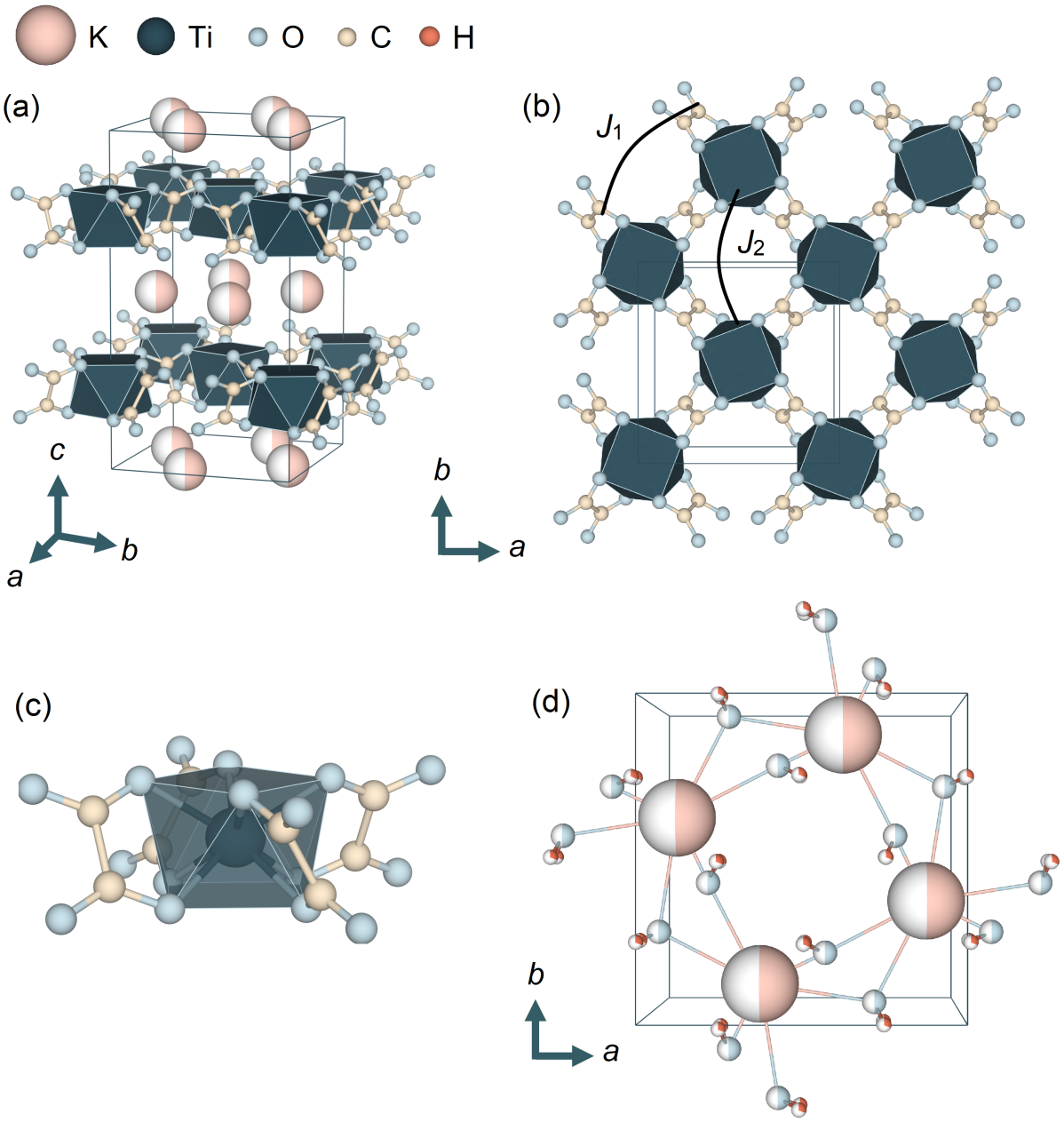

Figure 5.2: Tetragonal crystal structure of α-$KTi(C_2O_4)_2{\cdot}xH_2O$ as viewed along the (111) direction. (b) Square magnetic sublattice of α which is comprised comprised of square antiprismatic Ti^{3+} ions that are psuedo-edge shared through oxalate groups and separated along the crystallographic c-axis by a disordered K^+ and H_2O containing layer. The white color region of the spheres indicate the site occupancy. Figure generated using the `VESTA` visualization software[26].

Table 5.1: Structural parameters of α-$KTi(C_2O_4)_2{\cdot}2H_2O$ obtained from single-crystal X-ray diffraction data measured at 150 K.

Compound	α-$KTi(C_2O_4)_2{\cdot}2H_2O$
Crystal System	Tetragonal
Space Group	$I4/mcm$
a /Å	8.0401(4)
b /Å	8.0401(4)
c /Å	14.850(1)
α, β, γ	90°
V /Å	960.0(1)
Z	8
Crystal size /mm^3	0.07 × 0.07 × 0.03
Color	Orange
ρ /g cm^{-3}	2.069
F(000) /mm^3	596.0
Reflections collected /mm^3	3279
Independent reflections	281 [$R_{\text{int}} = 0.0614$, $R_\sigma = 0.0252$]
Goodness-of-fit on F^2	1.091
Final R indexes [I>=2σ(I)]	$R_1 = 0.0453$, $wR_2 = 0.1112$

Table 5.2: Atomic positions, occupancies, and isotropic displacement parameters of α-$KTi(C_2O_4)_2{\cdot}1.48(2)H_2O$ obtained through Rietveld refinement of the $I4/mcm$ model using powder neutron diffraction data measured at 1.8 K on the HRPD diffractometer. The resulting unit cell parameters are $a = b = 8.0440(6)$ Å and $c = 14.720(1)$ Å with goodness-of-fit parameters $\chi^2 = 4.80$ and $R_{\text{p}} = 2.83\%$.

Atom	x	y	z	$Occ.$	U_{iso}(Å^2)
Ti	0	0	$\frac{1}{4}$	1.0	0.009(4)
K	0.1266(7)	0.6266(7)	0	0.5	0.014(1)
O1	0.2100(1)	0.0940(1)	0.17287(7)	1.0	0.0065(2)
O2	0.0735(6)	0.2882(6)	0	0.37(1)	0.025(2)
C1	0.2170(1)	0.7170(1)	0.20541(8)	1.0	0.0063(3)
D	0.0104(5)	0.2540(8)	0.0505(4)	0.37(1)	0.037(6)

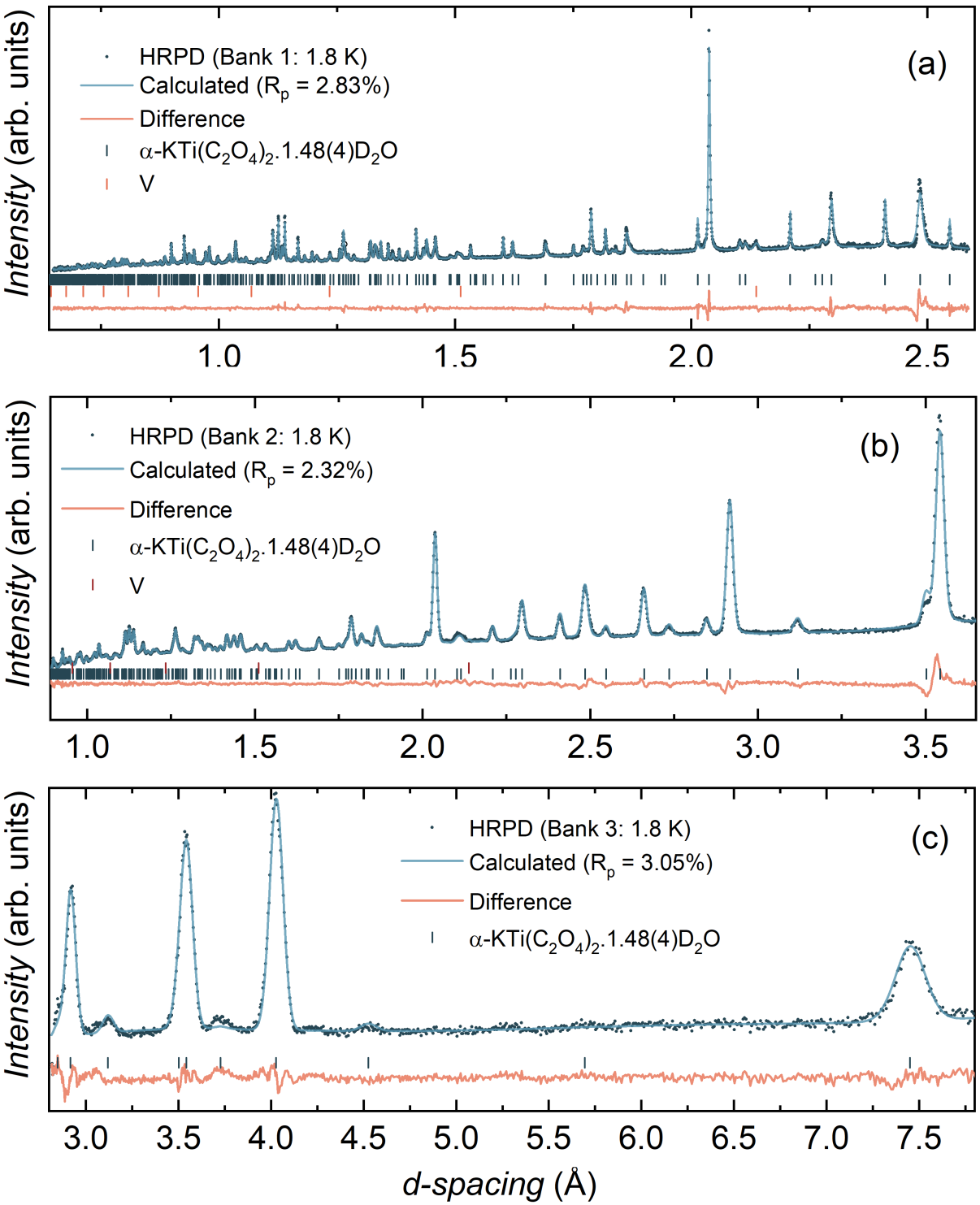

Figure 5.3: (a-c) Rietveld analysis of powder neutron diffraction data using the $I4/mcm$ structural model describing the crystal structure of α-$KTi(C_2O_4)_2 \cdot 1.48(4)H_2O$ with global goodness-of-fit parameters $\chi^2 = 4.8$ and $R_p = 2.83\%$. Data were collected at 1.8 K on the HRPD diffractometer at the ISIS Neutron and Muon Source.

5.3.2 Magnetometry and Specific Heat

The zero-field cooled temperature-dependent magnetic susceptibility, χ_{m}, measured in an applied field of 0.1 T is shown in Fig. 5.4(a,b). Fitting $\chi_{\mathrm{m}}(T)$ to the Curie-Weiss model (CW) while varying the minimum fitting temperature, T_{min}, between 20–200 K reveals that the model parameters are consistent for $T_{\mathrm{min}} > 45$ K (Fig. A.8). When using $T_{\mathrm{min}} = 45\ K$, $\chi_{\mathrm{m}}(T)$ follows CW behavior with model parameters $\theta_{\mathrm{CW}} = -8.13(1)$ K, $C = 0.233(1)$ emu K mol^{-1}, $g = 1.57(1)$, $\mu_{\mathrm{eff}} = 1.36(1)$ μ_{B}, and $\chi_0 = 1.19(2) \times 10^{-4}$ emu mol^{-1}. The resulting model reflects dominant antiferromagnetic interactions and an effective moment that is reduced from its expected spin-only value, $g\sqrt{S(S+1)} = 1.73$ μ_{B}, for a $S = 1/2$ system. While such a reduction is generally associated with an orbital contribution in a d^1 system, no orbital degeneracy arises in the ground state of a perfect square antiprismatic geometry, which is delocalized by a lone d_{z^2} orbital. This is confirmed by electronic structural calculations that reveal no contribution from any orbitally excited states (Sec.5.5). Hence, and as seen in other Ti^{3+}-containing materials[121,109,120], the reduction most likely stems from the presence of a diamagnetic anatase impurity which forms due to the instability of Ti^{3+} in air. Similarly, it could also be associated with a data normalization issue given the non-stoichiometric water content of the compound. Otherwise, upon cooling, the development of short-range correlations is suggested by a broad feature centered around 6 K. As seen in Fig. 5.4(c), a similarly broad feature is observed in the zero-field temperature dependent specific heat, C_{p}, albeit at a lower temperature of 3 K, as usually seen for low dimensional materials[258]. The onset of long range magnetic order then follows at a temperature of $T_{\mathrm{N}} \simeq 2$ K as evidenced by a sharper anomaly in C_{p}/T(T).

To estimate the leading magnetic exchange parameters, a 10^{th} order high temperature series expansion (HTE) calculation of the Heisenberg FSL model with a nearest neighbor exchange, J_1, a frustrating further neighbor exchange J_2, and an interplanar coupling, $J_\perp$,

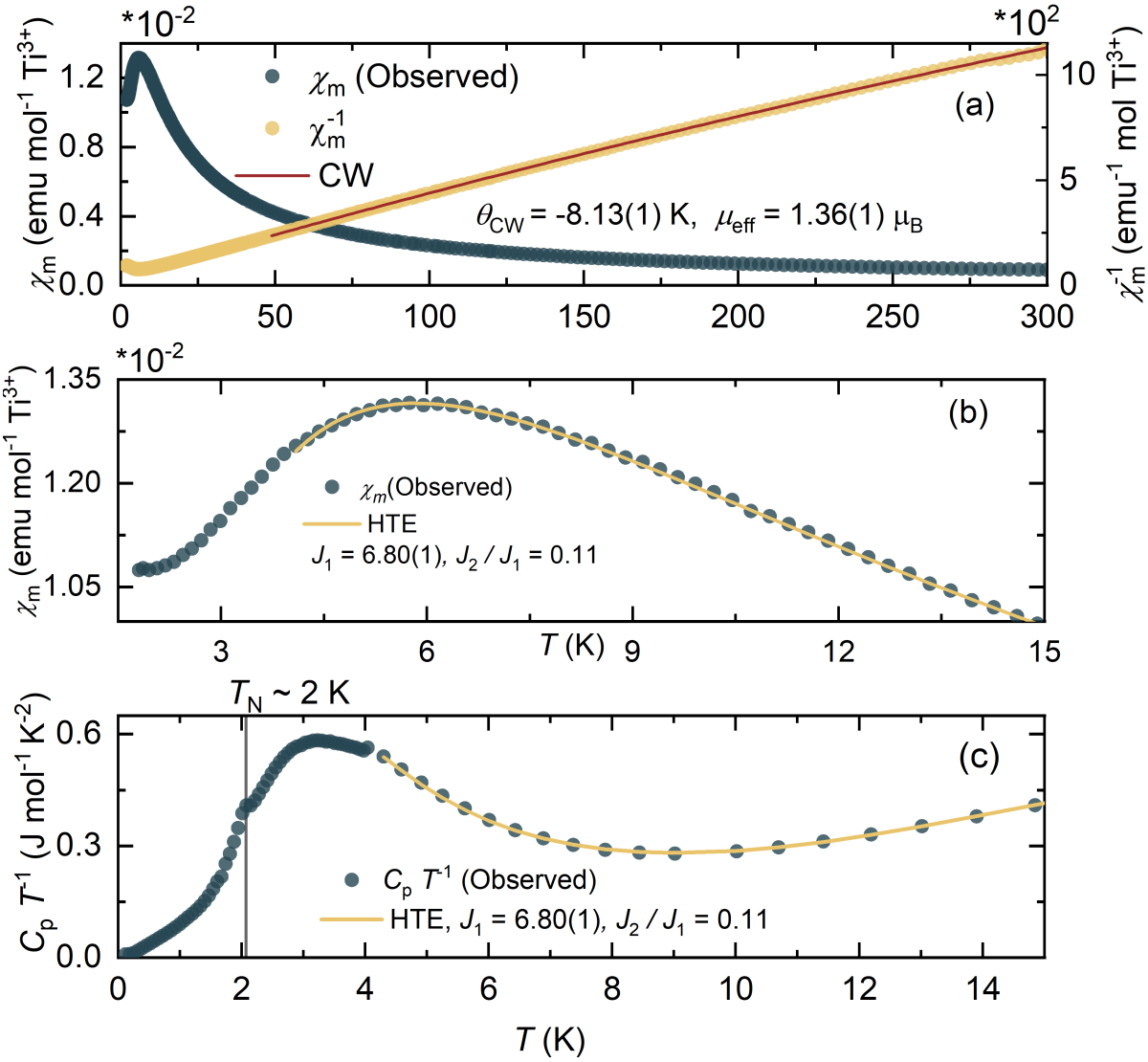

Figure 5.4: (a) Zero-field cooled temperature dependent magnetic susceptibility measured at 0.1 T. Above 45 K, $\chi_{\rm m}^{-1}$(T) is well described by the Curie-Weiss model with parameters $\theta_{\rm CW} = -7.86(1)$ K, $C = 0.233(1)$ emu K mol^{-1} ($g = 1.57(1)$), $\mu_{\rm eff} = 1.36(1)$ $\mu_{\rm B}$, and $\chi_0 = 1.19(2) \times 10^{-4}$ emu mol^{-1}. (b) Estimating the leading magnetic exchange interactions by simultaneously fitting both the magnetic susceptibility and (c) zero-field specific heat to a high temperature series sexpansion of the $S = 1/2$ Heisenberg square lattice antiferromagnet model above 7 K yields a dominant $J_1 = 6.80(1)$ K ($g = 1.61$), a further neighbor interaction, $J_2/J_1 = 0.11$, and no interplanar coupling, $J_\perp = 0$. The onset of long range magnetic order is highlighted by an anomaly centered around 2 K in the specific heat.

was performed using the `HTE10` code[76]. To constrain the model parameters, a simultaneous fitting procedure including $\chi_{\mathrm{m}}(T)$ and C_{p}(T) above 7 K and 5 K, respectively, was used. The phonon contribution to the specific heat was estimated using the phenomenological expression $C_{\mathrm{p}} = \alpha T^3 + \beta T^5 + \gamma T^7$, as has been applied for similar coordination framework materials[259,260]. Consistent with the expected d_{z^2} active magnetic orbital, the resulting minimal model yields a dominant antiferromagnetic $J_1 = 6.80(1)$ K ($g = 1.61$), minimal frustration with $J_2/J_1 = 0.11$, and no interplanar coupling $J_\perp = 0$. A small $J_\perp/J_1 \simeq 5 \times 10^{-3}$ is also suggested when applying the empirical expression relating T_{N} to $J_\perp$[261], $J_\perp = J_1 \exp(b - 4\pi\rho/T_{\mathrm{N}})$, calculated for two-dimensional systems. Here, $b = 2.43$ and $\rho/J_1 = 0.183$. Finally, as discussed through electronic structural calculations, regardless of the model used to describe the disordered K^+ and H_2O containing layer, the magnetic ground state and interplane exchange do not vary. The overall model hence suggests that α lies within the Néel ordered regime of the FSL phase diagram[43].

5.3.3 Magnetic Structure

To examine the long-range magnetic order in α, NPD data were collected well within the magnetically ordered state at 1.2 K and within the paramagnetic regime at 15 K. At 15 K, refining all atomic positions, lattice parameters, and isotropic thermal parameters, while fixing the 0.37(1) occupancy of the disordered D_2O site, results in the model depicted in Fig. 5.5 and the parameters shown in Table 5.3. For the 1.2 K refinement, all structural and instrumental parameters, except for the lattice parameters, were constrained to their values at 15 K to refine the magnetic only scattering.

Subtracting the 1.2 K data from the 15 K one reveals two magnetic Bragg peaks at forbidden nuclear positions for the $I4/mcm$ space group that are indexed using the commensurate propagation vector $\kappa = (0, 0, 0)$. Symmetry analysis using `BasiReps`[90] and `MAXMAGN`[156] results in four irreducible representations, $m\Gamma_{3+}$, $m\Gamma_{3-}$, $m\Gamma_{5+}$ and $m\Gamma_{5-}$ in

Table 5.3: Structural parameters of α-$KTi(C_2O_4)_2 \cdot 1.48H_2O$ as obtained through Rietveld refinement of the $I4/mcm$ model using powder neutron diffraction data measured at 15 K on the WISH diffractometer. The resulting unit cell parameters are $a = b = 8.047(1)$ Å and $c = 14.76(3)$ Å with goodness-of-fit parameters $\chi^2 = 6.88$ and $R_p = 2.48\%$.

Atom	x	y	z	$Occ.$	U_{iso}(Å^2)
Ti	0	0	$\frac{1}{4}$	1.0	0.008(5)
K	0.122(1)	0.621(1)	0	0.5	0.017(1)
O1	0.2112(3)	0.0961(3)	0.1717(2)	1.0	0.01(3)
O2	0.0594(9)	0.2782(9)	0	0.37	0.01(3)
C1	0.2166(2)	0.7166(2)	0.2069(2)	1.0	0.01(1)
D	0.011(2)	0.259(2)	0.050(2)	0.37	0.066(3)

Miller-Love notation[157], that are compatible with κ and the crystal symmetry. When refining these models, only the $I4/m'cm$ magnetic space group, in Belov-Neronova-Smirnova notation[97], which corresponds to the $m\Gamma_{3-}$ irreducible representation is compatible with the data, and results in goodness-of-fit parameters $\chi^2 = 1.81$ and $R_{mag} = 3.16\%$ (Fig. 5.6(a)).

The resulting Néel ordered magnetic structure is depicted in Fig. 5.6(b); the magnetic moments are aligned along the crystallographic c-axis. This is consistent with the high-temperature series expansion model parameters that place α within the Néel ordered regime of the FSL phase diagram. The extracted ordered magnetic moment, $\mu_{ord} = 0.62(3)$ μ_B, similarly suggests two-dimensional interactions as it is concomitant with the expected 0.6 μ_B moment for a Heisenberg square lattice antiferromagnet without frustration[262,263], as well as related materials pertaining to the same model[264,265].

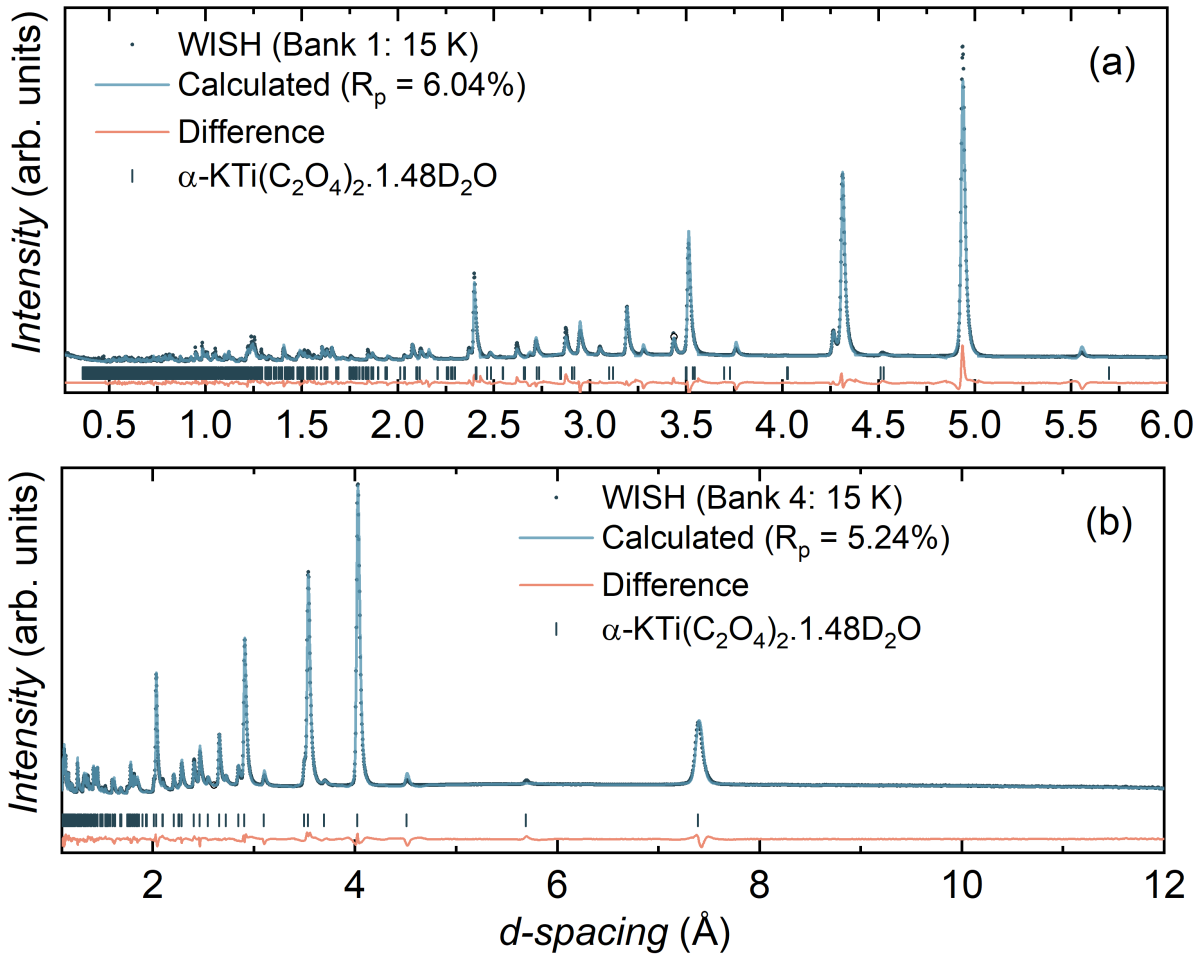

Figure 5.5: (a,b) Rietveld analysis of powder neutron diffraction data using the $I4/mcm$ structural model describing the crystal structure of α-$KTi(C_2O_4)_2 \cdot 1.48H_2O$ with global goodness-of-fit parameters $\chi^2 = 6.88$ and $R_p = 2.48\%$. Data were collected at 15 K on the WISH diffractometer at the ISIS Neutron and Muon Source, and two of the five banks are shown here.

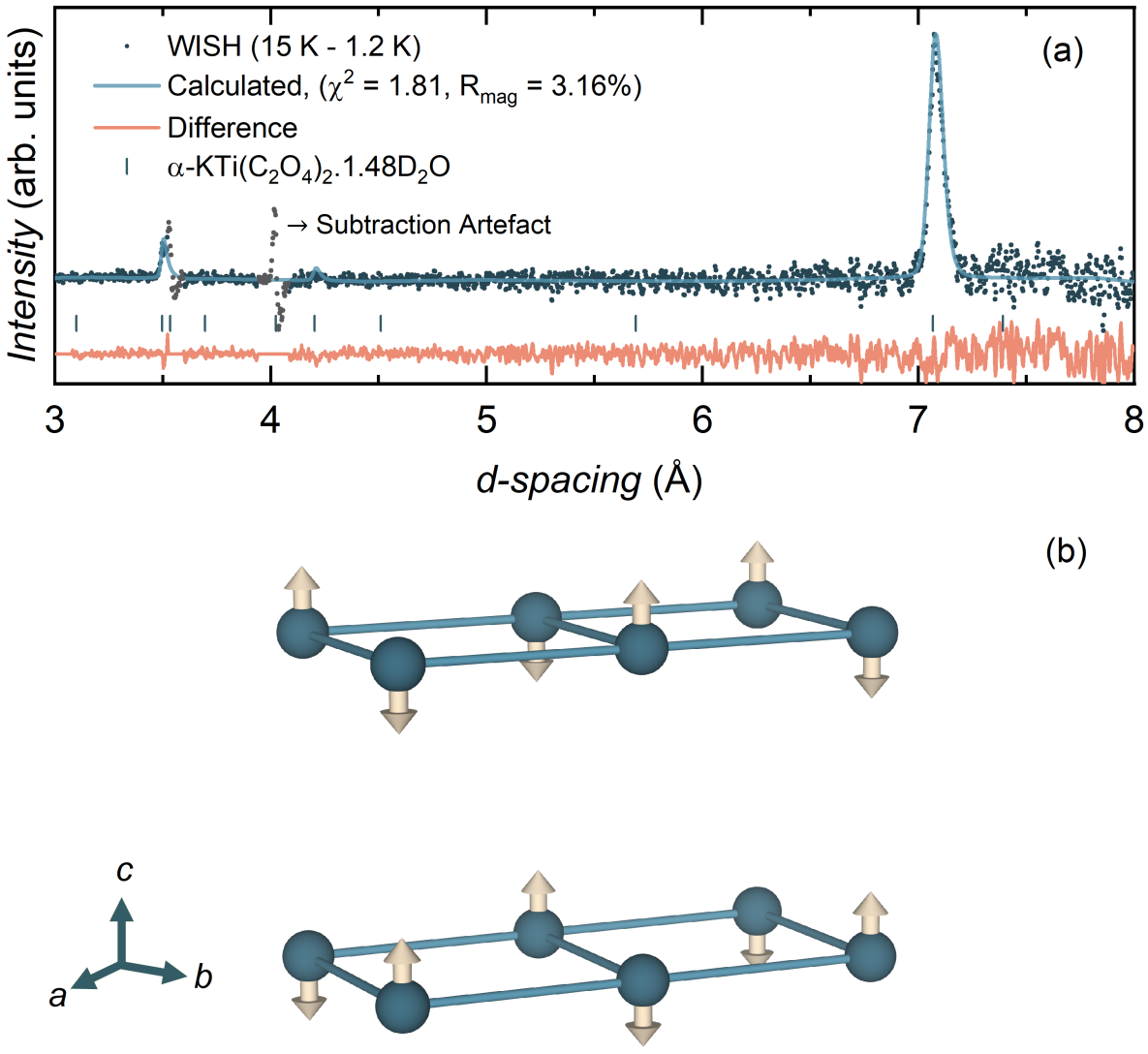

Figure 5.6: (a) Rietveld analysis of magnetic-only scattering using the $I4/m'cm$ magnetic space group model with an ordered moment of $\mu_{\mathrm{ord}} = 0.62(3)$ μ_{B}. (b) Antiferromagnetic structure of α-$KTi(C_2O_4)_2{\cdot}xH_2O$ where the moments align along the crystallographic c-axis.

5.4 Diamond Lattice, β-$KTi(C_2O_4)_2{\cdot}2H_2O$

5.4.1 Crystal Structure

Analysis of SC-XRD data confirms that the chiral $P6_222$ space group, previously suggested for the isotypic analogous compound $(NH_4)Ti(C_2O_4)_2{\cdot}2H_2O$, describes the symmetry of β-$KTi(C_2O_4)_2{\cdot}2H_2O$[237] (Table 5.4). The chirality is confirmed by previous studies on $(NH_4)Ti(C_2O_4)_2{\cdot}2H_2O$ which report either the $P6_222$[237] space group or its enantiomer, $P6_422$[238], for different single crystals. As shown in Fig. 5.8, Rietveld analysis of NPD data collected on the HRPD diffractometer using the SC-XRD model, whereby all lattice parameters, atomic positions, and isotropic thermal parameters are refined, confirms the validity of the $P6_222$ model at 1.8 K with goodness-of-fit parameters $\chi^2 = 3.10$ and $R_p = 1.82\%$. The resulting model is summarized in Table 5.2, and as powder samples are comprised of a racemic mixture of both enantiomorphic space groups, NPD cannot differentiate between the two[266].

The crystal structure of β is shown in Fig. 5.7; the Ti^{3+} polyhedra form a diamond-like network where Ti^{3+} ions are eight-coordinated by $(C_2O_4)^{2-}$ groups. Unlike in α, the Ti^{3+} square antiprismatic coordination geometry is slightly distorted through the presence of two unique oxalate groups such that the resulting bond distances are $d_{\text{Ti-O2}} = 2.257(2)$ Å and $d_{\text{Ti-O3}} = 2.125(2)$ Å (Fig. 5.7(b)). As shown in Figs. 5.7(a,c), the K^+ ions form a pillar-like structure along the crystallographic c-axis and are eight-coordinated by equal numbers of oxalate and water groups. The most probable superexchange mechanism runs along the Ti-O-C-O-Ti pathway with a nearest neighbor Ti-Ti distance of 5.72(1) Å corresponding to the exchange parameter, J_1. Frustration, through further neighbor interactions, however, is known to commonly arise in diamond-like magnetic sublattices[248,246] through further neighbor interactions as seen in Fig. 5.1(b). Those

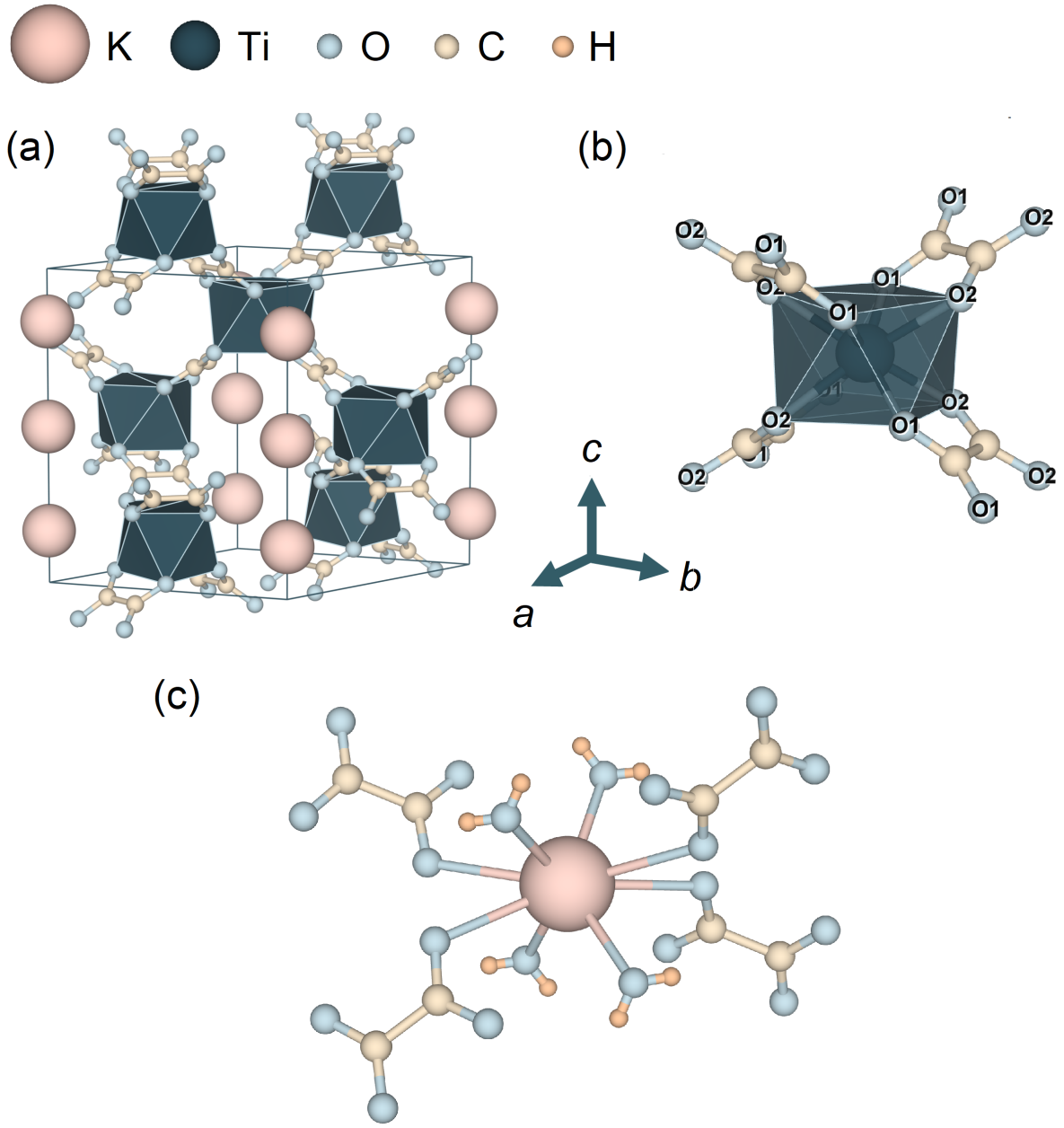

Figure 5.7: Hexagonal crystal structure of β-$KTi(C_2O_4)_2{\cdot}2H_2O$ as viewed along the (111) direction where (b) distorted square antiprismatic Ti^{3+} ions that are psuedo-edge shared through oxalate groups to form a diamond-like magnetic sublattice. (c) The coordination geometry of the K^+ ions and H_2O groups. Figure generated using the `VESTA` visualization software[26].

Table 5.4: Structural parameters of β-$KTi(C_2O_4)_2{\cdot}2H_2O$ obtained from single-crystal X-ray diffraction data measured at 150 K.

Compound	β-$KTi(C_2O_4)_2{\cdot}2H_2O$
Crystal System	Hexagonal
Space Group	$P6_222$ (or $P6_422$)
a /Å	8.7926(4)
b /Å	8.7926(4)
c /Å	11.125(1)
α, β	90°
γ	120°
V /Å	744.82(8)
Z	3
Crystal size /mm^3	0.12 × 0.06 × 0.05
Color	Maroon
ρ /g cm^{-3}	2.000
F(000) /mm^3	447.0
Reflections collected /mm^3	5932
Independent reflections	512 [$R_{\text{int}} = 0.0432$, $R_\sigma = 0.0186$]
Goodness-of-fit on F^2	1.087
Final R indexes [I>=2σ(I)]	$R_1 = 0.0214$, $wR_2 = 0.0509$

will be denoted J_2, J_3, and J_4 and correspond to Ti-Ti distances of 8.46(2) Å, 8.63(1) Å, 8.78(3) Å, respectively.

5.4.2 Magnetometry and Specific Heat

The zero-field cooled temperature dependent magnetic susceptibility $\chi_{\text{m}}(T)$ as measured in an applied field of 0.1 T is shown in Fig. 5.9. Varying the minimum temperature, T_{min}, used to fit the Curie-Weiss model between 50 K and 200 K reveals that the model parameters are most consistent above 180 K (Fig. A.9). When choosing $T_{\text{min}} = 180$ K, $\chi_{\text{m}}(T)$ follows CW behavior with model parameters $\theta_{\text{CW}} = -72.4(1)$ K, $C = 0.271(1)$ emu K mol^{-1}

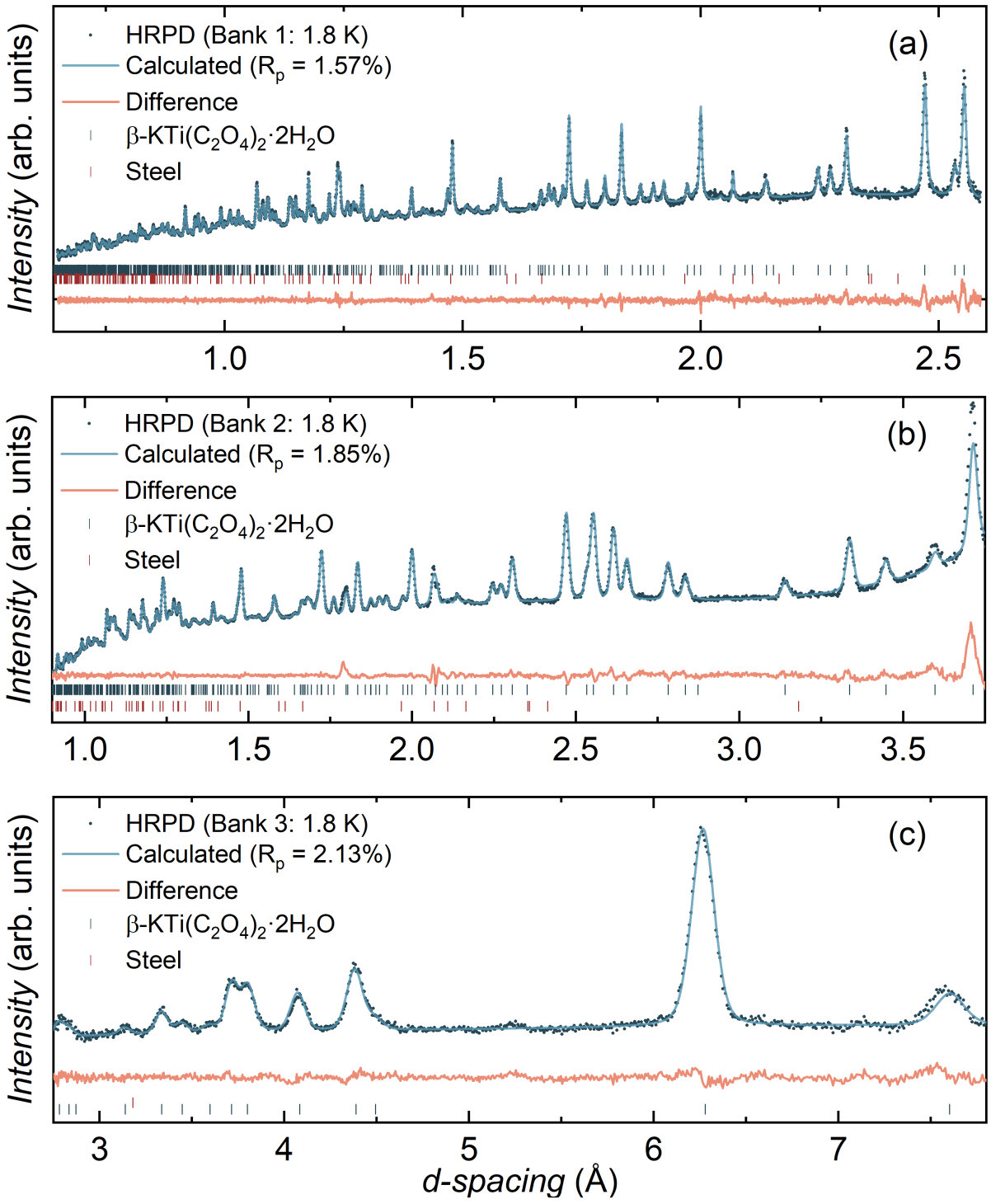

Figure 5.8: (a-c) Rietveld analysis of powder neutron diffraction data using the $P6_222$ structural model describing the crystal structure of β-$KTi(C_2O_4)_2 \cdot 2H_2O$ with global goodness-of-fit parameters $\chi^2 = 3.10$ and $R_p = 1.82\%$. Data were collected at 1.8 K on the HRPD diffractometer at the ISIS Neutron and Muon Source.

Table 5.5: Structural parameters of β-$KTi(C_2O_4)_2{\cdot}2H_2O$ obtained through Rietveld refinement of the $P6_222$ model using powder neutron diffraction data measured at 1.8 K on the HRPD diffractometer. The resulting unit cell parameters are $a = b = 8.778(1)$ Å and $c = 11.141(2)$ Å with goodness-of-fit parameters $\chi^2 = 3.10$ and $R_p = 1.82\%$.

Atom	x	y	z	U_{iso}(Å^2)
Ti	$\frac{1}{2}$	1	$\frac{1}{2}$	0.0012(6)
K	1	1	$\frac{1}{2}$	0.0019(2)
O1	0.2658(2)	0.9210(1)	0.4002(1)	0.0068(2)
O2	0.4495(2)	0.7614(4)	0.3923(1)	0.0063(2)
O3	0.7658(1)	0.7658(3)	$\frac{1}{3}$	0.0093(2)
C1	0.2095(1)	0.7905(1)	$\frac{1}{3}$	0.0055(5)
C2	0.3084(3)	0.6916(1)	$\frac{1}{3}$	0.0050(5)
H	0.7488(5)	0.6572(4)	0.3154(3)	0.0330(9)

($g = 1.70(1)$), $\mu_{eff} = 1.46(1)$ μ_B, and $\chi_0 = -5.8(2) \times 10^{-5}$ emu mol^{-1}. The resulting model is consistent with dominant antiferromagnetic interactions, an order of magnitude larger than those in α (Sec.5.3.2), and an effective moment that is similarly reduced from its full $S = 1/2$ value of 1.73 μ_B. The temperature independent background term, χ_0, most likely reflects the core diamagnetism of the material alongside the plastic sample container. Upon cooling, a broad feature, centered about 40 K, suggests the development of short-range correlations. The onset of long-range magnetic order is then evidenced by an inflection point, similarly present as an anomaly in the zero-field measured specific heat, at an ordering temperature of $T_N = 28$ K (Fig. 5.9(c)).

To extract the leading magnetic exchange parameters, a tenth-order high temperature series expansion of the $S = 1/2$ Heisenberg diamond lattice antiferromagnet model was calculated using the `HTE10` code[76]. Using a similar simultaneous fitting procedure as in α (Sec.5.3.2) with a minimum fitting temperature of 60 K and $\chi_0 = -5.8(2) \times 10^{-5}$ emu mol^{-1} (from the CW model) results in an antiferromagnetic nearest neighbor exchange parameter, $J_1 = 54.4(1)$ K (Fig. 5.9(b,c)). This is consistent with the predicted $T_N/J_1 \simeq 0.53$[245] for the $S = 1/2$ Heisenberg diamond lattice where $T_N/J_1 \simeq 0.51$ is obtained for β. The

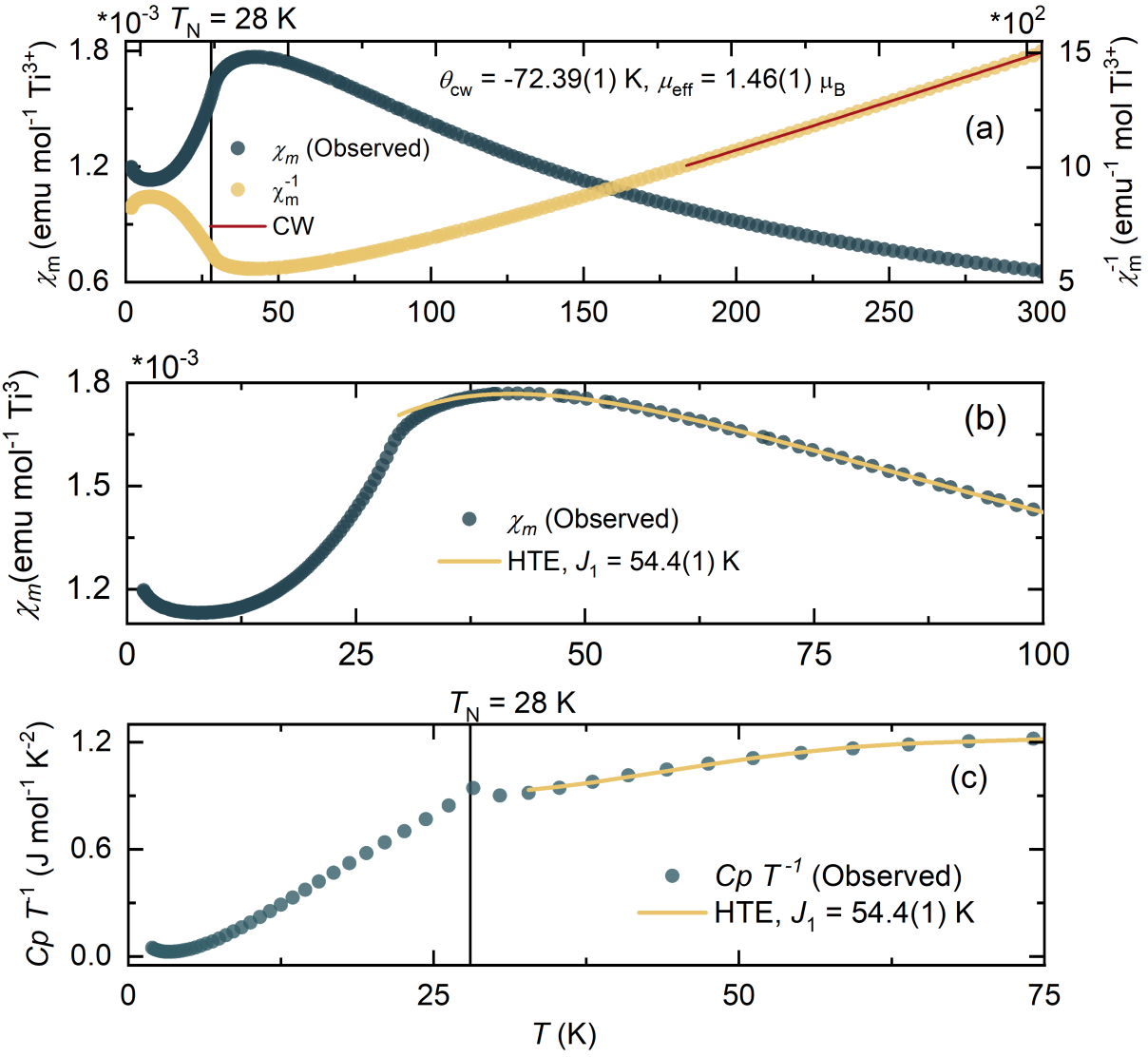

Figure 5.9: (a) Zero-field cooled temperature dependent magnetic susceptibility measured at 0.1 T. Above 180 K, χ_{m}^{-1}(T) is well described by the Curie-Weiss model with parameters $\theta_{\mathrm{CW}} = -72.4(1)$ K, $C = 0.271(1)$ emu K mol^{-1} ($g = 1.70(1)$), $\mu_{\mathrm{eff}} = 1.46(1)$ μ_{B}, and $\chi_0 = -5.8(2) \times 10^{-5}$ emu mol^{-1}. (b) The leading magnetic exchange interaction was estimated by simultaneously fitting both the magnetic susceptibility and (c) zero-field specific heat to a high temperature series expansion of the $S = 1/2$ Heisenberg diamond lattice antiferromagnet model above 60 K. An antiferromagnetic nearest neighbor interaction, $J_1 = 54.4(1)$ K, was found. Long range magnetic order is reflected by anomalies centered about 28 K in both χ_{m} and C_{p}.

energy scale of any further neighbor interaction parameters was also examined using a similar fitting procedure for the tenth-order HTE of the $S = 1/2$ FDL model with the four exchange parameters described in Sec.5.4.1. The resulting model, $J_2 \simeq J_3 \simeq J_4 = 0.03J_1$, revealed minimal frustration and results in parameters that are too small to accurately approximate using a HTE approach. Hence, when considering the magnetic phase diagram of the $S = 1/2$ FDL model[267], β most likely belongs to the non-frustrated Néel ordered regime.

5.4.3 Magnetic Structure

To investigate the nature of the magnetic ordered state below the anomaly observed at $T_N = 28$ K, neutron powder diffraction data were collected on a protonated sample of β on the WISH diffractometer at 1.2 K and 35 K. As shown in Fig. 5.10, and as summarized in Table 5.6, Rietveld analysis, where all atomic positions, lattice parameters, and isotropic thermal parameters were allowed to vary, confirms that β adopts the chiral $P6_222$ structure at 35 K. At 1.2 K, only the lattice parameters were refined, with all instrumental and atomic positions fixed to their values at 35 K. Subtracting the data collected in the paramagnetic state from that collected at 1.2 K reveals three peaks corresponding to the $(2\bar{1}0)$, (100), and (001) magnetic Bragg reflections, that can all be indexed with the commensurate propagation vector, $\kappa = (0, 0, 1/2)$ (Fig. 5.11). Symmetry analysis using the `ISODISTORT`[101] and `SARAh`[99] software packages yields five possible irreducible representations—mA_1, mA_3, mA_4, mA_5, and mA_6 in Miller-Love notation[157]—that are compatible with the paramagnetic symmetry and the propagation vector. Of these, only the mA_6 representation allows for the presence of the experimentally observed $(00l)$ reflections. Hence, the P_b2_1 magnetic space group (in Belov-Neronova-Smirnova notation[97]) that belongs to the mA_6 representation was used to model the data and results in goodness-of-fit parameters $\chi^2 = 3.91$ and $R_{mag} = 1.93\%$. The extracted ordered

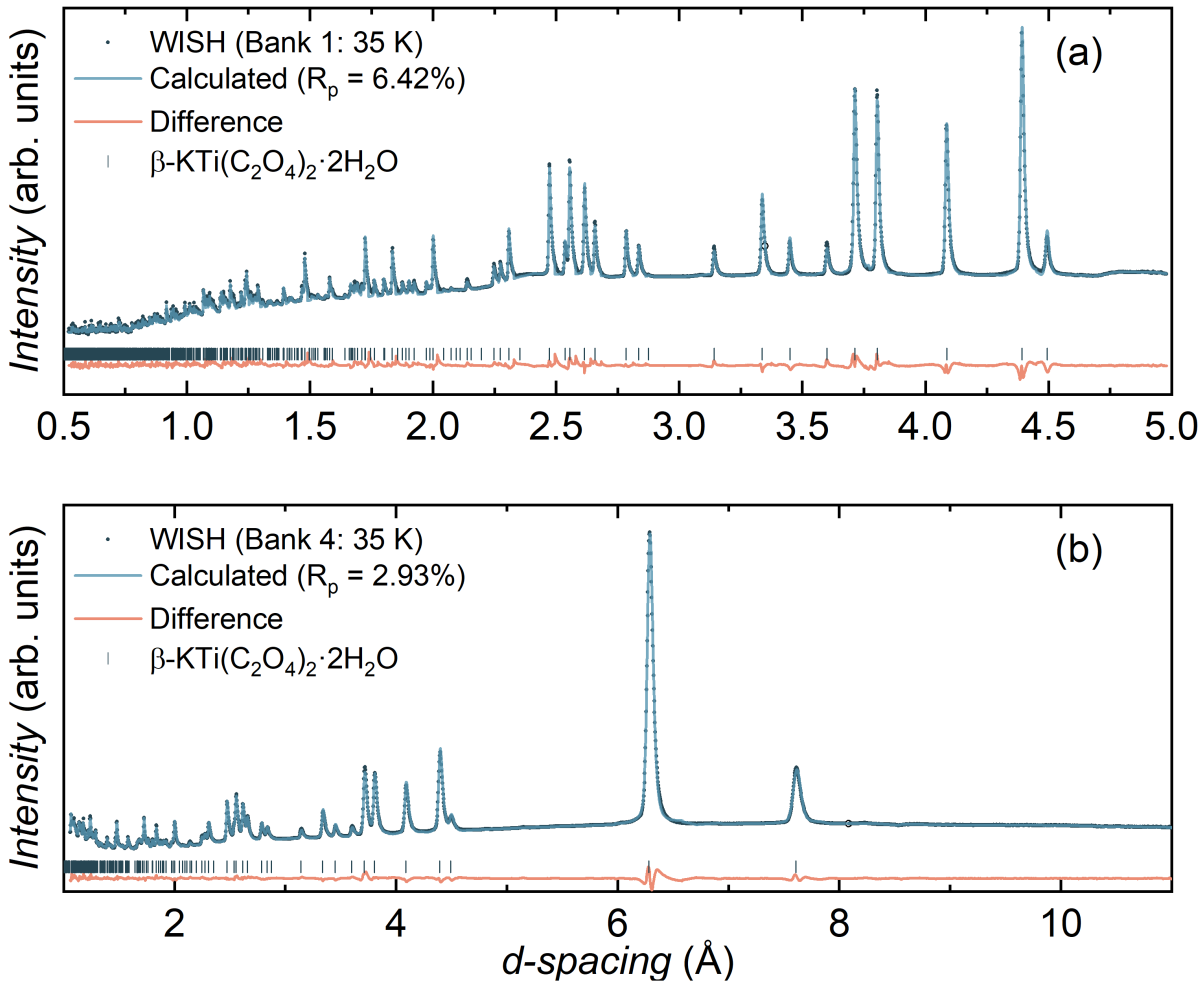

Figure 5.10: (a,b) Rietveld analysis of powder neutron diffraction data using the $P6_222$ structural model describing the crystal structure of β-$KTi(C_2O_4)_2 \cdot 2H_2O$ with global goodness-of-fit parameters $\chi^2 = 2.56$ and $R_p = 4.93\%$. Data were collected at 35 K on the WISH diffractometer at the ISIS Neutron and Muon Source.

moment, $\mu_{ord} = 0.79(2)$ μ_B, is consistent with the theoretically calculated moment of 0.76 μ_B [245] for the $S = 1/2$ Heisenberg diamond lattice antiferromagnet model and with the $gS \simeq 0.85$ μ_B obtained from fits to $\chi_m(T)$.

However, a unique direction for the ordered moment within the *ab*-plane could not be conclusively identified as the strongest reflection, corresponding to the (100) peak at ≈ 7.2 Å, is insensitive to the moment direction within the plane. Even if single crystals were available, the lowering of the parent paramagnetic $P6_2221'$ symmetry into the P_b2_1 magnetic space group that results in the formation of 12 domains. Hence, a conclusive

Table 5.6: Structural parameters of β-$KTi(C_2O_4)_2{\cdot}2H_2O$ as obtained through Rietveld refinement of the $P6_222$ model using powder neutron diffraction data measured at 35 K on the WISH diffractometer. The resulting unit cell parameters are $a = b = 8.812(4)$ Å and $c = 11.26(4)$ Å with goodness-of-fit parameters $\chi^2 = 2.56$ and $R_p = 4.93\%$.

Atom	x	y	z	U_{iso}(Å^2)
Ti	$\frac{1}{2}$	1	$\frac{1}{2}$	0.002(2)
K	1	1	$\frac{1}{2}$	0.003(2)
O1	0.2685(5)	0.9226(5)	0.3987(3)	0.009(2)
O2	0.4539(6)	0.7632(6)	0.3907(3)	0.009(2)
O3	0.7587(7)	0.7587(7)	$\frac{1}{3}$	0.009(2)
C1	0.2096(4)	0.7904(4)	$\frac{1}{3}$	0.008(3)
C2	0.3093(3)	0.6907(3)	$\frac{1}{3}$	0.008(3)
H	0.7518(7)	0.6514(7)	0.3152(5)	0.05(3)

determination of the moment direction will be difficult. One possible representation for the resulting magnetic model, where the nearest neighbor moments align antiferromagnetically and are constrained within the ab-plane, is shown in Figs. 5.11(b,c). Regardless, the resulting model is broadly consistent with the predicted Néel order and places β-$KTi(C_2O_4)_2{\cdot}2H_2O$ within the non-frustrated region of the magnetic phase diagram of the $S = 1/2$ Heisenberg FDL model.

5.5 Ground State: Electronic Structural Calculations

One of the interesting differences between the α and β pseudo-polymorphs is the order of magnitude difference in the magnetic exchange energy scales between the systems. To examine the source of this difference, fully relativistic density functional theory calculations were performed by Prof. Alexander Tsirlin at the University of Leipzig. Here, the Perdew-Wang approximation of the exchange correlation potential[268], as applied on the `FPLO`[142] code, was used. Given the K^+ and H_2O structural disorder in α, three models were used to approximate an ordered phase; the K^+ ions were either placed on the four

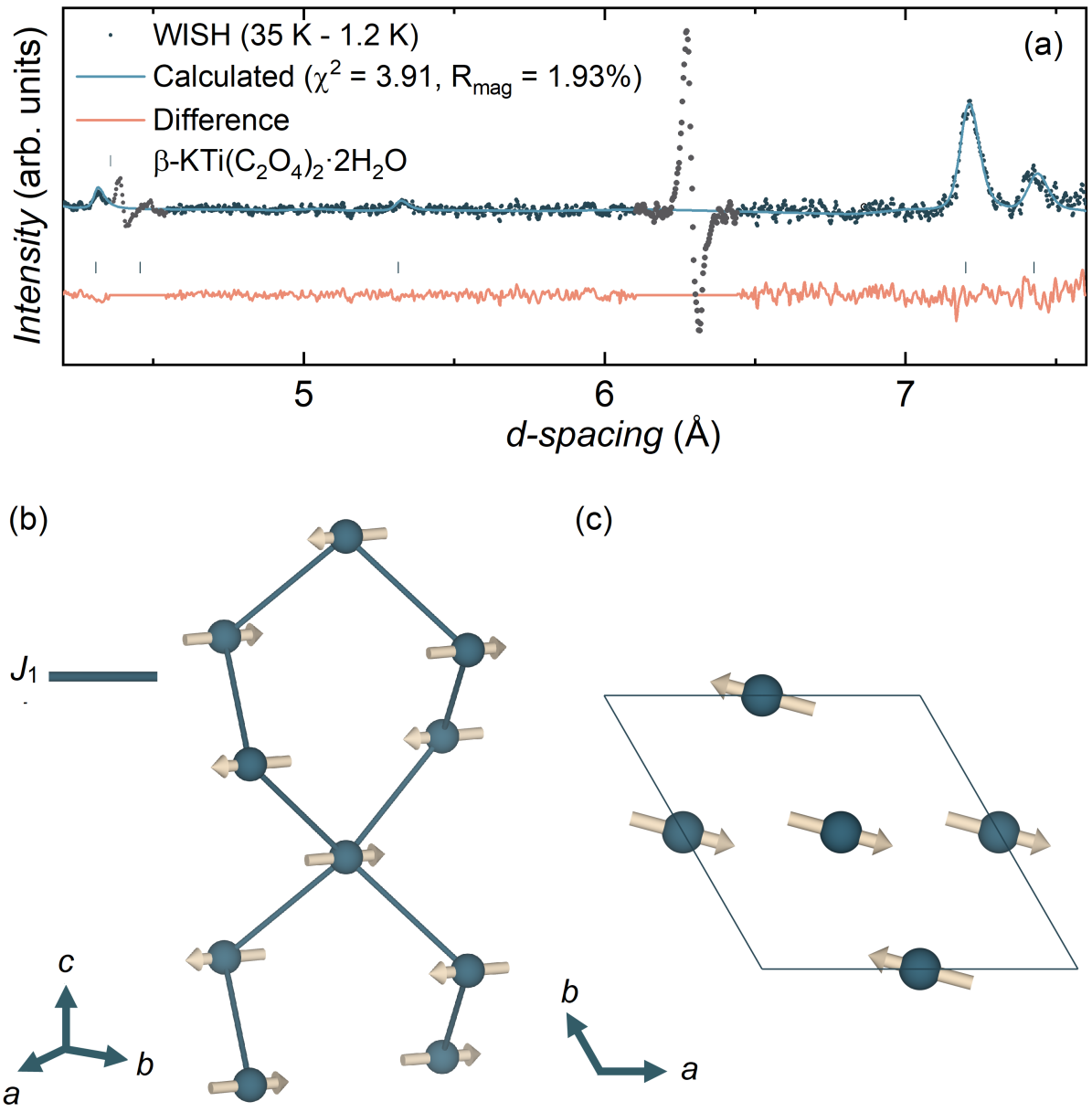

Figure 5.11: (a) Rietveld refinement of magnetic only-scattering using the P_b2_1 magnetic space group model. (b) Magnetic structure of β-KTi(C_2O_4)$_2$·2H_2O depicting one of the possible arrangements of the magnetic moments along the (111) direction and the (c) ab-plane.

fold axis of the $I4/m$ space group with two H_2O sites per formula unit, placed on the four fold axis of the $I4/mcm$ space group with no structural H_2O, or on half of their experimental sites with no structural H_2O in the $Ima2$ space group. The resulting density of states of all models produced almost identical bands around the Fermi level thus suggesting that the K^+ and H_2O containing layers do not contribute to the magnetic properties of the system. Otherwise, well converged k-meshes of 168 and 242 irreducible k-points were used for α and β, respectively. The resulting uncorrelated density of states of both psuedo-polymorphs are shown in Fig. 5.12. Consistent with the expected crystal field splitting for a square antiprismatic coordination environment, and with previous spectroscopic studies on $(NH_4)Ti(C_2O_4)_2{\cdot}H_2O$[238], an active d_{z^2} magnetic orbital is found to be the ground state of both compounds, despite the slight distortion of the coordination geometry in β. Similarly, and as expected from the large crystal field splittings due to the coordination environment, no contribution from any orbitally excited states is found.

As discussed for related oxalate containing materials[269,270], the relative strength of the exchange energies can be strongly influenced by the oxalate-metal bonding geometry. This varies considerably between both pseudo-polymorphs, as shown in the calculated Wannier functions in Figs. 5.12(c,d), where the oxalate groups lie either within or outside of the Ti-containing planes in α and β, respectively. In the case of β, this bonding geometry results in an overlap with the π orbitals of the oxalate groups which transmit the superexchange interaction. A reduced π-orbital overlap results when the oxalate groups lie within the Ti-containing planes[269,270] which results in the weaker superexchange observed in α. Alongside the lack of any orbital contribution and the experimental modelling, it can be concluded that α and β are near ideal realizations of the $S = 1/2$ Heisenberg square and diamond lattice antiferromagnetic models, respectively.

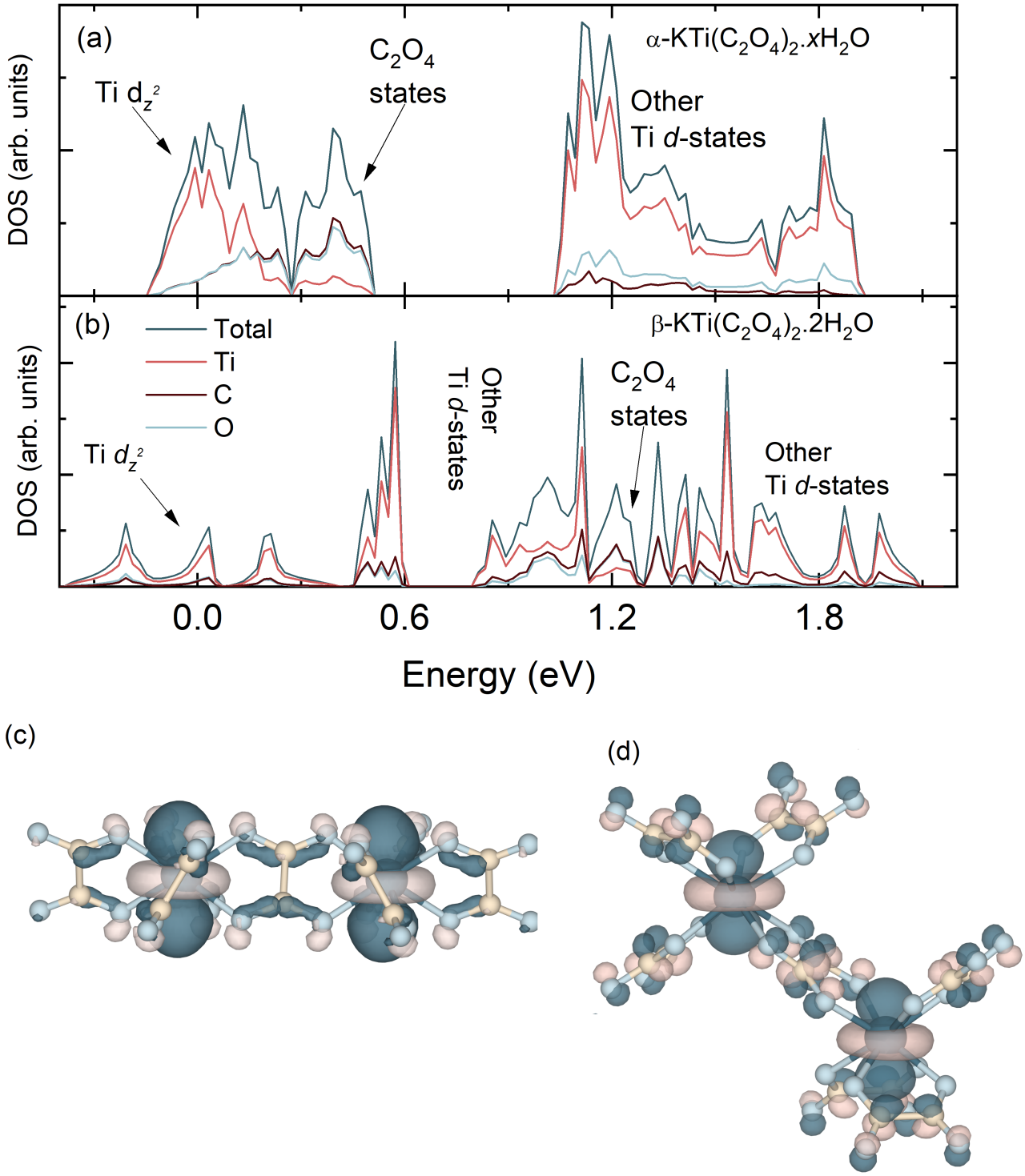

Figure 5.12: Perdew-Wang density of states for (a) α and (b) β. The Fermi level (E_F) is at zero energy. Ti^{3+} d_{z^2}-based Wannier functions highlighting the orbital overlap in (c) α-$KTi(C_2O_4)_2 \cdot xH_2O$ and (d) β-$KTi(C_2O_4)_2 \cdot 2H_2O$.

5.6 Conclusions

This chapter presents a comprehensive experimental study on the α and β pseudo-polymorphs of the $S = 1/2$, Ti^{3+} coordination framework, $KTi(C_2O_4)_2{\cdot}xH_2O$. The magnetic ground states of α and β were found to relate to the $S = 1/2$ square and diamond lattice antiferromagnet models using a combination of single-crystal X-ray diffraction, neutron powder diffraction, magnetometry, and electronic structural calculations as summarized below:

- A synthetic procedure modified from the previously reported ones for the alkali metal and ammonium analogues of $ATi(C_2O_4)_2{\cdot}xH_2O$ (A = NH_4, Na, Rb, Cs) confirms the pseudo-polymorphic nature of α and β as it was previously thought that it was the different monovalent ion sites that resulted in different symmetries—*i.e.* it was thought that only $NaTi(C_2O_4)_2 \cdot xH_2O$, for example, can host the α structure.

- Analysis of single crystal X-ray diffraction data confirms the previously predicted structure of α and revealed its tetragonal symmetry and the square-like arrangement of eight-coordinated square antiprismatic Ti^{3+} ions that are coordinated by oxalate groups in the ab-plane and separated along the c-axis by a K^+ and H_2O containing layer. Disorder within this K^+-containing layer, and the presence of non-stoichiometric structural water, was identified using neutron powder diffraction.

- Curie-Weiss analysis yields dominant antiferromagnetic interactions, and simultaneous fitting of magnetic susceptibility and specific heat data using a high-temperature series expansion approach confirms the relevance of the square lattice antiferromagnet model and indicates minimal frustration.

- The onset of long range magnetic order is evidenced by an anomaly in the specific

heat at the Néel temperature of $T_N = 2$ K. This was confirmed through analysis of neutron powder diffraction data that further reveal a collinear Néel ordered magnetic structure. A reduced ordered moment, consistent with that predicted for the $S = 1/2$ Heisenberg square lattice antiferromagnet model, confirms the relevance of this model for describing α

- A hexagonal chiral space group was found to describe the crystal structure of β using a combination of single crystal X-ray and neutron powder diffraction data. The structure can be described as forming a diamond-like magnetic sublattice of eight-coordinated, square antiprismatic Ti^{3+} ions that are bridged by oxalate groups. No structural disorder was found in β, and a stoichiometric $2H_2O$ water content was confirmed.

- Simultaneous analysis of magnetic susceptibility and specific heat data using a high temperature series expansion for the $S = 1/2$ diamond lattice antiferromagnet model confirms the relevance of this model for describing the magnetic ground state of β and highlights that the exchange energy is an order of magnitude larger than in α.

- Below an ordering temperature of $T_N = 28$ K, which is indicated by anomalies in both the magnetic susceptibility and the specific heat, analysis of neutron powder diffraction data reveals a commensurate propagation vector and a collinear Néel ordered magnetic structure where the magnetic moments align within the *ab*-plane. The direction of the moment within the *ab*-plane, however, could not be conclusively determined. A slightly reduced ordered moment is found, and is consistent with the theoretically predicted moment for a $S = 1/2$ diamond lattice antiferromagnet model.

- Electronic structure calculations confirm an active d_{z^2} magnetic orbital for both compounds and that there is no orbital contribution to the moment.

- Due to the differences in the Ti-oxalate bridging geometries in α and β, an order of

magnitude difference is observed between their exchange energies.

- The α and β psuedo-polymorphs of $KTi(C_2O_4)_2{\cdot}xH_2O$ could thus be concluded to be near-ideal realizations of the $S = 1/2$ Heisenberg square and diamond lattice antiferromagnet models, respectively. To the author's knowledge, β is the first coordination framework realization of the diamond lattice antiferromagnet model.

One of the features highlighted by this study is the difficulty associated with designing exchange frustration in coordination and metal-organic framework materials. This mainly stems from the complexity of the superexchange mechanisms governing the magnetic properties of such systems and the larger spatial separation of the magnetic ions. An advantage of molecular systems, however, is the diversity and versatility of organic linkers, which, combined with a more systematic understanding of superexchange mechanisms with different metals, could provide a pathway to a more rational design for unconventional magnetic ground states. Future studies on oxalate materials could hence focus on a few synthetic routes to examine the effects of such design aspects:

- Oxalate linkers are known to coordinate a variety of transition metal ions. The interplay of the spin and orbital degrees of freedom could hence be examined on the diamond and square lattice antiferromagnet models by preparing the Ru^{3+}, V^{3+}, or Mo^{3+} analogues of the Ti^{3+} compounds.

- Preparing $KV(C_2O_4)_2 \cdot 2H_2O$ in particular could prove quite interesting, as topological paramagnetic ground states have been theoretically predicted for the $S = 1$ Heisenberg diamond lattice model[251].

- The role of the oxalate ligand in determining the relative strength of the exchange energies could be examined by investigating the tetrathiooxalate (C_2S_4) analogues of the oxalate compounds.

Chapter 6

Summary and Outlook

This study has focused on demonstrating the magnetic properties of several quantum magnets that are pertinent to spin models that are theorized to host unconventional magnetic ground states. For this purpose, each material has been investigated using a combination of neutron scattering, magnetometry, specific heat, and *ab-initio* techniques that resulted in the following conclusions:

- AMoOP$_2$O$_7$ (A = Li Na, K, Cs): Despite a magnetic sublattice that is susceptible to a frustrating interchain coupling, the magnetic ground states of all AMoOP$_2$O$_7$ (A = Na, K, Cs) compounds were found to be relevant to the one-dimensional $S = 1/2$ Heisenberg antiferromagnet model. Underlying this one dimensionality is a distortion to the octahedral crystal field that results in an active magnetic orbital with spatial components that favor exchange interactions along the chain direction. While LiMoOP$_2$O$_7$ adopts a different magnetic sublattice comprised of three-legged spin ladders, it also features a similar octahedral distortion through which a non-frustrated magnetic ground state arises.

- RuP$_3$SiO$_{11}$: A novel synthetic route was devised for the preparation of the Ru^{3+}

honeycomb-based compound, RuP_3SiO_{11}. While the system was found to undergo long-range magnetic order, a combination of neutron scattering and *ab-initio* measurements provide evidence for the validity of a $j_{\text{eff}} = 1/2$ psuedospin and suggest that an extended Kitaev model could be relevant to the magnetic ground state. Crucially, this study marks the first experimental demonstration of Kitaev-type interactions involving a multi-atom superexchange mechanism and provides evidence for the *ab-initio* studies[199,200] that have theorized their emergence in such geometries.

- α- and β-$KTi(C_2O_4)_2{\cdot}xH_2O$: The study presented in Chapter 5 demonstrates the relevance of hybrid materials in realizing quantum spin models. However, it also highlights the difficulty associated with engineering frustrated interactions in hybrid systems due to the long and complex superexchange pathways commonly found in such systems. Through a combination of experimental and *ab-inition* techniques, α and β were found near-realizations of the $S = 1/2$ Heisenberg square and diamond lattice antiferromagnet models, respectively.

An underlying commonality between these studies is that they highlight the complexity of engineering spin models onto particular materials. As seen here and for many of the materials referenced across this study, despite following the "ingredients" presented in Chapter 1 that can promote the emergence of quantum ground states, structural distortions and disorder along with perturbating terms in the spin Hamiltonian can drive systems towards different ground states. Whilst hybrid materials were introduced as means to circumvent some of these issues, we have also highlighted the difficulty of realizing frustrated models in such systems. Hence, a continuing effort for the discovery of new model materials will be essential in search for unconventional magnetic ground states. In addition to oxides and hybrid materials, these can include a few new exciting avenues such as exfoliated low-dimensional magnetic materials.

Some of the work presented in this study has been published, or submitted for publication, in:

- **A. H. Abdeldaim**, A. A. Tsirlin, J. Ollivier, C. Ritter, D. Fortes, R. S. Perry, L. Clark, and G. J. Nilsen. One-dimensional Quantum Magnetism in the $S = 1/2$ Mo(V) System, $KMoOP_2O_7$. *arXiv:2207.01284*, 2022. (Physical Review B)
- **A. H. Abdeldaim**, T. Li, L. Farrar, A. A. Tsirlin, W. Yao, A. S. Gibbs, P. Manuel, P. Lightfoot, G. J. Nilsen, and L. Clark. Realizing Square and Diamond Lattice $S = 1/2$ Heisenberg Antiferromagnet Models in the α and β Phases of the Coordination Framework, $KTi(C_2O_4)_2{\cdot}xH_2O$. *Physical Review Materials*, 4:104414, 2020.

Additional work that has been published during this studentship includes:

- S. A. Ivko, K. Tustain, T. Dolling, **A. Abdeldaim**, O. H. J. Mustonen, P. Manuel, C. Wang, H. Luetkens, and L. Clark. Uncovering the $S = 1/2$ Kagome Ferromagnet within a Family of Metal–Organic Frameworks. Chemistry of Materials, 34:5409–5421, 2022.
- L. Clark and **A. H. Abdeldaim**. Quantum Spin Liquids from a Materials Perspective. *Annual Review of Materials Research*, 51:495–519, 2021.
- **A. H. Abdeldaim**, D. I. Badrtdinov, A. S. Gibbs, P. Manuel, H. C. Walker, M. D. Le, C. H. Wu, D. Wardecki, S.-G. Eriksson, Y. O. Kvashnin, A. A. Tsirlin, and G. J. Nilsen. Large Easy-axis Anisotropy in the One-Dimensional Magnet $BaMo(PO_4)_2$. *Physical Review B*, 100:214427, 2019.

Other publications are currently in preparation. Those include the study presented in Chapter 4 on RuP_3SiO_{11}, the study presented on $LiMoOP_2O_7$ in Chapter 3, and an inelastic neutron scattering study on $Zn_xCu_{4-x}(OH)_6FBr$.

Appendix A

Additional Figures

This appendix contains:

- Crystallographic information for the $KNbOP_2O_7$ sample prepared in Chapter 3.
- Simulations of $\kappa = 0$ magnetically ordered models for $KMoOP_2O_7$.
- Variation of Curie-Weiss model parameters with respect to the minimum fitting temperature for all studied materials.

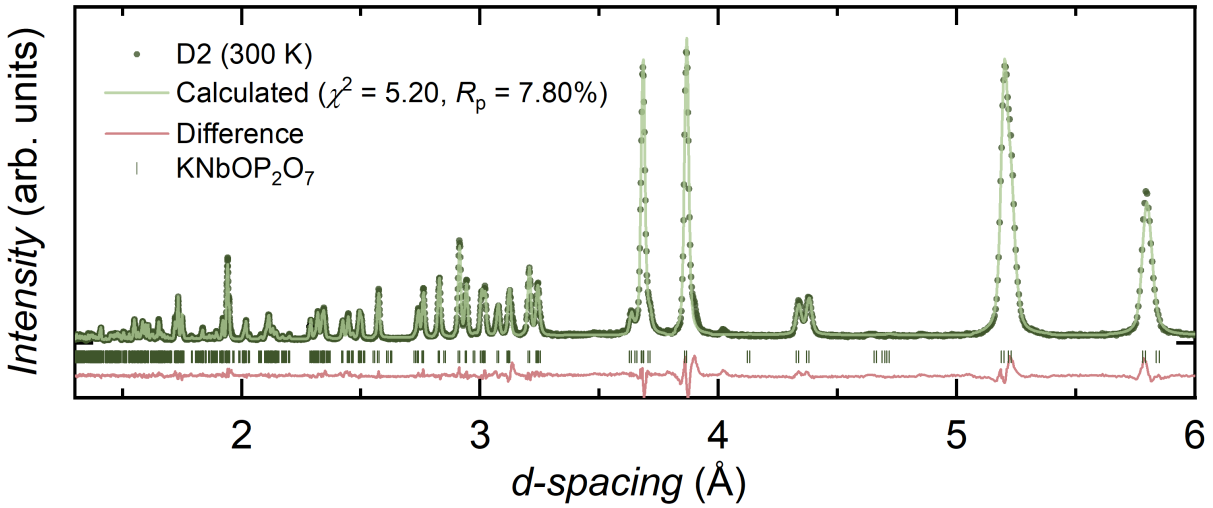

Figure A.1: Rietveld analysis of PXRD data collected at 300 K for the $P2_1/n$ model for $KNbOP_2O_7$.

Table A.1: Structural parameters of $KNbOP_2O_7$ as obtained through Rietveld refinement of the $P2_1/n$ model using powder X-ray diffraction data measured at 300 K on a D2 diffractometer. The resulting unit cell parameters are $a = 5.1714(1)$ Å, $b = 11.8290(4)$ Å, $c = 11.7138(3)$ Å, and $\beta = 90.901(3)°$ with goodness-of-fit parameters $\chi^2 = 5.20$ and $R_p = 7.80\%$.

Atom	x	y	z	$U_{iso}((Å^2))$
Nb	0.2596(7)	0.1222(3)	0.1695(3)	0.052(1)
K	0.735(2)	0.6264(7)	0.0622(6)	0.095(3)
P1	0.739(2)	0.9409(8)	0.1525(9)	0.051(4)
P2	0.773(2)	0.306(1)	0.144(1)	0.088(5)
O1	0.795(5)	0.886(2)	0.043(2)	0.20(1)
O2	0.959(2)	0.043(1)	0.163(1)	0.005(5)
O3	0.189(2)	0.655(1)	0.179(1)	0.051(8)
O4	0.041(2)	0.269(1)	0.157(1)	0.001(5)
O5	0.698(4)	0.421(1)	0.102(1)	0.069(9)
O6	0.565(3)	0.189(1)	0.139(1)	0.026(5)
O7	0.866(8)	0.852(4)	0.237(3)	0.72(5)
O8	0.470(2)	0.983(1)	0.161(1)	0.057(9)

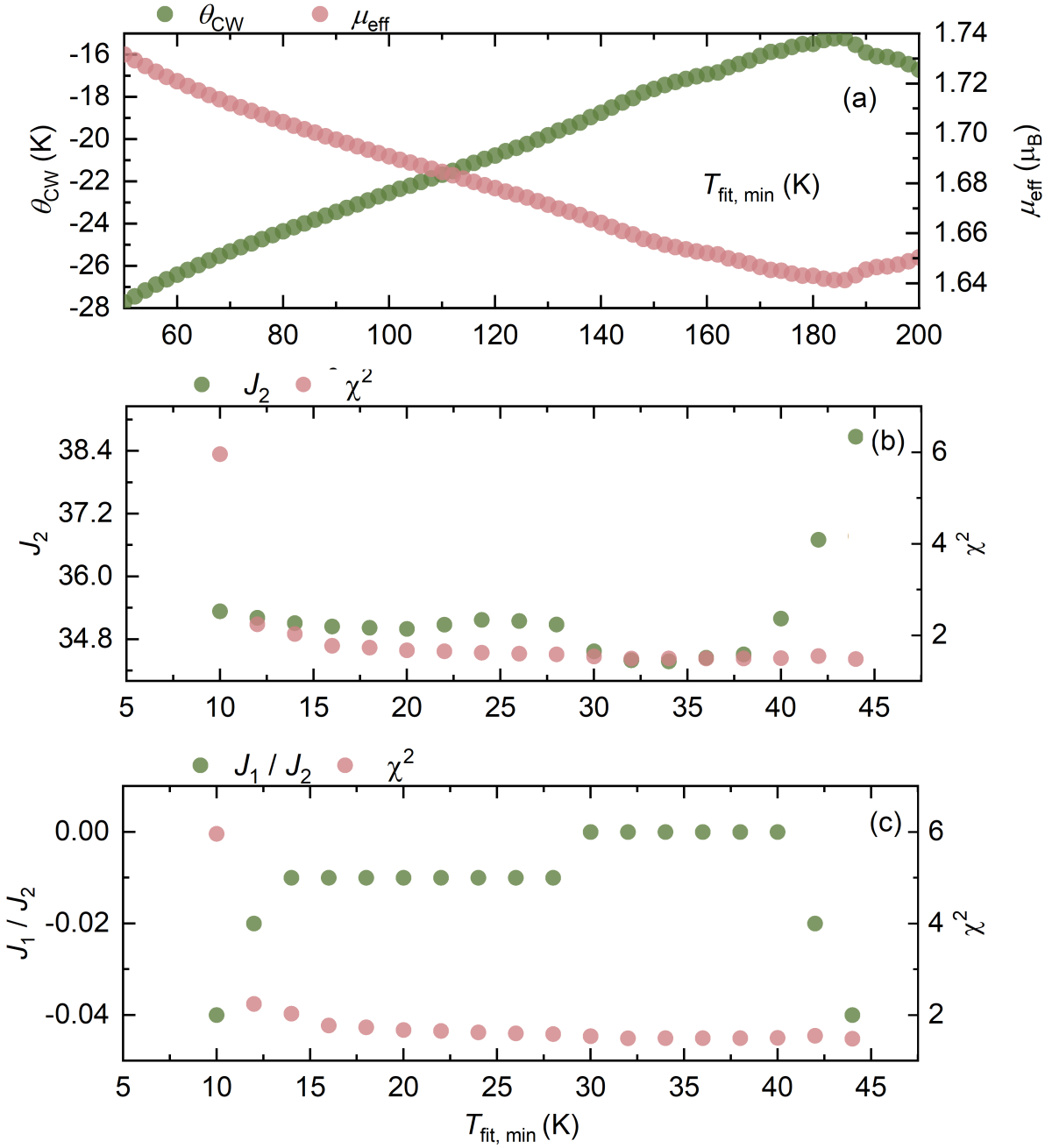

Figure A.2: Dependence of the (a) Curie-Weiss and (b,c) exact diagonalization model parameters on the minimum fitting temperature for $KMoOP_2O_7$.

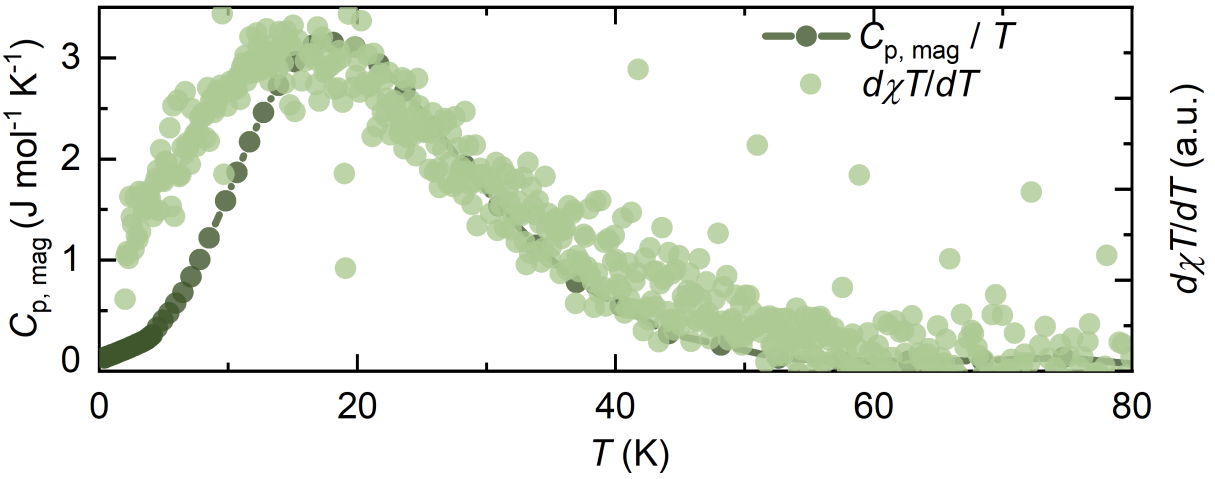

Figure A.3: Comparison between the magnetic specific heat of $KMoOP_2O_7$ and the Fisher specific heat, $d\chi T/dT$.

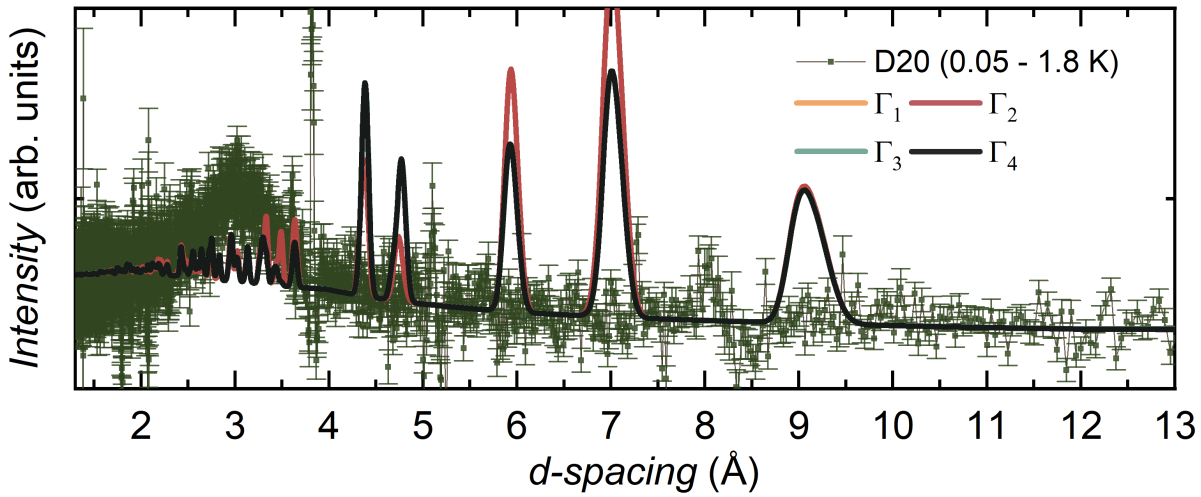

Figure A.4: Simulated assumed magnetic structural models for a propagation vector, $\kappa = 0$, on $0.05 - 1.8$ K subtracted neutron powder diffraction data collected for $KMoOP_2O_7$.

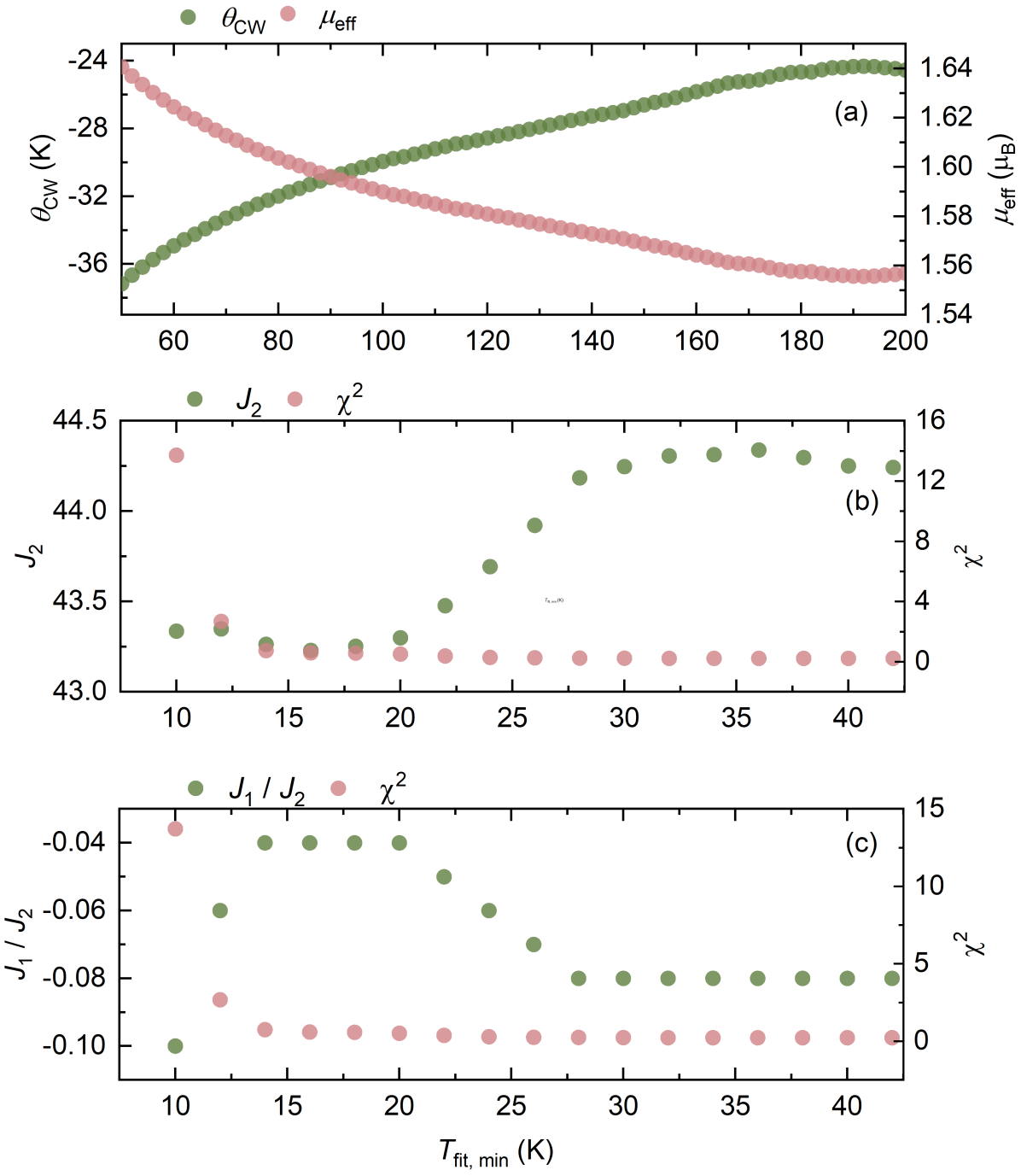

Figure A.5: Dependence of the (a) Curie-Weiss and (b,c) exact diagonalization model parameters on the minimum fitting temperature for $NaMoOP_2O_7$.

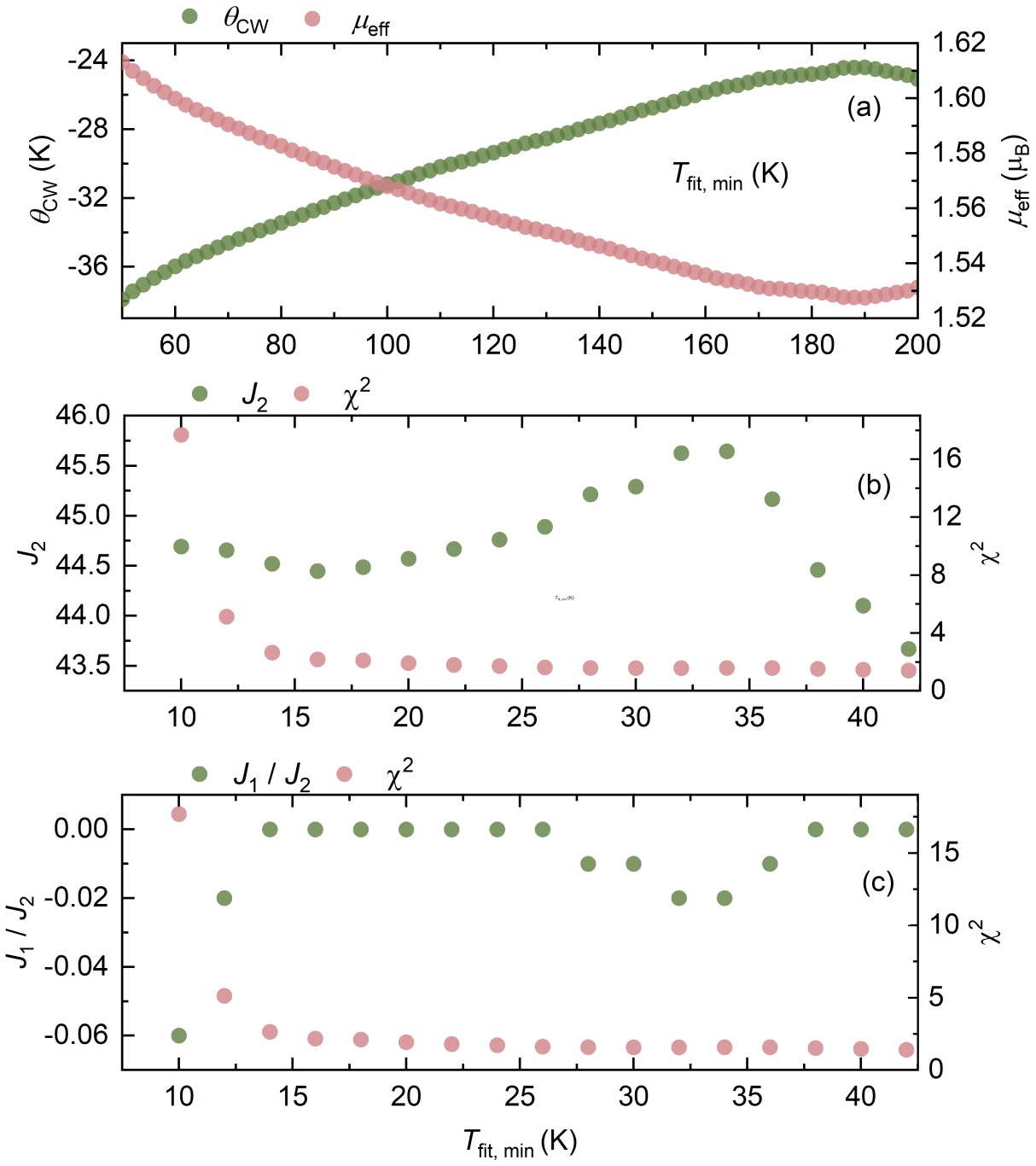

Figure A.6: Dependence of the (a) Curie-Weiss and (b,c) exact diagonalization model parameters on the minimum fitting temperature for $CsMoOP_2O_7$.

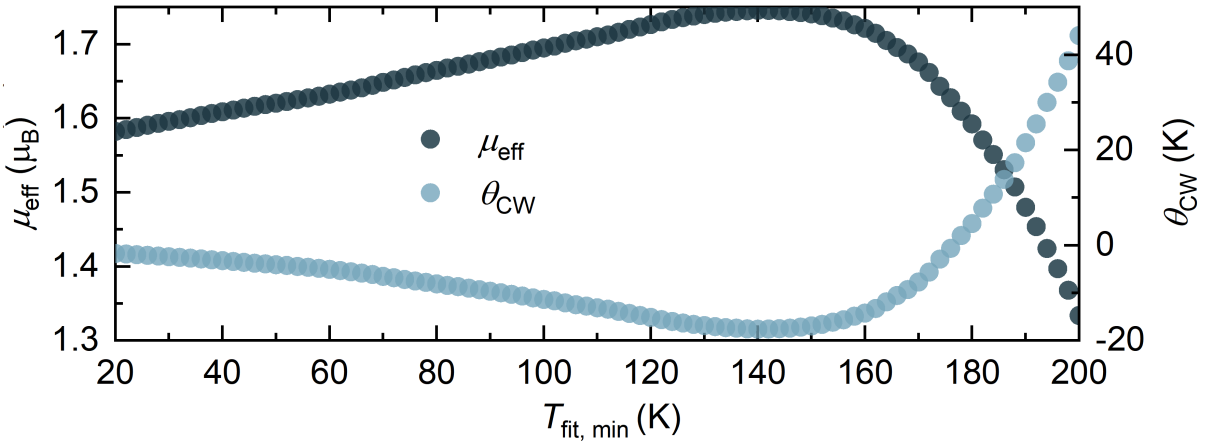

Figure A.7: Dependence of the CW model parameters on the minimum fitting temperature.

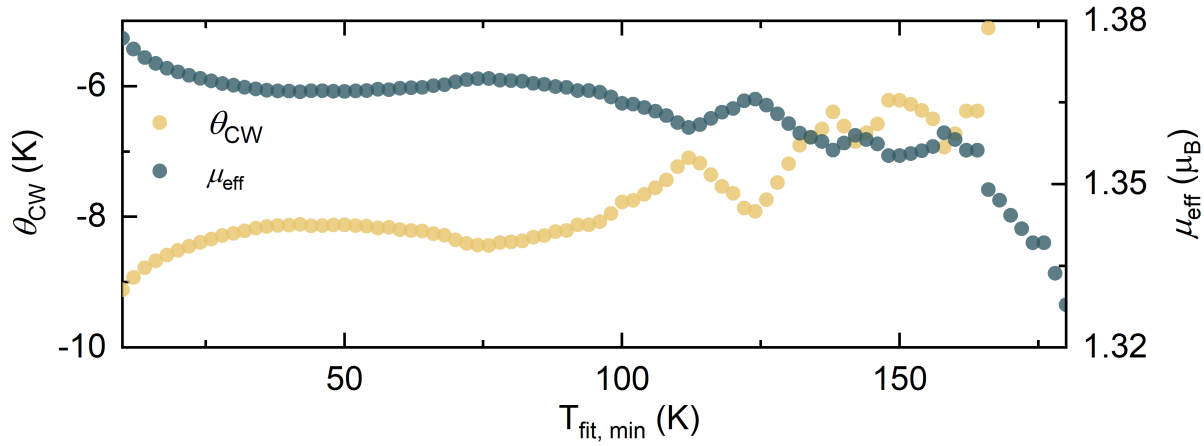

Figure A.8: Dependence of the CW model parameters on the minimum fitting temperature for α-$KTi(C_2O_4)_2{\cdot}xH_2O$.

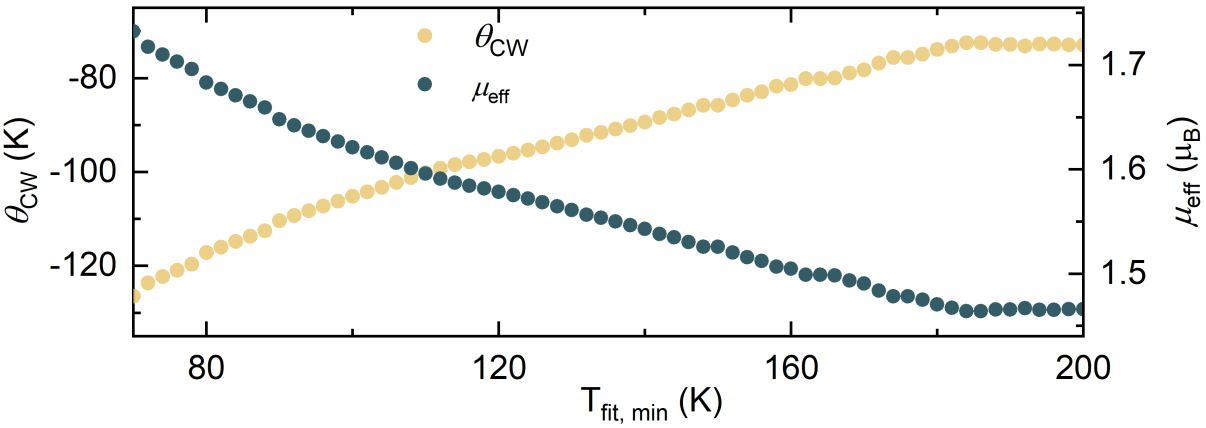

Figure A.9: Dependence of the CW model parameters on the minimum fitting temperature for β-$KTi(C_2O_4)_2 \cdot 2H_2O$.

Appendix B

Optimization of Syntheses

This appendix details the optimization of the synthetic procedures carried out across Chapters 3 and 4. The optimization of the syntheses carried out in Chapter 5 was performed by Dr. Teng Li (University of St. Andrews) and Dr. Wenjiao Yao (Chinese Academy of Sciences).

B.1 $A\mathrm{MoOP_2O_7}$

None of the previously reported methods for the preparation of $A\mathrm{MoOP_2O_7}$ (A = Li - Cs) produced pure powder products. For example, the synthetic procedure detailed for the preparation of $\mathrm{KMoOP_2O_7}$ [128] involves the same molar ratios used in this study but only contains two heating stages. Additionally, the finally heating stage occurs at a significantly higher temperature of 1100 K. Reproducing this method results in a multicolored product (Fig. B.1) containing bright green needle-like single crystals within the pellet and on the crucible (Fig. B.2), later confirmed as being KMP using SC-XRD, along with many unidentified different colored impurity phases.

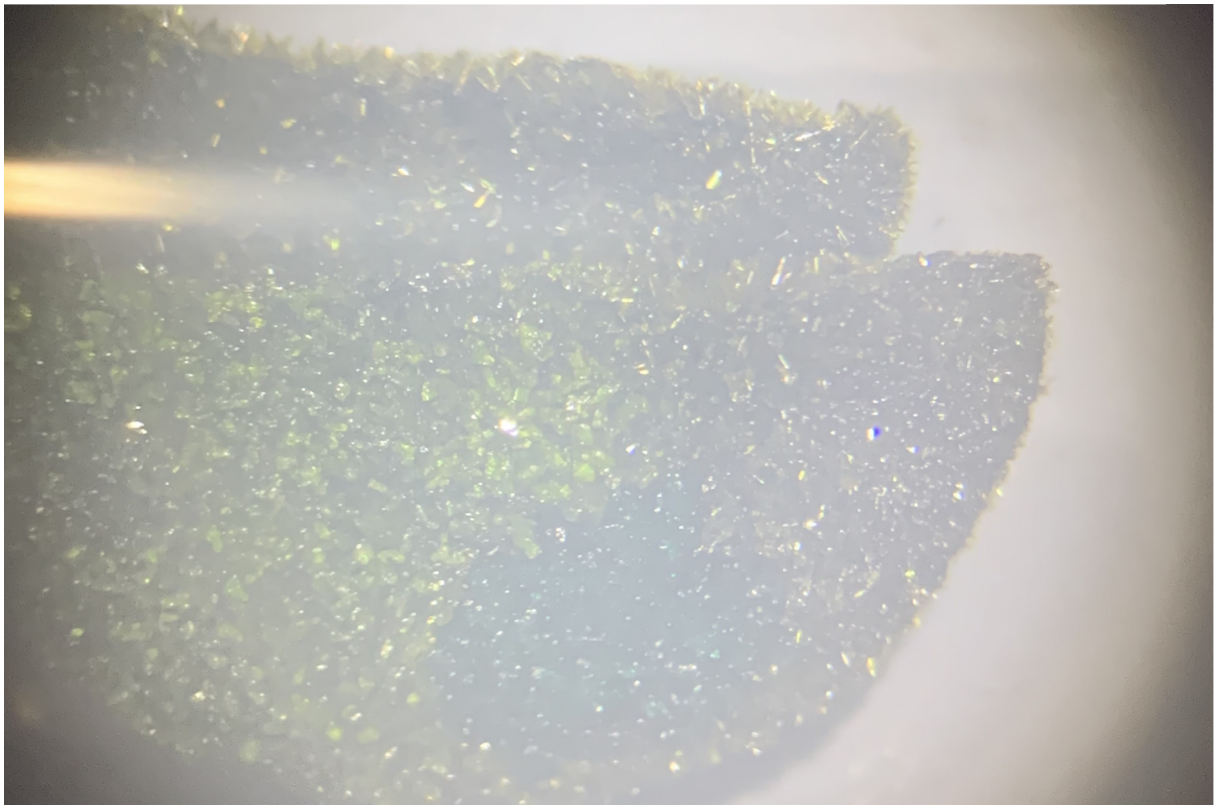

Figure B.1: Typical multi-colored pellets forming from the reaction detailed in Ref.[128] for the preparation of KMP.

As phosphates are known to stabilize many products and phases, the optimization focused on finding the temperature at which KMP is the thermodynamically favorable phase. The additional step acetone washing and heating stages were found to result in powder products with a green hue that is similar to that of the needle-like single crystals.

The optimization of the syntheses of the Na and Cs alkali metal analogues followed similar routes. In this case, the molar ratios of Mo and MoO_3 were also systematically varied to obtian pure powder products.

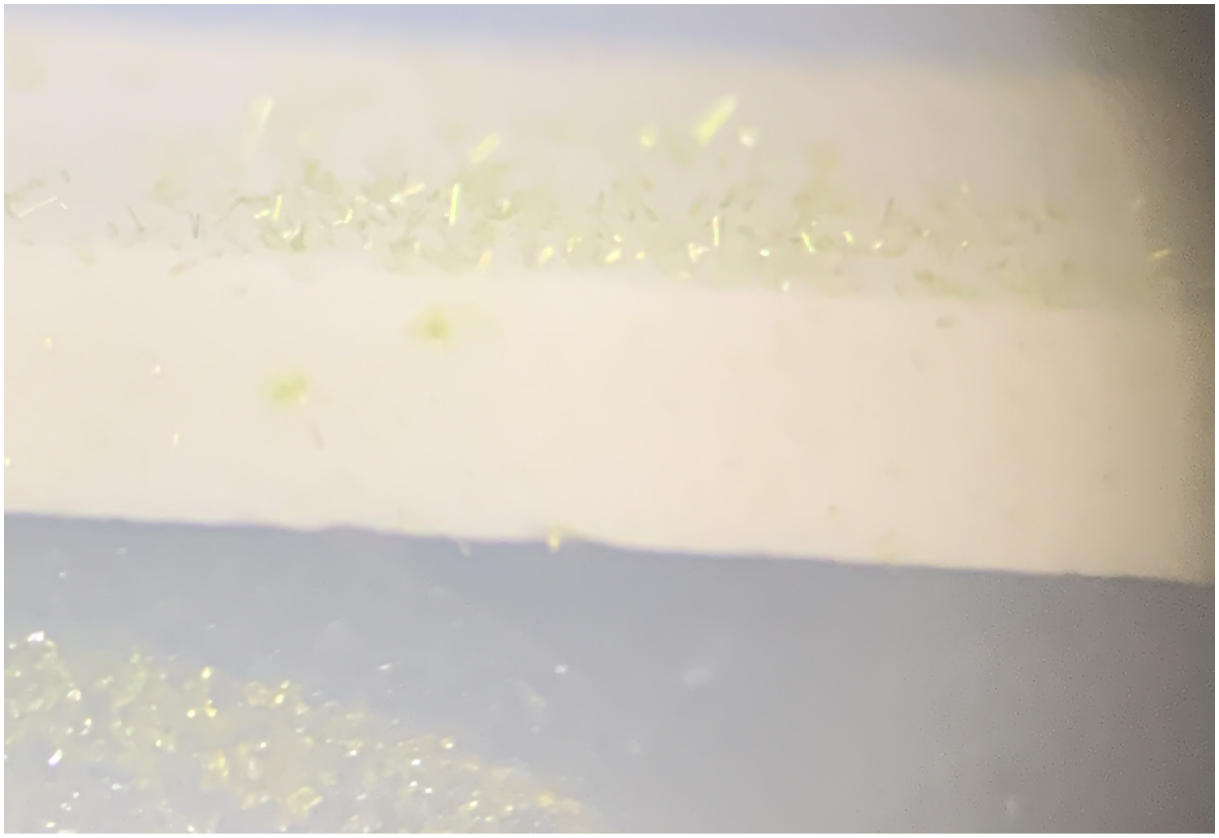

Figure B.2: Needle-like single crystals of KMP forming on the walls of the boat crucible.

B.2 RuP_3SiO_{11}

A summary of all synthetic attempts made is presented in Table B.1. All attempts at reproducing the previously published[203] RuP_3SiO_{11} synthetic procedure were unsuccessful. In a typical reaction, the yellow colored RuP_3SiO_{11} only formed as a minor phase on the cooler side of the sealed ampoule (Fig. B.3). Within this region of the tube, the product contained yellow single crystals that were later confirmed as RuP_3SiO_{11} through SC-XRD (Fig. B.4). The other side instead contained a combination of Ru metal, RuO_2, and an unidentified product.

As the published method uses the sealed tubes as the silica source for the reaction, a natural starting point for optimizing the reaction involved the direct addition of SiO_2 to the reaction mixture. This increased the amount of the RuP_3SiO_{11} phase in the final

product to about 30% wt., yet RuO_2 remained as the major phase. The formation of RuO_2 as the major product suggested the presence of an oxidizing reagent within the evacuated silica ampoules. Hence, the reaction was carried out in evacuated then Ar gas refilled quartz ampoules at varying Ar pressures. After optimizing for the reaction time and temperature, it found that an Ar gas pressure of $350 - 450$ mbar resulted in the best quality samples containing $80 - 90\%$ wt. RuP_3SiO_{11} for a dwell time of 168 hours and a reaction temparture of 1173 K.

To further improve the quality of the final product, other Ru^{3+} sources were considered. This was done as $H_2RuP_3O_{10}$ [203] only forms as an amorphous product and its quality could not be confirmed. A natural starting point was the previously reported crystalline compound, $Ru(PO_3)_3$ [201]. As three polymorphs of $Ru(PO_3)_3$ have been reported, all three were prepared. Reacting each polymorph with a stoichiometric amount of SiO_2 confirmed that only the monoclinic cyclo-hexaphosphate $Ru_2P_6O_{18}$ reacts to form the purest yellow colored (Fig. B.5) samples of RuP_3SiO_{11}.

Another synthetic procedure attempted for the preparation of RuP_3SiO_{11} followed a method similar to that developed for the AMoOP_2O_7 family of materials. In this method, RuO_2, Ru metal, SiO_2, and $(NH_4)H_2PO_4$ were combined in a $(1-x)$:x:1:3 molar ratio. Multiple reactions using different x values ranging from $0 - 0.4$ were attempted to reduce Ru^{4+} into Ru^{3+}. All of these were unsuccessful, and no reaction occured regardless of the molar ratios used.

.

Table B.1: Synthetic attempts for the preparation of RuP_3SiO_{11}. P_{Ar} refers to the argon gas pressure used in an evacuated quartz ampoule, whereas Si refers to a thermal treatment step.

Reaction	Attempts	Conditions	Product
$H_2RuP_3O_{10}$ + SiO_2	9	$723 - 923$ K, $60 - 240$ h $P_{Ar} = 0 - 500$ mbar	$0 - 30\%$ wt.
$H_2RuP_3O_{10}$ + SiO_2	12	$923 - 1073$ K, $60 - 240$ h $8P_{Ar} = 0 - 500$ mbar	$40 - 60\%$ wt.
$H_2RuP_3O_{10}$ + SiO_2	32	1173 K, $120 - 200$ h $P_{Ar} = 300 - 450$ mbar	$> 80\%$ wt.
$Ru(PO_3)_3$	8	$673 - 973$ K, 168 h $P_{Ar} = 0 - 500$ mbar	823-873 K $Ru_2P_6O_{18}$ 923-1073 K $Ru(PO_3)_3$
$Ru_2P_6O_{18}$ + SiO_2	18	1173 K, 168 h $P_{Ar} = 350 - 425$ mbar	$> 90\%$ wt.
$(1-x)RuO_2$ + SiO_2 + xRu + $3(NH_4)_2HPO_4$	9	$x = 0 - 0.4$ S1: 873 K, 24 h, Ar flow S2: 973 K, 24 h, Ar flow S3: 1173 K, 168 h, $P_{Ar} = 300 - 400$ mbar	Unreacted

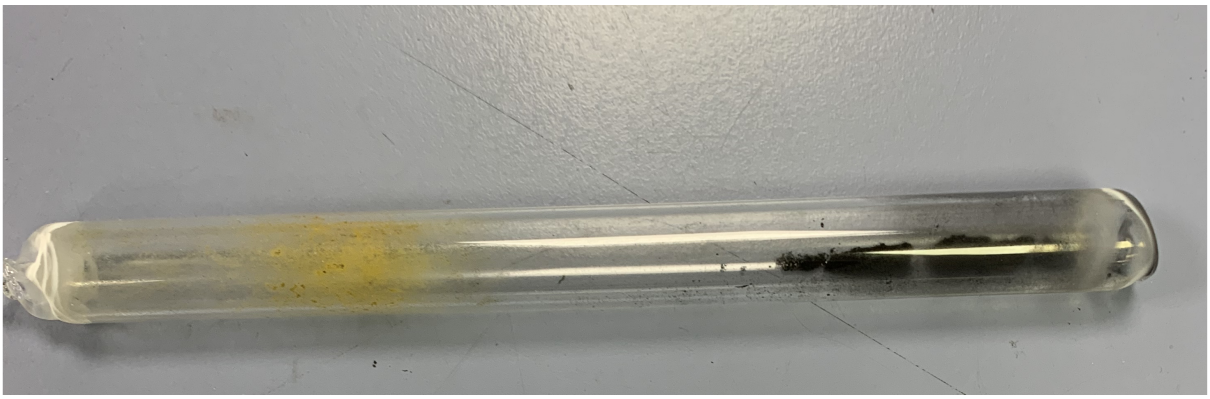

Figure B.3: A typical final product of the reaction detailed in Ref.[203] where the yellow region contains RuP_3SiO_{11}

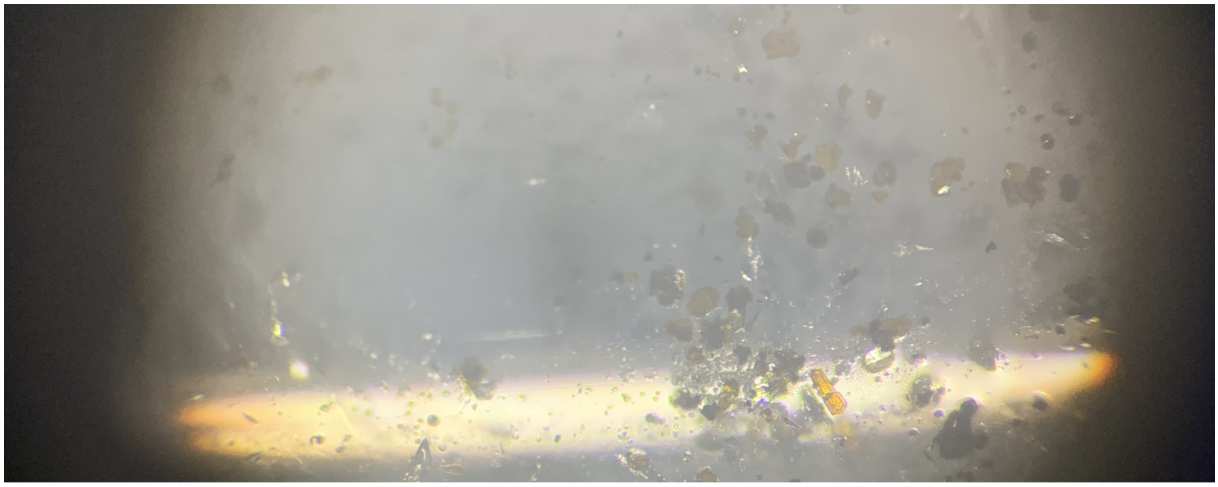

Figure B.4: Yellow region of the sealed quartz ampoule under a microscope where yellow single crystals of RuP_3SiO_{11} are found.

Figure B.5: Pellets of as prepared RuP_3SiO_{11} following the optimized method using $Ru(PO_3)_3$ as a starting reagent.

Bibliography

[1] V. Coropceanu, J. Cornil, D.A da Silva Filho, Y. Olivier, R. Silbey, and J.-L. Brédas. Charge Transport in Organic Semiconductors. *Chemical Reviews*, 107(4):926–952, 2007.

[2] L. Lu, J. D. Joannopoulos, and M. Soljačić. Topological Photonics. *Nature Photonics*, 8(11):821–829, 2014.

[3] I. Žutić, J. Fabian, and S. D. Sarma. Spintronics: Fundamentals and Applications. *Reviews of Modern Physics*, 76(2):323, 2004.

[4] L. Savary and L. Balents. Quantum Spin Liquids: A Review. *Reports on Progress in Physics*, 80(1):016502, 2016.

[5] W. Witczak-Krempa, G. Chen, Y. B. Kim, and L. Balents. Correlated Quantum Phenomena in the Strong Spin-Orbit Regime. *Annual Review of Condensed Matter Physics*, 5(1):57–82, 2014.

[6] A. Kitaev. Anyons in an Exactly Solved Model and Beyond. *Annals of Physics*, 321 (1):2–111, 2006.

[7] M. T. Greiner and Z.-H. Lu. Thin-film Metal Oxides in Organic Semiconductor Devices: Their Electronic Structures, Work Functions and Interfaces. *NPG Asia Materials*, 5(7):e55–e55, 2013.

[8] S. Trebst and C. Hickey. Kitaev Materials. *Physics Reports*, 950:1–37, 2022.

[9] L. Clark and A. H. Abdeldaim. Quantum Spin Liquids from a Materials Perspective. *Annual Review of Materials Research*, 51:495–519, 2021.

[10] J. Stöhr and H. C. Siegmann. *Magnetism: From Fundamentals to Nanoscale Dynamics*. Springer, 2006.

[11] D. Khomskii. *Transition Metal Compounds*. Cambridge University Press, 2014.

[12] D. Khomskii. *Basic Aspects of the Quantum Theory of Solids : Order and Elementary Excitations*. Cambridge University Press, 2010.

[13] J. J. Sakurai and E. D. Commins. *Modern Quantum Mechanics*. American Association of Physics Teachers, 1995.

[14] S. Blundell. *Magnetism in Condensed Matter*. Oxford University Press, 2003.

[15] I. J. Rhile. Visualization of a Large Set of Hydrogen Atomic Orbital Contours Using New and Expanded Sets of Parametric Equations. *Journal of Chemical Education*, 91:1739–1741, 2014.

[16] T. Takayama, J. Chaloupka, A. Smerald, G. Khaliullin, and H. Takagi. Spin–orbit-entangled Electronic Phases in $4d$ and $5d$ Transition-Metal Compounds. *Journal of the Physical Society of Japan*, 90(6):062001, 2021.

[17] A. Abragam and B. Bleaney. *Electron Paramagnetic Resonance of Transition Ions*. Oxford University Press, 2012.

[18] H. Takagi, T. Takayama, G. Jackeli, G. Khaliullin, and S. E. Nagler. Concept and Realization of Kitaev Quantum Spin Liquids. *Nature Reviews Physics*, 1(4): 264–280, 2019.

[19] R. Yadav, N. A. Bogdanov, V. M. Katukuri, S. Nishimoto, J. Van Den Brink, and L. Hozoi. Kitaev Exchange and Field-induced Quantum Spin-liquid States in Honeycomb α-$RuCl_3$. *Scientific Reports*, 6(1):1–16, 2016.

[20] M. R. Norman and T. Micklitz. Electronic Structure of Hyper-Kagome $Na_4Ir_3O_8$. *Physical Review B*, 81:024428, 2010.

[21] J. B. Goodenough. Theory of the Role of Covalence in the Perovskite-Type Manganites $[\mathrm{La}, M(\mathrm{II})]\mathrm{MnO}_3$. *Physical Review*, 100:564–573, 1955.

[22] J. Kanamori. Superexchange Interaction and Symmetry Properties of Electron Orbitals. *Journal of Physics and Chemistry of Solids*, 10(2):87–98, 1959.

[23] J. Girovsky, J. Nowakowski, Md. E. Ali, M. Baljozovic, H. R Rossmann, T. Nijs, E. A. Aeby, S. Nowakowska, D. Siewert, G. Srivastava, C. Wäckerlin, J. Dreiser, S. Decurtins, S.-X. Liu, P. M. Oppeneer, T. A. Jung, and N. Ballav. Long-range Ferrimagnetic Order in a Two-Dimensional Supramolecular Kondo Lattice. *Nature Communications*, 8:15388, 2017.

[24] K. Guratinder, V. Tsurkan, L. Prodan, L. Keller, J. P. Embs, F. Juranyi, M. Medarde, Ch. Rüegg, and O. Zaharko. Magnetic Order and Exchange Coupling in the Frustrated Diamond-Lattice Antiferromagnet $MnSc_2Se_4$. *Physical Review B*, 105:174423, 2022.

[25] M. M. Bordelon, C.-X. Liu, L. Posthuma, E. Kenney, M. J. Graf, N. P. Butch, A. Banerjee, S. Calder, L. Balents, and S. D. Wilson. Frustrated Heisenberg $J_1 - J_2$ Model Within the Stretched Diamond Lattice of $LiYbO_2$. *Physical Review B*, 103: 014420, 2021.

[26] K. Momma and F. Izumi. *VESTA*: A Three-dimensional Visualization System for Electronic and Structural Analysis. *Journal of Applied Crystallography*, 41(3):653–658, 2008.

[27] S. Toth and B. Lake. Linear Spin Wave Theory for Single-Q Incommensurate Magnetic Structures. *Journal of Physics: Condensed Matter*, 27(16):166002, 2015.

[28] T. Holstein and H. Primakoff. Field Dependence of the Intrinsic Domain Magnetization of a Ferromagnet. *Physical Review*, 58:1098–1113, 1940.

[29] N. N. Bogoljubov. On a New Method in the Theory of Superconductivity. *Il Nuovo Cimento (1955-1965)*, 7:794–805, 1958.

[30] J. H. Taylor and G. Müller. Limitations of Spin-wave Theory in $T = 0$ Spin Dynamics. *Physical Review B*, 28:1529–1533, 1983.

[31] N. D. Mermin and H. Wagner. Absence of Ferromagnetism or Antiferromagnetism in One- or Two-Dimensional Isotropic Heisenberg Models. *Physical Review Letters*, 17:1133–1136, 1966.

[32] H. Bethe. Zur Theorie der Metalle. *Zeitschrift für Physik*, 71:205–226, 1931.

[33] J.-D. Cloizeaux and J. J. Pearson. Spin-Wave Spectrum of the Antiferromagnetic Linear Chain. *Physical Review*, 128:2131–2135, 1962.

[34] G. Müller, H. Thomas, H. Beck, and J. C. Bonner. Quantum Spin Dynamics of the Antiferromagnetic Linear Chain in Zero and Nonzero Magnetic Field. *Physical Review B*, 24:1429–1467, 1981.

[35] M. Karbach, G. Müller, A. H. Bougourzi, A. Fledderjohann, and K.-H. Mütter. Two-spinon Dynamic Structure Factor of the One-dimensional $s = 1/2$ Heisenberg antiferromagnet. *Physical Review B*, 55:12510–12517, 1997.

[36] M. Mourigal, M. Enderle, A. Klöpperpieper, J.-S. Caux, A. Stunault, and H. M. Rønnow. Fractional Spinon Excitations in the Quantum Heisenberg Antiferromagnetic Chain. *Nature Physics*, 9:435–441, 2013.

[37] L.-P. Regnault. Bulk Magnetic Materials: Low-dimensional Systems. In *Encyclopedia of Materials: Science and Technology*, pages 856–864. Elsevier, Oxford, 2001.

[38] J. Vannimenus and G. Toulouse. Theory of the Frustration Effect. II. Ising Spins on a Square Lattice. *Journal of Physics C: Solid State Physics*, 10(18):L537, 1977.

[39] G. H. Wannier. Antiferromagnetism. The Triangular Ising Net. *Physical Review*, 79(2):357, 1950.

[40] M. J. Harris, S. T. Bramwell, D. F. McMorrow, T. Zeiske, and K. W. Godfrey. Geometrical Frustration in the Ferromagnetic Pyrochlore $Ho_2Ti_2O_7$. *Physical Review Letters*, 79:2554–2557, 1997.

[41] S. T. Bramwell and M. J. Harris. Frustration in Ising-type Spin Models on the Pyrochlore Lattice. *Journal of Physics: Condensed Matter*, 10(14):L215, 1998.

[42] S. T. Bramwell and M. J. Harris. The History of Spin Ice. *Journal of Physics: Condensed Matter*, 32(37):374010, 2020.

[43] N. Shannon, B. Schmidt, K. Penc, and P. Thalmeier. Finite Temperature Properties and Frustrated Ferromagnetism in a Square Lattice Heisenberg Model. *The European Physical Journal B-Condensed Matter and Complex Systems*, 38(4):599–616, 2004.

[44] M. J. P. Gingras and P. A. McClarty. Quantum Spin Ice: A Search for Gapless Quantum Spin Liquids in Pyrochlore Magnets. *Reports on Progress in Physics*, 77 (5):056501, 2014.

[45] P. W. Anderson. Resonating Valence Bonds: A New Kind of Insulator? *Materials Research Bulletin*, 8(2):153–160, 1973.

[46] X.-G. Wen. Quantum Orders and Symmetric Spin Liquids. *Physical Review B*, 65 (16):165113, 2002.

[47] Y. Li. $YbMgGaO_4$: A Triangular-Lattice Quantum Spin Liquid Candidate. *Advanced Quantum Technologies*, 2(12):1900089, 2019.

[48] M. R. Norman. Colloquium: Herbertsmithite and the Search for the Quantum Spin Liquid. *Reviews of Modern Physics*, 88(4):041002, 2016.

[49] K. Kitagawa, T. Takayama, Y. Matsumoto, A. Kato, R. Takano, Y. Kishimoto, S. Bette, R. Dinnebier, G. Jackeli, and H. Takagi. A Spin–Orbital–Entangled Quantum Liquid on a Honeycomb Lattice. *Nature*, 554(7692):341–345, 2018.

[50] J. Wang, W. Yuan, P. M. Singer, R. W. Smaha, W. He, J. Wen, Y. S. Lee, and T. Imai. Emergence of Spin Singlets with Inhomogeneous Gaps in the Kagome Lattice Heisenberg Antiferromagnets Zn-barlowite and Herbertsmithite. *Nature Physics*, 17(10):1109–1113, 2021.

[51] R. Yadav, R. Ray, M. S. Eldeeb, S. Nishimoto, L. Hozoi, and J. van den Brink. Strong Effect of Hydrogen Order on Magnetic Kitaev Interactions in $H_3LiIr_2O_6$. *Physical Review Letters*, 121:197203, 2018.

[52] C. Draxl, D. Nabok, and K. Hannewald. Organic/Inorganic Hybrid Materials: Challenges for Ab Initio Methodology. *Accounts of Chemical Research*, 47(11):3225–3232, 2014.

[53] V. L. Deringer, D. M. Proserpio, G. Csányi, and C. J. Pickard. Data-driven Learning and Prediction of Inorganic Crystal Structures. *Faraday Discussions*, 211:45–59, 2018.

[54] X. Yin and C. E. Gounaris. Search Methods for Inorganic Materials Crystal Structure Prediction. *Current Opinion in Chemical Engineering*, 35:100726, 2022.

[55] J. A. M. Paddison, H. Jacobsen, O. A. Petrenko, M. T. Fernández-Díaz, P. P. Deen, and A. L. Goodwin. Hidden Order in Spin-liquid $Gd_3Ga_5O_{12}$. *Science*, 350(6257): 179–181, 2015.

[56] J. A. Mydosh and P. M. Oppeneer. Colloquium: Hidden Order, Superconductivity, and Magnetism: The Unsolved Case of URu_2Si_2. *Reviews of Modern Physics*, 83: 1301–1322, 2011.

[57] V. Grover, Balaji P. Mandal, and A. K. Tyagi. *Handbook on Synthesis Strategies for Advanced Materials : Volume-I: Techniques and Fundamentals*, pages 1–49. Springer Singapore, 2021.

[58] M. Aykol, J. H. Montoya, and J. Hummelshøj. Rational Solid-state Synthesis Routes for Inorganic Materials. *Journal of the American Chemical Society*, 143(24):9244–9259, 2021.

[59] L. E. Smart and E. A. Moore. *Solid State Chemistry: An Introduction*. CRC press, 2012.

[60] A. Vartanian. Breaking Down Ceramic Synthesis. *Nature Reviews Materials*, 6(6): 464–464, 2021.

[61] K. A. Ross, L. R. Yaraskavitch, M. Laver, J. S. Gardner, J. A. Quilliam, S. Meng, J. B. Kycia, D. K. Singh, Th. Proffen, H. A. Dabkowska, and B. D. Gaulin. Dimensional Evolution of Spin Correlations in the Magnetic Pyrochlore $Yb_2Ti_2O_7$. *Physical Review B*, 84:174442, 2011.

[62] S. Rayaprol, Kausik Sengupta, and E. V. Sampathkumaran. Magnetic Frustration in the Stoichiometric Spin-chain Compound Ca_3CoIrO_6. *Physical Review B*, 67: 180404, 2003.

[63] T. Katsufuji, S. Mori, M. Masaki, Y. Moritomo, N. Yamamoto, and H. Takagi. Dielectric and Magnetic Anomalies and Spin Frustration in Hexagonal RMnO$_3$ (R = Y, Yb, and Lu). *Physical Review B*, 64:104419, 2001.

[64] S. J. Singh, S. J. Cassidy, M. Bristow, S. J. Blundell, S. J. Clarke, and A. I. Coldea. Optimization of Superconducting Properties of the Stoichiometric $CaKFe_4As_4$. *Superconductor Science and Technology*, 33(2):025003, 2019.

[65] M. Jansen. A Concept for Synthesis Planning in Solid-state Chemistry. *Angewandte Chemie International Edition*, 41(20):3746–3766, 2002.

[66] O. J. Rutt, G. R. Williams, and S. J. Clarke. Reversible Lithium Insertion and Copper Extrusion in Layered Oxysulfides. *Chemical communications*, (27):2869–2871, 2006.

[67] F. Kubel, M. Pantazi, N. Wandl, and H. Hagemann. Synthesis and Crystal Structures of a Stable, a Metastable and a High Temperature Modification of Pb_2NaIO_6. *Zeitschrift für anorganische und allgemeine Chemie*, 640(15):3184–3189, 2014.

[68] S. Mugiraneza and A. M. Hallas. Tutorial: A Beginner's Guide to Interpreting Magnetic Susceptibility Data with the Curie-Weiss Law. *Communications Physics*, 5(1):1–12, 2022.

[69] J. Clarke and A. I. Braginski. *The SQUID Handbook: Fundamentals and Technology of SQUIDs and SQUID Systems*. Wiley-Vch, 2003.

[70] R. L. Fagaly. Superconducting Quantum Interference Device Instruments and Applications. *Review of Scientific Instruments*, 77(10):101101, 2006.

[71] C.-L. Huang, A. M. Hallas, K. Grube, S. Kuntz, B. Spieß, K. Bayliff, T. Besara, T. Siegrist, Y. Cai, J. Beare, G. M. Luke, and E. Morosan. Quantum Critical Point in the Itinerant Ferromagnet $Ni_{1-x}Rh_x$. *Physical Review Letters*, 124(11):117203, 2020.

[72] A. M. Hallas, A. Z. Sharma, Y. Cai, T. J. Munsie, M. N. Wilson, M. Tachibana, C. R. Wiebe, and G. M. Luke. Relief of Frustration in the Heisenberg Pyrochlore Antiferromagnet $Gd_2Pt_2O_7$. *Physical Review B*, 94:134417, 2016.

[73] A. M Hallas and E. Morosan. $Sr(M,Te)_2O_6$ (M = Cr, Mn, Fe, Co, Ni): A Magnetically Dilute Family of Honeycomb Tellurates. *Inorganic Chemistry*, 58:6993–6999, 2019.

[74] A. H. Abdeldaim, D. I. Badrtdinov, A. S. Gibbs, P. Manuel, H. C. Walker, M. D. Le, C. H. Wu, D. Wardecki, S.-G. Eriksson, Y. O. Kvashnin, A. A. Tsirlin, and G. J.

Nilsen. Large Easy-axis Anisotropy in the One-Dimensional Magnet $BaMo(PO_4)_2$. *Physical Review B*, 100:214427, 2019.

[75] K. Tustain, B. Ward-O'Brien, F. Bert, T. Han, H. Luetkens, T. Lancaster, B. M. Huddart, P. J. Baker, and L. Clark. From Magnetic Order to Quantum Disorder in the Zn-barlowite Series of $S = 1/2$ Kagomé Antiferromagnets. *npj Quantum Materials*, 5(1):1–9, 2020.

[76] A. Lohmann, H.-J. Schmidt, and J. Richter. Tenth-order High-temperature Expansion for the Susceptibility and the Specific Heat of Spin-S Heisenberg Models with Arbitrary Exchange Patterns: Application to Pyrochlore and Kagome Magnets. *Physical Review B*, 89:014415, 2014.

[77] A. Hehn, N. van Well, and M. Troyer. High-temperature Series Expansion for Spin-1/2 Heisenberg Models. *Computer Physics Communications*, 212:180–188, 2017.

[78] A. Gaenko, A.E. Antipov, G. Carcassi, T. Chen, X. Chen, Q. Dong, L. Gamper, J. Gukelberger, R. Igarashi, S. Iskakov, M. Könz, J.P.F. LeBlanc, R. Levy, P.N. Ma, J.E. Paki, H. Shinaoka, S. Todo, M. Troyer, and E. Gull. Updated Core Libraries of the ALPS Project. *Computer Physics Communications*, 213:235–251, 2017. ISSN 0010-4655.

[79] B. Bauer, L. D. Carr, H. G. Evertz, A. Feiguin, J. Freire, S. Fuchs, L. Gamper, J. Gukelberger, E. Gull, S. Guertler, A. Hehn, R. Igarashi, S. V. Isakov, D. Koop, P. N. Ma, P. Mates, H. Matsuo, O. Parcollet, G. Pawłowski, J. D. Picon, L. Pollet, E. Santos, V. W. Scarola, U. Schollwöck, C. Silva, B. Surer, S. Todo, S. Trebst, M. Troyer, M. L. Wall, P. Werner, and S. Wessel. The ALPS Project Release 2.0: Open Source Software for Strongly Correlated Systems. *Journal of Statistical Mechanics: Theory and Experiment*, 2011(05):P05001, 2011.

[80] G. Ventura and M. Perfetti. *Thermal Properties of Solids at Room and Cryogenic Temperatures*. Springer, 2014.

[81] C. A. Pocs, I. A. Leahy, H. Zheng, G. Cao, E.-S. Choi, S.-H. Do, K.-Y. Choi, B. Normand, and M. Lee. Giant Thermal Magnetoconductivity in $CrCl_3$ and a General Model for Spin-phonon Scattering. *Physical Review Research*, 2(1):013059, 2020.

[82] Simon S. H. *The Oxford Solid State Basics.* OUP Oxford, 2013.

[83] O. Mustonen, S. Vasala, E. Sadrollahi, K. P. Schmidt, C. Baines, H. C. Walker, I. Terasaki, F. J. Litterst, E. Baggio-Saitovitch, and M. Karppinen. Spin-liquid-like State in a Spin-1/2 Square-lattice Antiferromagnet Perovskite Induced by $d10^{\smile}d0$ Cation Mixing. *Nature Communications*, 9:1085, 2018.

[84] B. Gao, T. Chen, D. W. Tam, C.-L. Huang, K. Sasmal, D. T. Adroja, F. Ye, H. Cao, G. Sala, M. B. Stone, C. Baines, J. A. T. Verezhak, H. Hu, J.-H. Chung, X. Xu, S.-W. Cheong, M. Nallaiyan, S. Spagna, M. B. Maple, A. H. Nevidomskyy, E. Morosan, G. Chen, and P. Dai. Experimental Signatures of a Three-dimensional Quantum Spin Liquid in Effective Spin-1/2 $Ce_2Zr_2O_7$ Pyrochlore. *Nature Physics*, 15(10):1052–1057, 2019.

[85] G. L. Squires. *Introduction to the Theory of Thermal Neutron Scattering.* Cambridge University Press, 1996.

[86] A. T. Boothroyd. *Principles of Neutron Scattering from Condensed Matter.* Oxford University Press, 2020.

[87] C. Kittel and P. McEuen. *Introduction to Solid State Physics.* John Wiley & Sons, 2018.

[88] H. M. Rietveld. A Profile Refinement Method for Nuclear and Magnetic Structures. *Journal of Applied Crystallography*, 2(2):65–71, 1969.

[89] B. H. Toby. R Factors in Rietveld Analysis: How Good is Good Enough? *Powder Diffraction*, 21(1):67–70, 2006.

[90] J. Rodríguez-Carvajal. Recent Advances in Magnetic Structure Determination by Neutron Powder Diffraction. *Physica B: Condensed Matter*, 192(1):55–69, 1993.

[91] B. H. Toby. *EXPGUI*, a Graphical User Interface for *GSAS*. *Journal of Applied Crystallography*, 34(2):210–213, 2001.

[92] B. H. Toby and R. B. Von Dreele. *GSAS-II*: The Genesis of a Modern Open-source All Purpose Crystallography Software Package. *Journal of Applied Crystallography*, 46(2):544–549, 2013.

[93] K. Tustain, L. Farrar, W. Yao, P. Lightfoot, I. da Silva, M. T. F. Telling, and L. Clark. Materialization of a Geometrically Frustrated Magnet in a Hybrid Coordination Framework: A Study of the Iron(II) Oxalate Fluoride Framework, $KFe(C_2O_4)F$. *Inorganic Chemistry*, 58:11971–11977, 2019.

[94] N. Qureshi. *Magnetic Properties of the Kagome Staircase Mixed System* $(Co_xNi_{1-x})_3V_2O_8$. PhD thesis, Technische Universität, Darmstadt, 2009.

[95] J. M. Perez-Mato, J. L. Ribeiro, V. Petricek, and M. I. Aroyo. Magnetic Superspace Groups and Symmetry Constraints in Incommensurate Magnetic Phases. *Journal of Physics: Condensed Matter*, 24(16):163201, 2012.

[96] J. González-Platas, N. A. Katcho, and J. Rodríguez-Carvajal. Extension of Hall Symbols of Crystallographic Space Groups to Magnetic Space Groups. *Journal of Applied Crystallography*, 54(1):338–342, 2021.

[97] N. V. Belov, N. N. Neronova, and T. S. Smirnova. Shubnikov Groups. *Kristallografiya*, 2(3):315–325, 1957.

[98] E. F. Bertaut. Representation Analysis of Magnetic Structures. *Acta Crystallographica Section A: Crystal Physics, Diffraction, Theoretical and General Crystallography*, 24(1):217–231, 1968.

[99] A. S. Wills. A New Protocol for the Determination of Magnetic Structures Using Simulated Annealing and Representational Analysis (SARAh). *Physica B: Condensed Matter*, 276-278:680–681, 2000.

[100] N. Qureshi. Mag2Pol: A Program for the Analysis of Spherical Neutron Polarimetry, Flipping Ratio and Integrated Intensity Data. *Journal of Applied Crystallography*, 52:175–185, 2019.

[101] B. J. Campbell, H. T. Stokes, D. E. Tanner, and D. M. Hatch. *ISODISPLACE*: A Web-based Tool for Exploring Structural Distortions. *Journal of Applied Crystallography*, 39(4):607–614, 2006.

[102] A. J. Princep, R. A. Ewings, S. Ward, S. Tóth, C. Dubs, D. Prabhakaran, and A. T. Boothroyd. The Full Magnon Spectrum of Yttrium Iron Garnet. *npj Quantum Materials*, 2(1):1–5, 2017.

[103] N. D. Mermin and H. Wagner. Absence of Ferromagnetism or Antiferromagnetism in One- or Two-dimensional Isotropic Heisenberg Models. *Physical Review Letters*, 17:1133–1136, 1966.

[104] L. Hulthén. *Über das Austauschproblem eines Kristalles*. PhD thesis, Stockholm College, 1938.

[105] A. Vasiliev, O. Volkova, E. Zvereva, and M. Markina. Milestones of Low-d Quantum Magnetism. *npj Quantum Materials*, 3:18, 2018.

[106] A. H. Abdeldaim, A. A. Tsirlin, J. Ollivier, C. Ritter, D. Fortes, R. S. Perry, L. Clark, and G. J. Nilsen. One-dimensional Quantum Magnetism in the $S = 1/2$ Mo(V) System, $KMoOP_2O_7$. *arXiv:2207.01284*, 2022.

[107] K. M. Kojima, Y. Fudamoto, M. Larkin, G. M. Luke, J. Merrin, B. Nachumi, Y. J. Uemura, N. Motoyama, H. Eisaki, S. Uchida, K. Yamada, Y. Endoh, S. Hosoya, B. J. Sternlieb, and G. Shirane. Reduction of Ordered Moment and Néel Temperature of

Quasi-One-Dimensional Antiferromagnets Sr_2CuO_3 and Ca_2CuO_3. *Physical Review Letters*, 78:1787–1790, 1997.

[108] H. Rosner, H. Eschrig, R. Hayn, S.-L. Drechsler, and J. Málek. Electronic Structure and Magnetic Properties of the Linear Chain Cuprates Sr_2CuO_3 and Ca_2CuO_3. *Physical Review B*, 56:3402–3412, 1997.

[109] G. J. Nilsen, A. Raja, A. A. Tsirlin, H. Mutka, D. Kasinathan, C. Ritter, and H. M. Rønnow. One-dimensional Quantum Magnetism in the Anhydrous Alum $KTi(SO_4)_2$. *New Journal of Physics*, 17:113035, 2015.

[110] L. S. Wu, S. E. Nikitin, Z. Wang, W. Zhu, C. D. Batista, A. M. Tsvelik, A. M. Samarakoon, D. A. Tennant, M. Brando, L. Vasylechko, M. Frontzek, A. T. Savici, G. Sala, G. Ehlers, A. D. Christianson, M. D. Lumsden, and A. Podlesnyak. Tomonaga–Luttinger Liquid Behavior and Spinon Confinement in $YbAlO_3$. *Nature communications*, 10(1):1–9, 2019.

[111] C. K. Majumdar and D. K. Ghosh. On Next-nearest-neighbor Interaction in Linear Chain. I. *Journal of Mathematical Physics*, 10(8):1388–1398, 1969.

[112] Chanchal K. Majumdar and Dipan K. Ghosh. On Next-nearest-neighbor Interaction in Linear Chain. II. *Journal of Mathematical Physics*, 10(8):1399–1402, 1969.

[113] F. D. M. Haldane. Spontaneous Dimerization in the $S = 1/2$ Heisenberg Antiferromagnetic Chain with Competing Interactions. *Physical Review B*, 25:4925–4928, 1982.

[114] S. Eggert. Numerical Evidence for Multiplicative Logarithmic Corrections from Marginal Operators. *Physical Review B*, 54:R9612–R9615, 1996.

[115] K. Okamoto and K. Nomura. Fluid-dimer Critical Point in $S = 1/2$ Antiferromagnetic Heisenberg Chain with Next Nearest Neighbor Interactions. *Physics Letters A*, 169:433–437, 1992.

[116] M. Kumar, S. Ramasesha, and Z. G. Soos. Bond-order Wave Phase, Spin Solitons, and Thermodynamics of a Frustrated Linear Spin-$\frac{1}{2}$ Heisenberg Antiferromagnet. *Physical Review B*, 81:054413, 2010.

[117] A. Berlie and I. Terry. Possible Realization of the Majumdar-Ghosh Point in the Mineral Szenicsite. *Physical Review B*, 105:L220404, 2022.

[118] S. Lebernegg, O. Janson, I. Rousochatzakis, S. Nishimoto, H. Rosner, and A. A. Tsirlin. Frustrated Spin Chain Physics Near the Majumdar-Ghosh Point in Szenicsite $Cu_3(MoO_4)(OH)_4$. *Physical Review B*, 95:035145, 2017.

[119] S. Vilminot, G. André, M. Richard-Plouet, F. Bourée-Vigneron, and M. Kurmoo. Magnetic Structure and Magnetic Properties of Synthetic Lindgrenite, $Cu_3(OH)_2(MoO_4)_2$. *Inorganic Chemistry*, 45:10938–10946, 2006.

[120] G. J. Nilsen, H. M. Rønnow, A. M. Läuchli, F. P. A. Fabbiani, J. Sanchez-Benitez, K. V. Kamenev, and A. Harrison. A New Realisation of The $S = 1/2$ Frustrated Chain Antiferromagnet. *Chemistry of Materials*, 20(1):8–10, 2008.

[121] D. Kasinathan, K. Koepernik, O. Janson, G. J. Nilsen, J. O. Piatek, H. M. Rønnow, and H. Rosner. Electronic Structure of $KTi(SO_4)_2 \cdot H_2O$: An $S = 1/2$ Frustrated Chain Antiferromagnet. *Physical Review B*, 88(22):224410, 2013.

[122] A. Leclaire, A. Benmoussa, M. M. Borel, A. Grandin, and B. Raveau. Two Forms of Sodium titanium (III) Diphosphate: α-$NaTiP_2O_7$ Closely Related to β-cristobalite and β-$NaTiP_2O_7$ Isotypic with $NaFeP_2O_7$. *Journal of Solid State Chemistry*, 77(2): 299–305, 1988.

[123] Y. E. Gorbunova, S. A. Linde, A. V. Lavrov, and L. V. Tananaev. Structure of Crystals of Potassium Vanadyl Pyrophosphate $K_2VOP_2O_7$. In *Soviet Physics Doklady*, volume 25, page 9, 1980.

[124] D. Bregiroux, K. Popa, and G. Wallez. Crystal Chemistry of $M^{II}M'^{IV}(PO_4)_2$ Double Monophosphates. *Journal of Solid State Chemistry*, 230:26–33, 2015.

[125] E. Canadell, J. Provost, A. Guesdon, M. M. Borel, and A. Leclaire. Magnetic Properties and New Structural Classification of Molybdenum Phosphates Containing Mo(V). *Chemistry of Materials*, 9:68–75, 1997.

[126] S. Boudin, A. Guesdon, A. Leclaire, and M.-M. Borel. Review on Vanadium Phosphates with Mono and Divalent Metallic Cations: Syntheses, Structural Relationships and Classification, Properties. *International Journal of Inorganic Materials*, 2(6):561–579, 2000.

[127] S. Ledain, A. Leclaire, M. M. Borel, J. Provost, and B. Raveau. A Molybdenum V Diphosphate with the $KMoOP_2O_7$ Structure: $NaMoOP_2O_7$. *Journal of Solid State Chemistry*, 124:24–28, 1996.

[128] C. Gueho, M. M. Borel, A. Grandin, A. Leclaire, and B. Raveau. Crystal Structure of the Molybdenum(V) Diphosphate $KMoP_2O_8$ Isotypic with $KNbP_2O_8$. *Zeitschrift für anorganische und allgemeine Chemie*, 615:104–108, 1992.

[129] A. Guesdon, M. M. Borel, A. Leclaire, A. Grandin, and B. Raveau. A Molybdenum (V) Diphosphate Closely Related to the α-$NaTiP_2O_7$ Structure: $Cs(MoO)P_2O_7$. *Journal of Solid State Chemistry*, 108:46–50, 1994.

[130] S. Ledain, M. M. Borel, A. Leclaire, J. Provost, and B. Raveau. A Molybdenum V Diphosphate Involving LiO_4 Tetrahedra: $LiMoOP_2O_7$. *Journal of Solid State Chemistry*, 120:260–267, 1995.

[131] D. Urushihara, S. Kawaguchi, K. Fukuda, and T. Asaka. Crystal Structure and Magnetism in the $S = 1/2$ Spin Dimer Compound $NaCu_2VP_2O_10$. *IUCrJ*, 7:656–662, 2020.

[132] P. K. Mukharjee, K. Somesh, K. M. Ranjith, M. Baenitz, Y. Skourski, D. T. Adroja, D. Khalyavin, A. A. Tsirlin, and R. Nath. Quantum Magnetism of Ferromagnetic Spin Dimers in $KVOPO_2$. *Physical Review B*, 104:224409, 2021.

[133] D. A. Tennant, S. E. Nagler, A. W. Garrett, T. Barnes, and C. C. Torardi. Excitation Spectrum and Superexchange Pathways in the Spin Dimer $VODPO_4 \cdot \frac{1}{2}D_2O$. *Physical Review Letters*, 78:4998–5001, 1997.

[134] A. W. Garrett, S. E. Nagler, D. A. Tennant, B. C. Sales, and T. Barnes. Magnetic Excitations in the $S = 1/2$ Alternating Chain Compound $(VO)_2P_2O_7$. *Physical Review Letters*, 79:745–748, 1997.

[135] M. A. de Vries, A. C. Mclaughlin, and J.-W. G. Bos. Valence Bond Glass on an fcc Lattice in the Double Perovskite Ba_2YMoO_6. *Physical Review Letters*, 104:177202, 2010.

[136] L. Clark, G. J. Nilsen, E. Kermarrec, G. Ehlers, K. S. Knight, A. Harrison, J. P. Attfield, and B. D. Gaulin. From Spin Glass to Quantum Spin Liquid Ground States in Molybdate Pyrochlores. *Physical Review Letters*, 113:117201, 2014.

[137] D. C. Johnston, R. K. Kremer, M. Troyer, X. Wang, A. Klümper, S. L. Bud'ko, A. F. Panchula, and P. C. Canfield. Thermodynamics of Spin $S = 1/2$ Antiferromagnetic Uniform and Alternating-Exchange Heisenberg Chains. *Physical Review B*, 61:9558–9606, 2000.

[138] B. Bernu and G. Misguich. Specific Heat and High-temperature Series of Lattice Models: Interpolation Scheme and Examples on Quantum Spin Systems in One and Two Dimensions. *Physical Review B*, 63:134409, 2001.

[139] H. J. Schulz. Dynamics of Coupled Quantum Spin Chains. *Physical Review Letters*, 77:2790–2793, 1996.

[140] D. G. Henshaw. Effect of the λ Transition on the Atomic Distribution in Liquid Helium by Neutron Diffraction. *Physical Review*, 119:9–13, 1960.

[141] A. A. Belik, S. Uji, T. Terashima, and E. Takayama-Muromachi. Long-range Magnetic Ordering of Quasi-one-dimensional $S = 1/2$ Heisenberg Antiferromagnet $Sr_2Cu(PO_4)_2$. *Journal of Solid State Chemistry*, 178:3461–3463, 2005.

[142] K. Koepernik and H. Eschrig. Full-potential Nonorthogonal Local-orbital Minimum-basis Band-Structure Scheme. *Physical Review B*, 59:1743–1757, 1999.

[143] J. P. Perdew, K. Burke, and M. Ernzerhof. Generalized Gradient Approximation Made Simple. *Physical Review Letters*, 77:3865–3868, 1996.

[144] A. A. Tsirlin. Spin-chain Magnetism and Uniform Dzyaloshinsky-Moriya Anisotropy in BaV_3O_8. *Physical Review B*, 89:014405, 2014.

[145] H. J. Xiang, E.J. Kan, S.-H. Wei, M.-H. Whangbo, and X.G. Gong. Predicting the Spin-lattice Order of Frustrated Systems from First Principles. *Physical Review B*, 84:224429, 2011.

[146] J.-S. Caux and R. Hagemans. The Four-spinon Dynamical Structure Factor of the Heisenberg Chain. *Journal of Statistical Mechanics: Theory and Experiment*, 2006: P12013–P12013, 2006.

[147] M. Kohno, O. A Starykh, and L. Balents. Spinons and Triplons in Spatially Anisotropic Frustrated Antiferromagnets. *Nature Physics*, 3:790–795, 2007.

[148] A. Leclaire, J. Chardon, and B. Raveau. Stabilization of the Tungstyl Ion Configuration: the W(V) Diphosphate $KWOP_2O_7$. *Journal of Materials Chemistry*, 11: 846–848, 2001.

[149] D. Mezaoui, S. Belkhiri, R. Belhouas, A. Leclaire, and H. Rebbah. Crystal Structure of $RbWOP_2O_7$ a New Diphosphate W(V) Isotypic with $KWOP_2O_7$. *Acta Crystallographica Section A*, 63(a1):s55, 2007.

[150] I. V. Tananaev. New Data on the Phosphates of Polyvalent Metals. *Pure and Applied Chemistry*, 52(4):1099–1115, 1980.

[151] A. B. Yaroslavtsev and A. E. Nikolaev. Synthesis and Proton Conductivity of Acid Tantalum Phosphate. *Mendeleev Communications*, 5(4):136–137, 1995.

[152] G. Kresse and J. Furthmüller. Efficiency of *Ab-initio* Total Energy Calculations for Metals and Semiconductors Using a Plane-wave Basis Set. *Computational Materials Science*, 6:15, 1996.

[153] G. Kresse and J. Furthmüller. Efficient iterative schemes for *ab initio* total-energy calculations using a plane-wave basis set. *Physical Review B*, 54:11169, 1996.

[154] E. Kanda, T. Haseda, and A. Ötsubo. Paramagnetic Susceptibility of Solid Oxygen. *Physica*, 20(1-6):131–132, 1954.

[155] R. Gover, J. Irvine, and A. Finch. Transformation of $LiTi_2O_4$ from Spinel to Ramsdellite on Heating. *Journal of Solid State Chemistry*, 132:382–388, 1997.

[156] J. M. Perez-Mato, S.V. Gallego, E.S. Tasci, L. Elcoro, G. de la Flor, and M.I. Aroyo. Symmetry-based Computational Tools for Magnetic Crystallography. *Annual Review of Materials Research*, 45(1):217–248, 2015.

[157] S. C. Miller and W. F. Love. *Tables of Irreducible Representations of Space Groups and Co-representations of Magnetic Space Groups*. Pruett Press, 1967.

[158] M. Roca, P. Amorós, J. Cano, M. Dolores Marcos, J. Alamo, A. Beltrán-Porter, and D. Beltrán-Porter. Prediction of Magnetic Properties in Oxovanadium(IV) Phosphates: The Role of the Bridging PO_4 Anions. *Inorg. Chem.*, 37(13):3167–3174, 1998.

[159] K. Paidi A, R. N. Devi, and K. Vidyasagar. Synthesis and Structural Characterization of AMV_2O_8 (A = K, Rb, Tl, Cs; M = Nb, Ta) Vanadates: A Structural

Comparison of $A^{+}M^{5+}V_2O_8$ Vanadates and $A^{+}M^{5+}P_2O_8$ Phosphates. *Dalton Transactions*, 44:17399–17408, 2015.

[160] A. Leclaire, A. Benmoussa, M.M. Borel, A. Grandin, and B. Raveau. Two Forms of Sodium Titanium(III) Diphosphate: α-$NaTiP_2O_7$ Closely Related to β-Cristobalite and β-$NaTiP_2O_7$ Isotypic With $NaFeP_2O_7$. *Journal of Solid State Chemistry*, 77 (2):299–305, 1988.

[161] M. Hermanns, I. Kimchi, and J. Knolle. Physics of the Kitaev Model: Fractionalization, Dynamic Correlations, and Material Connections. *Annual Review of Condensed Matter Physics*, 9:17–33, 2018.

[162] S. M. Winter, A. A. Tsirlin, M. Daghofer, J. van den Brink, Y. Singh, P. Gegenwart, and R. Valentí. Models and Materials for Generalized Kitaev Magnetism. *Journal of Physics: Condensed Matter*, 29(49):493002, 2017.

[163] P. A. Maksimov and A. L. Chernyshev. Rethinking α-$RuCl_3$. *Physical Review Research*, 2:033011, 2020.

[164] J. G. Rau, E. K.-H. Lee, and H.-Y. Kee. Generic Spin Model for the Honeycomb Iridates beyond the Kitaev Limit. *Physical Review Letters*, 112:077204, 2014.

[165] G. Jackeli and G. Khaliullin. Mott Insulators in the Strong Spin-Orbit Coupling Limit: From Heisenberg to a Quantum Compass and Kitaev Models. *Physical Review Letters*, 102(1):017205, 2009.

[166] P. P. Stavropoulos, D. Pereira, and H.-Y. Kee. Microscopic Mechanism for a Higher-Spin Kitaev Model. *Physical Review Letters*, 123(3):037203, 2019.

[167] H. Liu and G. Khaliullin. Pseudospin Exchange Interactions in d^7 Cobalt Compounds: Possible Realization of the Kitaev Model. *Physical Review B*, 97(1):014407, 2018.

[168] Y. Motome, R. Sano, S. Jang, Y. Sugita, and Y. Kato. Materials Design of Kitaev Spin Liquids Beyond the Jackeli–Khaliullin Mechanism. *Journal of Physics: Condensed Matter*, 32(40):404001, 2020.

[169] S.-Y. Park, S.-H. Do, K.-Y. Choi, D. Jang, T.-H. Jang, J. Schefer, C.-M. Wu, J. S. Gardner, J. M. S. Park, J.-H. Park, and S. Ji. Emergence of the Isotropic Kitaev Honeycomb Lattice with Two-dimensional Ising Universality in α-$RuCl_3$. *arXiv/1609.05690*, 2016.

[170] F. Bahrami, W. Lafargue-Dit-Hauret, O. I. Lebedev, R. Movshovich, H.-Y. Yang, D. Broido, X. Rocquefelte, and F. Tafti. Thermodynamic Evidence of Proximity to a Kitaev Spin Liquid in $Ag_3LiIr_2O_6$. *Physical Review Letters*, 123:237203, 2019.

[171] Faranak Bahrami, Eric M. Kenney, Chennan Wang, Adam Berlie, Oleg I. Lebedev, Michael J. Graf, and Fazel Tafti. Effect of Structural Disorder on the Kitaev Magnet $Ag_3LiIr_2O_6$. *Physical Review B*, 103:094427, 2021.

[172] H. B. Cao, A. Banerjee, J.-Q. Yan, C. A. Bridges, M. D. Lumsden, D. G. Mandrus, D. A. Tennant, B. C. Chakoumakos, and S. E. Nagler. Low-temperature Crystal and Magnetic Structure of α-$RuCl_3$. *Physical Review B*, 93:134423, 2016.

[173] K. W. Plumb, J. P. Clancy, L. J. Sandilands, V. V. Shankar, Y. F. Hu, K. S. Burch, H.-Y. Kee, and Y.-J. Kim. α-$RuCl_3$: A Spin-orbit Assisted Mott Insulator on a Honeycomb Lattice. *Physical Review B*, 90:041112(R), 2014.

[174] X. Zhou, H. Li, J. A. Waugh, S. Parham, H.-S. Kim, J. A. Sears, A. Gomes, H.-Y. Kee, Y.-J. Kim, and D. S. Dessau. Angle-resolved Photoemission Study of the Kitaev Candidate α- $RuCl_3$. *Physical Review B*, 94(16):161106, 2016.

[175] L. J. Sandilands, Y. Tian, A. A. Reijnders, H.-S. Kim, K. W. Plumb, Y.-J. Kim, H.-Y. Kee, and K. S. Burch. Spin-orbit Excitations and Electronic Structure of the Putative Kitaev Magnet α- $RuCl_3$. *Physical Review B*, 93(7):075144, 2016.

[176] H. Suzuki, H. Liu, J. Bertinshaw, K. Ueda, H. Kim, S. Laha, D. Weber, Z. Yang, L. Wang, H. Takahashi, K. Fürsich, M. Minola, B. V. Lotsch, B. J. Kim, H. Yavaş, M. Daghofer, J. Chaloupka, G. Khaliullin, H. Gretarsson, and B. Keimer. Proximate Ferromagnetic State in the Kitaev Model Material α-$RuCl_3$. *Nature Communications*, 12:4512, 2021.

[177] Y. Li, S. M. Winter, D. A. S. Kaib, K. Riedl, and R. Valentí. Modified Curie-Weiss Law for j_{eff} Magnets. *Physical Review B*, 103:L220408, 2021.

[178] M. Majumder, M. Schmidt, H. Rosner, A. A. Tsirlin, H. Yasuoka, and M. Baenitz. Anisotropic $Ru^{3+}4d^5$ Magnetism in the $\alpha - RuCl_3$ Honeycomb System: Susceptibility, Specific Heat, and Zero-field NMR. *Physical Review B*, 91:180401, 2015.

[179] S. Kim, B. Yuan, and Y.-J. Kim. α-$RuCl_3$ and Other Kitaev Materials. *APL Materials*, 10(8):080903, 2022.

[180] P. Lampen-Kelley, S. Rachel, J. Reuther, J.-Q. Yan, A. Banerjee, C. A. Bridges, H. B. Cao, S. E. Nagler, and D. Mandrus. Anisotropic Susceptibilities in the Honeycomb Kitaev System α- $RuCl_3$. *Physical Review B*, 98(10):100403, 2018.

[181] R. D. Johnson, S. C. Williams, A. A. Haghighirad, J. Singleton, V. Zapf, P. Manuel, I. I. Mazin, Y. Li, H. O. Jeschke, R. Valentí, and R. Coldea. Monoclinic Crystal Structure of α-$RuCl_3$ and the Zigzag Antiferromagnetic Ground State. *Physical Review B*, 92:235119, 2015.

[182] A. Banerjee, J. Yan, J. Knolle, C. A. Bridges, M. B. Stone, M. D. Lumsden, D. G. Mandrus, D. A. Tennant, R. Moessner, and S. E. Nagler. Neutron Scattering in the Proximate Quantum Spin Liquid α-$RuCl_3$. *Science*, 356(6342):1055–1059, 2017.

[183] C. Balz, P. Lampen-Kelley, A. Banerjee, J. Yan, Z. Lu, X. Hu, S. M. Yadav, Y. Takano, Y. Liu, D. A. Tennant, M. D. Lumsden, D. Mandrus, and S. E. Nagler. Finite Field Regime for a Quantum Spin Liquid in α- $RuCl_3$. *Physical Review B*, 100(6):060405, 2019.

[184] S. M. Winter, K. Riedl, P. A. Maksimov, A. L. Chernyshev, A. Honecker, and R. Valentí. Breakdown of Magnons in a Strongly Spin-Orbital Coupled Magnet. *Nature Communications*, 8(1):1–8, 2017.

[185] J. A. Sears, L. E. Chern, S. Kim, P. J. Bereciartua, S. Francoual, Y. B. Kim, and Y.-J. Kim. Ferromagnetic Kitaev Interaction and the Origin of Large Magnetic Anisotropy in α-$RuCl_3$. *Nature Physics*, 16(8):837–840, 2020.

[186] P. Laurell and S. Okamoto. Dynamical and Thermal Magnetic Properties of the Kitaev Spin Liquid Candidate α-$RuCl_3$. *npj Quantum Materials*, 5(1):1–10, 2020.

[187] J. G. Rau, E. K.-H. Lee, and H.-Y. Kee. Spin-orbit Physics Giving Rise to Novel Phases in Correlated Systems: Iridates and Related Materials. *Annual Review of Condensed Matter Physics*, 7(1):195–221, 2016.

[188] Jeffrey G. Rau and Hae-Young Kee. Trigonal Distortion in the Honeycomb Iridates: Proximity of Zigzag and Spiral Phases in Na_2IrO_3. *10.48550/arxiv.1408.4811*, 2014.

[189] S. C. Williams, R. D. Johnson, F. Freund, Sungkyun Choi, A. Jesche, I. Kimchi, S. Manni, A. Bombardi, P. Manuel, P. Gegenwart, and R. Coldea. Incommensurate Counterrotating Magnetic Order Stabilized by Kitaev Interactions in the Layered Honeycomb α-Li_2IrO_3. *Physical Review B*, 93(19):195158, 2016.

[190] F. Freund, S. C. Williams, R. D. Johnson, R. Coldea, P. Gegenwart, and A. Jesche. Single Crystal Growth From Separated Educts and its Application to Lithium Transition-Metal Oxides. *Scientific Reports*, 6(1):1–6, 2016.

[191] A. Biffin, R. D. Johnson, I. Kimchi, R. Morris, A. Bombardi, J. G. Analytis, A. Vishwanath, and R. Coldea. Noncoplanar and Counterrotating Incommensurate Magnetic Order Stabilized by Kitaev Interactions in γ-Li_2IrO_3. *Physical Review Letters*, 113(19):197201, 2014.

[192] A. Biffin, R. D. Johnson, S. Choi, F. Freund, S. Manni, A. Bombardi, P. Manuel, P. Gegenwart, and R. Coldea. Unconventional Magnetic Order on the Hyperhoneycomb Kitaev Lattice in β-Li_2IrO_3: Full Solution via Magnetic Resonant X-ray Diffraction. *Physical Review B*, 90(20):205116, 2014.

[193] Y. Singh and P. Gegenwart. Antiferromagnetic Mott Insulating State in Single Crystals of the Honeycomb Lattice Material Na_2IrO_3. *Physical Review B*, 82(6): 064412, 2010.

[194] H. Gretarsson, J. P. Clancy, X. Liu, J. P. Hill, E. Bozin, Y. Singh, S. Manni, P. Gegenwart, J. Kim, A. H. Said, D. Casa, T. Gog, M. H. Upton, H.-S. Kim, J. Yu, V. M. Katukuri, L. Hozoi, J. van den Brink, and Y.-J. Kim. Crystal-field Splitting and Correlation Effect on the Electronic Structure of A_2IrO_3. *Physical Review Letters*, 110(7):076402, 2013.

[195] K. Geirhos, P. Lunkenheimer, M. Blankenhorn, R. Claus, Y. Matsumoto, K. Kitagawa, T. Takayama, H. Takagi, I. Kézsmárki, and A. Loidl. Quantum Paraelectricity in the Kitaev Quantum Spin Liquid Candidates $H_3LiIr_2O_6$ and $D_3LiIr_2O_6$. *Physical Review B*, 101:184410, 2020.

[196] S. Bette, T. Takayama, V. Duppel, A. Poulain, H. Takagi, and R. E. Dinnebier. Crystal Structure and Stacking Faults in the Layered Honeycomb, Delafossite-Type Materials Ag_3 $LiIr_2O_6$ and $Ag_3LiRu_2O_6$. *Dalton Transactions*, 48(25):9250–9259, 2019.

[197] F. Bahrami, W. Lafargue-Dit-Hauret, O. I. Lebedev, R. Movshovich, H.-Y. Yang, D. Broido, X. Rocquefelte, and F. Tafti. Thermodynamic Evidence of Proximity to a Kitaev Spin Liquid in Ag_3 $LiIr_2O_6$. *Physical Review Letters*, 123(23):237203, 2019.

[198] J. H. Roudebush, K. A. Ross, and R. J. Cava. Iridium Containing Honeycomb

Delafossites by Topotactic Cation Exchange. *Dalton Transactions*, 45(21):8783–8789, 2016.

[199] M. G. Yamada, V. Dwivedi, and M. Hermanns. Crystalline Kitaev Spin Liquids. *Physical Review B*, 96(15):155107, 2017.

[200] M. G. Yamada, H. Fujita, and M. Oshikawa. Designing Kitaev Spin Liquids in Metal-Organic Frameworks. *Physical Review Letters*, 119(5):057202, 2017.

[201] H. Fukuoka, H. Imoto, and T. Saito. New Polymorphs of $Ru^{III}P_3O_9$: Cyclohexaphosphate $Ru_2P_6O_{18}$ and metaphosphate $Ru(PO_3)_3$ with a novel structure. *Journal of Solid State Chemistry*, 119(1):107–114, 1995.

[202] H. Fukuoka and H. Imoto. Mixed-valence Ruthenium Diphosphates with a Tunnel Structure: $ARu_2(P_2O_7)_2$ (A = Li, Na, Ag, and Cu) and $Ru_2(P_2O_7)_2$. *Bulletin of the Chemical Society of Japan*, 70:2703–2708, 1997.

[203] H. Fukuoka, H. Imoto, and T. Saito. Synthesis and Crystal Structure of a New Ruthenium Silicophosphate: RuP_3SiO_{11}. *Journal of Solid State Chemistry*, 121(1): 247–250, 1996.

[204] VA Lyutsko and AF Selevich. Etude de la sorption de l'ammoniac sur du tripolyphosphate d'aluminium acide $H_2AlP_3O_{10}{\cdot}2H_2O$. *Žurnal neorganičeskoj himii*, 30(7):1800–1806, 1985.

[205] V. Lutsko and G. Johansson. The Crystal Structures of Iron (III) and Potassium Dihydrogen Triphosphate. *Acta Chemica Scandinavica A*, 38(9), 1984.

[206] D. I. Badrtdinov, L. Ding, C. Ritter, J. Hembacher, N. Ahmed, Y. Skourski, and A. A. Tsirlin. MoP_3SiO_{11}: A $4d^3$ Honeycomb Antiferromagnet with Disconnected Octahedra. *Physical Review B*, 104:094428, 2021.

[207] L.K. Elbouaanani, B. Malaman, and R. Gérardin. Synthesis, Crystal Structure,

and Magnetic Properties of FeP_3SiO_{11}: First Example of Iron(III)Silicophosphate. *Journal of Solid State Chemistry*, 147(2):565–572, 1999.

[208] A. J. Perez, D. Batuk, M. Saubanère, G. Rousse, D. Foix, E. McCalla, E. J. Berg, R. Dugas, K. H. W. van den Bos, M.-L. Doublet, D. Gonbeau, A. M. Abakumov, G. Van Tendeloo, and J.-M. Tarascon. Strong Oxygen Participation in the Redox Governing the Structural and Electrochemical Properties of Na-rich Layered Oxide Na_2IrO_3. *Chemistry of Materials*, 28(22):8278–8288, 2016.

[209] H. B. Cao, A. Banerjee, J.-Q. Yan, C. A. Bridges, M. D. Lumsden, D. G. Mandrus, D. A. Tennant, B. C. Chakoumakos, and S. E. Nagler. Low-temperature Crystal and Magnetic Structure of α-$RuCl_3$. *Physical Review B*, 93:134423, 2016.

[210] J. Nasu, M. Udagawa, and Y. Motome. Thermal Fractionalization of Quantum Spins in a Kitaev Model: Temperature-linear Specific Heat and Coherent Transport of Majorana Fermions. *Physical Review B*, 92:115122, 2015.

[211] Y. Yamaji, T. Suzuki, T. Yamada, S.-I. Suga, N. Kawashima, and M. Imada. Clues and Criteria for Designing a Kitaev Spin Liquid Revealed by Thermal and Spin Excitations of the Honeycomb Iridate Na_2IrO_3. *Physical Review B*, 93:174425, 2016.

[212] C. Balz, L. Janssen, P. Lampen-Kelley, A. Banerjee, Y. H. Liu, J.-Q. Yan, D. G. Mandrus, M. Vojta, and S. E. Nagler. Field-Induced Intermediate Ordered Phase and Anisotropic Interlayer Interactions in α-$RuCl_3$. *Physical Review B*, 103:174417, 2021.

[213] D. T. Cromer and J. T. Waber. Scattering Factors Computed from Relativistic Dirac–Slater Wave Functions. *Acta Crystallographica*, 18(1):104–109, 1965.

[214] J. D. Reger, J. A. Riera, and A. P. Young. Monte Carlo Simulations of the Spin-1/2 Heisenberg Antiferromagnet in Two Dimensions. *Journal of Physics: Condensed Matter*, 1(10):1855–1865, 1989.

[215] J. P. Perdew, K. Burke, and M. Ernzerhof. Generalized Gradient Approximation Made Mimple. *Physical Review Letters*, 77:3865–3868, 1996.

[216] S. Agrestini, C.-Y. Kuo, K.-T. Ko, Z. Hu, D. Kasinathan, H. B. Vasili, J. Herrero-Martin, S. M. Valvidares, E. Pellegrin, L.-Y. Jang, A. Henschel, M. Schmidt, A. Tanaka, and L. H. Tjeng. Electronically Highly Cubic Conditions for Ru in α-$RuCl_3$. *Physical Review B*, 96:161107(R), 2017.

[217] P. Warzanowski, N. Borgwardt, K. Hopfer, J. Attig, T. C. Koethe, P. Becker, V. Tsurkan, A. Loidl, M. Hermanns, P. H. M. van Loosdrecht, and M. Grüninger. Multiple Spin-Orbit Excitons and the Electronic Structure of α-$RuCl_3$. *Physical Review Research*, 2:042007(R), 2020.

[218] J. Bertinshaw, Y. K. Kim, G. Khaliullin, and B. J. Kim. Square Lattice Iridates. *Ann. Rev. Condens. Matter Phys.*, 10:315–336, 2019.

[219] S. M. Winter, Y. Li, H. O. Jeschke, and R. Valentí. Challenges in Design of Kitaev Materials: Magnetic Interactions from Competing Energy Scales. *Physical Review B*, 93:214431, 2016.

[220] C. R. Anderson, K. H. Andersen, J. Bossy, W. G. Stirling, R. M. Dimeo, P. E. Sokol, J. C. Cook, and D. W. Brown. High-resolution Neutron-scattering Study of the Roton in Confined Superfluid ^{4}He. *Physical Review B*, 59:13588–13591, 1999.

[221] T. Droß. *Neue Vanadiumphosphate und das Redox-Verhalten von Phosphaten des Vanadiums und Urans: Phasengleichgewichte, Sauerstoffkoexistenzdrücke und kristallographische Untersuchungen*. PhD thesis, University of Bonn, 2004.

[222] H. Thauern. *Phosphate des ein-und zweiwertigen Indiums und Einbau von Chrom (III) und Mangan (III) in Indium (III)-phosphate*. PhD thesis, University of Bonn, 2006.

[223] C. N. R. Rao, A. K. Cheetham, and A. Thirumurugan. Hybrid Inorganic–organic Materials: A New family in Condensed Matter Physics. *Journal of Physics: Condensed Matter*, 20(15):159801, 2008.

[224] D. Z. T. Mulrooney, J. E. Clements, Daniel J. E., J. R. Price, I. A. Kühne, S. J. Coles, C. J. Kepert, and T. D. Keene. Phase Control of Ferromagnetic Copper(II) Carbonate Coordination Polymers through Reagent Concentration. *European Journal of Inorganic Chemistry*, 2018(48):5223–5228, 2018.

[225] J. Liu, P. A. Goddard, J. Singleton, J. Brambleby, F. Foronda, J. S. Möller, Y. Kohama, S. Ghannadzadeh, A. Ardavan, S. J. Blundell, T. Lancaster, F. Xiao, R. C. Williams, F. L. Pratt, P. J. Baker, K. Wierschem, S. H. Lapidus, K. H. Stone, P. W. Stephens, J. Bendix, T. J. Woods, K. E. Carreiro, H. E. Tran, C. J. Villa, and J. L. Manson. Antiferromagnetism in a Family of $S = 1$ Square Lattice Coordination Polymers $NiX_2(pyz)_2$ (X = Cl, Br, I, NCS; pyz = Pyrazine). *Inorganic Chemistry*, 55:3515–3529, 2016.

[226] S. A. Ivko, K. Tustain, T. Dolling, A. Abdeldaim, O. H. J. Mustonen, P. Manuel, C. Wang, H. Luetkens, and L. Clark. Uncovering the $S = 1/2$ Kagome Ferromagnet within a Family of Metal–Organic Frameworks. *Chemistry of Materials*, 34:5409–5421, 2022.

[227] E. A. Nytko, J. S. Helton, P. Müller, and D. G. Nocera. A Structurally Perfect $S = 1/2$ Metal-Organic Hybrid Kagomé Antiferromagnet. *Journal of the American Chemical Society*, 130(10):2922–2923, 2008.

[228] R. Chisnell, J. S. Helton, D. E. Freedman, D. K. Singh, R. I. Bewley, D. G. Nocera, and Y. S. Lee. Topological Magnon Bands in a Kagome Lattice Ferromagnet. *Physical Review Letters*, 115:147201, 2015.

[229] P. Kanoo, C. Madhu, G. Mostafa, T. K. Maji, A. Sundaresan, S. K. Pati, and C. N. R. Rao. A Planar Cu^{2+} ($S = 1/2$) Kagomé Network Pillared By 1,2-bis(4-

pyridyl) Ethane with Interesting Magnetic Properties. *Dalton Trans.*, pages 5062–5064, 2009.

[230] T. D. Keene, M. J. Murphy, J. R. Price, N. F. Sciortino, P. D. Southon, and C. J. Kepert. Multifunctional MOFs Through CO_2 Fixation: A Metamagnetic Kagome Lattice with Uniaxial Zero Thermal Expansion and Reversible Guest Sorption. *Dalton Trans.*, 43:14766–14771, 2014.

[231] M. O. Ajeesh, A. Yogi, M. Padmanabhan, and R. Nath. Tuning of Magnetic Frustration in $S = 1/2$ Kagomé Lattices $[Cu_3(CO_3)_2(bpe)_3](ClO_4)_{2n}$ and $[Cu_3(CO_3)_2(bpy)_3](ClO_4)_{2n}$ Through Rigid and Flexible Ligands. *Solid State Communications*, 207:16–20, 2015.

[232] M. J. Cliffe, O. Fabelo, and L. Cañadillas-Delgado. Magnetic Order in a Metal Thiocyanate Perovskite-Analogue. *CrystEngComm*, 24:7250–7254, 2022.

[233] B. Dalla Piazza, M. Mourigal, N. B. Christensen, G. J. Nilsen, P. Tregenna-Piggott, T.G. Perring, M. Enderle, D. F. McMorrow, D. A. Ivanov, and H. M. Rønnow. Fractional Excitations in the Square-Lattice Quantum Antiferromagnet. *Nature Physics*, 11(1):62–68, 2015.

[234] B. Zhang, Y. Zhang, Z. Wang, D. Wang, P. J. Baker, F. L. Pratt, and D. Zhu. Candidate Quantum Spin Liquid Due to Dimensional Reduction of a Two-Dimensional Honeycomb Lattice. *Scientific Reports*, 4:6451, 2014.

[235] H. Okawa, M. Sadakiyo, K. Otsubo, K. Yoneda, T. Yamada, M. Ohba, and H. Kitagawa. Proton Conduction Study on Water Confined in Channel or Layer Networks of LaIIIMIII$(ox)_3 \cdot 10H_2O$ (M = Cr, Co, Ru, La). *Inorganic Chemistry*, 54:8529–8535, 2015.

[236] D. J. Price, S. Tripp, A. K. Powell, and P. T. Wood. Hydrothermal Synthesis, X-ray Structure and Complex Magnetic Behaviour of $Ba_4(C_2O_4)Cl_2[\{Fe(C_2O_4)(OH)\}_4]$. *Chemistry–A European Journal*, 7(1):200–208, 2001.

[237] R. B. English and D. J. Eve. Ammonium di-μ-oxalatotitanate(III) Dihydrate: An Eight-Coordinate, Polymeric Titanium(III) Complex. *Inorganica Chimica Acta*, 203 (2):219–222, 1993.

[238] H. S. Sheu, J. C. Wu, Y. Wang, and R. B. English. Charge Density Studies in $NH_4Ti(C_2O_4)_2{\cdot}2H_2O$ Crystals at Two Wavelengths. *Acta Crystallographica Section B*, 52(3):458–464, 1996.

[239] M. G. B. Drew and D. J. Eve. Caesium Triaquabis(oxalato)titanate(III) Dihydrate. *Acta Crystallographica Section B*, 33(9):2919–2921, 1977.

[240] A. Stähler. Zur Kenntniss des Titans. II. (Zum Theil gemeinsam mit Heinz Wirthwein). *Berichte der deutschen chemischen Gesellschaft*, 38(3):2619–2629, 1905.

[241] R. Nath, A. A. Tsirlin, H. Rosner, and C. Geibel. Magnetic Properties of $BaCdVO(PO_4)_2$: A Strongly Frustrated Spin-$\frac{1}{2}$ Square Lattice Close to the Quantum Critical Regime. *Physical Review B*, 78:064422, 2008.

[242] K. Uematsu and H. Kawamura. Randomness-induced Quantum Spin Liquid Behavior in the $s = \frac{1}{2}$ Random $J_1{-}J_2$ Heisenberg Antiferromagnet on the Square Lattice. *Physical Review B*, 98:134427, 2018.

[243] M. Skoulatos, F. Rucker, G. J. Nilsen, A. Bertin, E. Pomjakushina, J. Ollivier, A. Schneidewind, R. Georgii, O. Zaharko, L. Keller, Ch. Rüegg, C. Pfleiderer, B. Schmidt, N. Shannon, A. Kriele, A. Senyshyn, and A. Smerald. Putative Spin-Nematic Phase in $BaCdVO(PO_4)_2$. *Physical Review B*, 100:014405, 2019.

[244] K. Yu. Povarov, V. K. Bhartiya, Z. Yan, and A. Zheludev. Thermodynamics of a Frustrated Quantum Magnet on a Square Lattice. *Physical Review B*, 99:024413, 2019.

[245] J. Oitmaa. Diamond lattice Heisenberg Antiferromagnet. *Journal of Physics: Condensed Matter*, 30(15):155801, 2018.

[246] S. Gao, O. Zaharko, V. Tsurkan, Y. Su, J. S. White, G. S. Tucker, B. Roessli, F. Bourdarot, R. Sibille, D. Chernyshov, T. Fennell, A. Loidl, and C. Rüegg. Spiral Spin-Liquid and the Emergence of a Vortex-Like State in $MnSc_2S_4$. *Nature Physics*, 13(2):157–161, 2017.

[247] L. Ge, J. Flynn, J. A. M. Paddison, M. B. Stone, S. Calder, M. A. Subramanian, A. P. Ramirez, and M. Mourigal. Spin Order and Dynamics in the Diamond-Lattice Heisenberg Antiferromagnets $CuRh_2O_4$ and $CoRh_2O_4$. *Physical Review B*, 96:064413, 2017.

[248] G. J. MacDougall, D. Gout, J. L. Zarestky, G. Ehlers, A. Podlesnyak, M. A. McGuire, D. Mandrus, and S. E. Nagler. Kinetically Inhibited Order in a Diamond-Lattice Antiferromagnet. *Proceedings of the National Academy of Sciences*, 108(38): 15693–15698, 2011.

[249] N. Tristan, J. Hemberger, A. Krimmel, H-A. Krug von Nidda, V. Tsurkan, and A. Loidl. Geometric Frustration in the Cubic Spinels $M Al_2O_4$ (M = Co, Fe, and Mn). *Physical Review B*, 72:174404, 2005.

[250] G. Chen. Quantum Paramagnet and Frustrated Quantum Criticality in a Spin-one Diamond Lattice Antiferromagnet. *Physical Review B*, 96(2):020412, 2017.

[251] C. Wang, A. Nahum, and T. Senthil. Topological Paramagnetism in Frustrated Spin-1 Mott Insulators. *Physical Review B*, 91(19):195131, 2015.

[252] N. Tsyrulin, T. Pardini, R. R. P. Singh, F. Xiao, P. Link, A. Schneidewind, A. Hiess, C. P. Landee, M. M. Turnbull, and M. Kenzelmann. Quantum Effects in a Weakly Frustrated $S = 1/2$ Two-Dimensional Heisenberg Antiferromagnet in an Applied Magnetic Field. *Physical Review Letters*, 102:197201, 2009.

[253] N. Tsyrulin, F. Xiao, A. Schneidewind, P. Link, H. M. Rønnow, J. Gavilano, C. P. Landee, M. M. Turnbull, and M. Kenzelmann. Two-Dimensional Square-Lattice $S = \frac{1}{2}$ Antiferromagnet $Cu(pz)_2(ClO_4)_2$. *Physical Review B*, 81:134409, 2010.

[254] A. H. Abdeldaim, T. Li, L. Farrar, A. A. Tsirlin, W. Yao, A. S. Gibbs, P. Manuel, P. Lightfoot, G. J. Nilsen, and L. Clark. Realizing Square and Diamond Lattice $S = 1/2$ Heisenberg Antiferromagnet Models in the α and β Phases of the Coordination Framework, $KTi(C_2O_4)_2 \cdot xH_2O$. *Physical Review Materials*, 4:104414, 2020.

[255] G. M. Sheldrick. *SHELXT* – Integrated Space-group and Crystal-structure Determination. *Acta Crystallographica Section A*, 71(1):3–8, 2015.

[256] G. M. Sheldrick. Crystal Structure Refinement with *SHELXL*. *Acta Crystallographica Section C*, 71(1):3–8, 2015.

[257] O. V. Dolomanov, L. J. Bourhis, R. J. Gildea, J. A. K. Howard, and H. Puschmann. *OLEX2*: A Complete Structure Solution, Refinement and Analysis Program. *Journal of Applied Crystallography*, 42(2):339–341, 2009.

[258] A. A. Tsirlin, R. Nath, A. M. Abakumov, Y. Furukawa, D. C. Johnston, M. Hemmida, H.-A. Krug von Nidda, A. Loidl, C. Geibel, and H. Rosner. Phase Separation and Frustrated Square Lattice Magnetism of $Na_{1.5}VOPO_4F_{0.5}$. *Physical Review B*, 84:014429, 2011.

[259] T. Lancaster, S. J. Blundell, M. L. Brooks, P. J. Baker, F. L. Pratt, J. L. Manson, M. M. Conner, F. Xiao, C. P. Landee, F. A. Chaves, S. Soriano, M. A. Novak, T. P. Papageorgiou, A. D. Bianchi, T. Herrmannsdörfer, J. Wosnitza, and J. A. Schlueter. Magnetic Order in the $S = 1/2$ Two-Dimensional Molecular Antiferromagnet Copper Pyrazine Perchlorate $Cu(Pz)_2(ClO_4)_2$. *Physical Review B*, 75:094421, 2007.

[260] R. Nath, M. Padmanabhan, S. Baby, A. Thirumurugan, D. Ehlers, M. Hemmida, H.-A. Krug von Nidda, and A. A. Tsirlin. Quasi-Two-Dimensional $S = \frac{1}{2}$ Magnetism of $Cu[C_6H_2(COO)_4][C_2H_5NH_3]_2$. *Physical Review B*, 91:054409, 2015.

[261] C. Yasuda, S. Todo, K. Hukushima, F. Alet, M. Keller, M. Troyer, and H. Takayama. Néel Temperature of Quasi-Low-Dimensional Heisenberg Antiferromagnets. *Physical Review Letters*, 94:217201, 2005.

[262] E. Manousakis. The Spin-½ Heisenberg Antiferromagnet on a Square Lattice and its Application to the Cuprous Oxides. *Reviews of Modern Physics*, 63:1–62, 1991.

[263] B.-G. Liu. Low-Temperature Properties of the Quasi-Two-Dimensional Antiferromagnetic Heisenberg Model. *Physical Review B*, 41:9563–9565, 1990.

[264] S. Bettler, F. Landolt, Ö. M. Aksoy, Z. Yan, S. Gvasaliya, Y. Qiu, E. Ressouche, K. Beauvois, S. Raymond, A. N. Ponomaryov, S. A. Zvyagin, and A. Zheludev. Magnetic Structure and Spin Waves in the Frustrated Ferro-Antiferromagnet $Pb_2VO(PO_4)_2$. *Physical Review B*, 99:184437, 2019.

[265] T. Koga, N. Kurita, M. Avdeev, S. Danilkin, T. J. Sato, and H. Tanaka. Magnetic Structure of the $S = \frac{1}{2}$ Quasi-Two-Dimensional Square-Lattice Heisenberg Antiferromagnet Sr_2CuTeO_6. *Physical Review B*, 93:054426, 2016.

[266] S. Fujio, K. Tanaka, and H. Inui. Formation Probability for Enantiomorphic Crystals (With the Space Groups of $P6_222$ and $P6_422$) in Transition-Metal Disilicides with the C40 Structure as Determined by Convergent-Beam Electron Diffraction. *Intermetallics*, 15(3):245–252, 2007.

[267] J. Oitmaa. Frustrated Diamond Lattice Antiferromagnet. *Physical Review B*, 99: 134407, 2019.

[268] J. P. Perdew and Y. Wang. Accurate and Simple Analytic Representation of the Electron-Gas Correlation Energy. *Physical Review B*, 45:13244–13249, 1992.

[269] O. Kahn. Dinuclear Complexes with Predictable Magnetic Properties. *Angewandte Chemie International Edition in English*, 24(10):834–850, 1985.

[270] J. Cano, P. Alemany, S. Alvarez, M. Verdaguer, and E. Ruiz. Exchange Coupling in Oxalato-Bridged Copper(II) Binuclear Compounds: A Density Functional Study. *Chemistry – A European Journal*, 4(3):476–484, 1998.